



저작자표시 2.0 대한민국

이용자는 아래의 조건을 따르는 경우에 한하여 자유롭게

- 이 저작물을 복제, 배포, 전송, 전시, 공연 및 방송할 수 있습니다.
- 이차적 저작물을 작성할 수 있습니다.
- 이 저작물을 영리 목적으로 이용할 수 있습니다.

다음과 같은 조건을 따라야 합니다:



저작자표시. 귀하는 원저작자를 표시하여야 합니다.

- 귀하는, 이 저작물의 재이용이나 배포의 경우, 이 저작물에 적용된 이용허락조건을 명확하게 나타내어야 합니다.
- 저작권자로부터 별도의 허가를 받으면 이러한 조건들은 적용되지 않습니다.

저작권법에 따른 이용자의 권리는 위의 내용에 의하여 영향을 받지 않습니다.

이것은 [이용허락규약\(Legal Code\)](#)을 이해하기 쉽게 요약한 것입니다.

[Disclaimer](#) 

공학박사 학위논문

자유수면이 수면관통물체 주위의
난류 경계층과 후류에 미치는 영향

**Free-Surface Effects on
Turbulent Boundary Layer and Near-Wake
Around a Surface-Piercing Body**

2016년 8월

서울대학교 대학원
조선해양공학과
서정화

자유수면이 수면관통물체 주위의
난류 경계층과 후류에 미치는 영향

지도교수 이 신 형

이 논문을 공학박사 학위논문으로 제출함
2016년 8월

서울대학교 대학원
조선해양공학과
서 정 화

서정화의 공학박사 학위논문을 인준함
2016년 7월

위 원 장	_____	(인)
부 위 원 장	_____	(인)
위 원	_____	(인)
위 원	_____	(인)
위 원	_____	(인)

Abstract

In this study, free-surface effects on boundary layer and near-wake around a slender free-surface piercing body were investigated by flow field and wave elevation measurements. To provide three different wave conditions, three Froude number (Fr) conditions were applied for model tests: 0.126, 0.282, and 0.400. In addition, models of three different sizes were chosen to range Reynolds number (Re) from 34,200 to 1,080,000.

Wave elevation was measured by capacitance type wave height gauge and observation. Wave breaking and bubbly free-surface were observed for $Fr = 0.400$, as reported in previous studies on the surface piercing body. At the bubbly free-surface region, the fluctuation of the free-surface elevation in certain frequency range appeared.

Flow field were measured by towed underwater stereoscopic particle image velocimetry (SPIV) system. Towed SPIV measured three-components of velocity on a two-dimensional planes, which were perpendicular to the longitudinal direction of the model. By the SPIV measurement, free-surface effects on the boundary layer development for $Fr = 0.126$, where wave was hardly generated, were identified first. At the juncture of the free-surface and the model surface, flow fluctuated in normal direction to the free-surface and it reduced the flow velocity. The turbulence strength and isotropy increased near the juncture. In the near-wake, the free-surface delayed the wake recovery and turbulence dissipation.

The free-surface wave was developed in the intermediate Fr condition. It was steady and smooth, thus orbital motion of water particles in waves was well observed at outside of the boundary layer. The boundary layer restrained

orbital motion due to no-slip wall effects. Behind the trailing edge of the model, the free-surface fluctuated and knobs were observed. At the free-surface and model surface juncture, reverse flow appeared and turbulence kinetic energy increased along the boundary of the stationary flow region, because of strong shear strain.

As Fr increased, the knobby free-surface region expanded upstream and bubbly free-surface affected the flow underneath it. The turbulence induced by the violent free-surface behavior was omnidirectional and decreased anisotropy near the free-surface. In the near-wake region, the knobby free-surface stimulated momentum transportation and turbulence dissipation. As the violent free-surface behavior dissipated turbulence in near-wake, dominant turbulence dynamics in low frequency decreased rapidly in downstream.

In addition, testing models of different sizes followed. By wave elevation measurement, it was confirmed that the wave elevation decreased in low Re conditions as viscous force became significant. Free-surface fluctuation also reduced and capillary wave appeared as Re decreased. Viscous force effects were also visible in flow fields. The boundary layer thickness ratio increased, but flow separation along the trailing edge in high Fr condition decreased and localized near the free-surface only.

Keywords: Free-Surface, Turbulent Boundary Layer, Wave Induced Separation, Model Test, Stereoscopic Particle Image Velocimetry

Student number: 2010-21102

Table of Contents

Abstract.....	i
Table of Contents	iii
List of Tables	vi
List of Figures.....	vii
Chapter 1. Introduction.....	1
1.1. Background.....	1
1.2. Theory and literature review	5
1.2.1. Free-surface wave around a model in a constant speed	5
1.2.2. Overview of literature review	6
1.2.3. Wave-induced separation and surface piercing body.....	7
1.2.4. Relevant free-surface behavior: juncture-bounded turbulence	14
1.2.5. Relevant free-surface behavior: hydraulic jump	15
1.2.6. Scale effects on the interaction of free-surface and turbulent flow.....	18
1.2.7. Experiments for turbulent flow field measurements in towing tanks	19
1.2.8. Analysis methods for turbulence research	23
1.3. Objectives and outline of thesis	26
Chapter 2. Test Design	28
2.1. Facility	28
2.2. Test model.....	30
2.3. Test conditions	33
2.4. Measurement systems	35
2.4.1. SPIV system: hardware.....	35
2.4.2. SPIV system: calibration.....	40
2.4.3. SPIV system: tracer particle.....	45

2.2.4. SPIV system: velocity field analysis.....	46
2.4.5. LDV system: hardware	52
2.4.6. LDV system: velocity analysis	56
2.4.7. Wave height gauge.....	58
2.5. Measurement locations	59
2.5.1. Velocity field measurement	59
2.5.2. Wave height measurement	61

Chapter 3. Test Uncertainty..... 62

3.1. Overview	62
3.2. Uniform flow measurement setup.....	65
3.2.1. Towing carriage speed	65
3.2.2. 1D LDV measurement	67
3.2.3. Towed underwater SPIV system.....	68
3.3. Uncertainty assessment: systematic error	70
3.3.1. 1D LDV measurement	70
3.3.2. SPIV measurement.....	72
3.4. Model ship nominal wake measurement.....	78
3.4.1. Test model and test conditions.....	78
3.4.2. Test results: data convergence	80
3.4.3. Test results: comparisons of mean velocity and turbulence.....	84

Chapter 4. Results and Discussion 90

4.1. Free-surface wave elevation: large model case.....	90
4.2. Boundary layer flows: large model case	98
4.2.1. $Fr = 0.126$ (smooth and steady free-surface with negligible wave)	98
4.2.2. $Fr = 0.282$ (smooth and steady free-surface waves)	106
4.2.3. $Fr = 0.400$ (bubbly and unsteady free-surface waves)	113
4.3. Wake field flows: large model case	125
4.3.1. $Fr = 0.126$ (smooth and steady free-surface with negligible waves) ...	125

4.3.2. Fr = 0.282 (smooth free-surface waves) and 0.400 (knobby wake).....	131
4.3. Coherent turbulence structure	145
4.3.1. Fr = 0.126 (smooth and steady free-surface with negligible wave)	145
4.3.2. Fr = 0.282 (smooth and steady free-surface waves)	153
4.3.3. Fr = 0.400 (bubbly and unsteady free-surface waves)	159
4.4. Scale effects on the free-surface wave and flow fields	166
4.4.1. Free-surface elevation in different scales.....	166
4.4.2. Boundary layer in different scales	168
4.4.3. Near-wake in different scales.....	170
Chapter 5. Summary and Conclusions	175
References	181
Abstract (Korean)	194

List of Tables

Table 2-1 Test conditions	33
Table 2-2. Comparison of restricted-water effects	34
Table 2-3. Time intervals of particle image frame acquisition	39
Table 3-1. Towing carriage speed measured by beacons and correction results	66
Table 3-2. Towing carriage speed measurement by rotary encoder	67
Table 3-3. Particle displacement in the uniform flow at $U = 1.0 \text{ m/s}$	69
Table 3-4. Uniform flow measurement by 1D LDV	70
Table 3-5. Errors of mean velocity and turbulence properties obtained by the uniform flow measurement.....	74
Table 3-6. The systematic error of mean velocity measurement by SPIV	77
Table 3-7. Total uncertainty of measurement systems	82

List of Figures

Figure 2-1. Schematic of SNUTT.	28
Figure 2-2. Cross section of the test model.....	30
Figure 2-3. Manufactured models.....	31
Figure 2-4. Schematic of the towed underwater SPIV system.	35
Figure 2-5. Laser system of the SPIV system: Evergreen 200- <i>mJ</i> laser head and power supply (left) and mirror arrangement and laser path (right).....	36
Figure 2-6. Arrangement of components in the submergible vertical cylinder.	37
Figure 2-7. Optical arrangement of the towed underwater SPIV system.	38
Figure 2-8. Calibration target.....	40
Figure 2-9. Calibration target images and field of view.	41
Figure 2-10. Dot identification.	41
Figure 2-11. Calibration results.	43
Figure 2-12. Comparisons of locations in the raw and corrected images.	43
Figure 2-13. Corrected calibration target images: reference plane at $z = 0$ (left) and -3 mm (right).....	44
Figure 2-14. Self-calibration procedure: (a) calibration target misaligned with the laser sheet; (b) disparity map between two cameras; and (c) corrected calibration on the measurement plane (LaVision GmbH, 2012).....	45
Figure 2-15. Particle image and interrogation windows.	46
Figure 2-16. Flow chart of SPIV vector computation (LaVision GmbH, 2012).	47
Figure 2-17. System components of the underwater LDV system.	53

Figure 2-18. Continuous argon ion laser head.	53
Figure 2-19. Beam splitter with Bragg cell and fiber manipulator.	54
Figure 2-20. 60X61 FlowLite waterproof LDV probe.	55
Figure 2-21. Schematic of LDV optics (Dantec A/S, 2014).	56
Figure 2-22. Screenshot of LDV data acquisition using BSA Flow v5.	57
Figure 2-23. Capacitance-type wave height gauge system.	58
Figure 2-24. Locations of measurement planes.	59
Figure 2-25. SPIV measurement plane locations.	60
Figure 2-26. Wave elevation measurement locations.	61
Figure 3-1. Principle of errors in measurement (ASME, 2005).	62
Figure 3-2. Arrangement of the towing tank and beacons.	66
Figure 3-3. Time history of uniform flow measurement by 1D LDV.	71
Figure 3-4. Mean velocity of uniform flow measurement results: u/U (top), v/U (middle), w/U (bottom).	72
Figure 3-5. Reynolds stress distribution of uniform flow measurement results.	73
Figure 3-6. Uniform flow measurements with particle displacement variations.	76
Figure 3-7. Lines of KVLCC2 hull.	78
Figure 3-8. Snapshots of local flow measurement tests: SPIV (top) and 1D LDV (bottom).	79
Figure 3-9. Data convergence results: u/U at $y/R = 0.6$ and $z/R = -0.6$	81
Figure 3-10. Convergence of Reynolds normal stress according to data sample number.	83
Figure 3-11. Mean velocity field at the propeller plane of the KVLCC2 model ship: u/U contours and on-plane vectors.	85
Figure 3-12. Comparisons of mean velocity at $z/R = -0.6$ (left) and 0.6 (right).	

.....	86
Figure 3-13. Reynolds normal stress distribution at the propeller plane of KVLCC2 model ship: $u'u'/U^2 \times 100$ contours.	87
Figure 3-14. Comparisons of Reynolds normal stresses at $z/R = -0.6$ (left) and 0.6 (right).....	89
Figure 4-1. Wave pattern around the large model.	90
Figure 4-2. Magnified snapshot of free-surface around large model at $Fr = 0.400$	92
Figure 4-3. Wave elevation from analytic solution and measurement for $Fr = 0.282$ and 0.400	93
Figure 4-4. Free-surface wave around the trailing edge of the large model: solid circles indicate wave elevation locations analyzed by FFT.	94
Figure 4-5. Wave elevation measurement results in undisturbed free-surface conditions.	95
Figure 4-6. Wave elevations in frequency domain around the large test model measurement results at $x/L = 0.25$	96
Figure 4-7. Wave elevation in frequency domain for two different Fr conditions.	97
Figure 4-8. Mean velocity fields of boundary layer region for $Fr = 0.126$. .	98
Figure 4-9. u/U distribution on the model surface for $Fr = 0.126$	99
Figure 4-10. Boundary layer thickness for $Fr = 0.126$: displacement thickness (solid line) and momentum thickness (broken line).	100
Figure 4-11. Reynolds normal stresses in boundary layer region for $Fr = 0.126$	102
Figure 4-12. Reynolds shear stresses in boundary layer region for $Fr = 0.126$	103
Figure 4-13. $k/U^2 \times 1000$ distribution in boundary layer region for $Fr = 0.126$	104

Figure 4-14. $k/U^2 \times 1000$ near the model surface for $Fr = 0.126$	105
Figure 4-15. Displacement thickness (broken lines) and spatial mean of k (solid line and symbols) for $Fr = 0.126$	106
Figure 4-16. Mean velocity fields of boundary layer region for $Fr = 0.282$	107
Figure 4-17. w/U in the outer region ($0.05 L$ from the model surface) for $Fr = 0.282$	108
Figure 4-18. Longitudinal velocity perturbation ($(u-U)/U$) in the outer region ($0.05 L$ from the model surface) for $Fr = 0.282$	109
Figure 4-19. Comparisons of w/U in the outer region ($0.05 L$ from the model surface) and near the model surface ($0.01 L$ from the model surface) for $Fr = 0.282$	110
Figure 4-20. Turbulent boundary layer effects on w/U in the outer region orbital motion for $Fr = 0.282$: non-dimensionalized by U (left) and $w(x)$ (right).	110
Figure 4-21. Reynolds normal stress distribution at $x/L = 0.45$ and $Fr = 0.282$	111
Figure 4-22. Reynolds shear stress distribution at $x/L = 0.45$ and $Fr = 0.282$	112
Figure 4-23. $k/U^2 \times 1000$ distribution in boundary layer region for $Fr = 0.282$	112
Figure 4-24. Mean velocity fields of the boundary layer region for $Fr = 0.400$	113
Figure 4-25. u/U distributions in the boundary layer region for $Fr = 0.400$	114
Figure 4-26. Reynolds normal stress distribution at $x/L = 0.45$ and $Fr = 0.400$	116
Figure 4-27. Reynolds shear stress distribution at $x/L = 0.45$ and $Fr = 0.400$	117
Figure 4-28. Comparisons of Reynolds normal stress distributions at $x/L =$	

0.450.....	118
Figure 4-29. Anisotropy distribution at $x/L = 0.45$	120
Figure 4-30. $k/U^2 \times 1000$ distribution of boundary layer region at $Fr = 0.400$	121
Figure 4-31. Turbulence kinetic energy distribution on the model surface at $x/L = 0.45$	122
Figure 4-32. Schematic of flow characteristics in the boundary layer region: (A) free-surface and solid-wall juncture layer, (B) free-surface boundary layer, (C) solid-wall boundary layer, and (D) outer flow.....	123
Figure 4-33. Mean velocity distribution in the near-wake fields for $Fr = 0.126$	125
Figure 4-34. u/U distribution in near-wake region for $Fr = 0.126$	126
Figure 4-35. Wake width from the centerline in the near-wake region for $Fr =$ 0.126 : displacement width (solid line) and momentum width (broken line).	127
Figure 4-36. Reynolds normal stress distribution in the near-wake region for $Fr = 0.126$	128
Figure 4-37. Reynolds shear stress distributions in the near-wake region for Fr $= 0.126$	129
Figure 4-38. $k/U^2 \times 1000$ distribution in the near-wake region for $Fr = 0.126$	130
Figure 4-39. $k/U^2 \times 1000$ distribution in the near-wake region at $z/L = -0.01$ and -0.1 and $Fr = 0.126$	130
Figure 4-40. Spatial mean of $k/U^2 \times 1000$ in the near-wake region for $Fr =$ 0.126	131
Figure 4-41. Mean velocity distribution in the near-wake fields for $Fr = 0.282$	132
Figure 4-42. Mean velocity distribution in the near-wake fields for $Fr = 0.400$	132

Figure 4-43. u/U distributions at $x/L = 0.5$ (solid line) and 0.6 (broken line).	133
Figure 4-44. Difference of u/U between $x/L = 0.5$ (solid line) and 0.6 (broken line).	134
Figure 4-45. Reynolds normal stress distribution in the near-wake region for $Fr = 0.282$	135
Figure 4-46. Reynolds normal stress distribution in the near-wake region for $Fr = 0.282$	136
Figure 4-47. Reynolds normal stress distribution in the near-wake region for $Fr = 0.400$	138
Figure 4-48. Reynolds normal stress distribution in the near-wake region for $Fr = 0.282$	139
Figure 4-49. Anisotropy distribution at $x/L = 0.5$ (solid line) and 0.6 (broken line).	141
Figure 4-50. $k/U^2 \times 1000$ distribution in the near-wake region for $Fr = 0.282$	142
Figure 4-51. $k/U^2 \times 1000$ distribution in the near-wake region for $Fr = 0.282$	142
Figure 4-52. $k/U^2 \times 1000$ changes in near-wake region at $z/L = -0.01$ (solid line) and -0.1 (broken line).	143
Figure 4-53. Comparison of $k/U^2 \times 1000$ in the near-wake region.	144
Figure 4-54. Coherent turbulence structures for low modes at $x/L = 0.4$ and $Fr = 0.126$	146
Figure 4-55. Frequency of turbulence fluctuation for low modes at $x/L = 0.4$ and $Fr = 0.126$	147
Figure 4-56. Coherent turbulence structures for low modes at $x/L = 0.5$ and $Fr = 0.126$	149
Figure 4-57. Frequency of turbulence fluctuation for low modes at $x/L = 0.5$ and $Fr = 0.126$	150
Figure 4-58. Coherent turbulence structures for low modes at $x/L = 0.6$ and Fr	

= 0.126.....	151
Figure 4-59. Frequency of turbulence fluctuation for low modes at $x/L = 0.6$ and $Fr = 0.126$	152
Figure 4-60. Coherent turbulence structures for low modes at $x/L = 0.4$ and Fr = 0.282.....	153
Figure 4-61. Coherent turbulence structures for low modes at $x/L = 0.5$ and Fr = 0.282.....	154
Figure 4-62. Coherent turbulence structures for low modes at $x/L = 0.6$ and Fr = 0.282.....	155
Figure 4-63. Frequency of turbulence fluctuation for low modes at $x/L = 0.4$ and $Fr = 0.282$	156
Figure 4-64. Frequency of turbulence fluctuation for low modes at $x/L = 0.5$ and $Fr = 0.282$	157
Figure 4-65. Frequency of turbulence fluctuation for low modes at $x/L = 0.6$ and $Fr = 0.282$	158
Figure 4-66. Coherent turbulence structures for low modes at $x/L = 0.4$ and Fr = 0.400.....	159
Figure 4-67. Coherent turbulence structures for low modes at $x/L = 0.5$ and Fr = 0.400.....	160
Figure 4-68. Coherent turbulence structures for low modes at $x/L = 0.6$ and Fr = 0.400.....	161
Figure 4-69. Frequency of turbulence fluctuation for low modes at $x/L = 0.4$ and $Fr = 0.400$	162
Figure 4-70. Frequency of turbulence fluctuation for low modes at $x/L = 0.5$ and $Fr = 0.400$	163
Figure 4-71. Frequency of turbulence fluctuation for low modes at $x/L = 0.6$ and $Fr = 0.400$	164
Figure 4-72. Energy distributions of POD results at $x/L = 0.5$	165
Figure 4-73. Free-surface wave changes for $Fr = 0.400$ according to Re variations.	166

Figure 4-74. Wave elevation around the model for $Fr = 0.400$ and 0.282 with Re variations.	167
Figure 4-75. u/U contours and on-plane velocity vectors in the boundary layer region for $Fr = 0.400$	169
Figure 4-76. u/U contours and on-plane velocity vectors at TE with Re variations for $Fr = 0.126$	170
Figure 4-77. $k/U^2 \times 1000$ distribution at TE with Re variations for $Fr = 0.126$	171
Figure 4-78. Mean velocity (top) and $k/U^2 \times 1000$ (bottom) distribution at TE with Re variations for $Fr = 0.400$	172
Figure 4-79. Comparisons of mean velocity at $x/L = 0.6$ with Fr and Re variations.	173

Chapter 1. Introduction

1.1. Background

Problems on turbulent flow with free-surface have been studied widely and profoundly in naval architecture and civil, ocean, and coastal engineering as those engineering fields deal with macro-scale water flows, such as flow around a ship, offshore platform, and piers. Those problems include turbulence, which is complicated and hard to investigate owing to non-linear nature and high degrees of freedom; traditionally, analyses on the free-surface behavior have been based on the potential flow theory which use linear governing equations assuming that flow is inviscid and non-linearity is negligible. Analyses using the potential flow theory have produced results swiftly which are reliable in global tendency qualitatively, *i.e.*, wave-making resistance and wave profiles; however, they have limitations in accessing local flow features and flows in extreme conditions, which have been discussed majorly in modern fluid dynamics.

At the intersection of turbulent boundary layer and free-surface, flows are similar with wall-bounded corner, but they are affected by multi-scale physical characteristics of free-surface, those are, surface tension, anisotropic turbulence development and dissipation, and pressure gradient generated by waves. Owing to those physics, three-dimensional (3D) flow separation, water film generation on the model surface, wave breaking, capillary waves, air entrainment, water spray, and necklace vortex generation appear in flow fields. They have been investigated by means of experiments, analytic methods, and numerical simulations to understand free-surface effects on turbulent flows.

The free-surface effects on turbulent flow are applicable to various engineering fields, as described above. For example, in designing high-speed vessels, flow near the hull results in wave breaking and spray which function as additional resistance and instability of the ship. In general, the ship resistance is predicted by model tests which follow Froude's scaling law, but scale effects of wave breaking and spray are not yet fully understood and the method to deal with them is in demand (Savitsky *et al.*, 2007; Taunton *et al.*, 2010). Turbulence-induced-hydroacoustic noise around a hull is also a good instance of application. The noise around the stern of a naval vessel increases possibilities of being detected. In the case of offshore wind turbines of commercial vessels, hydroacoustic noise caused by free-surface and the structure cause harm to marine animals like whales (Richardson *et al.*, 1995; Soto *et al.*, 2006).

For the research on free-surface and turbulent flow, a free-surface piercing body, which has infinite draft and constant cross section, has been frequently used. In flow fields around a free-surface piercing body, two-dimensional (2D) flow fields obtained in deep locations are compared with the flow near the free-surface to identify free-surface effects. Tests with free-surface piercing body were first suggested in the experimental and analytic study performed by Wigley (1934). The cross section of the model is intersection of two parabolic curves. By using the free-surface piercing body with large draft, 3D flow from the bottom of the model is excluded, thus the flow physics is simpler than that around a vessel with limited draft and easy to study.

Because of the simplified flow phenomena, free-surface piercing bodies with various cross sections have been studied in the field of hydrodynamics computationally and experimentally. Surface piercing flat plate, hydrofoil cross section, and circular cylinder have been utilized frequently. As circular

cylinder model accompanies severe flow separation due to its blunt geometry rather than the free-surface waves, slender models like a flat plate or hydrofoils have been used for examining free-surface effects on turbulent boundary layer flow fields, rather than effects of intense flow separation.

By using slender free-surface piercing bodies, wave-induced separation, 3D flow separation under the interface due to adverse pressure gradient caused by free-surface waves in certain Froude number (Fr) conditions has been studied. It is one of the most renowned complicated flow phenomena in interactions between free-surface and turbulent boundary layer. The wave-induced separations are observed even though the model is slender enough to prevent flow separation at deep location where 2D flow is expected. The flow separation is localized near the free-surface and the separated region is identified by violent free-surface. It usually occurs behind the wave trough and around trailing edge of the model.

As the free-surface behavior with turbulent flow is affected by multi-scale physics, scale effects exist on the free-surface bounded turbulent flow. Changes in turbulent flow features according to Reynolds number (Re) conditions are important research topic, as researches are conducted in laboratory scales and results are extrapolated to massive scales for practical applications.

To understand scale effects on turbulence and free-surface flows in depth, novel research techniques which deal with unsteady turbulent flows have been required. Thanks to improvements in experimental and computational methods, novel measurements and analysis methods enable direct approach to unsteady turbulent flow features. Non-invasive measurements, *e.g.*, laser Doppler velocimetry (LDV) and particle image velocimetry (PIV), have been

introduced to the experiments. They can measure instantaneous velocity fields. For numerical analyses, computational fluid dynamics methods using unsteady Reynolds-averaged Navier Stokes (URANS) equation and large eddy simulation (LES) have been used and produced meaningful results recently.

1.2. Theory and literature review

1.2.1. Free-surface wave around a model in a constant speed

Wave-induced separation and breaking waves result from adverse pressure gradient. Kelvin wave, model geometry, and viscosity contribute to the adverse pressure gradient. Principles of those three physics are described in this section.

When a surface piercing body advance in a constant speed (U), a Kelvin wave with corresponding wave length (λ) is generated. The advance speed of the wave is same with U . λ is proportional to the square of U ,

$$\lambda = 2\pi Fr^2 L = 2\pi U^2 / g \quad (1-1)$$

where g , L , and Fr are the gravitational acceleration, model length, and model length based Froude number, respectively. When the flow progresses downstream from the wave trough to the wave crest, the adverse pressure gradient due to difference in gravitational potential between the wave trough and the crest retards the flow velocity. On the contrary, flow from the wave crest to wave trough suffers favorable pressure gradient.

The pressure gradient due to Kelvin wave is proportional to the wave steepness (H/λ), thus the wave height (H) should be also taken into account as well as λ . According to the analytic methods (Wigley, 1934), H increases as the fourth power of U ; H/λ is proportional to the square of U . When U increases, H/λ of the Kelvin wave and corresponding adverse pressure gradient also increase, resulting in 3D flow separation and breaking wave.

The bluntness of free-surface piercing body also induces pressure gradient as well as Fr condition. According to the inviscid flow analysis, the stagnation points locate at the leading and trailing edge of the model. At the stagnation

points, flow velocity is zero and the static pressure increases, whereas pressure reduces and velocity increases at the mid-body. As the flow streams from the mid-body to the trailing edge, there exists adverse pressure gradient which diminishes the flow velocity. When the cross section of the free-surface piercing body is too blunt, *e.g.*, a circular cylinder, the adverse pressure gradient become large enough to prompt the flow separation without free-surface effects; for study of wave-induced separation, too blunt model should be avoided.

In boundary layer, kinetic energy of the flow changes into thermal energy by friction and turbulence dissipation, therefore the flow speed degrades. The head loss in the laminar or turbulent boundary layer flow also results in the adverse pressure gradient. In the laminar boundary layer, viscous shear stress dominates head loss, while the head loss from Reynolds stresses generation is prevalent in turbulent boundary layer.

A number of researches on wave-induced separation have been focused on the flow fields at Fr around 0.4. At Fr of 0.399, corresponding λ is identical to L . The wave crest locates near the leading and trailing edge of the model and the wave trough is near the mid-body; the adverse pressure gradient from wave and the model geometry is superposed, thus the wave-induced separation is easy to occur.

1.2.2. Overview of literature review

The present study concentrates on the wave-induced effects on turbulent flow around a slender free-surface piercing body and its scale effects. To achieve the purpose, a comprehensive review on the physical phenomena and experiment and analysis methods are needed. There have been a number of

studies on turbulent flow, but only limited number of researches concern wave-induced effects on turbulent boundary layer and wake fields. This literature review consists of five subjects: wave-induced separation, relevant free-surface behaviors (junction-bounded turbulence and hydraulic jump), scale effects on the interaction of free-surface and turbulent flow, experiments for turbulent flow field measurements in towing tanks, and analysis method for turbulence research.

1.2.3. Wave-induced separation and surface piercing body

Wave-induced separation is one of the main objects of this thesis. As described above, wave-induced separation occurs when adverse pressure gradient from wave, model geometry, and viscous/turbulent boundary layer is excessive and the wave cannot retain its form. For understanding free-surface wave effects on the flow separation, the adverse pressure gradient from waves should be more dominant than the others. The waves generated externally or Kelvin wave from the model itself have utilized in previous studies. To eliminate the 3D effects from model bottom, the model which has large draft, *i.e.*, free-surface piercing body, has been generally used in the study of wave-induced separation.

Stern *et al.* (1987) design a model test with a vertical flat plate and horizontal hydrofoil. The plate is too thin to generate Kelvin wave in meaningful magnitude, thus a horizontal hydrofoil is located in front of the vertical plate to make a 2D Stokes wave train. The wave height and steepness are controlled by adjusting vertical location of the foil. The concept for generating external Stokes waves is firstly attempted by Salvesen (1969). When the foil is located near the free-surface, the wave steepness increases

enough to result in wave breaking.

In the experimental and numerical study using the horizontal foil-vertical surface piercing flat plate (Stern *et al.* 1989), wave profile observation and three-holes Pitot tube measurements on vertical and streamwise flow velocity are compared with computation results. It is confirmed that streamwise flow from the wave trough to crest is decelerated by the adverse pressure gradient of waves. Taking the deceleration into account, the turbulent boundary layer thickens and wall shear stress reduces. The wave-induced separation happens when the wave steepness is large as adverse pressure gradient is dominant in the turbulent boundary layer.

As a succeeding research, Stern *et al.* (1993) measure wake fields of the vertical plate and horizontal hydrofoil. Velocity fields with three components (3C) are measured by five-holes Pitot tube. Free-surface wave effects on development of wake fields are identified by comparisons of the results with and without Stokes waves. A complementary RANS computation on the same condition with experiments is also performed in the study. The computations is coincident with the experiments overall, although there are quantitative differences in prediction of wave-induced effects on velocity fields.

Albeit invaluable information on wave effects on mean velocity field is provided by the study of Stern *et al.* (1993), there have been requirements of quantitative turbulent properties measurement. Longo *et al.* (1998) use LDV system in a towing tank to acquire the Reynolds-averaged flow field around the surface piercing vertical plate without Stokes waves to focus on the solid/free-surface juncture flow. Near the free-surface, retardation of streamwise flow velocity and increase of turbulent kinetic energy are observed. Time-mean flow is analyzed in terms of streamwise vorticity to find that the

anisotropic Reynolds stresses are correlated with the vorticity distributions. It is concluded that the anisotropy of the Reynolds stresses causes the streamwise vortex.

Marquardt (2009) introduce stereoscopic particle image velocimetry (SPIV) system into the horizontal hydrofoil and vertical plate problem. Wave elevation, turbulent boundary layer, and wake fields are measured. The results coincide with previous Pitot tube and LDV measurement. Boundary layer thickness is altered by the Stokes wave. The Stokes wave diminishes downstream due to viscous damping on the plate surface. As SPIV measurement can provide the Reynolds-averaged velocity fields with higher spatial resolution, streamwise vortex is able to be detected more clearly than the LDV measurements.

A similar experimental approach is conducted by Logory *et al.* (1996) to measure wake fields behind a surface piercing plate. By LDV measurement, it is proved that the wake with retarded longitudinal velocity widen near the free-surface. There are vertical vortices in the wake fields and their strength decreases near the free-surface. The free-surface effects reported in this study are consistent with the results of Longo *et al.* (1998) and Marquardt (2009).

The vertical plate tests have provided precious insights on free-surface effects on turbulent flow fields, but they have dealt with effects of Stokes wave on the boundary layer flow solely. The horizontal hydrofoil generates its wake with retarded streamwise velocity and an array of Karman vortices (Chen and Chwang, 2002). Definitely, the wake of horizontal hydrofoil affects the boundary layer flow of the vertical plate, as well as the Stokes waves. To generate free-surface waves by the surface piercing body itself, the cross section of free-surface piercing body with meaningful width is appropriate,

rather than a flat plate in external Stokes waves. Surely, the cross section should also be slender enough to prevent flow separation.

A surface piercing NACA 0024 foil is used in the numerical simulation conducted by Zhang and Stern (1996). Three different Fr conditions (0.2, 0.37, and 0.55) are applied to investigate changes of flow features: wave pattern, pressure and wall shear stress, topology of flow, and vortex structures. The wave induced separation is identified by negative wall shear stress. Even at the lowest Fr condition (0.2), wave induced separation is observed, but it is limited near the stagnation point at trailing edge and flow topology at the region is relatively simple. The wave steepness increases in high Fr conditions, resulting in expansion of wave induced separation region. Flow fields at Fr of 0.37 and 0.55 share common features, *i.e.*, bow vortex, recirculation in separated region, and distorted Kelvin wave pattern. However, in high Fr condition, the separation delay downstream and the separated flow does not reattach to the model surface. In addition, it is found that the free-surface functions as a sink of vorticity; vortices are generated at the body surface flow to the free-surface, as well as the wake.

In the experimental study by Metcalf *et al.* (2006), free-surface elevation and model surface pressure are measured in three Fr conditions (0.19, 0.37, and 0.55). Measured data are analyzed by fast Fourier transform (FFT), to sort the flow physics in different scales, *i.e.*, shear layer, Karman shedding, and flapping instabilities. The wave induced separation region is identified by large fluctuations of the surface pressure and wave elevation. In the experiments, instability of flow features is mainly discussed. In the medium and high Fr condition, shear layer shedding is stronger than the Karman-like shedding. In high Fr condition, Strouhal number of shear layer shedding decreases, implying that the free-surface suppresses vortex shedding in large

scale.

In the computation of Zhang and Stern (1996), Baldwin-Lomax model, a zero-equation turbulence model, is employed, and the authors suggest reducing the modeling uncertainties as a future work. Computational studies with improved turbulent and free-surface modeling have been conducted for the free-surface piercing NACA 0024 model problem.

In the numerical simulation by Rhee *et al.* (2005), three different discretization schemes for volume of fluid method are compared to provide the hierarchy in interface capturing scheme for simulating wave-induced separation. The realizable $k-\varepsilon$ model, a two-equation turbulence model, is implanted into the URANS computation. The comparison focused on the wave elevation at Fr of 0.37, where the wave-induced separation is clearly observed in the experiments by Metcalf *et al.* (2006). The authors recommend the high-resolution interface capturing scheme (Muzaferija *et al.*, 1998), as it is robust enough and agrees well with experiments.

The problem is considered as steady state although URANS computation is used in the previous computations; time-mean features were mainly investigated rather than instable turbulence behavior. Kandasamy *et al.* (2009) perform URANS simulation on the surface piercing NACA 0024 foil, using blended $k-\varepsilon/k-\omega$ model and a free-surface tracking method. The numerical simulation results are first compared with experiments (Metcalf *et al.*, 2006) for validation and instability of vortical structures is mainly investigated. By the URANS method, fluctuations in the separation bubble due to standing wave are detected.

Kim and Cokljat (2007) apply a URANS-LES hybrid scheme, so-called detached eddy simulation (DES), to the surface piercing NACA 0024 problem.

Results are compared with LES computations for same model and test condition (Kim and Rhee, 2006), to ascertain the characteristics of DES approach. The DES produces results with reasonable accuracy, but tends to underpredict the wave fluctuation and show less detailed flow features than LES.

Xing *et al.* (2007) conduct a numerical simulation on the surface piercing NACA 0024 foil by DES and single phase level set method. LES is applied to the separated region and outside is computed using URANS. By the computation, turbulent flow features in the wave induced separated region are obtained and analyzed, which are not acquirable in URANS computations with two-equations turbulence model. The velocity and pressure fluctuation due to the wave induced separation, also reported in the URANS computation (Kandasamy *et al.*, 2009), increases the turbulent kinetic energy. Moreover, Reynolds stresses are revealed to be anisotropic. They increase near the boundary of the separated region and the streamwise component of Reynolds normal stress is dominant.

Throughout the series of studies on the surface piercing NACA 0024 foil, physics of wave-induced separation have been investigated; but there has been a lack of experimental results of turbulent flow field measurements. Turbulent flow field measurements can give insights for understanding the turbulence structures affected by the wave induced separation. In addition, the experimental results can be used for the validation data of CFD analysis. There are a few experimental studies on turbulent flow field measurements around a slender surface piercing body, although the cross section is not the NACA 0024 foil.

Pogozelski *et al.* (1997) use a PIV system to measure the flow field around

a surface piercing hydrofoil. The chord-thickness ratio of the model is 1/3. Because of the blunt cross section geometry, wave induced separation is observed in lower Fr condition than those in the NACA0024 tests, thus the tests are conducted primarily at Fr of 0.255. At the Fr condition, reversal flow is not observed, although bubbly free-surface exist. The result implies that the adverse pressure gradient from the free-surface wave is not strong enough to cause reversal flow; the reversal flow is observed in higher Fr condition over 0.30, where the wave steepness increases. In spite of the absence of the reversal flow, the 3D wave induced separation can be identified by counter-rotating streamwise vortices generation. Although the experimental study provides the flow structures of the separated region, quantitative turbulence properties are not obtained, as the number of acquired instantaneous velocity vector fields is not sufficient to derive statistically significant results.

To acquire turbulent characteristics in the wake of a surface piercing body with wave-induced separation, Seol *et al.* (2013) conduct 2D PIV measurements in a towing tank. To eliminate the bow wave effects, the test model has sharp leading edge and small chord-thickness ratio, 1/10. Results at two Fr conditions (0.2 and 0.4) are compared. Even at the low Fr condition, the flow retards and turbulent kinetic energy increases. At high Fr condition, reversal flow near the trailing edge and flow around the stagnated flow are observed.

Throughout the literature review on the experimental and computational study on a surface piercing body, major characteristics of free-surface effects and wave-induced separation can be summarized, as follows.

— The free-surface changes velocity into turbulent properties, even at low Fr conditions where distinguishable wave does not exist.

- The wave induced separation is caused by the adverse pressure gradient of wave, thus it usually occurs behind the wave trough. It can be identified by fluctuation of free-surface and velocity.
- Reversal flow is inadequate criteria for judging the occurrence of wave induced separation, as reversal flow is not observed at low Fr conditions even there are spilling wave breaking and bubble entrainment on wave.

1.2.4. Relevant free-surface behavior: juncture-bounded turbulence

Although this study deals with free-surface/solid juncture flow, it shares common features of solid juncture-bounded flow; to review studies on solid juncture flows and identify major characteristics are helpful to understand the free-surface bounded flow phenomena, especially in low Fr conditions where free-surface wave was not developed well.

When the boundary layer flow meet an obstacle, a horseshoe shaped vortex is generated from the leading edge of the obstacle and it causes flow separation. It is highly unstable and easy to dissipate into small scale eddies periodically (Simpson, 2001). The horseshoe vortex dynamics dominates the boundary layer flow. At the trailing edge, horseshoe vortex instability attributes to vortex shedding.

The horseshoe vortex generation has been studied frequently (Paik *et al.*, 2007), but there has been limited number of studies on fully developed boundary layer around the juncture and its wake field, which can provide insights to understand the free-surface juncture flow. The horseshoe vortex displaces the boundary layer and streamlines in the wake. In addition, Reynolds stress gradients near the wall causes additional vortex (Bradshaw,

1987).

Based on the understandings of juncture flow, difference between the flow at solid-wall/solid-wall and solid-wall/rigid-lid juncture is investigated in the study of Sreedhar and Stern (1998). The free-surface deformation is not considered in the LES simulation; only it works as an inviscid wall and kinematic and dynamic boundary conditions, *i.e.*, flow normal to the boundary is restrained and pressure at the rigid-lid is constant, were applied. At the corner, a vortex is generated because of gradients in Reynolds stresses, but secondary vortex is not developed in the slip-wall condition.

1.2.5. Relevant free-surface behavior: hydraulic jump

By reviewing studies on wave induced separation, flow velocity retardation and turbulent free-surface appearance are suggested as the main flow behavior. It shares common features of the hydraulic jump, which is caused by sudden deceleration of flow. After the hydraulic jump, the flow become highly turbulent and it lose its kinetic energy by turbulent dissipation. In the same manner, serious loss of kinetic energy under the wave induced separation region with bubbly free-surface is reported in the experimental study of Pogozelski *et al.* (1997). Researches on hydraulic jump can suggest a breakthrough for understanding the wave-induced separation. In this literature review, studies on turbulence property changes by hydraulic jump are reviewed.

Battjes and Sakai (1981) investigated hydraulic jump in a wake field of a horizontal hydrofoil near free-surface. The hydrofoil has angle of attack for lift generation, thus strong downwash flow is observed in the wake and hydraulic jump occurs. By LDV measurement, it is revealed that the turbulent

shear stress concentrate at the circulating region and the flow phenomena are free of scale effects under Froude's law.

Svendsen *et al.* (2000) conduct 2D LDV measurements and wave elevation around a flow field with hydraulic jump. By flow field measurement, recirculating of turbulent flow near the free-surface, *i.e.*, roller region, is identified in three Fr conditions. The measurement results are verified by the continuity and momentum conservation equation. In the hydraulic jump region, pressure contribution on the momentum flux change into turbulent normal stress. In addition, vortex generation at the roller region is investigated quantitatively.

PIV measurement on hydraulic jump is performed by Lennon and Hill (2006). The PIV results are similar with previous LDV measurements, but PIV measurement can provide velocity fields with spatially high resolution and enables better understanding of flow structures than LDV results. In addition, viscous shear stress distribution is visualized and investigated in the study.

Misra *et al.* (2008) also investigate flow structure of hydraulic jump by PIV measurement. The hydraulic jump is caused by an undershot weir, in the same manner with test design by Svendsen *et al.* (2000). By analyzing particle images, free-surface elevation and 2D flow velocity fields can be acquired. Under the bubbly free-surface, large gradient of longitudinal velocity exist which causes strong shear strain. Reverse flow is observed at the free-surface of the circulation region. Free-surface behavior is identified by introducing the intermittency function, and it shows good agreement with analytic solution.

In hydraulic jump region, air entrainment in the roller region is important characteristic as well as the turbulence stress generation. Murzyn *et al.* (2007) measure wave height and recorded video in the hydraulic jump region. The

experiments design is similar with that suggested by Svendsen *et al.* (2000). The appearance of hydraulic jump is characterized by Fr and Weber number conditions. Free-surface fluctuation is analyzed quantitatively to figure out the changes of free-surface form downstream: the flow changes rapidly from flat to knobble form at the toe of the roller region, and gradually alters to waves.

Chanson (2007) introduce phase-detection system to the hydraulic jump in large Reynolds number (Re) condition. By the void fraction measurement, characteristic time and length scale of air entrainment in the mixing layer can be obtained. An analogous experiments are attempted by Kucukali and Chanson (2008), to find a linear correlation between the free-surface fluctuation and the flow velocity.

Flow field in the air-entrained region is hard to be measured by PIV, thus Lin *et al.* (2012) utilized bubble image velocimetry (BIV) technique. In the measurement results, flow velocity of bubbles is lower than that of water flow due to drag force in the shear layer, but the global tendency is similar to each other and maximum velocity is found in same vertical location. By the investigation on the bubble dynamics, it is revealed that the bubbles produce turbulence in small scales.

Previous experimental studies on the hydraulic jump provide insights on violent free-surface behavior which are applicable to the free-surface separation problem, as follows.

- Hydraulic jump causes a recirculation of flow near the free-surface with bubble entrainment and turbulence generation. In the wave-induced separation, similar recirculation of flow phenomena have been reported.
- Fr is the most dominant condition for occurrence of hydraulic jump, as well as the wave-induced separation. Weber is also important, as it determines

the degree of violence of the free-surface.

- At the toe of the roller region, there is intense shear strain and vorticity caused by the recirculation. Under the roller region, flow become stable and turbulence reduces rapidly.

1.2.6. Scale effects on the interaction of free-surface and turbulent flow

The present study treats scale effects on free-surface induced flow behavior. When Fr is identical in different scale, scale effects are usually caused by difference Re . Scale effects on the turbulent flow with free-surface have been researched in naval architecture for practical purpose: prediction of ship performance in full scale. Numerical simulations have been attempted to identify Reynolds number effects on the flow fields around a vessel (Castro *et al.*, 2011; Park *et al.*, 2015). In high Re conditions, viscosity is less effective and the flow fields become similar to ideal flow, resulting in increase of wake velocity and decrease of viscous damping. In those CFD researches, however, the differences in the propulsive performance are primarily focused and scale effects on free-surface behavior are hardly discussed.

As reviewed above, free-surface piercing body is applicable for research on the free-surface behavior and the scale effects can be also investigated by the model. Surface piercing body problems with scale effects have been studied, but most of them are focused on a circular cylinder. Rhee (2009) conducts URANS computation on a circular cylinder at different Re conditions. Re effects are investigated focusing on the drag coefficient, to conform that the Reynolds number effects on the wave making resistance is less effective than those on total resistance.

Koo *et al.* (2014) perform LES computation of flow fields around a surface piercing circular cylinder. With Re variations with fixed Fr condition (0.84), Re effects on the separation and free-surface behavior can be identified. As Re increases, separated region decreases and the separation point delayed. Moreover, Reynolds normal stresses in wake field also decrease near the free-surface.

Previous researches focus on the circular cylinder, thus 2D separation and vortex shedding are dominant and free-surface effects are minor. In the case of slender surface piercing body, on the other hand, flow separation is only caused by the free-surface waves and the Re effects are expected to be different with the circular cylinder case; nevertheless, some of Re effects reported in the previous studies are also effectual in the slender surface piercing body problem: turbulent boundary layer thickness near free-surface, strength of streamwise vortices generated from the boundary of separated region, and turbulence properties near the violent free-surface. In addition, surface tension, which is not considered in the CFD cases, may affect the flow field at low Re condition where laminar flow is dominant. Capillary waves and restraint of violent free-surface motion are renowned surface tension effects.

1.2.7. Experiments for turbulent flow field measurements in towing tanks

To measure flow fields under the free-surface, various experimental techniques have been introduced. Recently, LDV and PIV are widely used in the experimental hydrodynamics. They are optical measurement technique, thus non-invasive measurement can be achieved. PIV has advantages in planar measurement, while LDV can measure flow fields near the model surface with high repetition rate. PIV and LDV are first introduced in circulate water

channel and cavitation tunnel tests. In the test facilities, it is facile to arrange a test model and to measure system and it is feasible to measure continuously. By using those measurement systems, flow fields around ship and propeller model have been measured and produced significant results with turbulent properties (Stella *et al.*, 2000; Di Felice *et al.*, 2004; Lee *et al.*, 2004; El Lababidy *et al.*, 2005; Felli and Di Felice, 2005; Felli *et al.*, 2009; Lee *et al.*, 2009; Felli and Falchi, 2011; Bertetta *et al.*, 2012).

The circulation water channel tests have problems of free stream turbulence, as the flow is provided by thrust from impellers. To eliminate the initial turbulence for precise turbulence measurements, towing tank tests have been challenged for local turbulent flow measurement, which require special design of measurement system for underwater operation.

The towed underwater PIV test is first performed by Gui *et al.* (2001). By using a 2D PIV system in a towing tank, a wake field of a surface combatant model is measured. Measured 2D2C velocity fields are stacked to reconstruct a 3D3C velocity field. By the reconstruction method, mean velocity fields and Reynolds stresses distribution in the wake field are depicted. Longo *et al.* (2007) measure wake field of a surface ship model in head seas by towed underwater 2D PIV system. The model has pitch and heave motion during tests and periodic changes in 3D3C velocity fields are investigated, by using the reconstruction method suggested by Gui *et al.* (2001).

Scarano *et al.* (2002) measure wing tip vortex of an airplane model in a towing tank. A 2D PIV system is used of which measurement plane is perpendicular to the towing direction. Vortex trajectory and structures are investigated, to yield information of wing tip vortex generation and decay. Similar research on vortex decay is performed by Aloisio and Di Felice (2006).

Flow around the bilge keel during free roll decay tests without advance speed are measured by an underwater 2D PIV system and its periodic behavior is investigated. It is concluded that the vortex strength shed from the bilge keel is proportional to the motion amplitude. Similarly, Irvine *et al.* (2013) conduct free roll decay tests with advance speed and measured flow around the bilge keel. Besides, as referred above, Seol *et al.* (2013) measure wake fields of a slender surface piercing body by a towed underwater 2D PIV system for examining free-surface effects on turbulent flow.

Recently, stereoscopic PIV, which measures 2D3C velocity field by two cameras, has been introduced to towing tank facilities and replacing traditional five-holes Pitot tube system. Chen and Chang (2006) develop an underwater SPIV system for a towing tank and measure velocity fields near a ship model. Anschau and Mach (2007) compare propeller wake measurement results acquired in a cavitation tunnel and towing tank. A towing tank test on wake field measurement of a contra-rotating propeller behind a ship is performed by Paik *et al.* (2015). By complementary study through CFD analysis, tip vortex trajectories affected by interactions between propellers are investigated.

In towing tank test environments, spatially uniform flow is achievable; calibration and uncertainty assessment technique using the uniform flow measurements have suggested. Grizzi *et al.* (2010) develop a calibration method for towing tank SPIV tests. It uses the uniform flow measurements for calibration of streamwise component. Similarly, Seo *et al.* (2013) assessed test uncertainty of towing tank SPIV tests based on the uniform flow measurement. The uniform flow measurement results are compared with the reference input speed, to obtain the systematic error of the mean velocity and turbulence properties measurement. After the test uncertainty assessment, wake fields measured by the SPIV system are compared with other experiments, *i.e.*, five-

holes Pitot tube, hotwire anemometer, and Pitot-static tube. They show good agreement overall, but local maxima of turbulence properties from SPIV tests is larger than those from hotwire anemometer.

As maneuvering and seakeeping tests are achievable in a towing tank facility, flow field measurements around a ship model in motions have been performed by towed underwater SPIV systems. Kim (2014) measure nominal wake fields of a crude oil carrier model in waves. Phase-averaged wake fields in different wave conditions are acquired and provided as a validation data for CFD analysis. Falchi *et al.* (2014) measure flow fields around a catamaran model in steady drift condition. Unsteady vortex shedding under the keel and interaction between flow fields around two hulls are mainly focused on. Flow fields measurements around a surface combatant model in planar motion mechanism maneuvers are carried out by Yoon *et al.* (2015). Development of longitudinal vortices from the sonar dome and hull bottom are detected by the SPIV measurement.

Recently, underwater tomographic PIV system enabled measurement of 3D3C volumetric flow fields. Yoon *et al.* (2014) investigate vortex shedding on the surface combatant hull surface in drift angles. By the volumetric measurements, development of instantaneous vortical structures in turbulence and interactions between longitudinal vortices are investigated.

History of LDV tests in towing tank is longer than that of PIV. Anthony and Willmarth (1992) make LDV measurements of jet flow under the free-surface in a towing tank. Longo *et al.* (1998) measure solid/free-surface juncture flow by 2D LDV system, as described in the previous section. Wake field of a fully appended model ship is measured by Felli and Di Felice (2004). A 2D LDV system is used in a towing tank and propeller-hull interaction is

mainly examined. It is noteworthy that the LDV measurements, the pointwise measurement technique, require amount of test time and are inadequate for towing tank environment where the measuring time is limited.

As reviewed above, flow field measurement tests in towing tanks have focused on ships and propulsors, thus there are lack of experiments on fundamental fluid dynamics by the novel measurement system. Towing tank tests, however, can exclude the initial turbulence and guarantees controlled flow conditions, thus flow field measurement around a surface piercing body in a towing tank is essential for acquiring reliable turbulence properties and understanding turbulence phenomena affected by free-surface behavior.

1.2.8. Analysis methods for turbulence research

Turbulence flow is very complicated and has large degrees of freedom temporally and spatially; to analyze and describe the turbulent flow field, a method to low-dimensionalize and extract predominant characteristics is required. The simplest low-dimensionalizing method is the Reynolds decomposition, where the instantaneous velocity is divided into mean and fluctuation part. In 3D turbulent flow field, mean velocity and Reynolds normal and shear stresses in three directional components are provided, thus the nine physical properties are yield as the low-dimensionalization results. Turbulence intensity can be quantified by the turbulence kinetic energy and Reynolds stresses, but it cannot indicate the turbulence structure which consists of local eddies.

To understand the turbulence structure, a method that treats coherent turbulence structure has been developed. The proper orthogonal decomposition (POD) is the most frequently used method in the turbulence

fluid dynamics. The basic idea of applying POD into turbulent flow analysis is first suggested by Lumley (1967). For reducing computational resources for analysis, an efficient method, so-called snapshot POD, is developed by Sirovich (1987). By POD analysis on a series of velocity fields, an instantaneous velocity field is decomposed into a sum of basis vector fields. The zeroth basis of the decomposed velocity field is recognized as the time-mean velocity field and the bases are aligned in the order of turbulent energy level; thus, initial bases demonstrate coherent turbulent structures which contain dominant turbulence energy (Smith *et al.*, 2005).

POD has been used for fundamental turbulent researches and practical applications. Analyses based on POD have been attempted to various flow phenomena: jet flows (Patte-Rouland *et al.*, 2001; Jung *et al.*, 2004; Meyer *et al.*, 2007; Arienti and Soteriou, 2009), turbulent boundary layer (Berkooz *et al.*, 1993; Rowley, 2005; Gurka *et al.*, 2006; Sen *et al.*, 2007) and wake fields (Johansson *et al.*, 2002; Johansson and George, 2006; Diamessiss *et al.*, 2010; Liberge and Hamdouni, 2010; Schmid, 2010). Besides, for engineering application, POD method have been applied. Paik *et al.* (2010) investigate tip vortex dynamics in a marine propeller wake by POD analysis on the PIV measurements. Similarly, Sherry *et al.* (2013) utilize POD for examine the tip and root vortices dynamics in a wind turbine wake. Throughout those studies on application, it is revealed that the POD is a very effective tool to identify the dominant vortex behavior in turbulent flow fields.

Turbulence flow consists of anisotropic eddies and they dissipate by the energy cascade. To perceive the nature of turbulence, vortical structure in different scales should be detected from the measured instantaneous flow fields. Vorticity, which is proportional to the angular velocity of flow, is the simplest method to discover vortices in turbulent flow. The vorticity

distributions are, however, also affected by shear strain of the flow field. To precisely identify existence and center of vortices, vorticity is insufficient. Jeong and Hussain (1995) developed a novel vortex center identification method, λ_2 criterion. Graftieaux *et al.* (2001) combine a vortex identification and POD to distinguish large vortices and small turbulent eddies in flow fields.

1.3. Objectives and outline of thesis

The motivation of the present study is to understand free-surface wave effects on flow fields in various scales, from laminar to turbulent flow region. Throughout the literature review, it is revealed that a surface piercing body with slender cross section is the most appropriate model for investigating free-surface effects. A series of geosim tests is required to achieve different Fr and Re conditions. Wave elevation and flow field measurements near the model surface should be conducted for comparisons of flow features. SPIV measurement in a towing tank is the most adequate technique, as it can provide instantaneous and statistically processed planar velocity fields. Before the main tests, test uncertainty should be assessed to quantify reliability of measurement system. Mean velocity and coherent turbulence structures can be obtained by the SPIV tests and analyzed for the comparison. In addition, Kelvin wave observation is also needed for the research.

There are two novel aspects of this study in test setup and research object. The SPIV tests in towing tank tests have focused on practical purpose, such as mean velocity measurements of nominal wake of vessels and propeller wake; thus, test system for turbulence measurement should be validated prior to the main tests. Methods to assess the test uncertainty for towing tank tests based on repeated uniform flow measurement tests were suggested. Nominal wake field of a model ship was measured by SPIV and LDV and the results were compared to existing database with assessed uncertainty in means velocity and turbulence properties.

Research topic suggestion is another new contribution. Although PIV measurements have been conducted in various fluid dynamics fields, but it has been seldom applied to the surface piercing body problem, as reviewed above.

The present thesis consists of four parts: test design, test uncertainty assessment for measurements, identification of free-surface effects by the largest model tests, and scale effects investigation. In the chapter of test design, there are detailed description of test facility, test model and conditions, and measurement systems. Test uncertainty of measurement systems is assessed through the standards of American Society of Mechanical Engineers (ASME). By using the test system, tests on the largest model are carried out first and test results at different Fr conditions, *i.e.*, different free-surface wave conditions, are compared first to identify the free-surface wave effects on the flow field. Confirmed free-surface effects are also examined for the geosim models, and the scale effects on the flow fields are inspected.

Chapter 2. Test Design

2.1. Facility

Model tests were conducted in Seoul National University Towing Tank (SNUTT), which has a length, width (W), and depth (h) of 110, 8, and 3.5 m, respectively. Figure 2-1 shows a schematic of the towing tank.

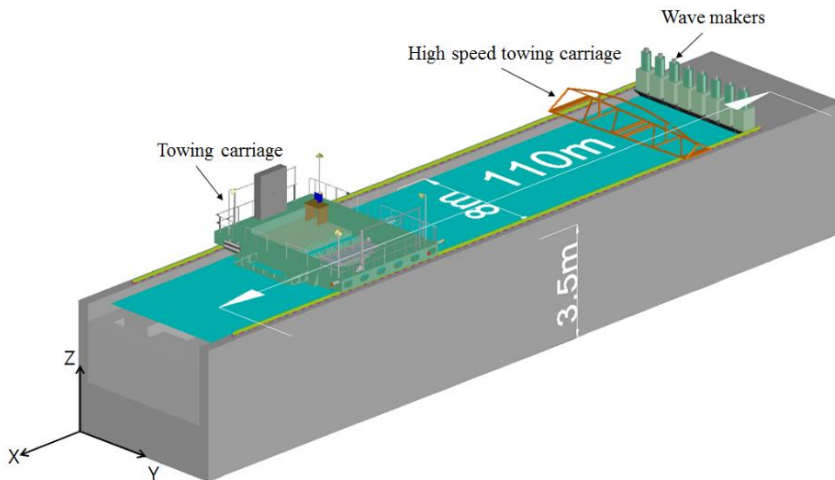


Figure 2-1. Schematic of SNUTT.

The test model and measurement systems were installed on the towing carriage, which was driven by four AC servo motors with maximum powers of 8 kW. The servo motors were controlled by a negative feedback system to maintain a constant speed. The control software was based on Labview (developed by National Instruments Corporation, Austin, TX) to maintain a constant towing carriage speed (U) using the negative feedback system. Power from the AC servo motors was transferred to the wheel by a reduction gear

with a reduction ratio of 2:1. The circumferences of the carriage wheels were 2,000 *mm*. The maximum speed of the carriage was 5,000 *mm/s* with accuracy under 2.0 *mm/s*.

2.2. Test model

The test model was a cylindrical body with a cross section comprising the intersection of two symmetric parabolic curves. Figure 2-2 shows the cross section of the test model. The same geometry was used in the experimental study by Seol *et al.* (2013). The length-width ratio (L/B) of the test model was 10. As the model had a sharp bow and slender cross section, the bow wave effects (*e.g.*, necklace vortex from the leading edge and spilling bow wave breaking) could be minimized.

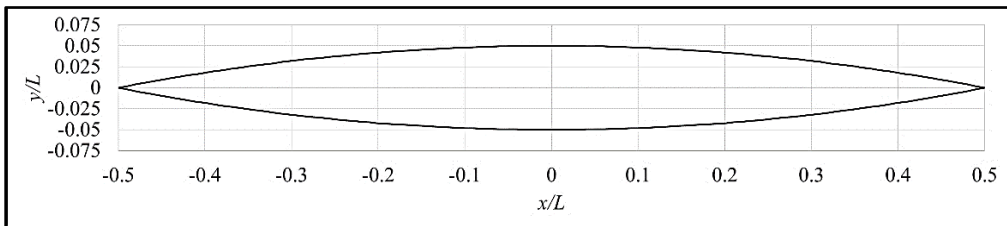


Figure 2-2. Cross section of the test model.

Figure 2-3 shows the three different manufactured models. Test models with three different scales were used in the present study. The values of L for the models were 1.0, 0.464, and 0.215 m. For the same Fr , the corresponding Re of the smallest model was 1/10 that of the largest model and $1/\sqrt{10}$ that of the medium model. The surfaces of the models were painted matte black to prevent laser reflection. Turbulence stimulators were not attached to the models because experiments in low Re conditions are designed to be performed in laminar flow fields. The draft of the model (T) was set at twice the longitudinal length to prevent the effects of bottom flow. The models were manufactured using fiber-reinforced plastics with an accuracy of 0.02 mm.



Figure 2-3. Manufactured models.

A right-handed Cartesian coordinate system was used in this study. The origin of the coordinate system was located at the intersection of the model centerline, calm water-free-surface, and midship (equal distance between the leading and trailing edge). The positive x , y , and z directions were downstream, starboard, and upward, respectively. Lengths were non-dimensionalized by the length (L) of the model in the results.

A 3D velocity vector, \mathbf{V} , comprising three components u , v , and w in the x , y , and z directions, respectively, is given as follows:

$$\mathbf{V} = (u, v, w). \quad (2-1)$$

Velocity components were non-dimensionalized by U . As the length and velocity dimensions were non-dimensionalized by L and U , respectively,

The test conditions were defined by Fr and Re based on L and U as

$$Fr = U/\sqrt{gL} \quad \text{and} \quad (2-2)$$

$$Re = \rho LU/\mu, \quad (2-3)$$

where g , ρ , and μ are the gravitational acceleration, density of water, and dynamic viscosity of water, respectively.

2.3. Test conditions

Table 2-1 shows the model test conditions. In the present study, following the experimental study of the same model (Seol *et al.*, 2013), model tests at $Fr = 0.400$ were conducted to investigate the wave-induced separation wherein the Kelvin wavelength was the same as the model length. In addition, two Fr conditions were selected. At the intermediate Fr (0.282) condition, the corresponding wavelength was half the model length, and linear wave motion without wave-induced separation was expected. At the lowest Fr (0.126) condition, free-surface waves were expected to be rare. As shown in Table 1, the corresponding Re at the lowest Fr condition (0.126) was the same as that of the smaller model at the highest Fr condition (0.400); flow fields with and without wave-induced separation at identical Re conditions were then compared.

Table 2-1 Test conditions

Model length (mm)	Scale ratio	Fr	Towing speed (m/s)	Re
215	1/4.65	0.126	0.183	34,200
		0.282	0.409	76,200
		0.400	0.581	108,000
464	1/2.16	0.126	0.269	108,000
		0.282	0.601	241,000
		0.400	0.853	342,000
1000	1	0.126	0.395	342,000
		0.282	0.883	761,000
		0.400	1.252	1,080,000

The international towing tank conference (ITTC) suggests criteria to avoid restricted-water effects based on the towing tank and model size (ITTC, 2002). The criteria are summarized and compared with previous studies in Table 2-2. The criteria were designed for model ship tests; thus, the criteria for the model should be excluded in surface-piercing body tests with deep draft. By comparison, it was confirmed that restricted-water effects were negligible in this study.

Table 2-2. Comparison of restricted-water effects

Item	Fr	$\frac{h}{T}$	W/c	W/B	Wh/BT
Criteria	≤ 0.7	≥ 4	≥ 0.35	≥ 4	≥ 4
Related fluid dynamic physics	Wave making resistance	Model bottom flow	Bow wave reflection to stern flow	Flow field on the model side	Blockage effect
Chow, 1967	0.13–0.31	1	2.33	8.97	7.58
Zhang and Stern, 1996	0.12–0.35	2	2.5	10	20.8
Pogozelski <i>et al.</i> , 1997	0.04–0.4	1.1	3.33	10	11.1
Metcalf <i>et al.</i> , 2006	0.12–0.35	2	2.5	10	20.8
Large model	0.12–0.4	1.75	8	80	140
Medium model	0.12–0.4	3.77	17.2	172	650
Small model	0.12–0.4	8.13	37.2	372	3028

2.4. Measurement systems

2.4.1. *SPIV system: hardware*

A towed underwater SPIV system was used to measure the flow fields around the model. The hardware organization of the SPIV system, designed by LaVision GmbH (Gottingen, Germany), was used in towing tank environments and underwater. The hardware comprised the laser optics, two submersible cameras, a timing system, and a personal computer (PC) for image acquisition and analysis. Figure 2-4 shows the schematic of the towed underwater SPIV system.

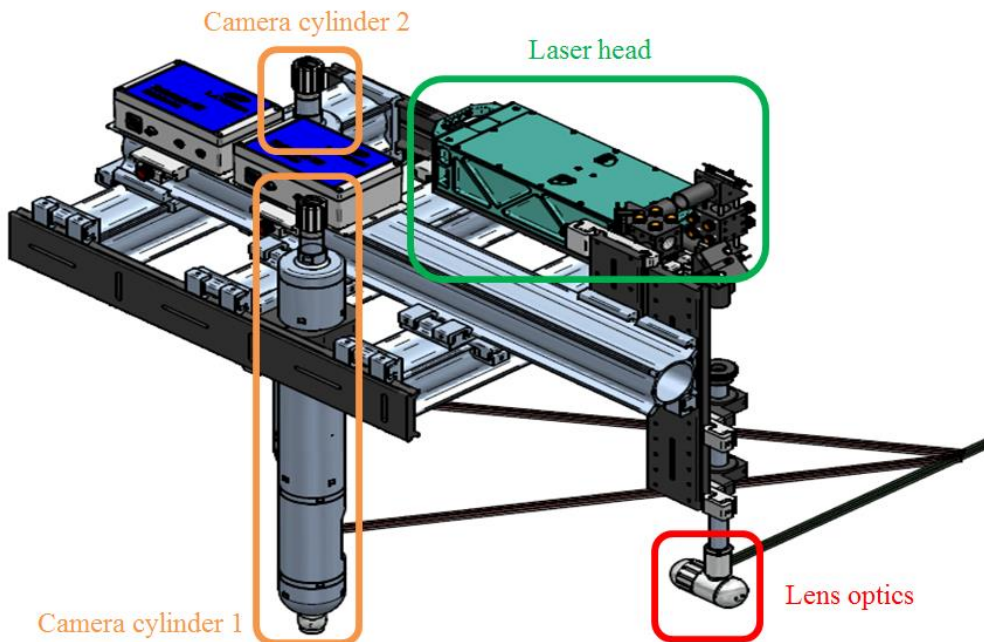


Figure 2-4. Schematic of the towed underwater SPIV system.

Figure 2-5 shows the laser illumination system. A water-cooled dual head Nd:YAG laser (EverGreen 200, manufactured by Quantel laser, Les Ulis,

France) with wavelength, pulse power, and repetition rate of 532 nm , 200 mJ , and 15 Hz , respectively, was used as the illumination source of the SPIV system. The lamps and Q-switch of the laser head were triggered by a 5-V Transistor-transistor logic (TTL) signal. The green laser beam was expanded by an array of optical lenses to form a laser sheet. The thickness of the laser sheet could be varied, and a thickness of 2.0 mm was used in the present study. The lens array was covered by waterproof housing.



Figure 2-5. Laser system of the SPIV system: Evergreen 200- mJ laser head and power supply (left) and mirror arrangement and laser path (right).

For underwater operation, a monochrome charge-coupled device (CCD) camera (Imager pro SX 5M, manufactured by LaVision GmbH) was located in submergible housing, as shown in Figure 2-6. Its resolution was 2448×2050 pixels with 12-bit dynamic range. The CCD camera can take two frames of particle images with a minimum time interval of 600 ns . The maximum frame rate was 14.2 frames per second. The acquired images were transferred to the PC through a GigaBit Ethernet interface. The CCD camera was attached

on a Scheimpflug angle adaptor, which can rotate the angle of the CCD camera. A camera lens with focal length of 85 mm (Canon EF $85\text{ mm f}/1.8\text{ USM}$) was combined with the CCD camera. The focus, aperture, and Scheimpflug angle were controlled remotely. The aperture was set to $f/5.4$ in the tests. The Scheimpflug angle and focus were also adjusted to obtain clear particle images.

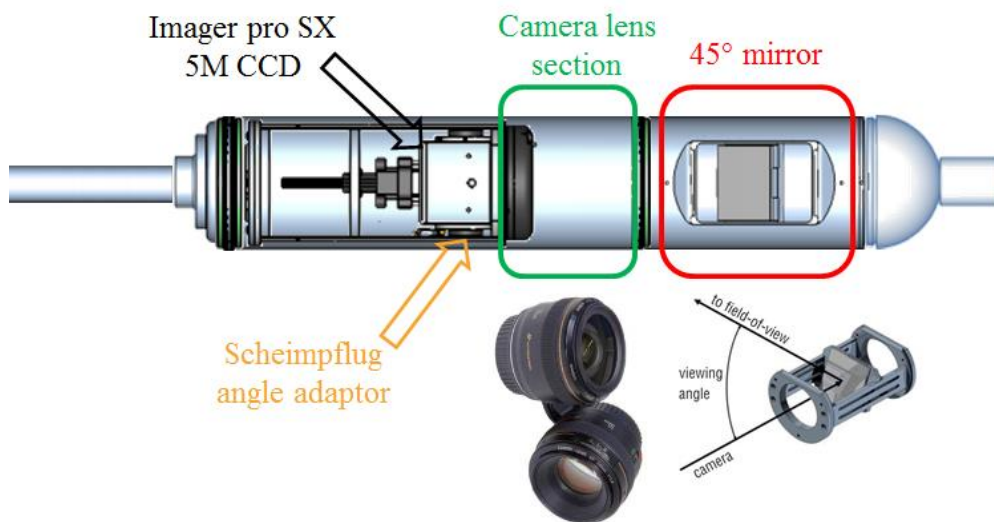


Figure 2-6. Arrangement of components in the submersible vertical cylinder.

Figure 2-7 shows the optical arrangement of the SPIV system. The size of the field of view was $140\text{ mm} \times 115\text{ mm}$. Camera cylinders were located behind the measurement plane to exclude the effects of flow around the blunt camera cylinders. The angle between the measurement plane and camera centerline was 25.8° for camera 1 and 52.1° for camera 2. The effects of optical arrangement were examined by uniform flow measurements, as discussed in the next chapter.

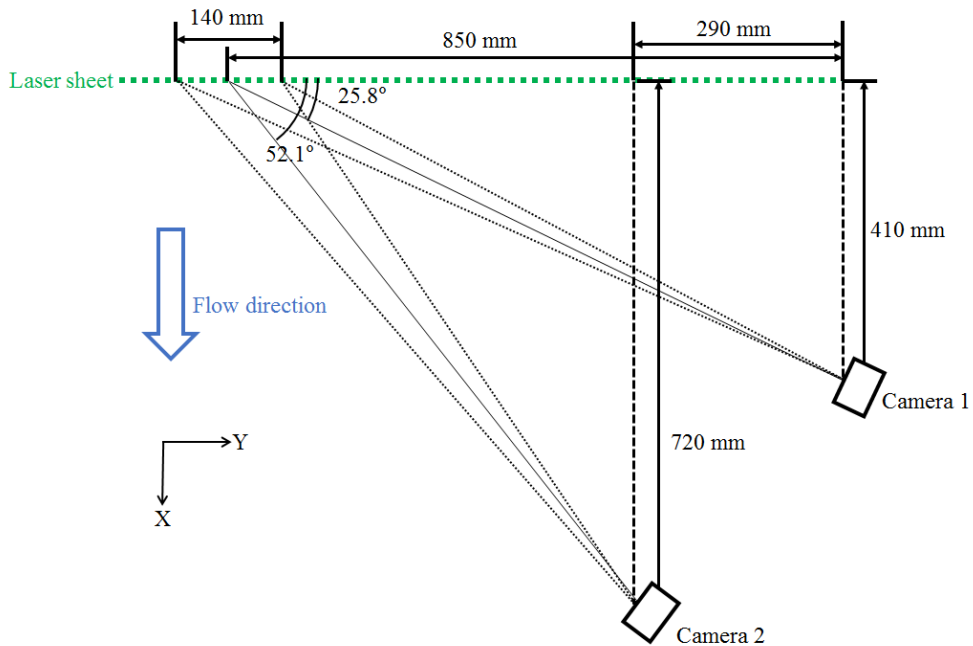


Figure 2-7. Optical arrangement of the towed underwater SPIV system.

A programmable timing unit manufactured by a LaVision GmbH (model number 1108057) synchronized the image acquisition and laser light illumination. It generated a 5-V TTL signal to trigger the laser power supply and cameras.

DaVis version 8.2, a PIV software developed by LaVision GmbH, was used for particle image acquisition and data analysis. In all test cases, the time interval between two particle image frames, Δt , was adjusted such that the particle displacement in the far field was less than 30% of the laser sheet thickness, 0.45 mm. With the time intervals, particle displacements on the particle images were less than 5 pixels. The time intervals for the test conditions are detailed in Table 2-3. The repetition rate of particle image acquisition was 7.2 Hz for all cases.

Table 2-3. Time intervals of particle image frame acquisition

Model length (<i>mm</i>)	<i>Fr</i>	Towing speed (<i>m/s</i>)	Δt (μs)	Particle displacement (<i>mm</i>)
215	0.126	0.183	2000	366.0
	0.282	0.409	1000	409.0
	0.400	0.581	650	377.65
464	0.126	0.269	1500	403.5
	0.282	0.601	650	390.65
	0.400	0.853	450	383.85
1000	0.126	0.395	1000	395.0
	0.282	0.883	450	397.35
	0.400	1.252	300	375.6

2.4.2. SPIV system: calibration

In SPIV calibration, a two-tiered calibration target manufactured by LaVision GmbH was used to match the coordinate system on particle images of two cameras and measurement plane. On the calibration target, white dots with diameters of 3 mm and spacings of 15 mm were marked. The groove depths were 3 mm. Figure 2-8 shows the calibration target. The target was fixed in an adaptor and located in the towing tank during calibration.

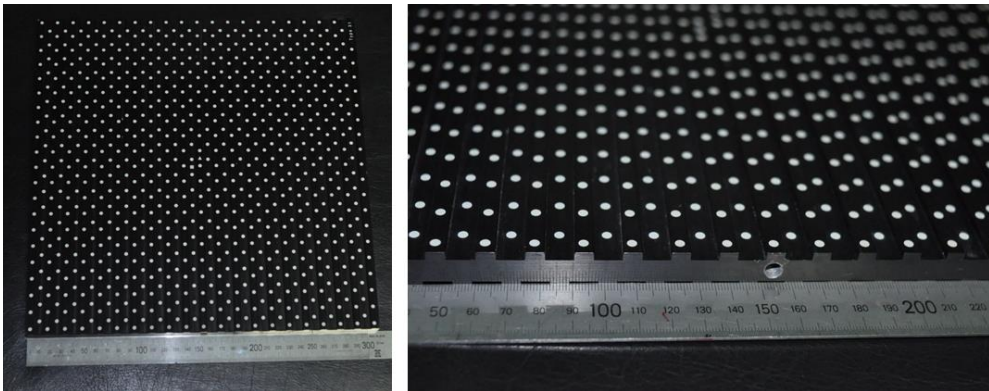


Figure 2-8. Calibration target.

The calibration target was aligned with the laser sheet and an external underwater light was used to illuminate the target. As shown in Figure 2-9, the field of view of Camera 1 was wider than that of Camera 2, and the images acquired by Camera 1 included those of Camera 2. After acquiring an image of the calibration target, the centers and boundaries of dots on the calibration target were identified by detecting the local maxima of contrast on the images. Figure 2-10 shows the acquired calibration target images with identified dots. In the views of Camera 1 and Camera 2, 251 and 163 dots were detected, respectively.

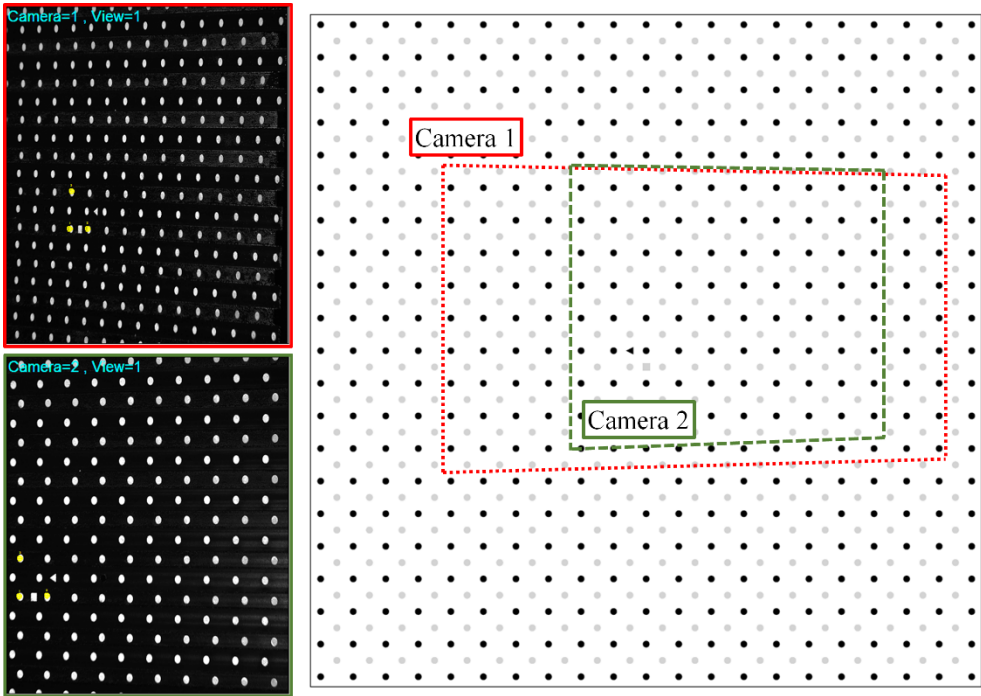


Figure 2-9. Calibration target images and field of view.

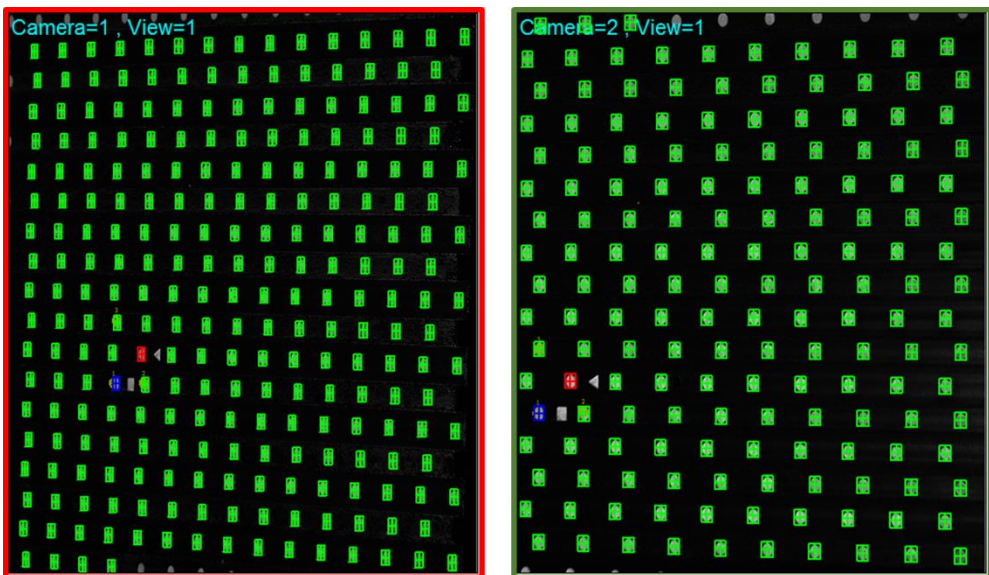


Figure 2-10. Dot identification.

The locations of dots on the calibration target were identified in 2D coordinate system on the particle images were matched to the position in the 3D real coordinate system by third-order polynomials. In DaVis 8.2, the mapping function of coordinate (X', Y') on raw images to coordinate (X, Y) on corrected image are defined as

$$X = X' - dX(s(X'), t(Y')) \text{ and} \quad (2-4)$$

$$Y = Y' - dY(s(X'), t(Y')), \quad (2-5)$$

where $s(X')$ and $t(Y')$ are distances to the origin (X_0, Y_0) . They are non-dimensionalized by half of the horizontal (X_H) and vertical (Y_V) sizes of the overlapped region direction in dimension of pixel numbers:

$$s(X') = 2(X' - X_0)/X_H \quad (2-6)$$

$$t(Y') = 2(Y' - Y_0)/Y_V \quad (2-7)$$

In the present study, X_0 , Y_0 , X_H , and Y_V were 766.5, 730.4, 2058, and 2456, respectively.

By calibration, dX and dY were derived in third-order polynomials as follows:

$$\begin{aligned} dX = & A_{00} + A_{10}s + A_{20}s^2 + A_{30}s^3 + A_{01}t + A_{02}t^2 \\ & + A_{03}t^3 + A_{11}st + A_{21}s^2t + A_{12}st^2 \end{aligned} \quad (2-8)$$

$$\begin{aligned} dY = & B_{00} + B_{10}s + B_{20}s^2 + B_{30}s^3 + B_{01}t + B_{02}t^2 \\ & + B_{03}t^3 + B_{11}st + B_{21}s^2t + B_{12}st^2 \end{aligned} \quad (2-9)$$

As two cameras and a two-tiered calibration target were used, the number of polynomials was set as four in the SPIV calibration. Figure 2-11 shows the calibration results for the two cameras and two depths on the calibration target

($Z = 0$ and 3 mm). The root-mean-square (RMS) of mapping error, which was derived from the disparity between the mapped position in Figure 2-12 and the identified position in Figure 2-10, was under 0.16 pixels.

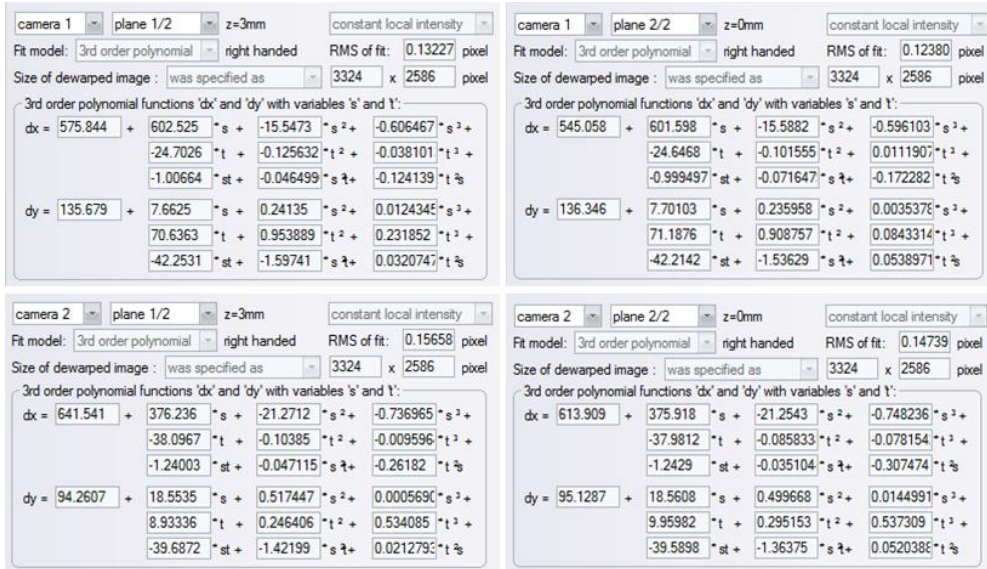


Figure 2-11. Calibration results.

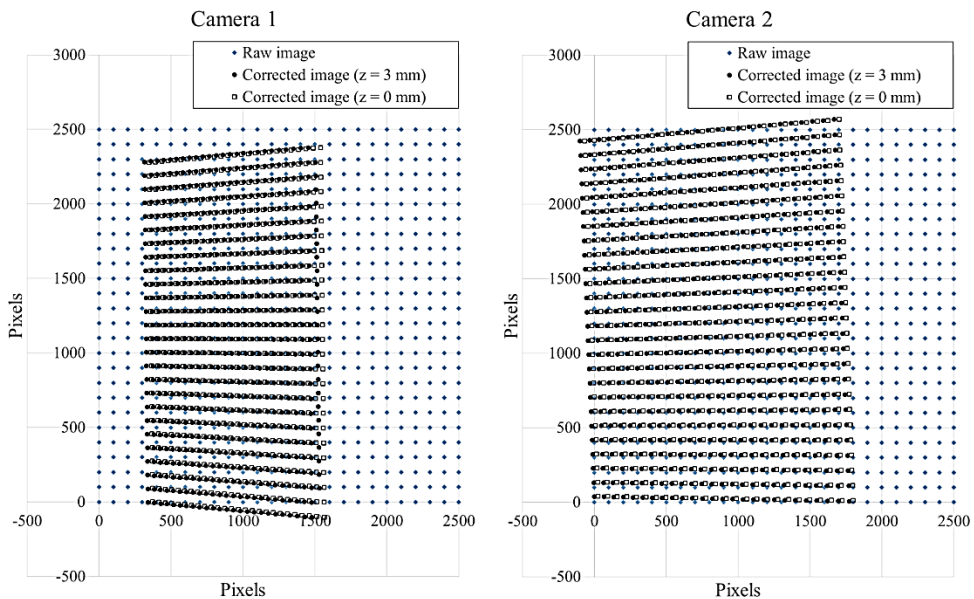


Figure 2-12. Comparisons of locations in the raw and corrected images.

Based on the results, dots in the physical coordinate system were mapped on the image plane, as shown in Figure 2-12. Captured particle images were corrected using the third-order polynomials. In the corrected images, disparity between the two camera images appeared only in the direction normal to the image. The corrected images of the calibration target overlapped and are shown in Figure 2-13. The acquired particle images were also corrected in the same manner as for the calibration target images before cross correlation.

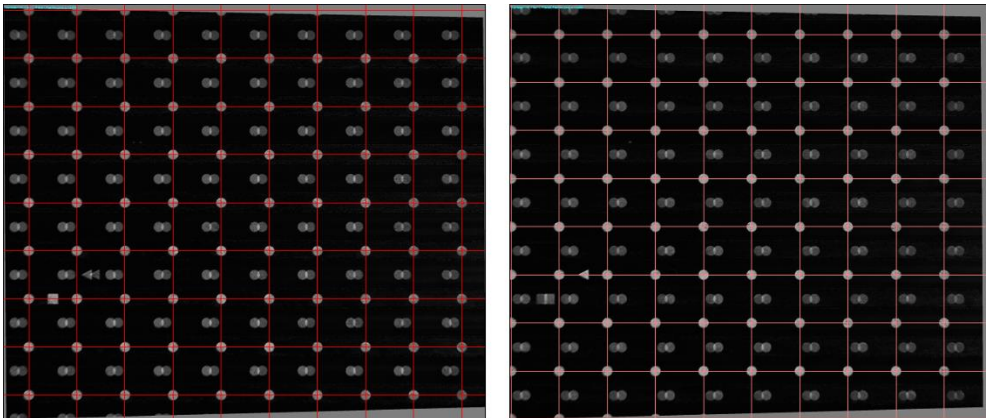


Figure 2-13. Corrected calibration target images: reference plane at $z = 0$ (left) and -3 mm (right).

After the calibration using the calibration target, self-calibration was applied to refine the calibration results. This method was first suggested in the study by Wieneke (2005). The basic idea is that particle images acquired from different cameras at the same time should be identical after being corrected by the calibration results. Disparity between the corrected particle images, which can be quantified by cross correlation, implies that the calibration target and measurement plane were not aligned correctly, as shown in Figure 2-14. The self-calibration method corrects the calibration results using the disparity map.

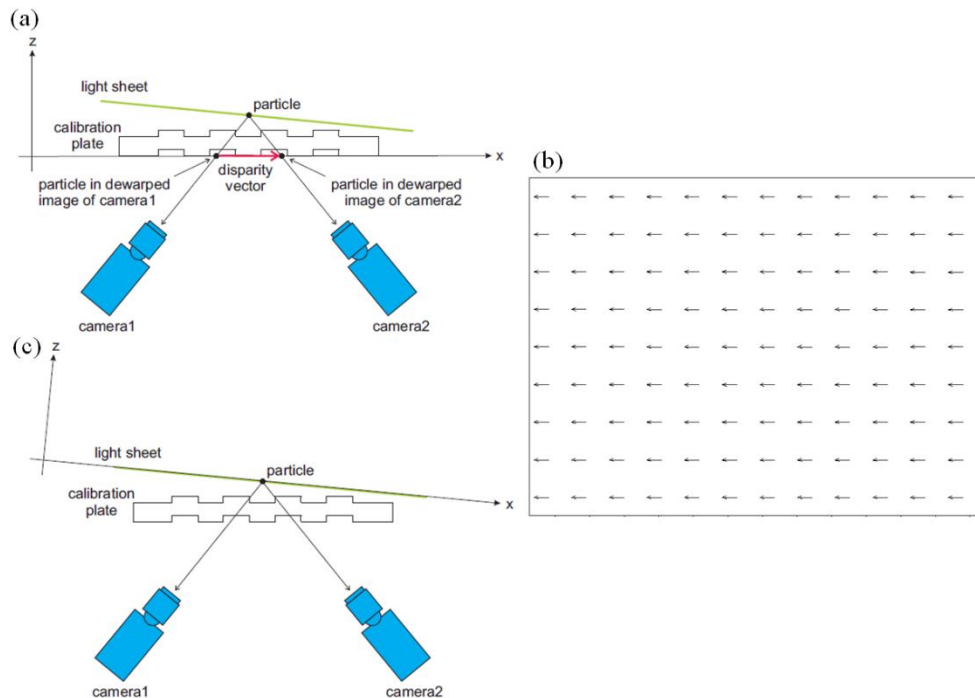


Figure 2-14. Self-calibration procedure: (a) calibration target misaligned with the laser sheet; (b) disparity map between two cameras; and (c) corrected calibration on the measurement plane (LaVision GmbH, 2012).

2.4.3. *SPIV system: tracer particle*

White-colored polyamide powder was used as tracer particles. Polyamide particles provide good reflection at a reasonable price; thus, they are applicable to towing tank tests, which require a large quantity of particles. A series of Vestosint®, manufactured by Evonik Industries (Essen, Germany), with different mean diameters was first tested in the towing tank to identify the optimal size of tracer particles. The mean diameters of the Vestosint® particles ranged from 56 to 20 μm , and the particle size and brightness in particle images were examined. Vestosint® 2161, with a mean diameter of 28

μm , was determined to be optimal. The density was 1.016 kg/m^3 , and buoyancy effects were negligible in the velocity field measurement. At each test day, 1 kg of tracer particles and 40 L of water were mixed and poured into the towing tank. A small amount ($< 5 \text{ g}$) of surfactant was added to the mixture, but its effects on the surface tension of water was negligible. Figure 2-15 shows a magnified particle image.

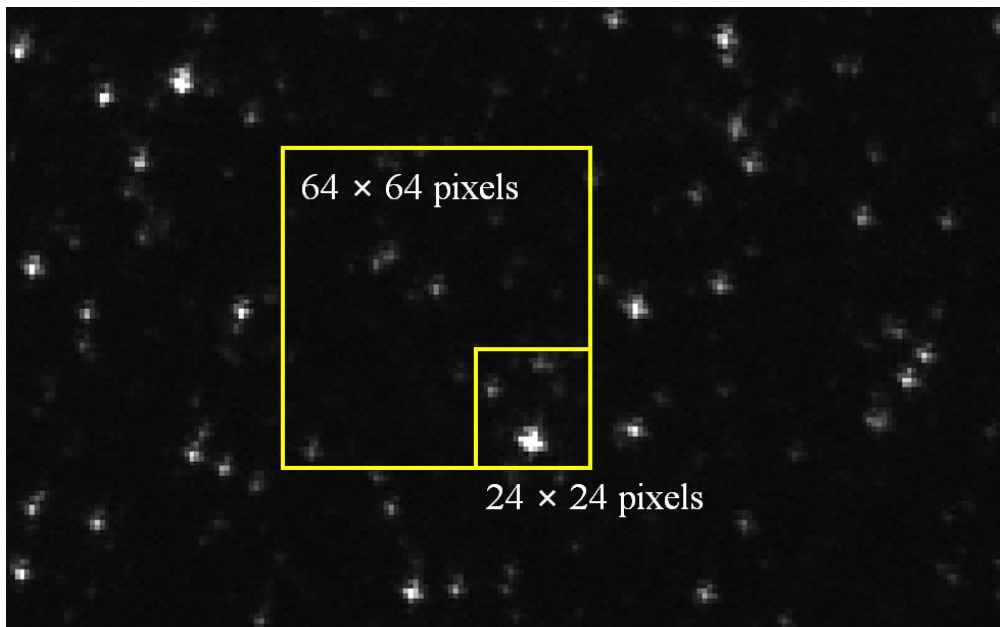


Figure 2-15. Particle image and interrogation windows.

2.2.4. *SPIV system: velocity field analysis*

The particle images acquired during carriage runs were first stored in the RAM of the PC and then moved into data storage after each carriage run. Figure 2-16 shows the flow chart of SPIV vector computation in DaVis 8.2.

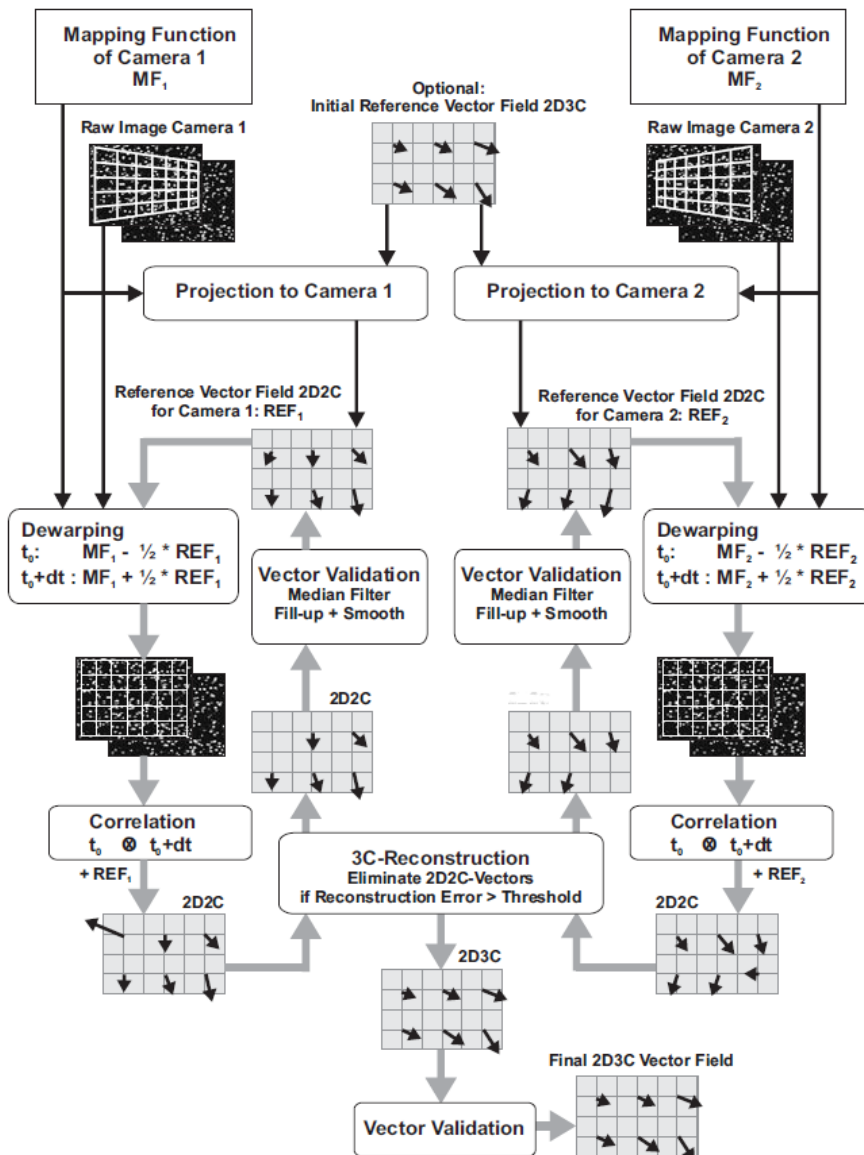


Figure 2-16. Flow chart of SPIV vector computation (LaVision GmbH, 2012).

The acquired particle images were first corrected using the mapping function obtained by calibration, and 2D velocity vectors were then derived by multi-pass cross correlation. The initial pass was carried out using an

interrogation window with dimensions of 64×64 pixels and without overlap. In the initial pass, the reference vector field was not applied. For the second and final pass, the size of interrogation window and overlap were 24×24 pixels and 50%, respectively. The vector field obtained by the initial pass was used as the reference vector field for the second pass. For both passes, the cross-correlation of intensity between two frames at (X, Y) ($I_1(X, Y)$ and $I_2(X, Y)$) was applied without normalization:

$$C(dX, dY) = \sum_{X=0, Y=0}^{X<n, Y<n} I_1(X, Y)I_2(X + dX, Y + dY) \quad (2-10)$$

For the final pass, the correlation results were non-dimensionalized:

$$C(dX, dY) = \frac{\sum_{X=0, Y=0}^{X<n, Y<n} (I_1(X, Y) - I_{1,ave}(X, Y))(I_2(X + dX, Y + dY) - I_{2,ave}(X + dX, Y + dY))}{RMS(I_1(X, Y) - I_{1,ave}(X, Y))RMS(I_2(X + dX, Y + dY) - I_{2,ave}(X + dX, Y + dY))} \quad (2-11)$$

As dX and dY were discretized, sub-pixel displacement should be estimated to acquire precise velocity. In the present study, Gaussian curve fitting was applied. To apply Gaussian curve fitting, dX and dY with local maximum of cross correlation ($C(dX, dY)$) was first identified. In addition, the cross-correlation results of surrounding locations, *i.e.*, $C(dX-1, dY)$, $C(dX + 1, dY)$, $C(dX, dY - 1)$, and $C(dX, dY + 1)$, were obtained and compared to derive the exact displacements, X_E and Y_E :

$$X_E = X + \frac{\ln C(dX-1, dY) - \ln C(dX+1, dY)}{2\ln C(dX-1, dY) - 4\ln C(dX, dY) + 2\ln C(dX+1, dY)} \quad (2-12)$$

$$Y_E = Y + \frac{\ln C(dX, dY-1) - \ln C(dX, dY+1)}{2\ln C(dX, dY-1) - 4\ln C(dX, dY) + 2\ln C(dX, dY+1)} \quad (2-13)$$

Once the velocity vector field was derived, the vector needed to be validated. In the present study, two validation methods were utilized: median and range filter. For median filter, the velocity vector was compared with the

median of its surrounding eight vectors. To define the threshold, the RMS errors of the surrounding vectors were also considered:

$$(X_E - X_{E,median}) > 2.5 \times \text{RMS of surrounding vectors} \quad (2-14)$$

$$(Y_E - Y_{E,median}) > 2.5 \times \text{RMS of surrounding vectors} \quad (2-15)$$

The particle displacement filtered by the median filter was a 2D representative particle displacement of the interrogation window. The disparity in 2D displacement between the two cameras was used to reconstruct the velocity component perpendicular to the measurement plane. If the disparity between 2D displacements from the two cameras was incoherent with the direction obtained by the calibration, and the error was larger than 2.5 pixels, the first peak was regarded as an error vector and the peak with second highest magnitude was used for the 3D reconstruction. After the reconstruction, the 3D particle displacement was divided by Δt to obtain the representative velocity at the interrogation window.

A range filter was applied to the velocity results. The filter used the magnitude of U to eliminate unrealistic vectors. The threshold of the range filter was $0.5U$ in the y and z directions and $1.5U$ in the x direction. When a velocity vector was deleted, another peak in the cross-correlation map was selected to derive an alternative velocity vector. Processed velocity vector fields were analyzed statistically. In the present study, Reynolds decomposition and proper orthogonal decomposition (POD) were utilized. Using Reynolds decomposition, the instantaneous velocity vector at time t ($\mathbf{V}(t)$) was decomposed into a time-mean ($\bar{\mathbf{V}}$) and fluctuating component at t ($\mathbf{V}'(t)$):

$$\mathbf{V}(\mathbf{x}, t) = \bar{\mathbf{V}}(\mathbf{x}) + \mathbf{V}'(\mathbf{x}, t) \quad (2-16)$$

Reynolds stress ($\overline{\mathbf{V}'\mathbf{V}'}$) has three normal and three shear components, which are derived from correlation of velocity fluctuations. Reynolds normal stresses were derived from the correlation of velocity fluctuation in same directional component:

$$\overline{u'u'}(\mathbf{x}) = \frac{1}{N} \sum_{i=1}^N u'(\mathbf{x}, i)u'(\mathbf{x}, i) \quad (2-17)$$

$$\overline{v'v'}(\mathbf{x}) = \frac{1}{N} \sum_{i=1}^N v'(\mathbf{x}, i)v'(\mathbf{x}, i) \quad (2-18)$$

$$\overline{w'w'}(\mathbf{x}) = \frac{1}{N} \sum_{i=1}^N w'(\mathbf{x}, i)w'(\mathbf{x}, i) \quad (2-19)$$

Turbulence kinetic energy, k , was derived from Reynolds normal stresses as half the sum of Reynolds normal stresses, which was non-dimensionalized by U^2 :

$$k(\mathbf{x}) = (\overline{u'u'}(\mathbf{x}) + \overline{v'v'}(\mathbf{x}) + \overline{w'w'}(\mathbf{x}))/2U^2 \quad (2-20)$$

Reynolds shear stress was defined as the correlation of velocity fluctuation in two different components:

$$\overline{u'v'}(\mathbf{x}) = \frac{1}{N} \sum_{i=1}^N u'(\mathbf{x}, i)v'(\mathbf{x}, i) \quad (2-21)$$

$$\overline{u'w'}(\mathbf{x}) = \frac{1}{N} \sum_{i=1}^N u'(\mathbf{x}, i)w'(\mathbf{x}, i) \quad (2-22)$$

$$\overline{v'w'}(\mathbf{x}) = \frac{1}{N} \sum_{i=1}^N v'(\mathbf{x}, i)w'(\mathbf{x}, i) \quad (2-23)$$

In the same manner as k , Reynolds stresses were non-dimensionalized by U^2 in the results.

Using POD, coherent turbulence structures were acquired from a time series of vector fields, $\mathbf{V}(\mathbf{x})$. $\mathbf{V}(\mathbf{x}, t)$ could be approximated by sum of products

of coherent turbulence structure independent on time and coefficient dependent on time,

$$\mathbf{V}(\mathbf{x}, t) = \sum_{n=0}^N a_n(t) \boldsymbol{\Phi}_n(\mathbf{x}), \quad (2-24)$$

where $a_n(t)$ and $\boldsymbol{\Phi}_n(\mathbf{x})$ are the n -th coefficients and mode, respectively, and N is the number of instantaneous flow field samples. In this study, N was 1,000. When n was zero, $a_0(t)\boldsymbol{\Phi}_0(\mathbf{x})$ was defined as the time mean flow field, $\bar{\mathbf{V}}(\mathbf{x})$.

Using the snapshot method (Sirovich, 1987), $a_n(t)$ and $\boldsymbol{\Phi}_n(\mathbf{x})$ can be obtained from the eigenvectors of a matrix, C . The elements of C , C_{ki} , are defined as the inner products of velocity at different times (Adrian and Westerweel, 2001):

$$C_{ki} = \frac{1}{N} \int \mathbf{V}(\mathbf{x}, t_k) \cdot \mathbf{V}(\mathbf{x}, t_i) d\mathbf{x} \quad (2-25)$$

By solving the eigenvalue problem, $C\mathbf{V}^* = \lambda\mathbf{V}^*$, a set of eigenvectors that consist of coefficients are acquired:

$$\mathbf{V}^{*n} = [a_n(t_1), a_n(t_2), \dots, a_n(t_N)]^T \quad (2-26)$$

The inner products of eigenvectors are normalized to obtain normalized eigenvalues:

$$\frac{1}{N} (\mathbf{V}^{*n} \cdot \mathbf{V}^{*m}) = \lambda_n \delta_{nm} \quad (2-27)$$

$\boldsymbol{\Phi}_n(\mathbf{x})$ can be derived from N , λ_n , $a_n(t)$, and $\mathbf{V}(\mathbf{x}, t)$:

$$\boldsymbol{\Phi}_n(\mathbf{x}) = \frac{1}{N\lambda_n} \sum_{k=1}^N a_n(t_k) \mathbf{V}(\mathbf{x}, t_k) \quad (2-28)$$

$a_n(t)\boldsymbol{\Phi}_n(\mathbf{x})$ are orthonormal:

$$a_n(t)\boldsymbol{\Phi}_n(\mathbf{x}) \cdot a_m(t)\boldsymbol{\Phi}_m(\mathbf{x}) = \delta_{nm} \quad (2-29)$$

$\Phi_n(\mathbf{x})$ is arranged in the order of energy; thus, the product of $a_n(t)$ and $\Phi_n(\mathbf{x})$ gives the energy level of turbulence. When n is high, the turbulence is localized and has low energy. To investigate coherent turbulence structure, modes in low order of n , under ten, are used. To obtain coherent turbulence structure independent of time, the product of the RMS of n -th coefficients and n -th mode is derived as an n -th representative coherent turbulence structure of the velocity field measurement.

2.4.5. LDV system: hardware

An underwater LDV system was designed to measure the one-dimensional (1D) velocity component, particularly in the x direction. Mean x -directional velocity and Reynolds normal stress in x -direction were provided from the measurement results for comparison with the SPIV results.

The LDV system was designed and manufactured by Dantec Dynamics A/S (Skovlunde, Denmark). It comprises a continuous laser, a beam transmitter, fiber manipulators, a waterproof probe, back-scatter receiving optics, and an FFT analyzer. Figure 2-17 shows the LDV system used in this study.

An air-cooled Argon ion laser (Stellar-Pro-L Multi-Line/300) manufactured by Modu-Laser LLC (Centerville, UT) was used. Figure 2-18 shows the design of the laser head. Its maximum total output power was 300 mW , and it generated a continuous laser beam with a diameter of 0.75 mm and a wavelength in the range from 457.9 to 514.5 nm .

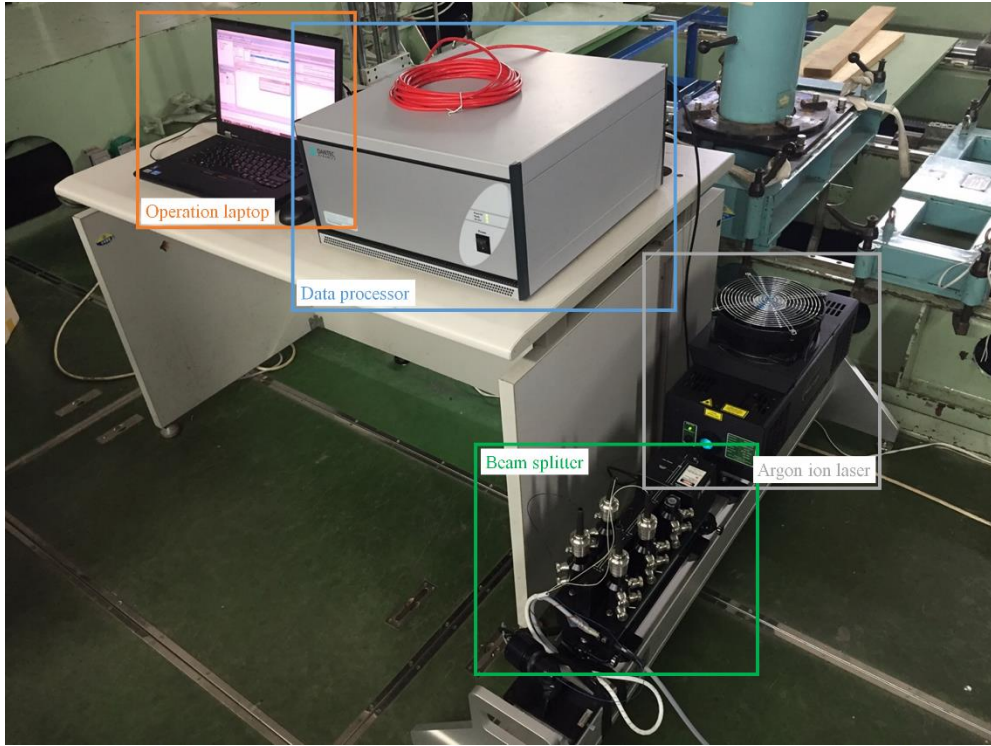


Figure 2-17. System components of the underwater LDV system.

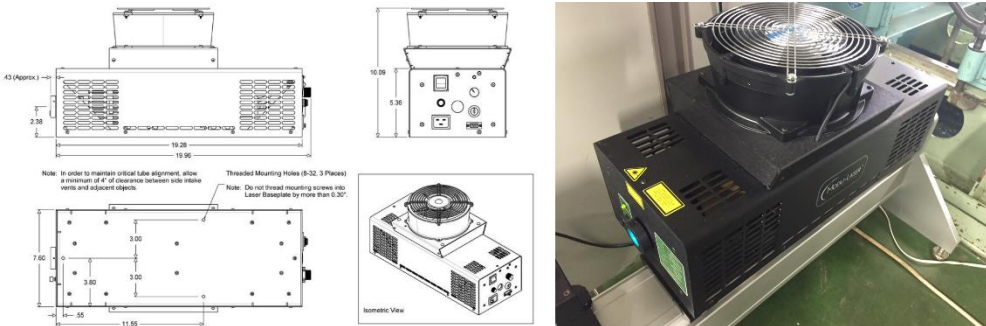


Figure 2-18. Continuous argon ion laser head.

The laser beam from the laser head passed through a 60X41 Bragg cell to shift the frequency of the laser beam by 40 MHz. Figure 2-19 shows the beam splitter and Bragg cell. The original and frequency-shifted beam entered the beam transmitter and were distributed according to wavelength (λ). As a 1D LDA system was used, only a laser beam with a wavelength of 514 nm was used. Laser beam which entered to the waterproof probe can be adjusted by 60X24 fiber manipulators, to make good laser beam intersection at the measurement volume location.

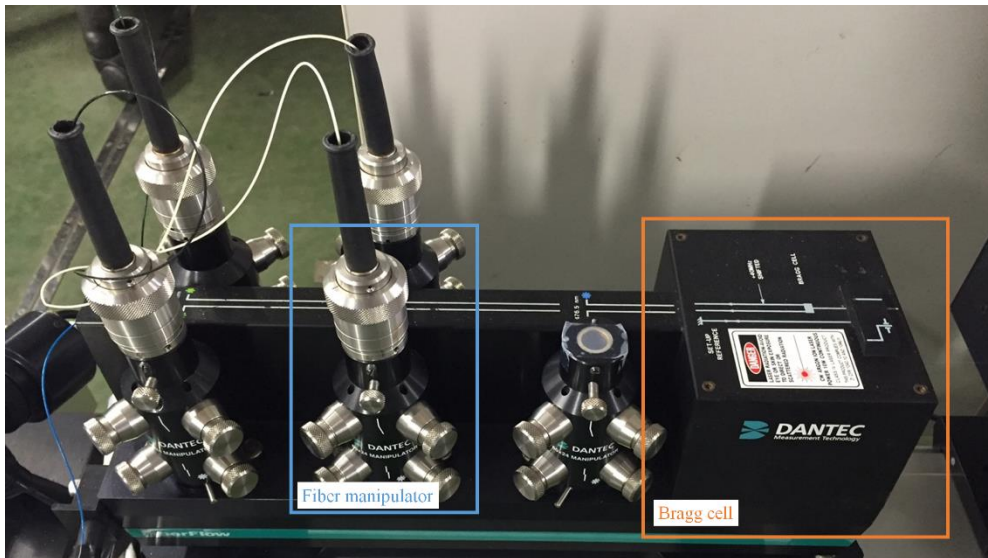


Figure 2-19. Beam splitter with Bragg cell and fiber manipulator.

A 60X61 FlowLite waterproof LDV probe (manufactured by Dantec Dynamics A/S) with a diameter of 60 mm was used. The laser beam spacing at the probe head was 38.00 mm. The diameter of laser beam from the probe was 1.350 mm. A circular convex lens with a focal length of 399.5 mm was used to converge the laser beams at the measurement volume.



Figure 2-20. 60X61 FlowLite waterproof LDV probe.

2.4.6. LDV system: velocity analysis

The brightness at the intersection of two laser beams was recorded by back-scatter receiving optics, and the frequency of the scattered signal was analyzed by a BSA F60 flow processor. The velocity in the x direction in the LDV measurement volume, $u(\mathbf{X}, t)$, was derived from the parameters of optical arrangement and f_D , the frequency of the backscattered signal:

$$u(\mathbf{X}, t) = d_f f_d = (\lambda f_D) / (2 \sin(\theta/2)). \quad (2-30)$$

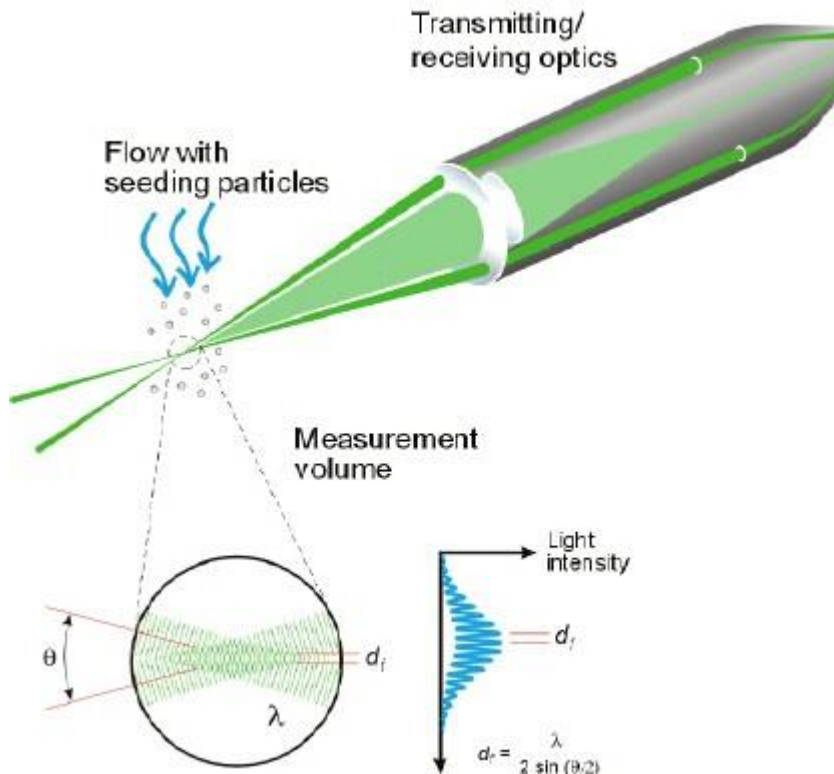


Figure 2-21. Schematic of LDV optics (Dantec A/S, 2014).

BSA Flow Software version 5.20, developed by Dantec Dynamics A/S, was used to acquire and record the velocity at the measurement point from the frequency signal. Figure 2-22 shows the screenshot of data acquisition.

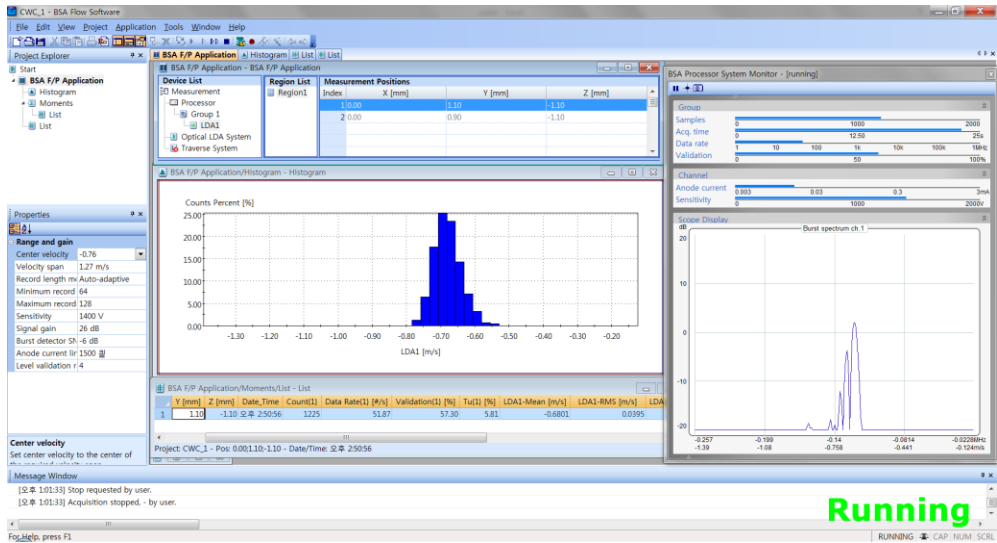


Figure 2-22. Screenshot of LDV data acquisition using BSA Flow v5.

In the LDA measurement, the acquisition rate of velocity measurement varied by flow speed and particle seeding density. In the low-speed region, the data acquisition rate decreased. Overall, the data acquisition rate was around 50 Hz; thus, the number of obtained velocity data from one towing carriage run was around 2,000 for 40 s of data acquisition. Tests were repeated to obtain 10,000 samples for each measurement location.

2.4.7. Wave height gauge

A capacitance-type wave height gauge was used to measure wave elevation around the test model. The wave height gauge system was manufactured by Digi-tech (Seoul, Korea). The amplifier output voltage signal, which is proportional to capacitance change of the wire of the probe and of water immersion. The magnitude of the voltage signal from the amplifier was recorded by a data acquisition system (MGC plus and CatmanEasy version 3.1; Hottinger Baldwin Messtechnik GmbH, Darmstadt, Germany). A multi-channel voltage measurement board (AP801) was installed in the MGC plus system.

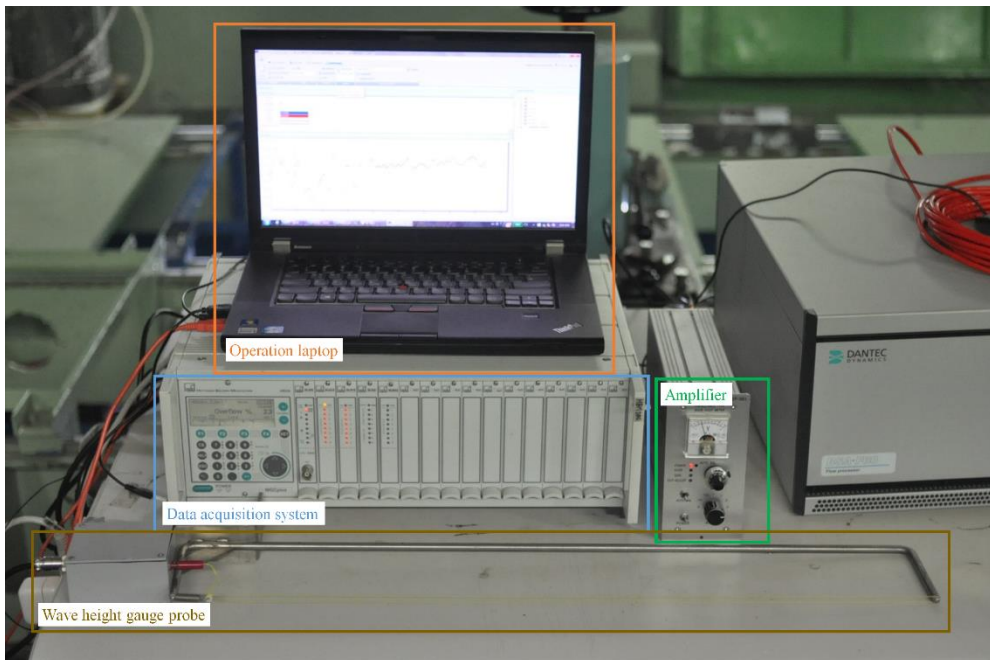


Figure 2-23. Capacitance-type wave height gauge system.

2.5. Measurement locations

2.5.1. *Velocity field measurement*

Underwater SPIV measurements were conducted to investigate the flow field around the model. The measurement planes were perpendicular to the towing direction. Figure 2-24 shows the locations of SPIV measurement. For the large model, the x -directional location of the measurement planes ranged from $0.25 L$ to $0.7 L$.

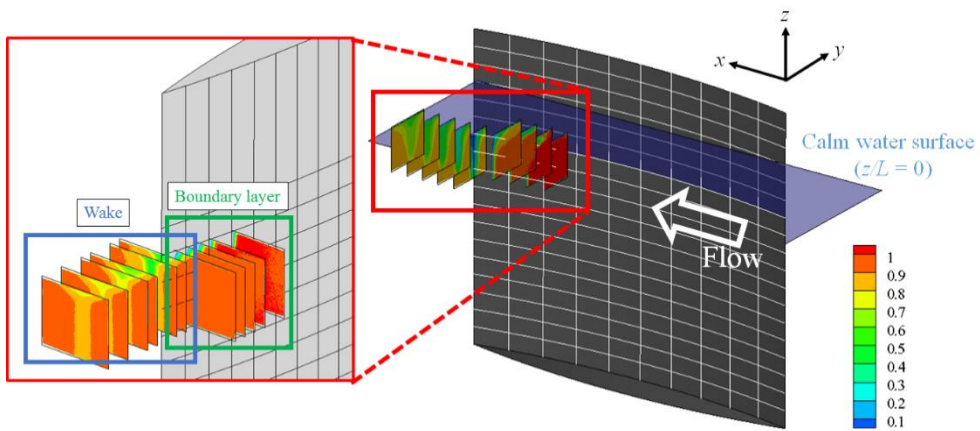
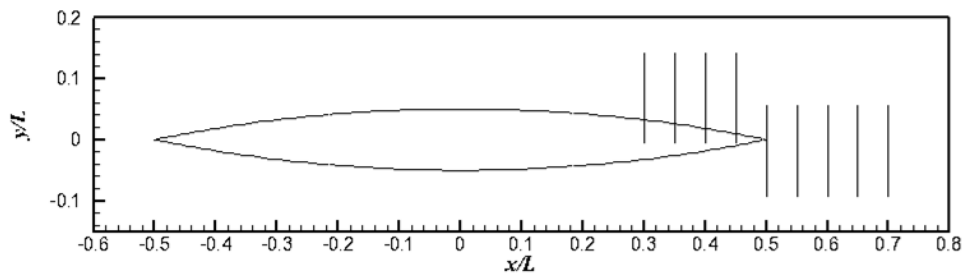


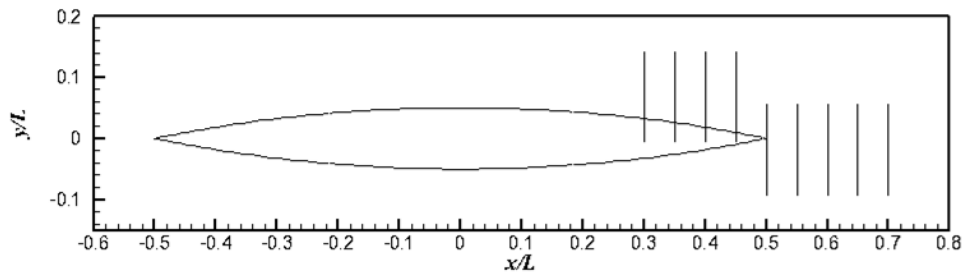
Figure 2-24. Locations of measurement planes.

Figure 2-25 shows the x -directional locations of the measurement planes for the three model sizes. For the large model, the gaps between measurement planes were $0.025 L$, except $x/L = 0.625$ and 0.675 . In the medium and small models, the intervals were $0.05 L$. From $0.25 L$ to $0.5 L$, the boundary layer flow fields on the model surface were focused. The flow field measurement in the near-wake region ($0.5 L$ to $0.7 L$) provides information on velocity recovery, turbulence dissipation, and coherent turbulence structure.

$L = 215 \text{ mm}$



$L = 464 \text{ mm}$



$L = 1000 \text{ mm}$

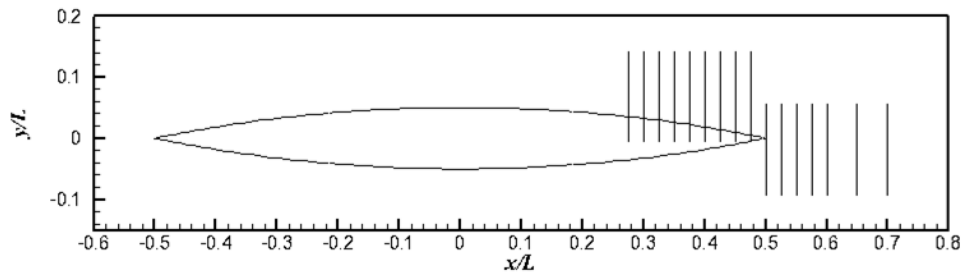


Figure 2-25. SPIV measurement plane locations.

2.5.2. Wave height measurement

The main purpose of the wave height gauge measurement was to analyze wave height fluctuation in violent free-surface region in frequency domain; therefore, The wave elevations in two Fr conditions were measured: steady and smooth free-surface wave ($Fr = 0.282$) and unsteady and entrained wave ($Fr = 0.400$). Time mean of wave height around the model in the two Fr conditions was measured first. The distance between the model surface and wave height gauge was $0.02 L$ in the large model. The longitudinal locations of the wave elevation measurements ranged from $-0.5 L$ to $0.5 L$ with a distance of $0.05 L$. In the wake region ($x/L > 0.5$), the wave elevations at $0.6L$ and $0.7L$ were also measured.

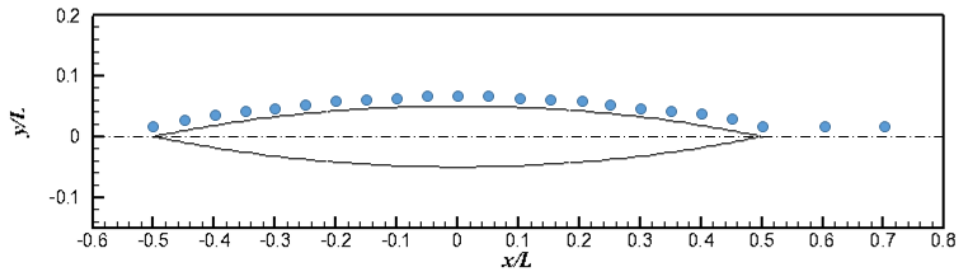


Figure 2-26. Wave elevation measurement locations.

Chapter 3. Test Uncertainty

3.1. Overview

Measurement uncertainties different test systems including SPIV, LDV, and wave height gauge were assessed following standard procedures provided by the American Society of Mechanical Engineers (ASME) (ASME, 2005). In principle, test uncertainty consists of both systematic and random error. Systematic error refers to the difference between the average of repeated test results and the true value. Random error is defined as the scatter in the test results. Figure 3-1 demonstrates the principle of test uncertainty.

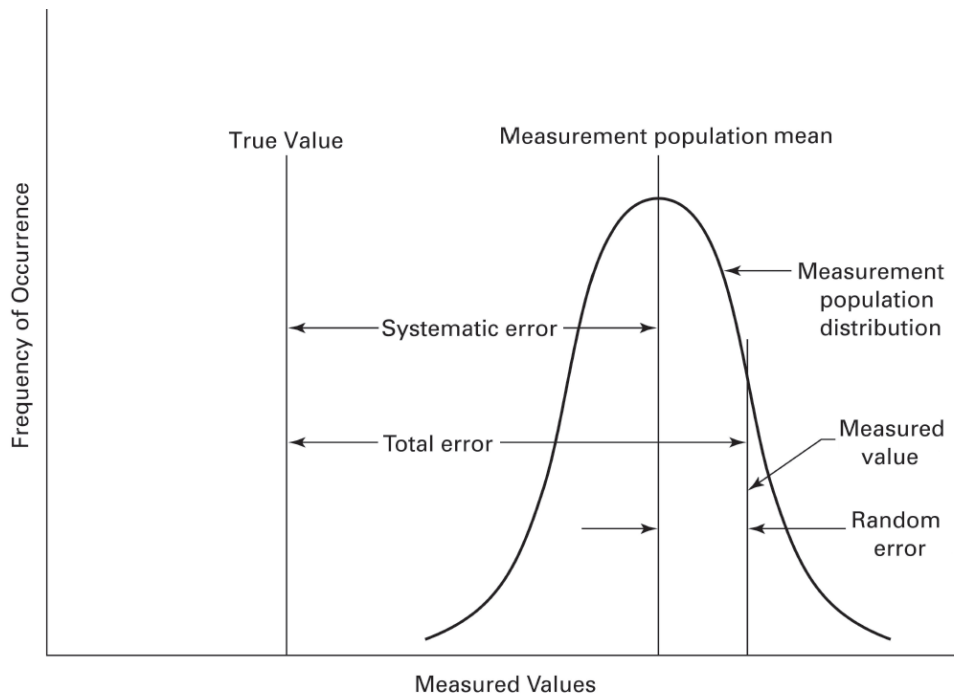


Figure 3-1. Principle of errors in measurement (ASME, 2005).

To estimate systematic error, ASME suggests to first construct a data reduction equation comprising the systematic errors and sensitivities of the individual measurements. For example, pressure coefficient, C_p , is derived from pressure, p , density of the fluid, ρ , projected area, A , and inflow velocity, U , as shown in Eq. 3-1.

$$C_p = \frac{p}{0.5\rho(T)AU^2} \quad (3-1)$$

Typically, the systematic error of commercially-available measurement devices can be obtained from the manufacturer. For example, the systematic errors of the thermometer, pressure gauge, and model size accuracy are provided by the manufacturer. U can be measured with a Pitot-static tube, LDV, or flow meter; thus, the systematic error of the measurement system is known.

After acquiring the systematic errors of elements, the partial derivatives of data reduction equation is derived to yield the sensitivity of measurement elements. As shown in Eq. 3-2, the systematic error of C_p is defined as the root-sum-square of the product of the systematic error and sensitivity.

$$\delta C_p = \sqrt{\left(\frac{\partial C_p}{\partial p} \delta p\right)^2 + \left(\frac{\partial C_p}{\partial \rho} \delta \rho\right)^2 + \left(\frac{\partial C_p}{\partial A} \delta A\right)^2 + \left(\frac{\partial C_p}{\partial U} \delta U\right)^2} \quad (3-2)$$

Occasionally, the data reduction equation is too complex to solve numerically. For instance, the SPIV measurement includes image correction, cross-correlation, filtering, and 3D reconstruction. Although there have been studies to assess the PIV measurement test uncertainty, they have focused on cross-correlation algorithms, which are mostly applicable to 2D PIV systems (Nobach and Bodenschats, 2009; Timmins *et al.*, 2012; Sciacchitano *et al.*, 2013).

ASME suggests an alternative method to assess systematic error of a test system. Here, a reference value is measured with known systematic error. The difference in the measurement results and the reference is combined with the systematic error of the reference to yield the total systematic error.

In the present study, the reference was towing carriage speed, which was obtained from towing tank tests in open water. The open water allows for temporally- and spatially-uniform flow, providing a reliable reference to test uncertainty (Di Felice *et al.*, 2010). The mean and fluctuation of the towing carriage speed were estimated first.

By comparison with the reference, systematic error could be assessed. To investigate the effects of flow speed around submerged measurement systems, the towing speed was varied. In addition, Δt for the SPIV measurement was varied in the uniform flow measurement to examine the effects of particle displacement on the particle images on the systematic error.

The random error was obtained from repeated tests. The nominal wake of a model ship was measured and random error was assessed. Data convergence of the SPIV and LDV systems according to the data sample number was also examined. The results were compared with an existing experimental database. To characterize the flow measurement systems, mean velocity and Reynolds normal stresses were compared with the estimated total uncertainty.

3.2. Uniform flow measurement setup

3.2.1. Towing carriage speed

The accuracy of the towing tank carriage speed is the most crucial component to assess test uncertainty. Therefore, the uncertainties of the mean and fluctuations of the towing carriage speed should be assessed first.

To measure the towing carriage speed, the mean revolution rate of the carriage wheels and the time required to pass beacons distributed over a certain distance were measured independently and compared. The circumference of the carriage wheel was 2,000 mm. The revolution rate of the wheel was measured by a 12-bit rotary encoder. Its angular displacement resolution was 0.088° and the measurement sampling rate was 100 Hz. The systematic error in the mean velocity measurement by the rotary encoder was 0.244 mm/s.

Figure 3-2 shows the arrangement of the towing tank and beacons. Three beacons (A-C) were placed on the towing carriage rail 10,000 mm apart (A-B: 10,000 mm, B-C: 10,000 mm, A-C: 20,000 mm) for the mean speed measurement. The time required to pass each beacon was measured by optical sensors. Two optical sensors were installed on the towing carriage; thus, six mean velocities could be obtained from one towing carriage run. Tests were repeated five times, providing 30 mean velocity values for one towing carriage speed condition. The data sampling rate of the optical sensor was 200 Hz. Systematic error of the measurement system was 0.05 mm/s at $U = 1,000$ mm/s.

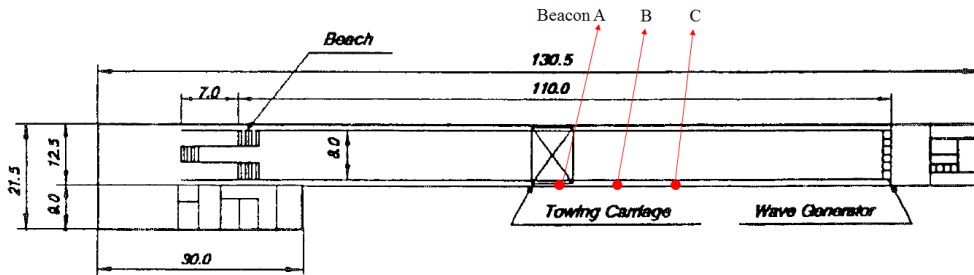


Figure 3-2. Arrangement of the towing tank and beacons.

The mean and fluctuation in the towing carriage speed measurements are shown in Table 3-1. Towing carriage speed ranged from 500 *mm/s* to 1,500 *mm/s*. Initially, the measured towing carriage speed was slower than the input, but the difference decreased linearly as the input speed increased. The towing carriage speed was expected to be identical to the input at 2,192 *mm/s*. The towing carriage speed was corrected by a linear approximation to decrease the disparity between input and towing carriage speed.

Table 3-1. Towing carriage speed measured by beacons and correction results

Input speed (<i>mm/s</i>)	Speed measured by beacons (<i>mm/s</i>)	Difference (<i>mm/s</i>)	Difference / Input speed (%)	Speed after correction (<i>mm/s</i>)
500	494.5	-5.5	1.10	500.6
1000	995.9	-4.1	0.41	1000.3
1500	1497.8	-2.2	0.15	1500.6

After the speed correction, the towing carriage speed was measured by the rotary encoder of the AC servo motor on the towing carriage wheel. The mean and standard deviation of the towing carriage speed measurements are shown in Table 3-2. In general, the standard deviation of the towing carriage speed was around 0.7% of the input speed. The standard deviation of the towing carriage speed was compared with the turbulent properties in the uniform flow measurements from the SPIV and LDV measurements as discussed in the following section.

Table 3-2. Towing carriage speed measurement by rotary encoder

Input speed (<i>mm/s</i>)	Speed measured by beacons (<i>mm/s</i>)	Rotary encoder measurement		
		Mean speed (<i>mm/s</i>)	Standard deviation (<i>mm/s</i>)	Standard deviation/Mean speed (%)
500	500.6	500.92	3.42	0.68
1000	1000.3	1001.7	7.28	0.73
1500	1500.6	1502.8	10.57	0.70

3.2.2. 1D LDV measurement

For the LDV measurement in open water, the towing carriage speed varied from 500 *mm/s* to 1,500 *mm/s*. the number of data samples acquired was 2,000, which showed good convergence in mean and fluctuation. Data convergence was reported with the KVLCC2 nominal wake measurement results as described in the following section. The error in the angular disparity of the LDV measurement and flow direction alignment was 0.5°. The systematic error caused by the misalignment was 0.87% of the measured velocity.

3.2.3. Towed underwater SPIV system

In the uniform flow measurement by towed underwater SPIV, the average image particle displacement and towing carriage speed were varied. Similar to the LDV installation, the error in the measurements caused by the misalignment under 0.5° was 0.87%. Towing speeds ranged from 500 *mm/s* to 1,500 *mm/s* in intervals of 500 *mm/s*.

Variation in the particle displacement was only applied to the medium towing speed (1,000 *mm/s*). The time interval between two image frames was varied from 50 to 800 μs to achieve different particle displacements.

Table 3-3 summarizes the time interval, corresponding particle displacements on the particle images, and actual displacement. The particle movement in the uniform flow measurement was normal to the measurement plane. The actual particle displacement was non-dimensionalized by the laser sheet thickness of 2.0 *mm*. The number of data samples for the uniform flow measurement was 1,000.

Table 3-3. Particle displacement in the uniform flow at $U = 1.0 \text{ m/s}$

Time interval (Δt) (μs)	50	100	200	350	450	550	650	800
Particle displacement (μm)	50	100	200	350	450	550	650	800
Particle displacement /laser sheet thickness (%)	2.5	5.0	20	27.5	33.5	37.5	32.5	40
Particle displacement in Camera A (pixels)	0.50	1.0	2.0	3.5	4.5	5.5	6.5	8.0
Particle displacement in Camera B (pixels)	0.57	1.1	2.3	4.0	5.1	6.3	7.4	9.1

3.3. Uncertainty assessment: systematic error

3.3.1. *1D LDV measurement*

Figure 3-3 shows the temporal evolution of the uniform flow measurement from the 1D LDV system. Based on the instantaneous velocity measurements, temporal evolution, the time-mean longitudinal velocity and $\overline{u'u'}$ was derived. The standard deviation of the velocity was 4.8% of the towing carriage speed at $U = 1,000 \text{ mm/s}$. Since the towing carriage speed deviation was around 0.7% of U , the fluctuation in the 1D LDV measurement seemed to be caused by local turbulence and random particle motion. Based on the standard deviation, $\overline{u'u'}$ measured in the uniform flow could be obtained. Systematic errors of the measurement are summarized in Table 3-4.

Table 3-4. Uniform flow measurement by 1D LDV

Input speed (mm/s)	Measurement results		Systematic error	
	Mean velocity (10^{-2})	Standard deviation (10^{-2})	u/U (10^{-2})	$\overline{u'u'}/U^2$ (10^{-4})
500	99.72	3.40	0.28	11.6
1000	99.65	4.82	0.35	23.2
1500	99.5	4.77	0.5	22.8

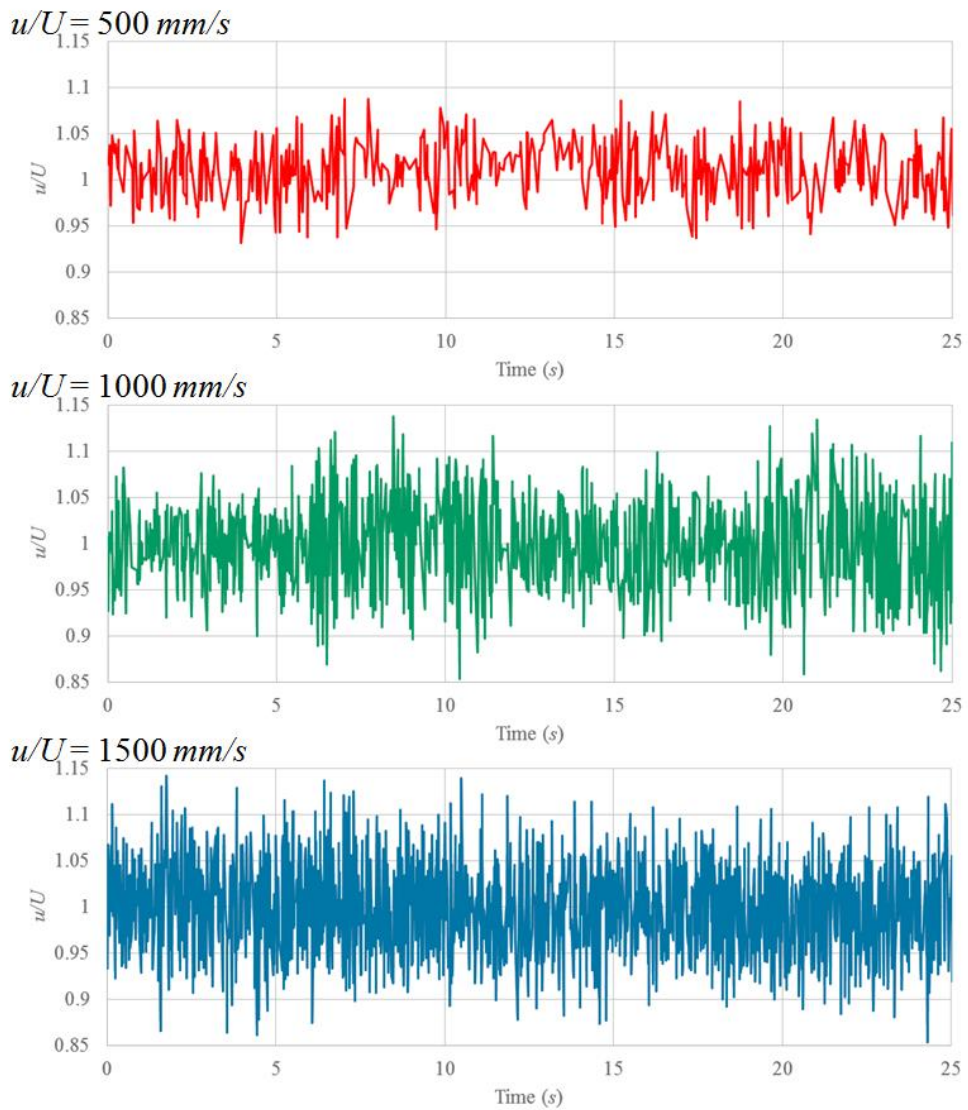


Figure 3-3. Time history of uniform flow measurement by 1D LDV.

3.3.2. SPIV measurement

Figures 3-4 and 3-5 show uniform flow measurement results, which indicate the difference between the measurement and reference values. The reference for the mean u/U was 1.0, whereas the reference for other components was zero. Particle displacement between frames in every case was identical to the reference case ($U = 1,000 \text{ mm/s}$, $\Delta t = 350 \mu\text{s}$).

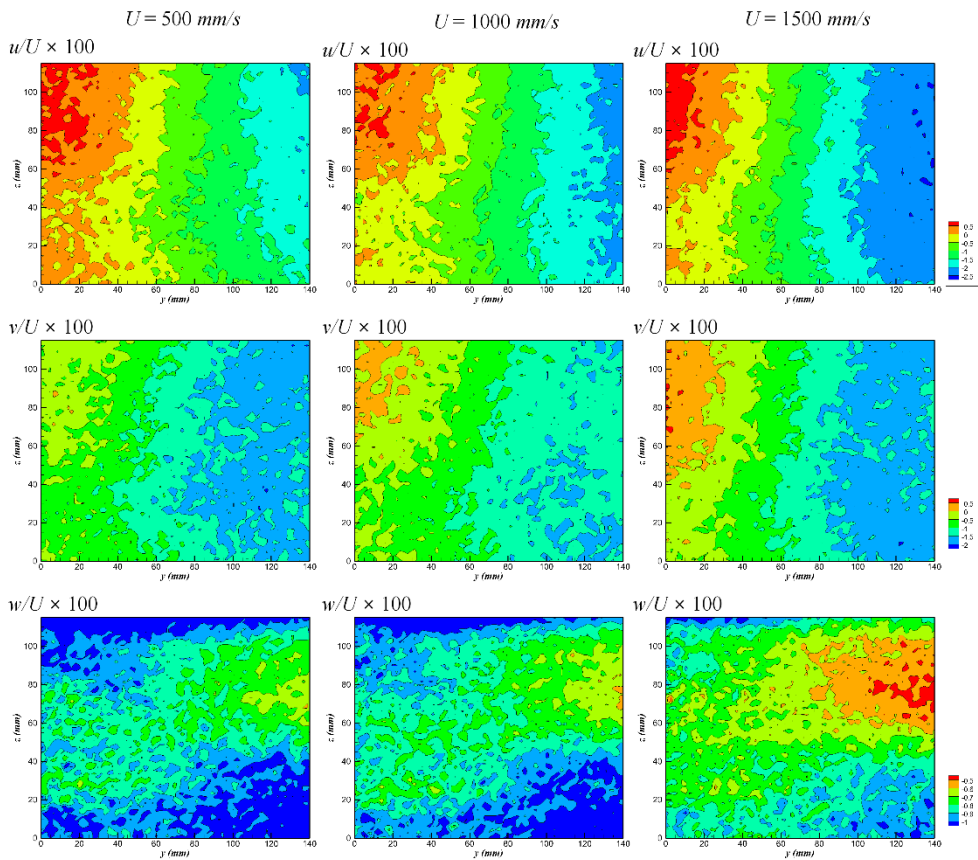


Figure 3-4. Mean velocity of uniform flow measurement results: u/U (top), v/U (middle), w/U (bottom).

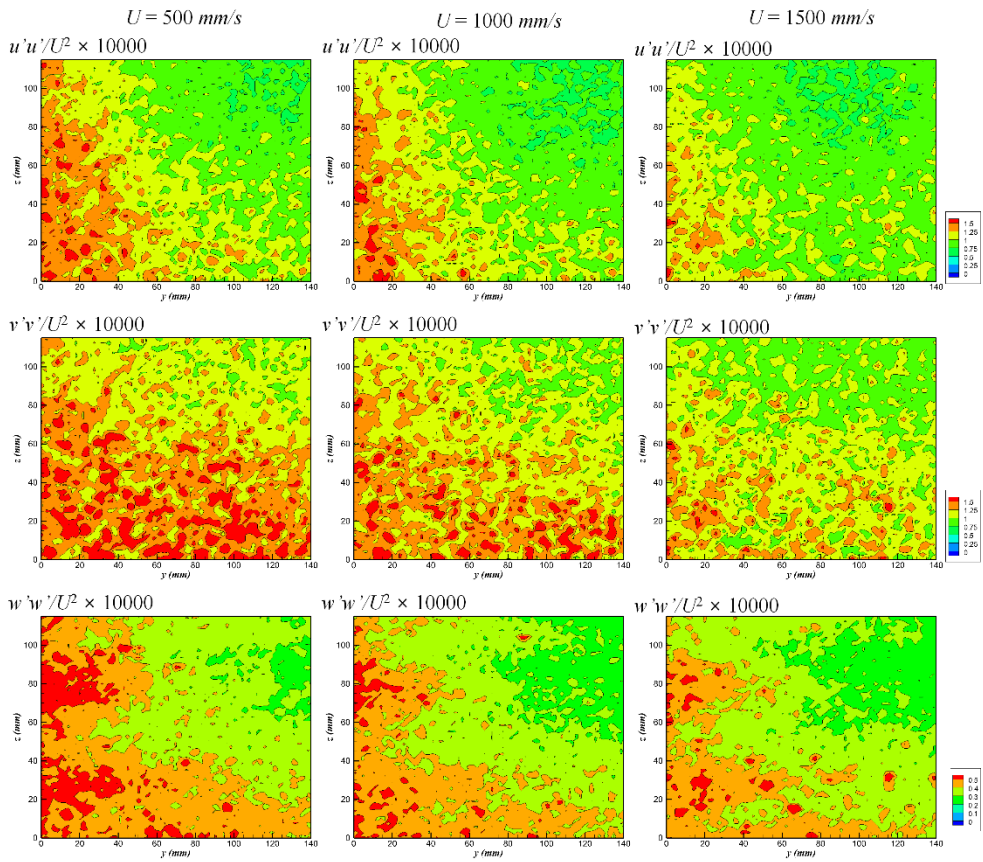


Figure 3-5. Reynolds stress distribution of uniform flow measurement results.

The velocity difference changes gradually in the measurement plane, which reflects the optical characteristics of the towed underwater SPIV system. The error increased near $y = 0 \text{ mm}$, where the particle image distortion was maximized in the view of Camera 1.

Since the SPIV system has a narrow angle between the camera centerline and measurement plane in the z -direction, the error in u/U and v/U was larger than that in w/U . In addition, the fluctuation in the towing carriage speed caused errors in u/U and v/U as well as the optical arrangement, which resulted

in perturbations to the particle displacement in the particle images, especially in the horizontal displacement, ΔX . As shown in the test setup of the SPIV system, Δx and Δy were greatly affected by ΔX on the particle images; thus, errors in u/U and v/U increased as well as the uncertainty of the x - and y -directional components of mean speed and Reynolds normal stress.

Table 3-5 shows the mean and spatial RMS of the measurement results for different towing speeds. In addition to the mean and standard deviation, cross-correlation between the two velocity components were obtained to derive Reynolds shear stress.

Table 3-5. Errors of mean velocity and turbulence properties obtained by the uniform flow measurement

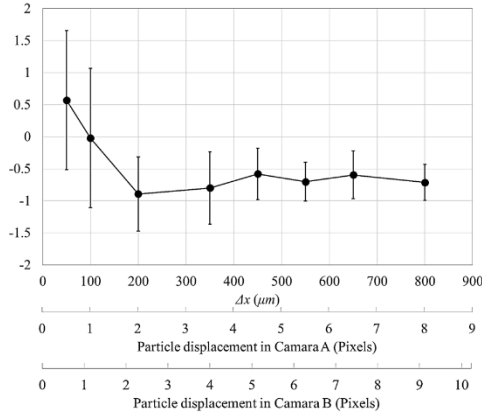
Input speed (mm/s)		500		1000		1500	
		Spatial mean	Spatial RMS	Spatial mean	Spatial RMS	Spatial mean	Spatial RMS
Error of mean velocity (10^{-2})	u/U	-0.69	0.77	-0.90	0.91	-1.13	0.94
	v/U	-1.14	0.48	-1.05	0.59	-0.98	0.65
	w/U	-0.92	0.13	-0.84	0.12	-0.75	0.13
Error of turbulence properties (10^{-4})	$\overline{u'u'}/U^2$	1.07	0.51	1.01	0.50	0.95	0.52
	$\overline{v'v'}/U^2$	1.26	0.40	1.15	0.38	1.09	0.41
	$\overline{w'w'}/U^2$	0.20	0.07	0.18	0.05	0.17	0.07
	$\overline{v'w'}/U^2$	0.09	0.03	0.10	0.04	0.09	0.04
	$\overline{u'w'}/U^2$	0.11	0.04	0.11	0.04	0.10	0.04
	$\overline{u'v'}/U^2$	0.43	0.18	0.41	0.18	0.41	0.17
	k/U^2	1.23	0.51	1.17	0.51	1.00	0.49

As the towing speed varied, the behavior and magnitudes of the errors were very similar. Therefore, the uncertainty assessed for the reference case could be applied to the test results at different speeds.

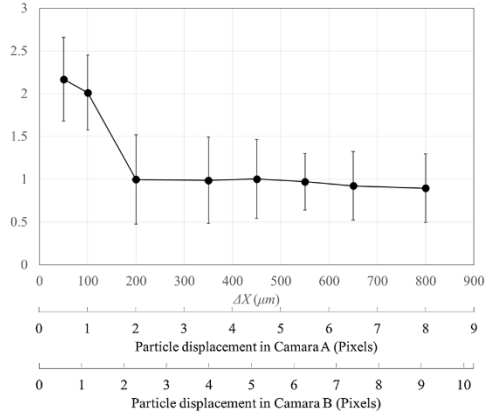
Notably, the magnitude of the error in the Reynolds normal stress was much smaller than that of the 1D LDV system. Since the SPIV obtained a representative velocity vector in the interrogated window area based on cross-correlation, local velocity fluctuations could be easily neglected in this spatially uniform flow.

Figure 3-6 shows the spatial mean and RMS of the mean velocity and Reynolds normal stresses in the uniform flow measurement with particle displacement variations. When the particle displacement was less than one pixel, the error in the mean and standard deviation increased. The maximum particle displacement in the uniform flow measurement was 40% of the laser sheet thickness, implying that 60% of tracer particles in the first particle image frame remained in the second frame. In the particle displacement case, however, SPIV results showed error in uniform level.

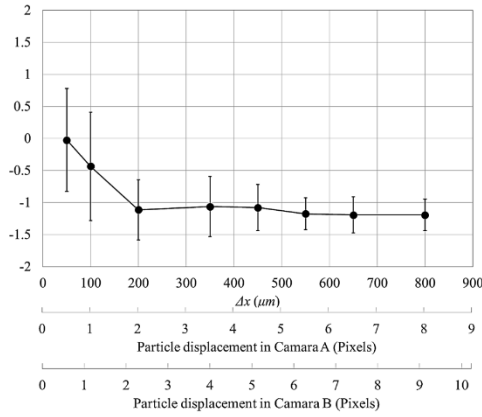
$u/U \times 100$



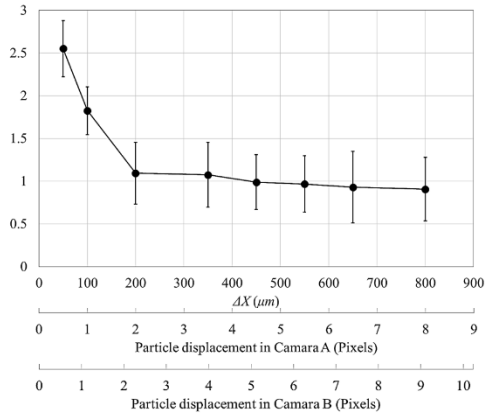
$u'u'/U^2 \times 10000$



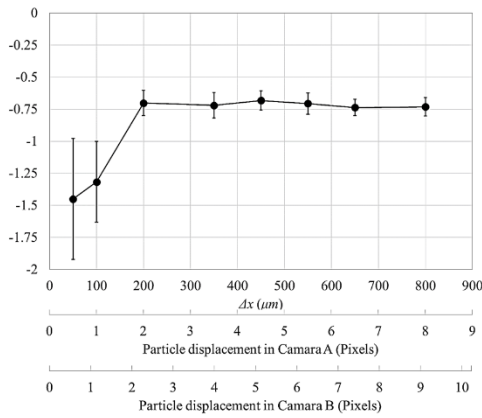
$v/U \times 100$



$v'v'/U^2 \times 10000$



$w/U \times 100$



$w'w'/U^2 \times 10000$

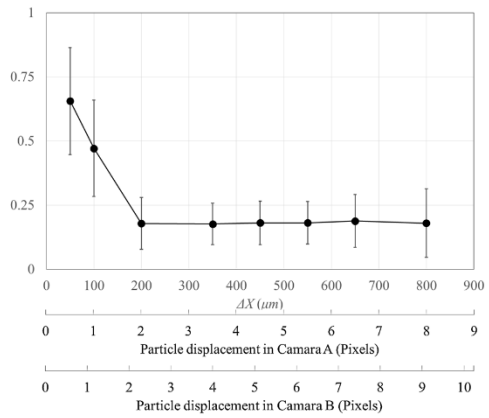


Figure 3-6. Uniform flow measurements with particle displacement variations.

The systematic error assessments by repeated uniform measurements of mean velocity and Reynolds stresses are summarized in Table 3-6. As discussed above, the SPIV tended to yield low levels of Reynolds normal stress compared to the LDV system; test uncertainty of the Reynolds normal stresses exhibited by the SPIV measurement was assessed from the 1D LDV results.

For the mean velocity measurement, the magnitude of the systematic error for undisturbed flow and high-velocity region was around 1% of the towing carriage speed. However, in the low-velocity region such as the turbulent boundary layer, the uncertainty increased when the particle displacement was less than one pixel.

Table 3-6. The systematic error of mean velocity measurement by SPIV

		High velocity region	Low velocity region
Mean velocity (10^{-2})	u/U	1.38	2.25
	v/U	1.42	1.60
	w/U	0.747	1.73
Reynolds normal stress (10^{-4})	$\overline{u'u'}/U^2$	23.2	23.3
	$\overline{v'v'}/U^2$	23.2	23.3
	$\overline{w'w'}/U^2$	23.2	23.2
Reynolds shear stress (10^{-4})	$\overline{v'w'}/U^2$	0.136	0.262
	$\overline{u'w'}/U^2$	0.128	0.374
	$\overline{u'v'}/U^2$	0.546	1.42

3.4. Model ship nominal wake measurement

3.4.1. Test model and test conditions

A 1/100 scale model of a VLCC designed by the Korea Research Institute of Ships and Ocean Engineering was used, as documented by Kim *et al.* (2001), hereafter KVLCC2. Figure 3-7 shows the lines of the hull geometry. The design speed of the ship in the full scale was 15*knots*, equivalent to 7.97*m/s*. Using Froude similarity, the advance speed of the test model was 0.797*m/s* with *Fr* of 0.142 and a *Re* of 2,300,000.

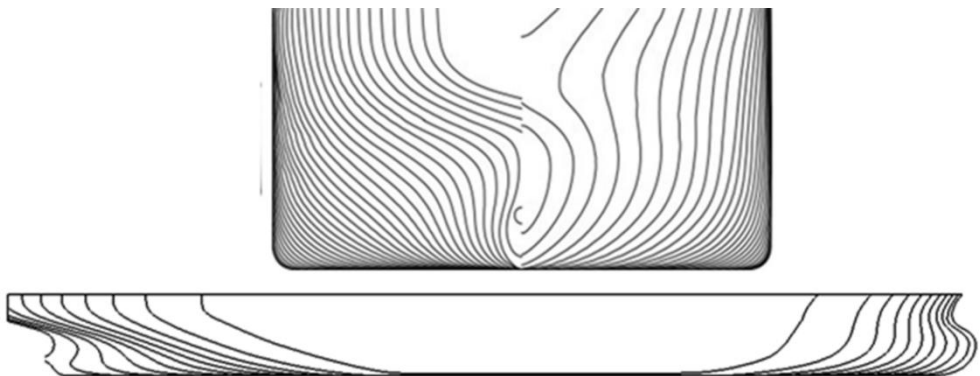


Figure 3-7. Lines of KVLCC2 hull.

The flow field at the propeller plane was measured without the propeller. This plane was located at 98.25% of the ship length (length between perpendiculars) from the intersection of the free-surface and the bow. The test model was painted in matte black to prevent surface reflection. The model was fixed in all cases to prevent pitching and heaving, which may change the location of the measurement plane. To stimulate the development of the turbulent boundary layer, stud lines were located on the bow, following the

ITTC recommendation. Figure 3-8 shows snapshots of towing tank tests by SPIV and LDV.

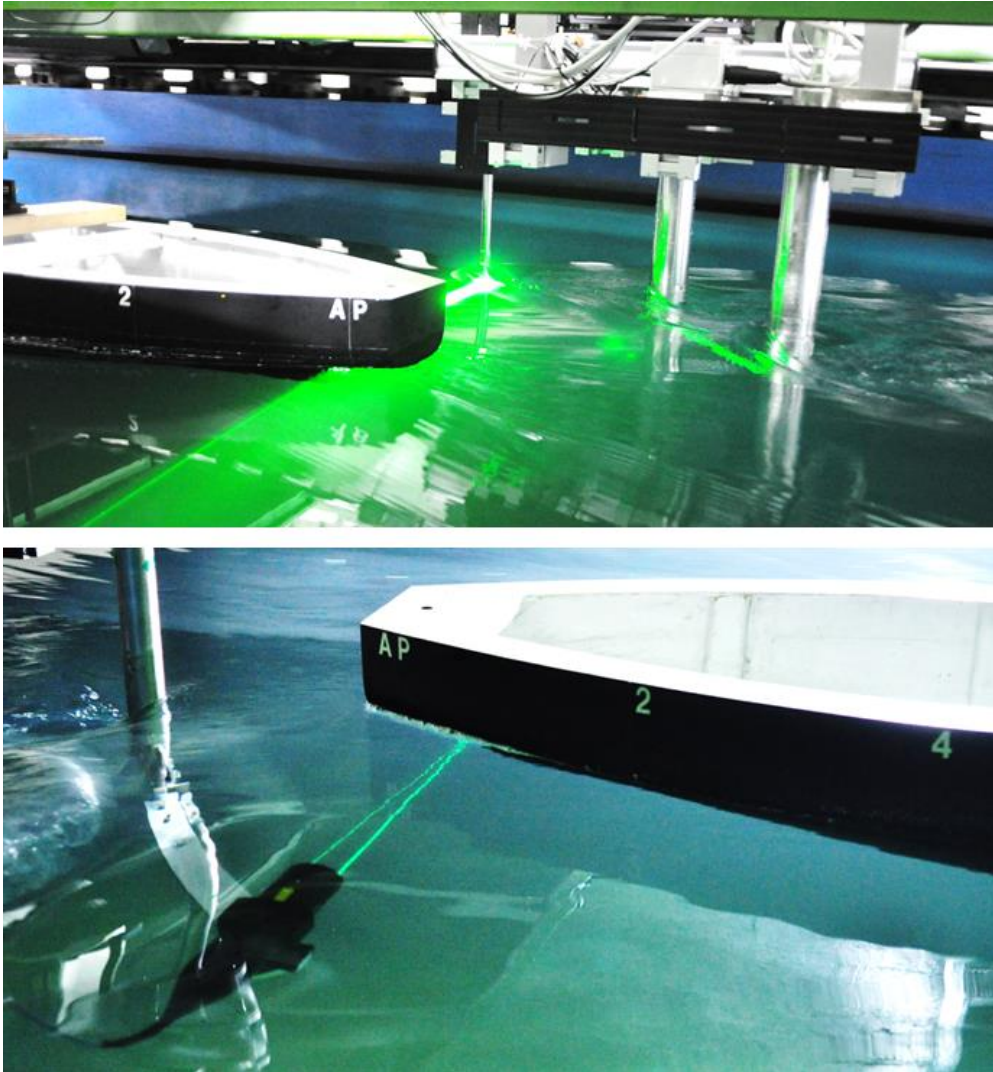


Figure 3-8. Snapshots of local flow measurement tests: SPIV (top) and 1D LDV (bottom).

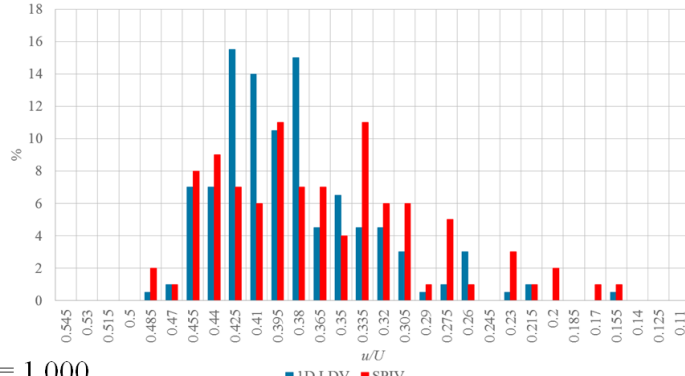
3.4.2. Test results: data convergence

The flow field measurement at the propeller plane was repeated to assess the random error of the measurement. The number of SPIV and LDV samples was 10,000. After confirming that the data converged, the mean and fluctuation of the velocity at $y/R = 0.6$ and $z/R = -0.6$ were compared. At the location of the measurement, a maximum in k appeared in the hotwire anemometer measurement (Lee *et al.*, 2003) and the turbulence measurement could be characterized.

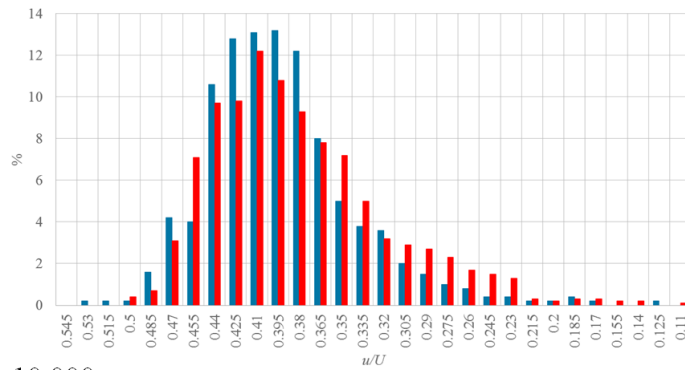
Figure 3-9 shows changes of velocity magnitude distributions according to data sample number. As the number of data samples increased, the u/U distribution became similar to that at $N = 10,000$. In general, the mean velocity of two different measurements systems was similar with a large number of data samples. However, the LDV results exhibit less scatter than SPIV; the Reynolds normal stress measured by LDV was expected to be smaller than the SPIV.

The disparity in scatter was caused by the measurement characteristics of the systems. The SPIV measures a representative velocity vector in an interrogation window, whereas the LDV measures instantaneous velocity of single tracer particle passing the measurement volume. As shown in the uniform flow measurement results, velocity fluctuation in LDV measurements was larger than that in SPIV. However, in the wake field where velocity changed rapidly, there were velocity gradients in the SPIV interrogation window area, and the representative velocity vector in the window also changed according to an irregular tracer particle distribution.

$N = 100$



$N = 1,000$



$N = 10,000$

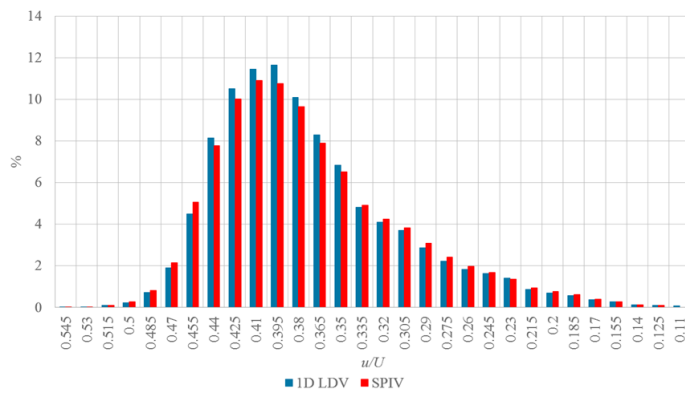


Figure 3-9. Data convergence results: u/U at $y/R = 0.6$ and $z/R = -0.6$.

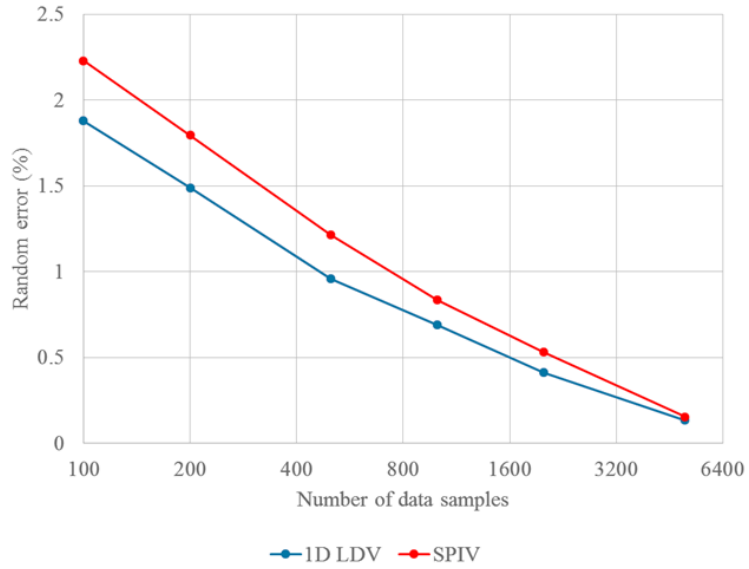
Figure 3-10 shows changes of the random error in mean velocity and Reynolds normal stress according to the number of data samples. The random error decreased logarithmically. When the number of samples was 1,000 and 2,000 for SPIV and 1D LDV, respectively, the random error was 0.835% and 0.411% for mean velocity measurement of SPIV and LDV, respectively. The random error in the Reynolds normal stress of SPIV and 1D LDV were 15.9% and 6.78%, respectively.

The total measurement uncertainty of the ship wake measurements with 95% confidence level was assessed as shown in Table 3-7. Due to the measurement characteristics described previously, the test uncertainty of SPIV was larger than that of LDV.

Table 3-7. Total uncertainty of measurement systems

	SPIV		LDV	
	u/U (10^{-2})	$\overline{u'u'}/U^2$ (10^{-4})	u/U (10^{-2})	$\overline{u'u'}/U^2$ (10^{-4})
Measure value	73.5	233.8	67.0	226.4
Systematic error	2.25	23.3	0.35	23.2
Random error	0.613	37.2	0.275	15.3
Total uncertainty (10^{-2}) (95% confidence level)	2.33	43.9	0.445	27.8
Total uncertainty /Measured value	3.17	18.8	0.664	12.3

Mean velocity



Reynolds normal stress

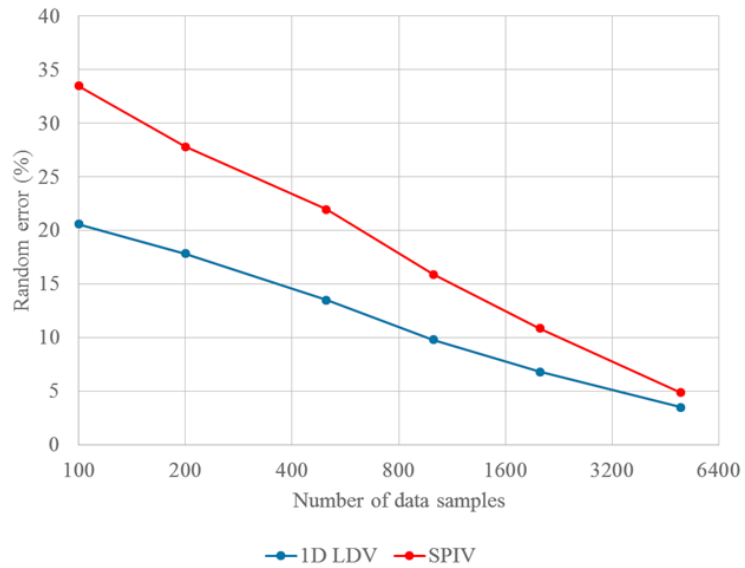


Figure 3-10. Convergence of Reynolds normal stress according to data sample number.

3.4.3. Test results: comparisons of mean velocity and turbulence

Mean velocity measurement results at the propeller plane of KVLCC2 model ship is shown in Figure 3-11. Test results in the present study were compared with those using 5-hole Pitot tubes (Kim *et al.*, 2001) and hot wire anemometers (Lee *et al.*, 2003). 3D reconstruction of the test results was achieved by stacking 2D PIV results (Seo *et al.*, 2016), and 1D Pitot-static tube (Seo *et al.*, 2013).

In the measurement results, the origin was located at the center of the propeller and the length dimension was normalized by the radius of the propeller, R . The flow field around the VLCC model were clearly characterized in the mean velocity field, namely, the hook-shaped contour and longitudinal bilge vortex. Due to the concave geometry of the stern, the flow in the boundary layer was retarded and thickened rapidly, resulting in 3D separation and the strong longitudinal vortex. These phenomena are well known and have been reported in previous VLCC model studies (Kim *et al.*, 2001; Lee *et al.*, 2003).

Notably, one strong vortex was observed just below the propeller center, which rotates in the direction opposite to that of the bilge vortex, and was confined in the region of the lowest level of u/U . This vortex was due to the detachment of the limiting streamlines on the surface of the propeller boss, the structure of which was hardly identifiable with invasive methods that have limited spatial resolution.

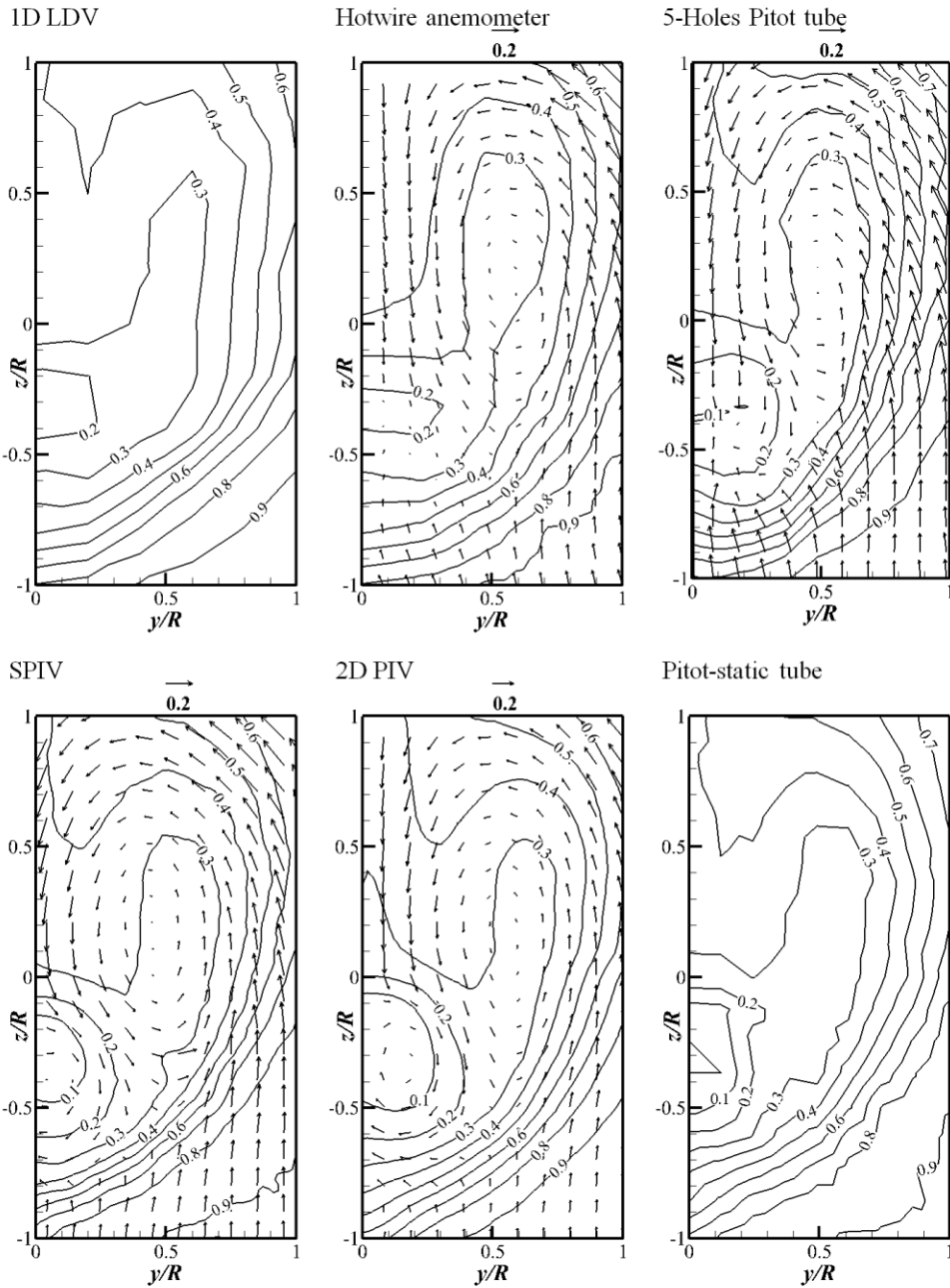


Figure 3-11. Mean velocity field at the propeller plane of the KVLCC2 model ship: u/U contours and on-plane vectors.

Figure 3-12 shows comparisons of u/U extracted from $z/R = -0.6$ and 0.6 lines. Measurement results showed good agreement, but near the center line, where $0 < y/R < 0.2$, the measured value based on the hot wire anemometer results is much larger magnitude than the others.

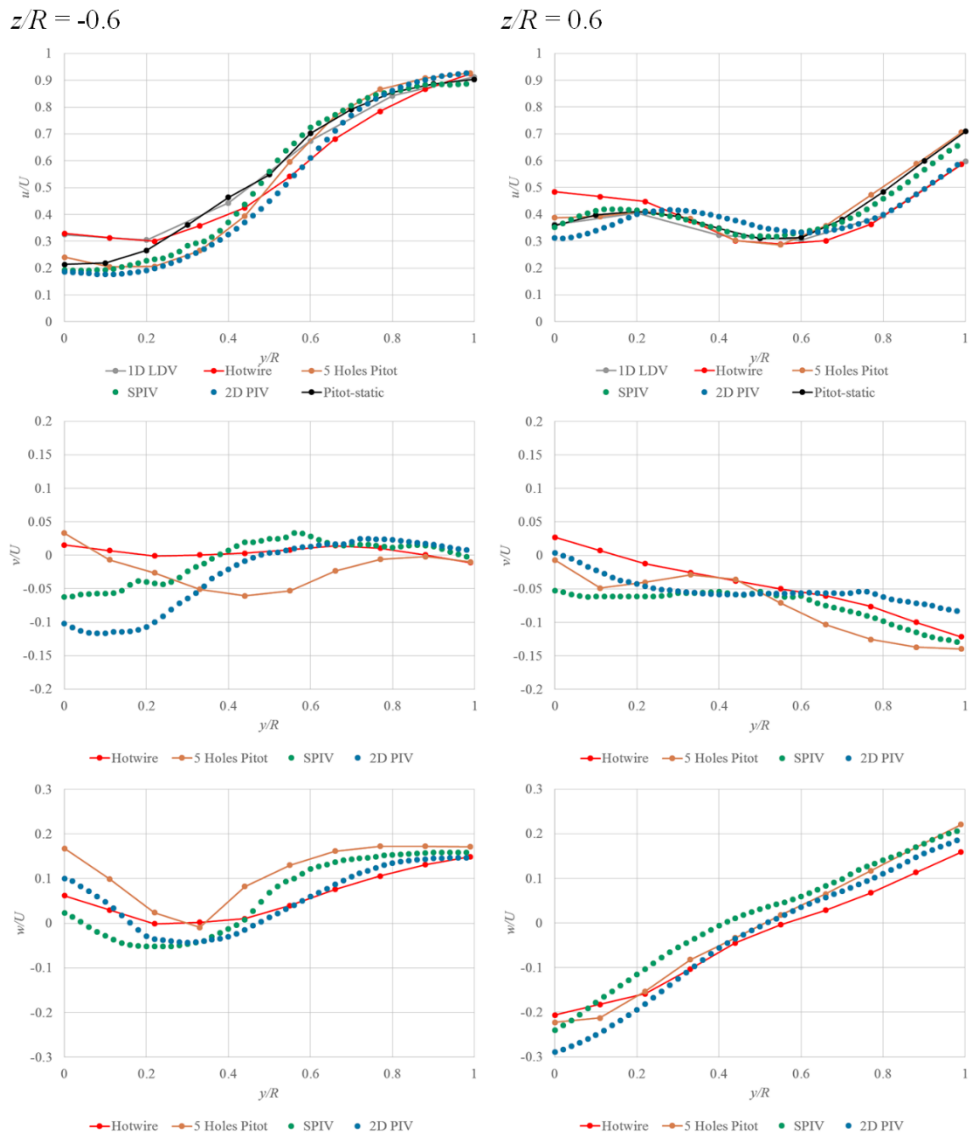


Figure 3-12. Comparisons of mean velocity at $z/R = -0.6$ (left) and 0.6 (right).

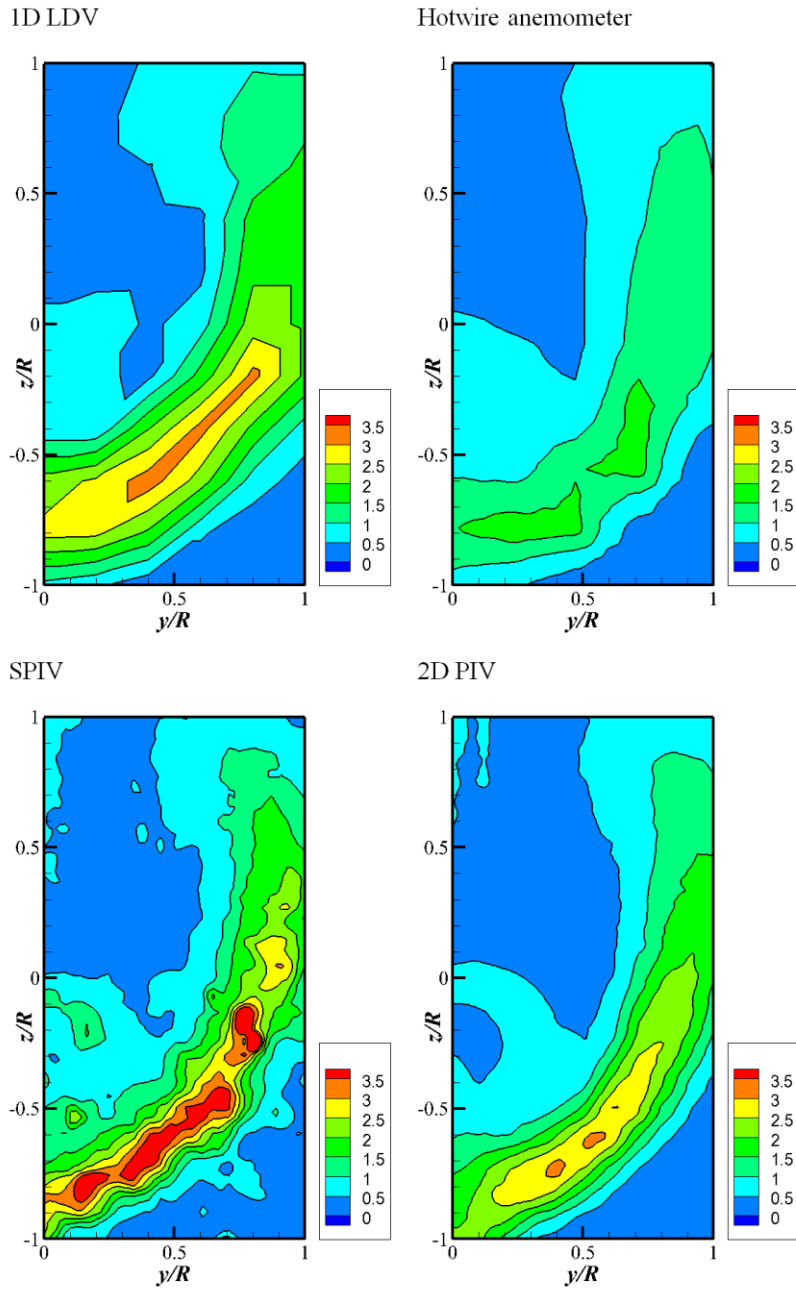


Figure 3-13. Reynolds normal stress distribution at the propeller plane of KVLCC2 model ship: $\overline{u'u'}/U^2 \times 100$ contours.

Figure 3-13 shows $\overline{u'u'}/U^2$ contours at the propeller plane of the model ship. High-level Reynolds normal stress was concentrated where the velocity gradient was large, especially for the longitudinal velocity. The boundary of the concentrated turbulence strength also agreed well.

Figure 3-14 shows a comparison of Reynolds normal stresses at $z/R = -0.6$ and 0.6 . 2D PIV, SPIV, and LDV exhibited a similar magnitude of Reynolds normal stresses, but the hotwire measurement results was smaller than them, as the test Re condition was different.

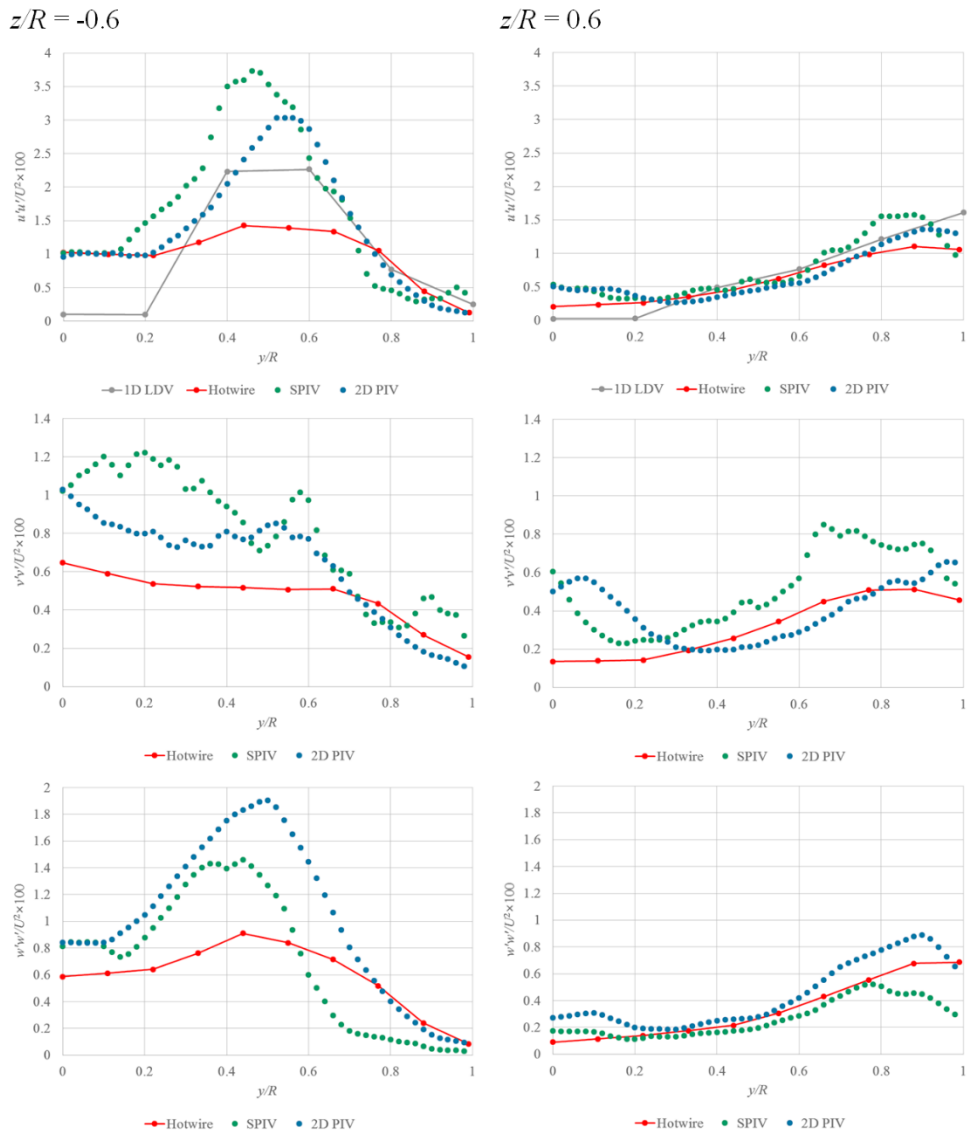


Figure 3-14. Comparisons of Reynolds normal stresses at $z/R = -0.6$ (left) and 0.6 (right).

Chapter 4. Results and Discussion

4.1. Free-surface wave elevation: large model case

Figure 4-1 shows the wave pattern around the large test model for three different Fr conditions. At the lowest Fr condition ($Fr = 0.126$), a Kelvin wave pattern was distinguishable only near the leading edge (LE) at $x/L = -0.5$, and the water surface was flat and steady. Thus, free-surface effects without any pressure gradient in the waves on the underneath flow could be expected.

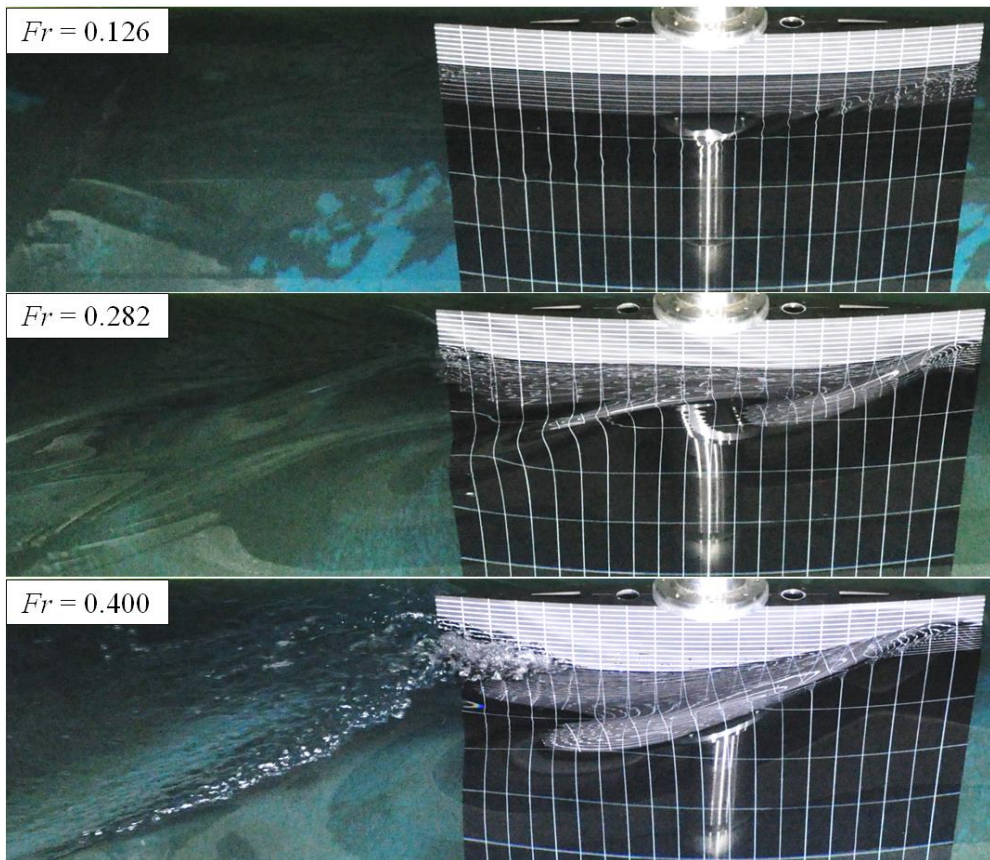


Figure 4-1. Wave pattern around the large model.

Kelvin wave development was obvious at the intermediate Fr condition ($Fr = 0.282$), where wave crests were found at the LE, mid-body, and tailing edge (TE), as the wave length was approximately half of the model length. As the static pressure increased at the stagnation points of the LE and TE, wave crests near the LE and TE were clear with a large and well-developed elevation and wave pattern.

The model has the shoulder at mid-body ($x/L = 0$), where static pressure decreased whereas the flow speed increased. At the intermediate Fr condition, a wave crest occurred at the shoulder, but its elevation was lower than those at the LE and TE because of low static pressure at the midbody.

Free-surface fluctuation was observed near the TE for this Fr condition, but it was moderate as no air entrainment developed, as reported in previous studies using the NACA 0024 foil (Metcalf *et al.*, 2006).

At the highest Fr condition ($Fr = 0.400$), the wave length was expected to be same as the model length. In the observation, wave crests were located near the LE and TE. Similar to the wave elevation at $Fr = 0.282$, a Kelvin wave pattern and fluctuation of the free-surface near the TE were observed. Free-surface fluctuation at $Fr = 0.400$ was more violent than that at $Fr = 0.282$. Figure 4-2 shows a magnified snapshot of the free-surface behavior at $Fr = 0.400$. Air rapidly entrained from $x/L = 0.30$ to the TE and the bubbly free-surface behind the TE was transformed into a knobby free-surface without any air entrainment.

The boundary between the violent and smooth free-surface regions could be clearly distinguished by a recirculation line, as in hydraulic jump cases, whereas the boundary between the knobby free-surface and the entrainment region was unclear. Recirculation and violent free-surface behavior for

increasing wave heights have been previously researched in hydraulic jump studies (see literature review section in Introduction). In the recirculation region, strong shear stress and rapid turbulence generation have also been reported in hydraulic jump studies. In this study, similar flow phenomena were studied by flow field measurement.

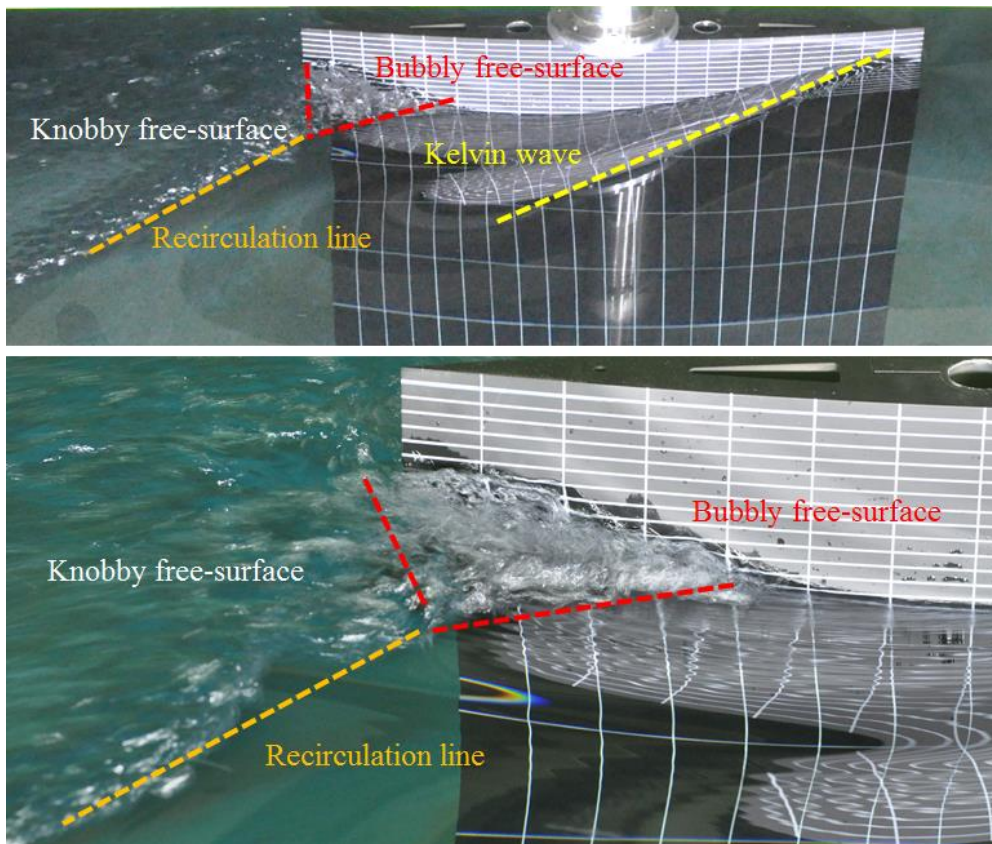


Figure 4-2. Magnified snapshot of free-surface around large model at $Fr = 0.400$.

As shown in Figure 4-3, wave height measurements from observation data were compared with those from analytic solutions for $Fr = 0.282$ and 0.400 (Wigley, 1937). Following the study of Wigley (1937), a free-surface wave around a parabolic body in inviscid flow was recognized as a superposition of

the LE wave, shoulder wave, TE wave, and wave elevation due to static pressure due to the model geometry; thus, the wave profile around the model could be calculated.

In the results, wave elevation measurements near the TE for $Fr = 0.400$ was larger than those from the analytic solution. Due to air entrainment, the free-surface was more elevated in the experiment than in the analytic solution and numerical simulation, in which a smooth and steady wave was obtained.

Besides, as reported in the study of Wigley (1934), observed wave elevation at the wave trough was higher than that by calculation, as the viscous nature of the fluid degraded the wave elevation change downstream. For $Fr = 0.282$, the observation results showed good agreement with the analytic solution.

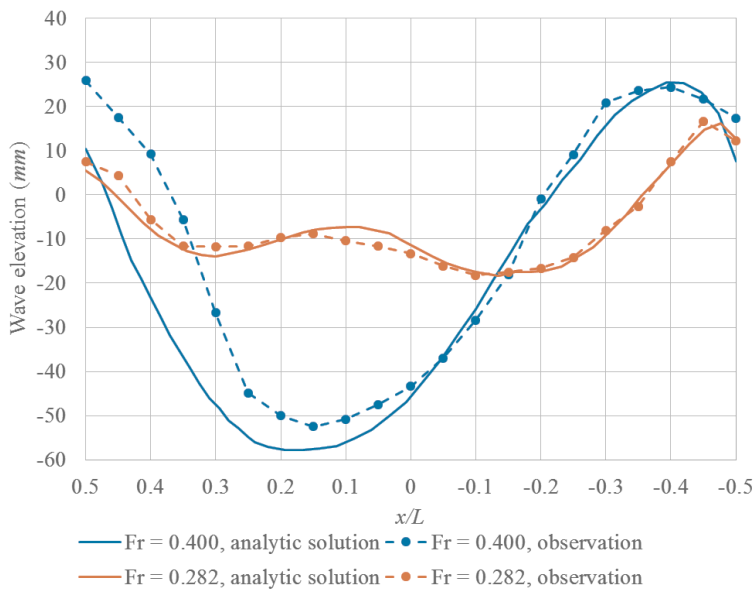


Figure 4-3. Wave elevation from analytic solution and measurement for $Fr = 0.282$ and 0.400 .

The free-surface fluctuation in the violent free-surface was analyzed by fast Fourier transform (FFT), to identify the dominant wave behavior. Figure 4-4 shows the locations of the wave elevations analyzed by FFT. Four x -directional locations were selected at $x/L = 0.4, 0.5, 0.6,$ and 0.7 . At $x/L = 0.4$ and 0.5 , there was air entrainment, while the free-surface at $x/L = 0.6$ and 0.7 was knobby. In addition, to compare the steady and smooth wave results, $x/L = 0.25$ was also chosen. Wave elevations for $Fr = 0.282$ at the same x -directional locations were analyzed and compared.

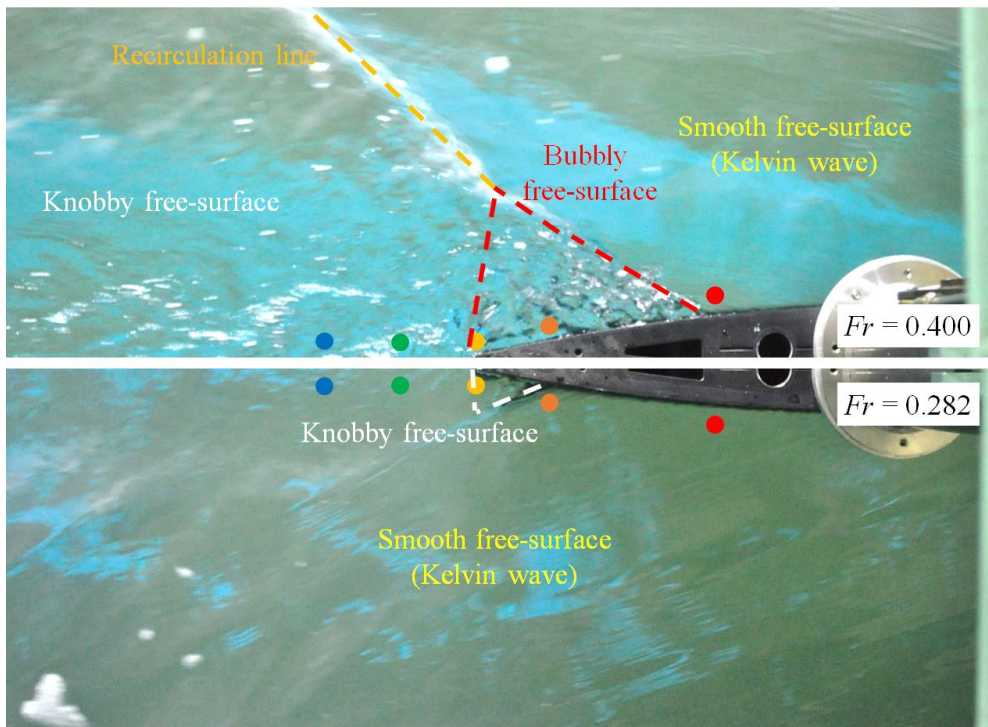


Figure 4-4. Free-surface wave around the trailing edge of the large model: solid circles indicate wave elevation locations analyzed by FFT.

To examine the characteristics of the wave height gauge, first, wave elevations in open water conditions at $U = 1.252$ ($Fr = 0.400$ for the large model) and 0.883 m/s ($Fr = 0.282$ for the large model) were measured and analyzed, as shown in Figure 4-5. A peak amplitude fluctuation at 9.98 Hz was observed irrespective of the Fr condition, which may have been caused by the electrical capacitance characteristics of the wave height gauge.

There were fluctuations due to the vibration of the towing carriage wheels. As the circumference of the towing carriage wheel was 2000 mm , the frequency of the vibration induced by the wheel rotation at $U = 1.252$ ($Fr = 0.400$) and 0.883 m/s ($Fr = 0.282$) were 0.626 and 0.441 Hz , respectively. In the free-surface around the model measurement, peaks at those frequencies were eliminated in the analyses.

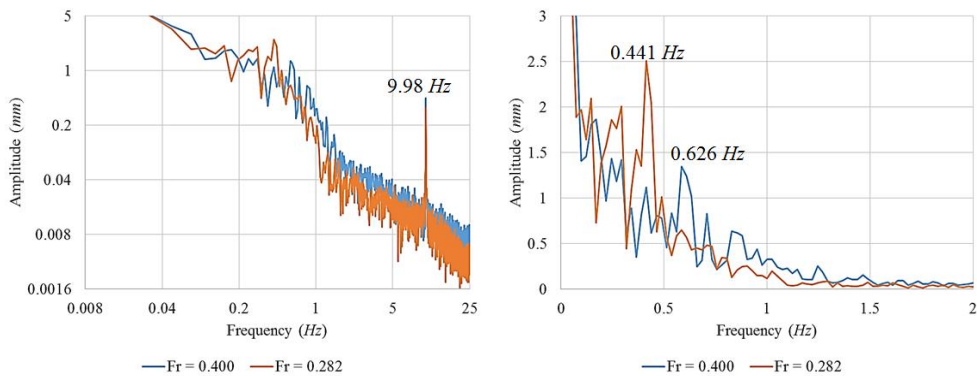


Figure 4-5. Wave elevation measurement results in undisturbed free-surface conditions.

Figure 4-6 shows the wave elevation at $x/L = 0.25$, where a smooth and steady wave was observed regardless of the Fr conditions. These results were similar to those in the undisturbed condition. The only observed peaks were those caused by the towing carriage vibration and electrical characteristics.

The magnitude of the fluctuation at the towing carriage vibration frequency was greater than that in the undisturbed condition, as the vibration of the towed model might have resulted in additional free-surface fluctuation in the frequency region.

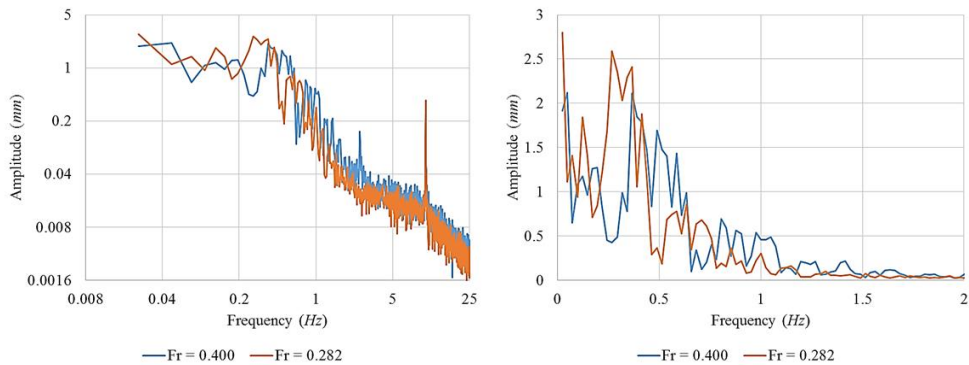


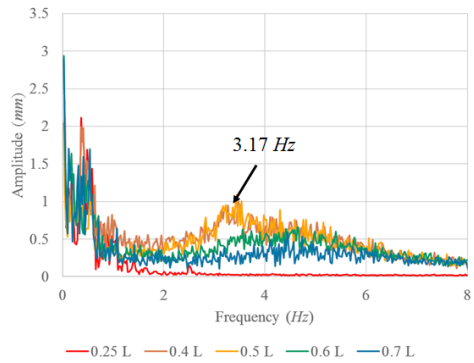
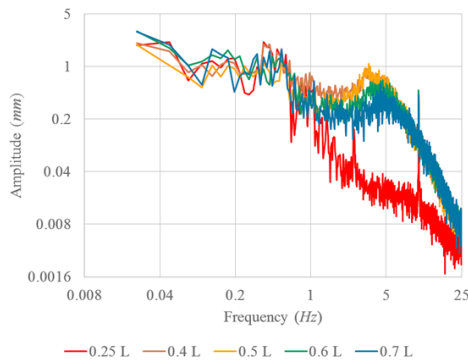
Figure 4-6. Wave elevations in frequency domain around the large test model measurement results at $x/L = 0.25$.

Figure 4-7 shows comparisons of the free-surface fluctuation in the violent free-surface region for $Fr = 0.400$ and smooth free-surface waves for $Fr = 0.282$. In the air-entrained bubbly free-surface region ($x/L = 0.4$ and 0.5), peaks at 0.976 and 3.17 Hz were observed. In the experimental study of Metcalf *et al.* (2006), free-surface fluctuations due to Karman vortex shedding (at 0.77 Hz) and the shear layer (1.98 Hz) were reported and the frequencies observed in this study were of a similar order.

The amplitude in the two frequency regions at $x/L = 0.40$ and 0.50 were almost the same, while they became degraded downstream as the free-surface changed into a knobby form. In particular, fluctuation at 3.17 Hz was reduced while fluctuation in the higher frequency region was maintained. This implies

that the frequency of the air entrainment was 3.17 Hz overall, and that the air bubble bursts caused turbulence. The turbulence then dissipated into the small scale downstream by the turbulence cascade.

$Fr = 0.400$



$Fr = 0.282$

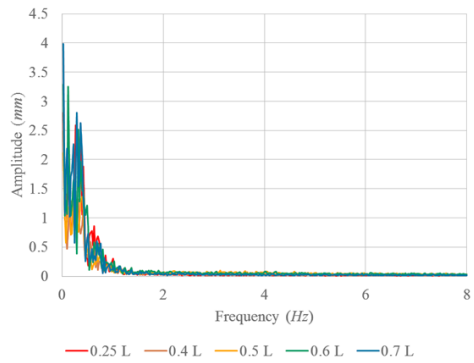
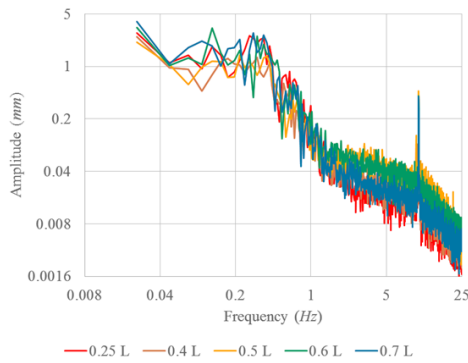


Figure 4-7. Wave elevation in frequency domain for two different Fr conditions.

4.2. Boundary layer flows: large model case

Flow fields in the boundary layer near the TE ($x/L = 0.25$ to 0.5) were first investigated by SPIV, to study the boundary layer development with an adverse pressure gradient caused by the model geometry, free-surface wave, and viscous drag on the no-slip wall.

4.2.1. $Fr = 0.126$ (smooth and steady free-surface with negligible wave)

Figure 4-8 shows the time mean of the boundary layer flow for the lowest Fr condition, where the free-surface wave effects on the flow field were negligible. The most outstanding free-surface effect was flow retardation near the free-surface. Even though there was no distinguishable free-surface wave, the flow underneath was affected, the flow velocity decreased, and the boundary layer widened.

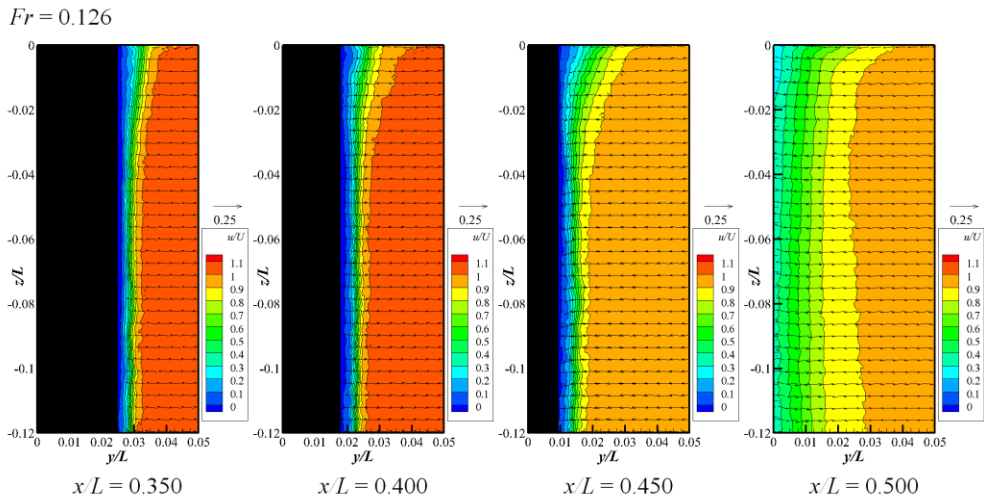


Figure 4-8. Mean velocity fields of boundary layer region for $Fr = 0.126$.

Figure 4-9 shows the u/U variation along the y -direction from the model surface. Due to the no-slip wall condition on the model surface, the u/U value at the model surface was zero. The u/U value increased in the turbulent boundary layer region and converged with the flow velocity, as the distance from the wall increased. The converged flow velocity was uniform with depth, as no free-surface wave had developed in this Fr condition, and the flow became 2D.

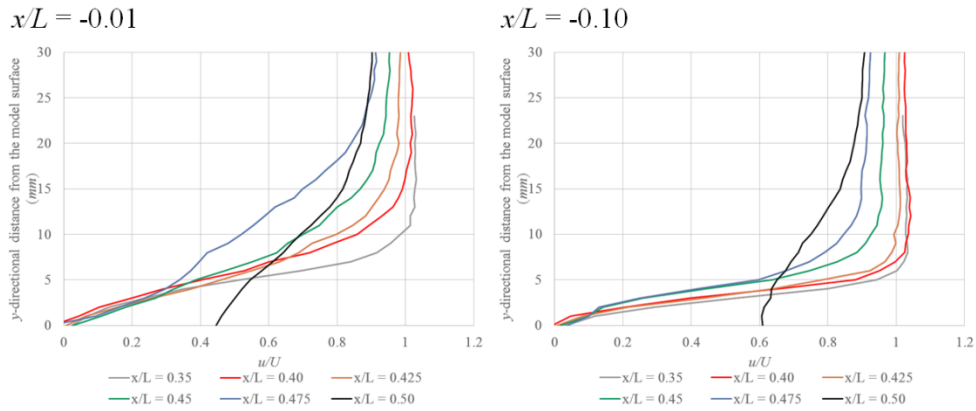


Figure 4-9. u/U distribution on the model surface for $Fr = 0.126$.

Figure 4-10 shows the displacement thickness variation in the x - and z -directions. The velocity retardation in the boundary layer region directly increased the thickness of the boundary layer. At the TE, the boundary layer thickness decreased rapidly as the no-slip wall effects of the model surface ended when the flow left the TE.

The boundary layer flow slowed as it progressed to the TE. The flow lost its momentum by viscous drag from the model surface. In addition, the adverse pressure gradient on the model surface degraded the flow velocity. The boundary layer flow at $x/L = 0.5$ recovered rapidly, as effects of the model surface ended after the TE.

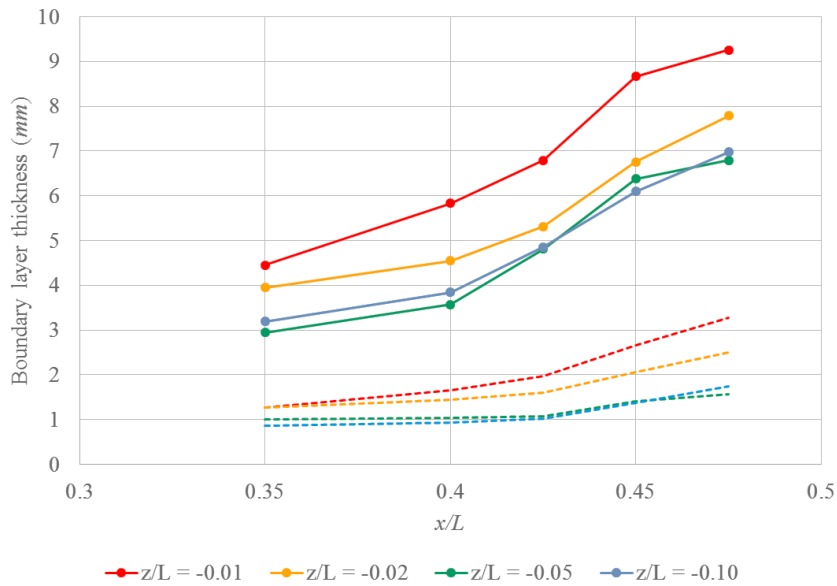


Figure 4-10. Boundary layer thickness for $Fr = 0.126$: displacement thickness (solid line) and momentum thickness (broken line).

Observing the momentum thickness, flow retardation near the free-surface was obvious, even when there was no free-surface wave for the given Fr condition. This implies that drag increased near the juncture of the free-surface and model surface. Microscale free-surface fluctuation that generates turbulence is known to cause additional drag near the free-surface.

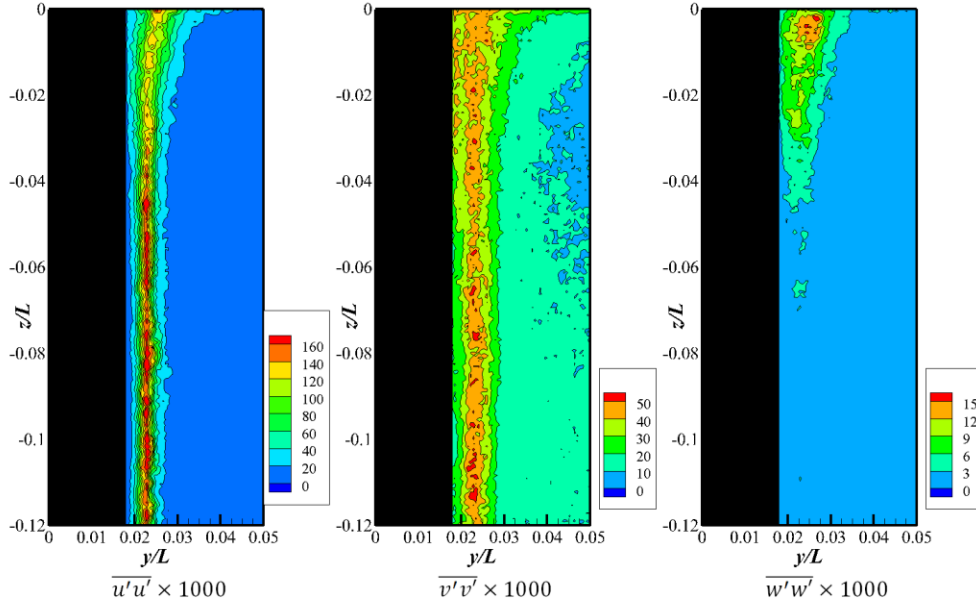
The turbulent structure was investigated by analyzing the Reynolds stress distributions. Figures 4-11 and 4-12 show the Reynolds normal and shear stresses at $x/L = 0.40$ and 0.45 , respectively. The turbulence in the boundary layer was highly anisotropic and the x -directional Reynolds normal stress was dominant. The magnitude of $\overline{u'u'}$ was great in deep locations and decreased near the free-surface, as the thickness of the boundary layer increased.

In deep locations, the flow was considered to be a horizontal 2D boundary layer flow and the $\overline{w'w'}$ value was negligible at $x/L = 0.40$. At the juncture of the turbulent boundary layer and the free-surface, the velocity and pressure fluctuation in the turbulent boundary layer caused small-scale free-surface elevation, while vertical fluctuation was restricted in the 2D deep flow; thus generating $\overline{w'w'}$.

As the flow progressed downstream, the eddies generated in the turbulent boundary layer transferred momentum in random directions and contributed to a decrease in anisotropy, as shown in the results at $x/L = 0.45$. Still, the turbulent boundary layer was dominated by the no-slip wall, so the flow could not be completely isotropic in this study.

The Reynolds shear stress distribution also supports this idea. The Reynolds shear stress was derived from the cross-correlation between the velocity fluctuations in orthogonal directions, and the Reynolds shear stress distribution indicates the rotational directions of eddies and shear stress in turbulence. In isotropic turbulence, the magnitude of the Reynolds shear stress in all directions will be the same. As $\overline{u'v'}$ became overwhelming in the turbulent boundary layer, it can be concluded that eddies in this region mainly rotated in the z -direction. $\overline{u'v'}$ decreased in the downstream, whereas $\overline{u'w'}$ and $\overline{v'w'}$ increased due to the turbulent eddies.

$x/L = 0.40$



$x/L = 0.45$

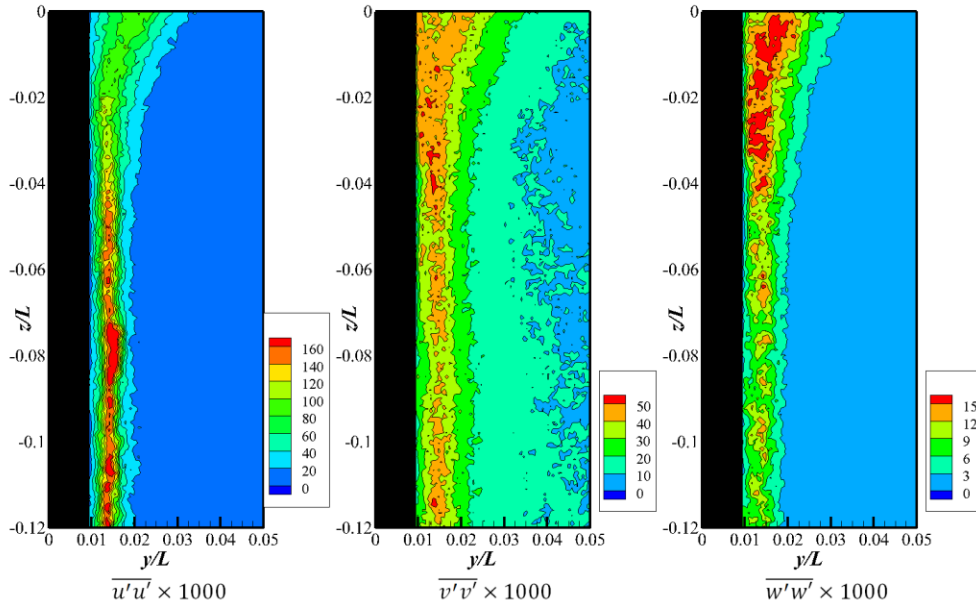
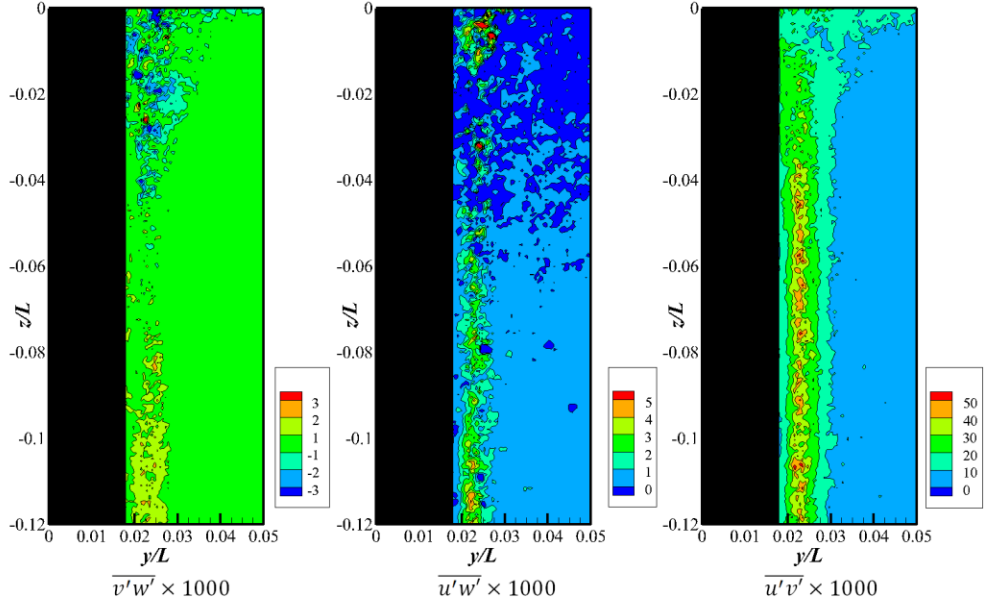


Figure 4-11. Reynolds normal stresses in boundary layer region for $Fr = 0.126$.

$x/L = 0.40$



$x/L = 0.45$

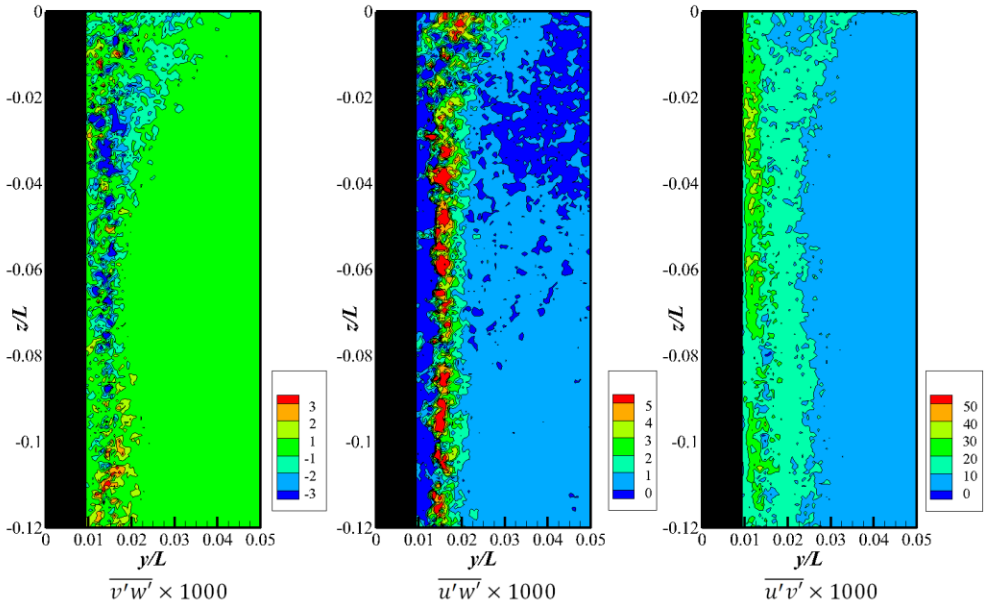


Figure 4-12. Reynolds shear stresses in boundary layer region for $Fr = 0.126$.

The turbulence kinetic energy represents the magnitude of the velocity fluctuation. Figure 4-13 shows the k distribution in the boundary layer region. The large k region expanded in the y -direction near the free-surface, along with the boundary layer thickness.

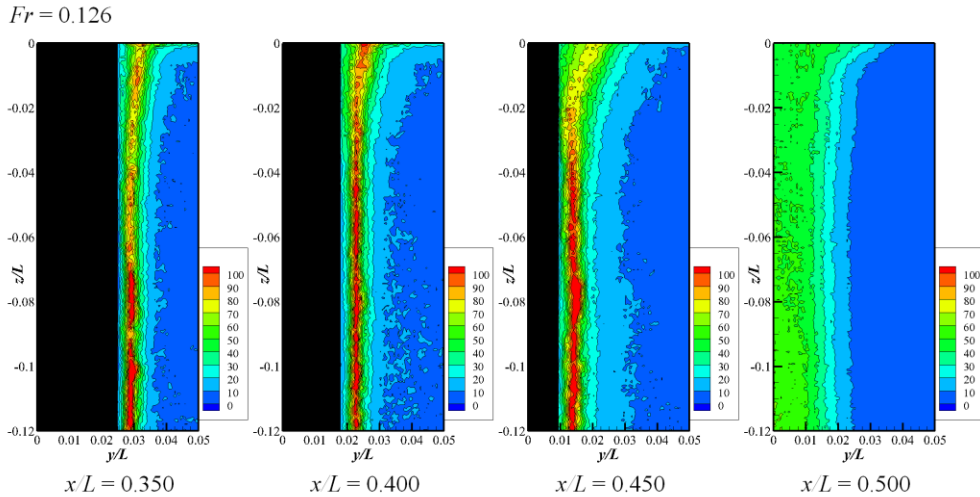


Figure 4-13. $k/U^2 \times 1000$ distribution in boundary layer region for $Fr = 0.126$.

From the mean velocity measurement, it was confirmed that the free-surface and solid-wall juncture caused additional drag force. The loss of momentum converted into free-surface fluctuation or turbulence; thus, the additional drag could be examined by quantifying the turbulence generation.

Figure 4-14 compares the k distributions along the y -direction from the model surface at $z/L = -0.01$ and -0.1 for $Fr = 0.126$. Near the free-surface, the local maxima of k decreased, but the high- k region broadened.

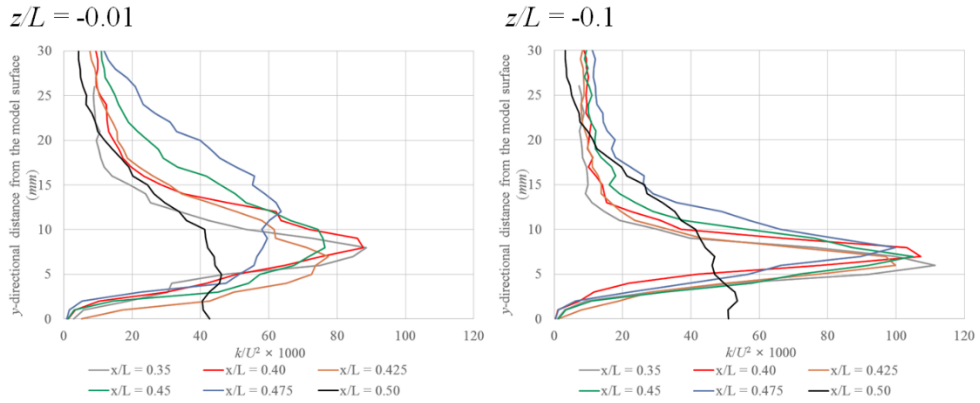


Figure 4-14. $k/U^2 \times 1000$ near the model surface for $Fr = 0.126$.

To compare the turbulence generation near the free-surface with that in deep locations, the spatial mean of k in the turbulent boundary layer was obtained, from 0 mm to 25 mm away from the model surface, as shown in Figure 4-15. Note that the spatial mean of k is proportional to the turbulence generation. The turbulence generation increased near the free-surface and along the x -direction. Its tendency was similar to that of the displacement thickness. As discussed in the mean velocity results, the additional drag at the juncture produced more turbulence and caused the reduced momentum of the boundary layer flow than at the 2D deep locations. At the TE, there was no turbulence produced from the wall and only dissipation occurred, such that k reduced rapidly.

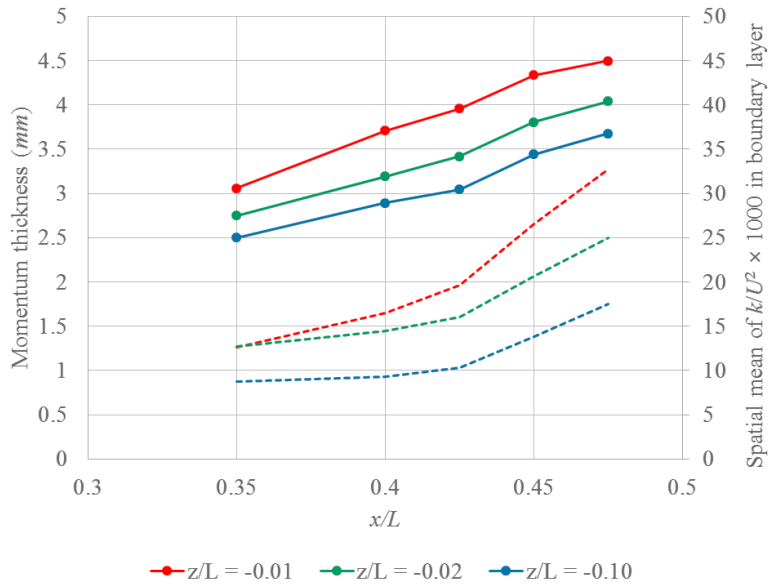


Figure 4-15. Displacement thickness (broken lines) and spatial mean of k (solid line and symbols) for $Fr = 0.126$.

4.2.2. $Fr = 0.282$ (smooth and steady free-surface waves)

Figure 4-16 shows the mean velocity field for $Fr = 0.282$. The free-surface wave was smooth, but small fluctuations near the TE were observed. The flow fields at $0.35 \leq x/L \leq 0.475$ were expected to display the flow field characteristics of a smooth and steady free-surface wave. As the free-surface wave induced the orbital motion of water particles, z -directional velocity appeared in the mean velocity fields.

The boundary layer was too thin to be clearly identified by the SPIV measurement for this Fr condition. Near the wave trough at $x/L = 0.25$, the flow velocity increased due to the orbital motion in the wave and the decrease in static pressure. This thinned the boundary layer, but the boundary layer thickness increased as the flow was diminished downstream.

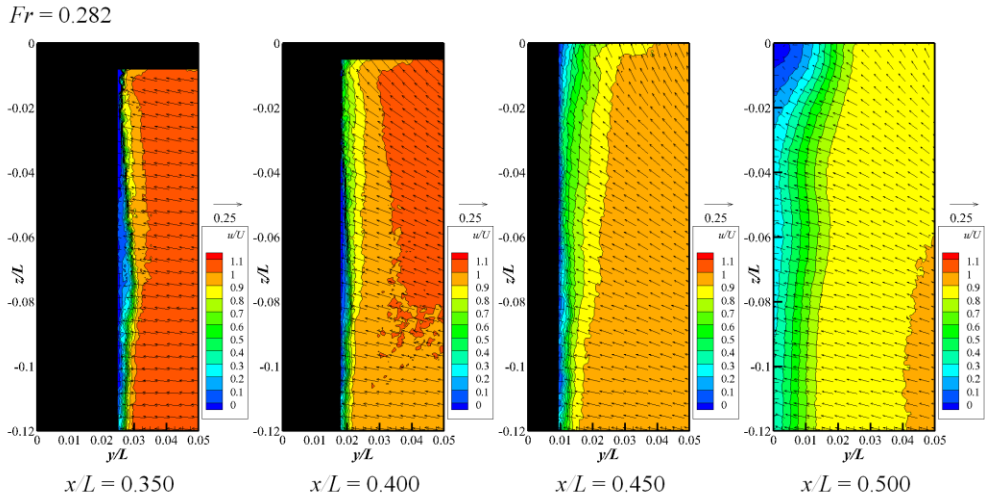


Figure 4-16. Mean velocity fields of boundary layer region for $Fr = 0.282$.

In free-surface waves, the flow from the wave trough to the wave crest suffered an adverse pressure gradient as the kinetic energy was transformed into gravitational potential energy. The momentum loss in the adverse pressure gradient caused stationary flow and knobby free-surface behavior at the TE. For this Fr condition, the primary interests were the effects of the boundary layer on the flow induced by the free-surface waves.

To examine the orbital motion by the Stokes wave, the w/U distribution was extracted from the boundary layer ($0.05 L$ from the model surface), as shown in Figure 4-17. The vertical velocity reached its maximum at $x/L = 0.45$, and its magnitude exponentially decreased with depth, as expected, following the wave theory of inviscid flow with infinite depth. This signifies that the flow field was negligible from the boundary layer, which was dominated by Stokes wave and viscous effects.

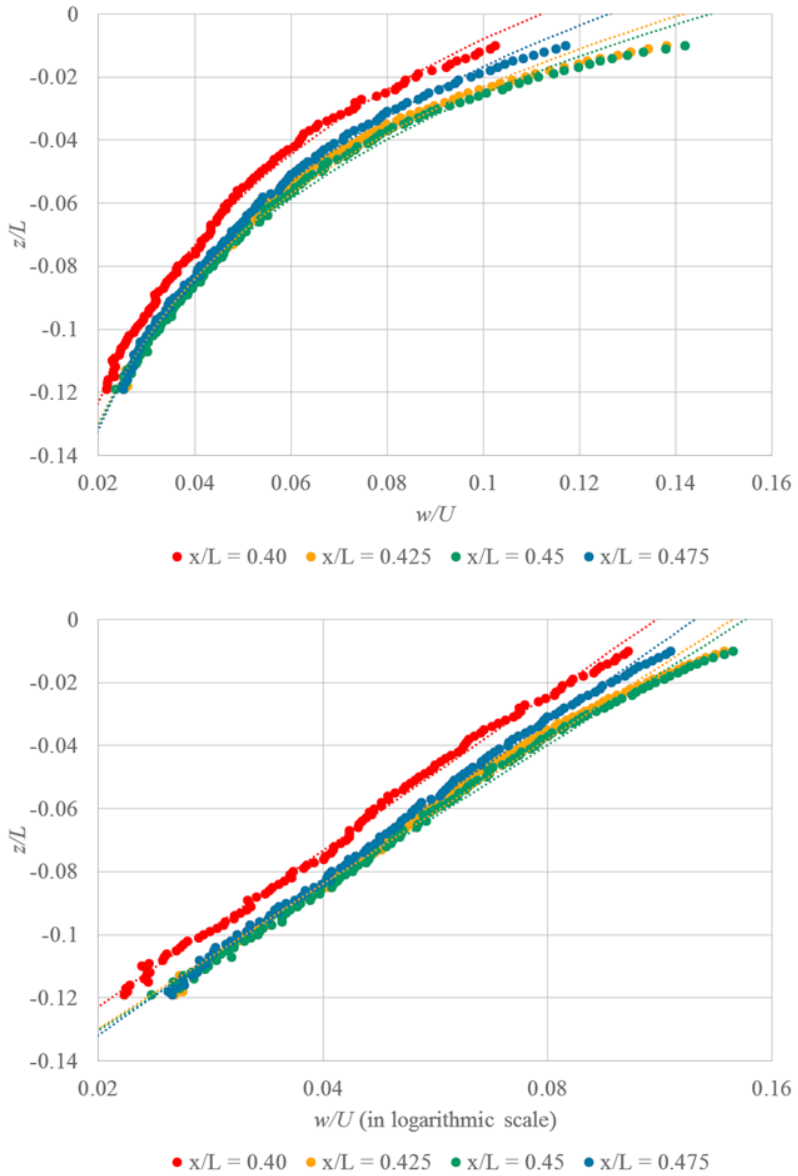


Figure 4-17. w/U in the outer region ($0.05 L$ from the model surface) for $Fr = 0.282$.

Similarly, the u/U induced by the adverse pressure gradient around the model in the outer region was extracted, as shown in Figure 4-19. The velocity perturbation increased near the free-surface, similar to the results, of w/U . The

pressure gradient due to the model geometry, however, was dominant in the velocity perturbation; Effects of the orbital motion in waves could not be abstracted from the results.

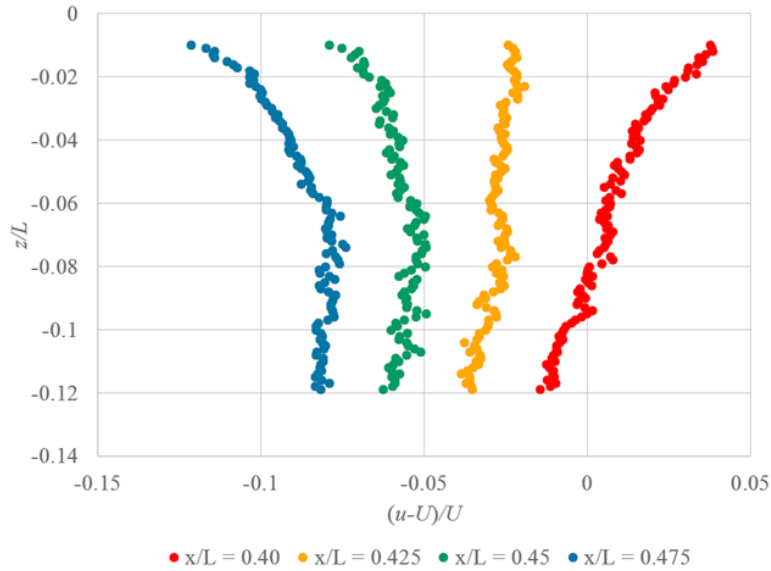
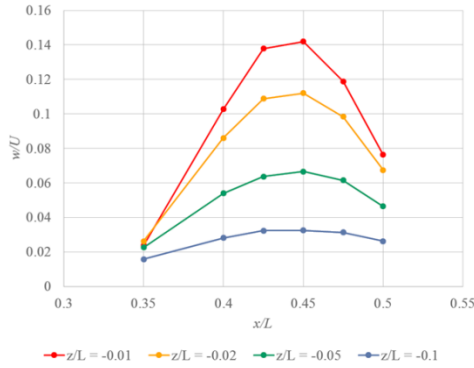


Figure 4-18. Longitudinal velocity perturbation $((u-U)/U)$ in the outer region ($0.05 L$ from the model surface) for $Fr = 0.282$.

The turbulent boundary layer and no-slip condition on the model surface obviously affected the flow induced by the free-surface wave. Figure 4-19 shows comparisons of the w/U distribution between the outer region ($0.05 L$ from the model surface) and near the model ($0.01 L$ from the model surface). As the flow progressed to the TE, drag from the no-slip wall decreased the vertical velocity, as well as the longitudinal velocity in the boundary layer. In addition, vertical flow near the free-surface at the TE was slower than that in deeper locations, as the stationary flow overwhelmed the Stokes wave effects.

Outer region



Near boundary layer

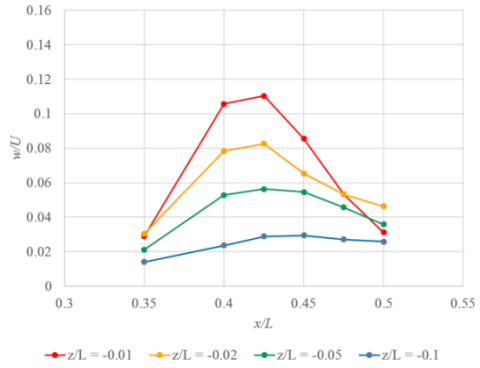


Figure 4-19. Comparisons of w/U in the outer region ($0.05 L$ from the model surface) and near the model surface ($0.01 L$ from the model surface) for $Fr = 0.282$.

The effects of the boundary layer on w/U were identified by obtaining $\Delta w/U$, which was defined as the difference in w/U between the outer and near-surface regions. Figure 4-20 shows the results. As the boundary layer degraded the flow velocity in any direction, $\Delta w/U$ should be negative, but due to test uncertainty, a positive $\Delta w/U$ was observed in some locations where the $\Delta w/U$ value was near zero.

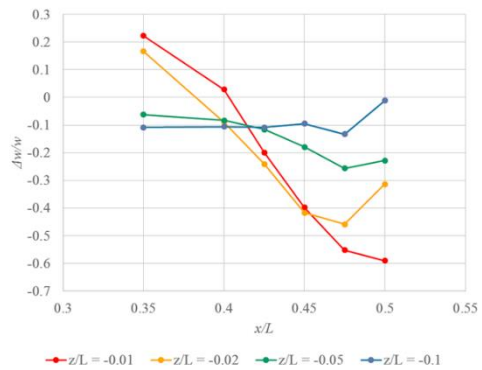
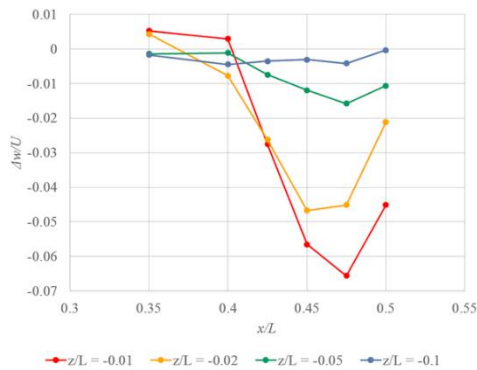


Figure 4-20. Turbulent boundary layer effects on w/U in the outer region orbital motion for $Fr = 0.282$: non-dimensionalized by U (left) and $w(x)$ (right).

Figures 4-21 and 4-22 show the Reynolds normal and shear stress distributions at $x/L = 0.45$ and $Fr = 0.282$, respectively. The free-surface in waves was smooth for the Fr condition and the turbulence characteristics were similar with those of $Fr = 0.126$, where no free-surface wave was observed: the turbulent region expanded to y -direction near the free-surface, while the magnitude of $\overline{u'u'}$ decreased. At the intersection of the free-surface and model surface, $\overline{w'w'}$ increased. However, the magnitude of the non-dimensionalized Reynolds stress for $Fr = 0.282$ was smaller than that for low Fr conditions, as the Re also increased in high- Fr conditions with a fixed model size.

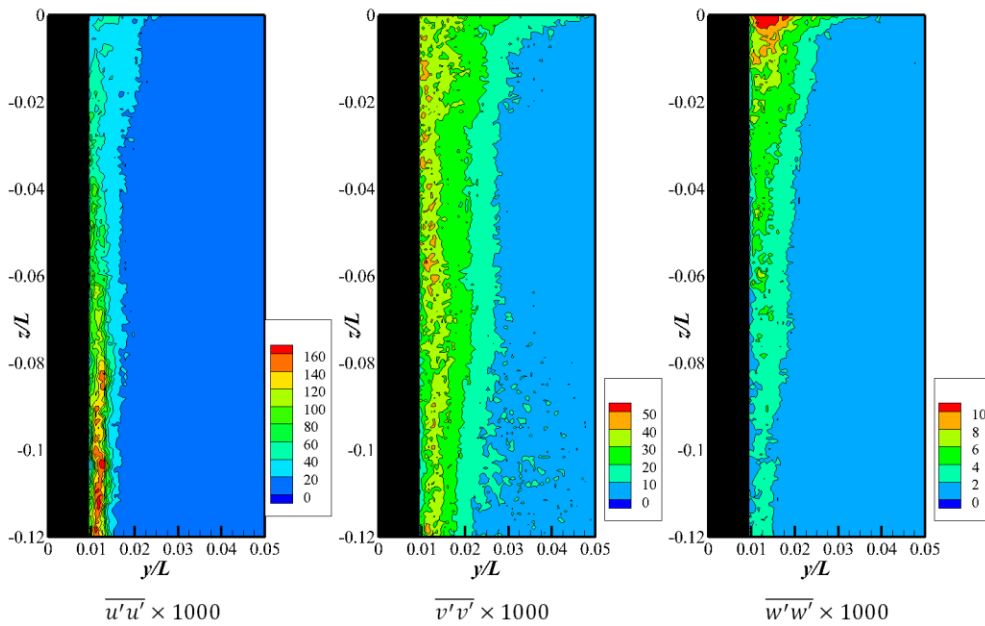


Figure 4-21. Reynolds normal stress distribution at $x/L = 0.45$ and $Fr = 0.282$.

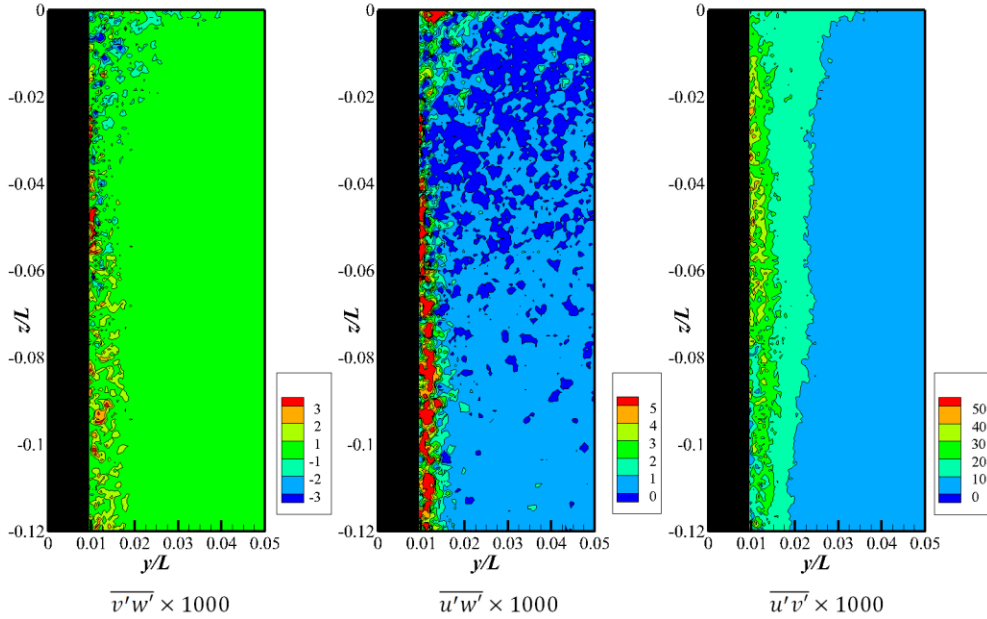


Figure 4-22. Reynolds shear stress distribution at $x/L = 0.45$ and $Fr = 0.282$.

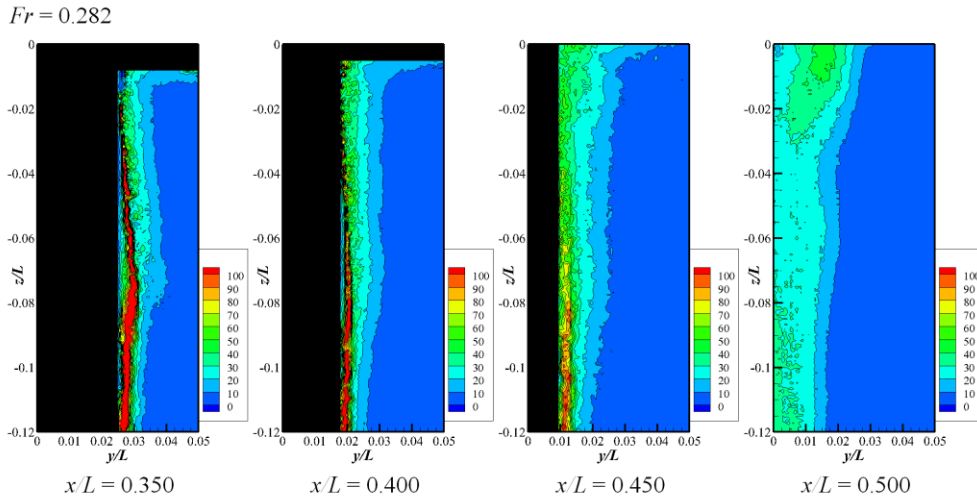


Figure 4-23. $k/U^2 \times 1000$ distribution in boundary layer region for $Fr = 0.282$.

Figure 4-23 shows the k distribution in the boundary layer region for $Fr = 0.282$. The intense k values in the turbulent boundary layer decreased

downstream. The orbital motion in the Stokes wave also transported turbulent kinetic energy in the vertical direction, stimulating the dissipation of turbulence. At the TE, only the k around the stationary flow region was significant.

4.2.3. $Fr = 0.400$ (bubbly and unsteady free-surface waves)

Figure 4-24 shows the mean velocity measurement results for $Fr = 0.400$. Note that the violent free-surface behavior began at $x/L = 0.30$, thus the entire measurement plane was affected by the bubbly free-surface. Stationary flow in the mean velocity field was observed from $x/L = 0.35$, and it grew in the vertical direction, rather than in the horizontal direction, as the flow progressed downstream. Near the stationary flow region, the vertical motion of the fluid due to the orbital motion in the wave was suppressed, as discussed in the results above for $Fr = 0.282$.

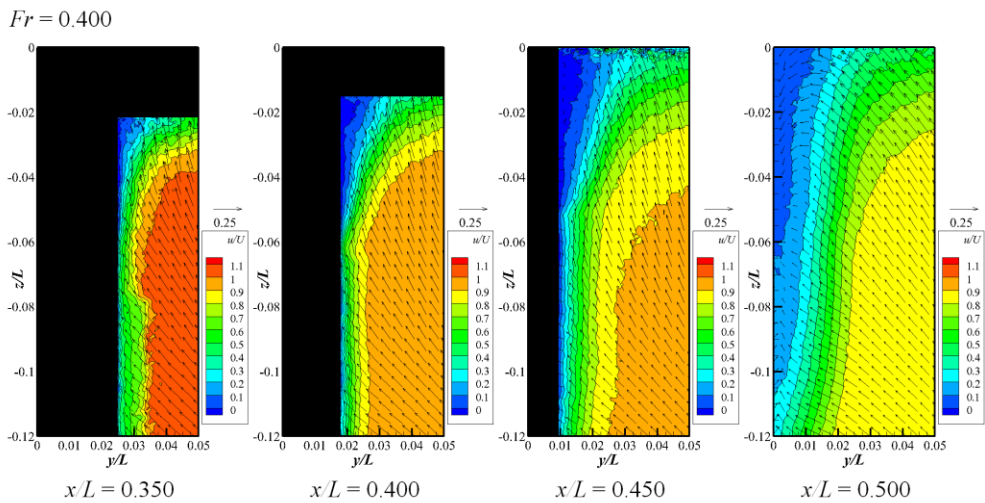


Figure 4-24. Mean velocity fields of the boundary layer region for $Fr = 0.400$.

In addition, there were notches on the u/U contours at the bottom of the stationary flow region on the measurement planes, which has also been reported in flow-field measurements around a vertical flat plate (Longo *et al.*, 1997).

Figure 4-25 shows the u/U distributions for $Fr = 0.400$. In the stationary flow region near the free-surface, reverse flow was observed. This implies the existence of flow separation at the juncture. At the deep location ($z/L = -0.1$), u/U was positive as the stationary flow region did not extend to this depth and flow was not separated.

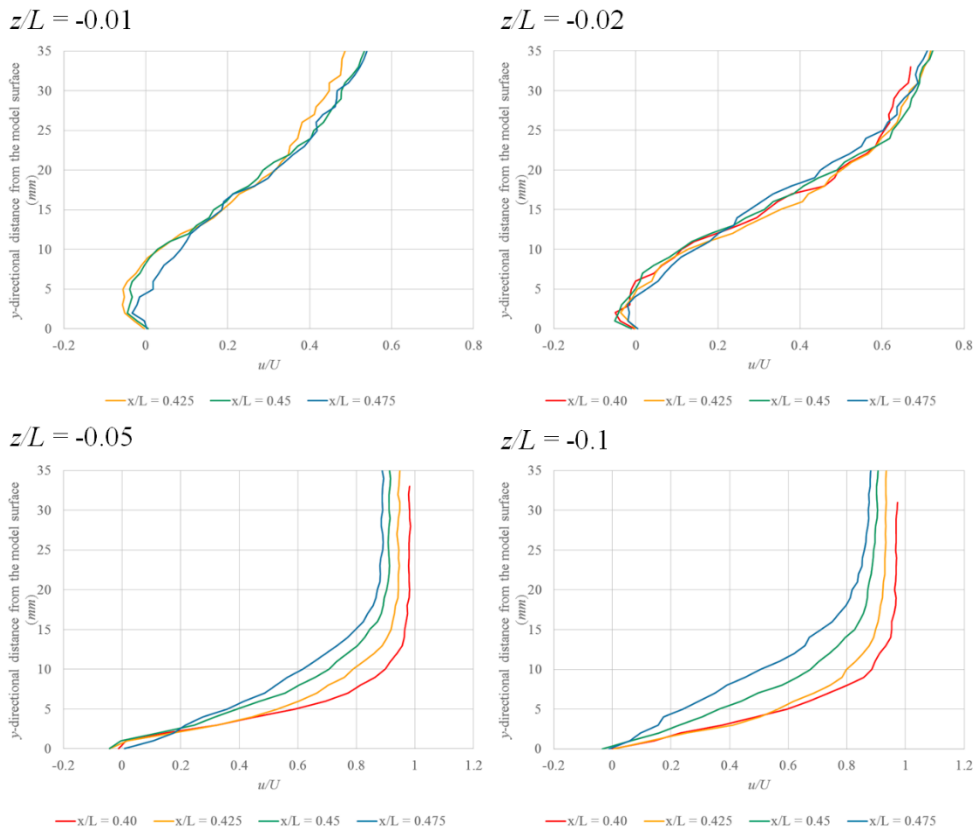


Figure 4-25. u/U distributions in the boundary layer region for $Fr = 0.400$.

Flow separation was observed when the free-surface became bubbly; thus, the bubbly free-surface behavior could be explained by the flow separation. Although the small fluctuation at the free-surface juncture caused additional momentum loss in the turbulent boundary layer in low- Fr conditions, the flow separation was not developed. However, when the adverse pressure gradient from the wave became strong, the turbulent boundary layer flow near the free-surface lost its entire momentum and separated from the surface. The flow separation accompanied a pressure drop and air entrainment.

It is significant that the bubbly free-surface expanded in the x - and y -directions, but that no reverse flow was observed under the entire bubbly free-surface region. The stationary flow region was located near the model surface only and grew in the z -direction. Flow separation was caused by both a momentum loss in the turbulent boundary layer and the presence of an adverse pressure gradient from the free-surface wave. If the adverse pressure gradient by the free-surface wave had been excessively large, such that it resulted in wave breaking, *i.e.*, in a large wave slope or hydraulic jump, flow separation might appear solely from the effect of the wave, but this situation was not part of this study's test conditions and as such, the boundary layer effects were essential to the development of flow separation.

Figure 4-26 shows the Reynolds normal stress distributions at $x/L = 0.45$ and $Fr = 0.400$. Turbulence strength and a structure around the stationary flow region can be identified. $\overline{u'u'}$ was concentrated at the boundary of the stationary flow region, while it was intense in the turbulent boundary layer in the smooth free-surface cases. In the boundary layer, the $\partial u / \partial y$ value was large and resulted in an intense $\overline{u'u'}$. For this Fr condition, however, there was frequent turbulence at the boundary or separation bubble, although the $\partial u / \partial y$

at the boundary of the stationary flow region was smaller than that in the 2D boundary layer. The existence of reverse flow contributed most to the generation of turbulence.

At the flow separation region, $\overline{v'v'}$ was distributed regularly. Eddies in the flow separation transferred the turbulence energy to nearby flows, thus activating the transport of the turbulence energy along the y-direction. Violent free-surface behavior strengthened the $\overline{w'w'}$, which was observed at the boundary of the stationary region and under the free-surface. In principle, a free-surface restricts velocity fluctuation in the normal direction to the surface, however, the bubbly behavior enabled turbulent velocity and wave elevation fluctuation of the flow underneath the free-surface, resulting in the high $\overline{w'w'}$ values.

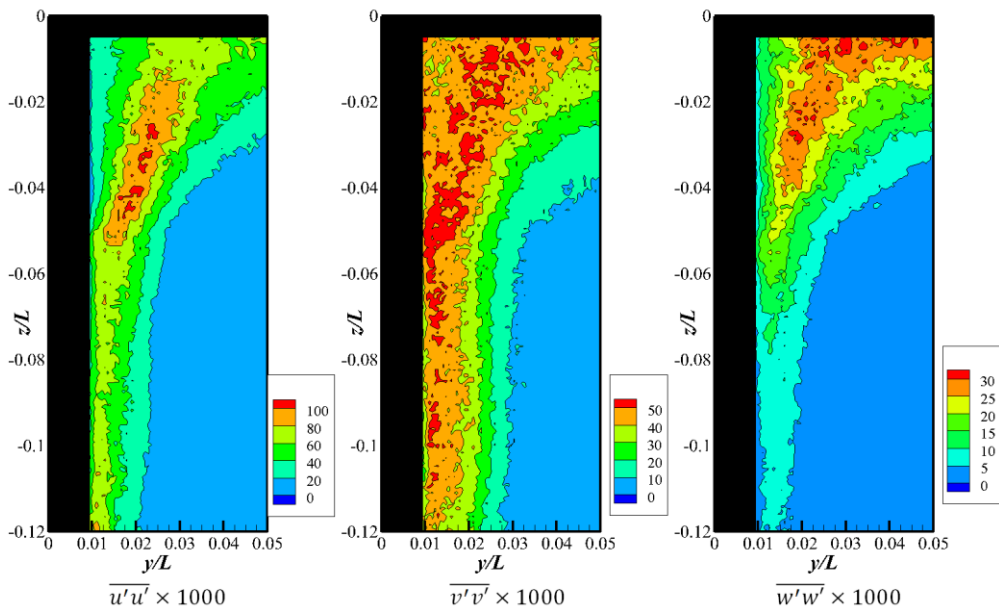


Figure 4-26. Reynolds normal stress distribution at $x/L = 0.45$ and $Fr = 0.400$.

By analyzing the Reynolds shear stress distributions, it was revealed that the turbulence structure at the flow separation region was completely different from that in the boundary layer. Figure 4-27 shows the Reynolds shear stress distributions at $x/L = 0.450$ and $Fr = 0.400$. $\overline{v'w'}$ and $\overline{u'w'}$, which indicate eddy rotation in the x - and y -directions, respectively, increased near the free-surface and the boundary of the flow separation region, whereas $\overline{u'v'}$ was concentrated at the boundary layer region in deep locations.

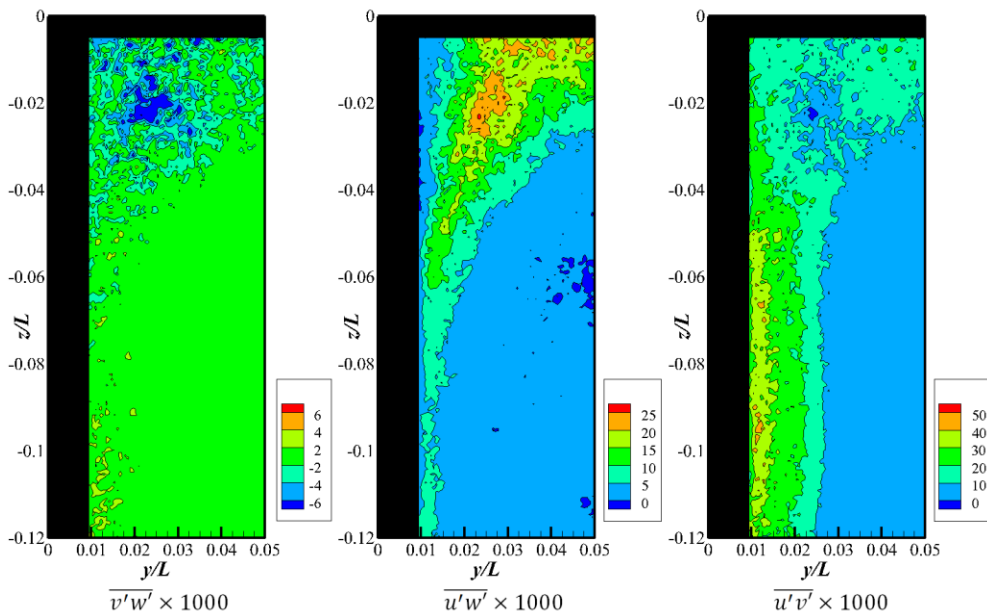
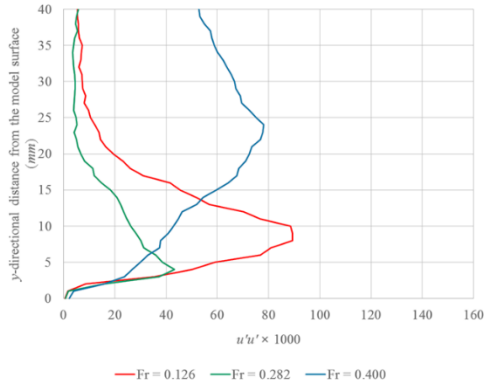


Figure 4-27. Reynolds shear stress distribution at $x/L = 0.45$ and $Fr = 0.400$.

$z/L = -0.01$



$z/L = -0.1$

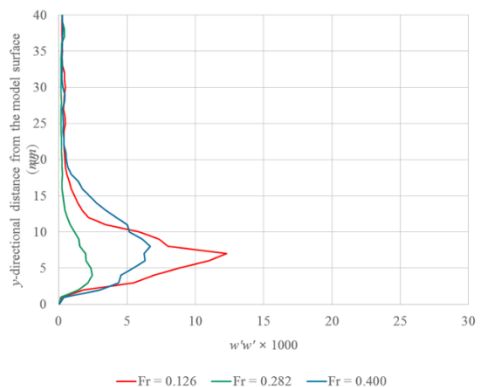
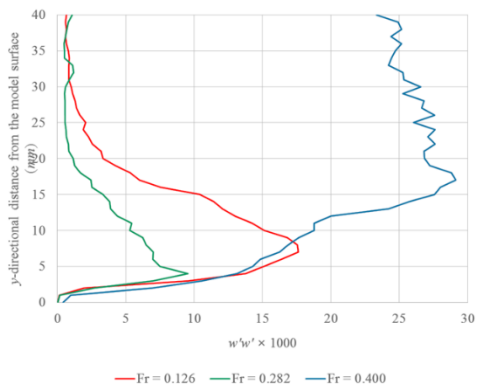
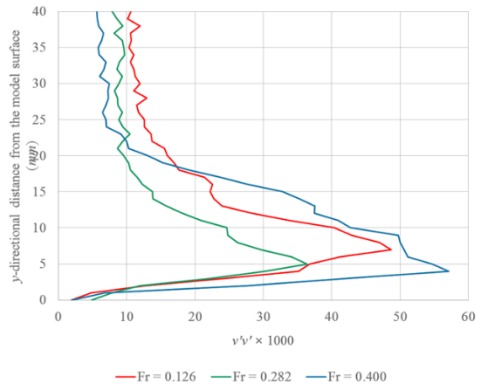
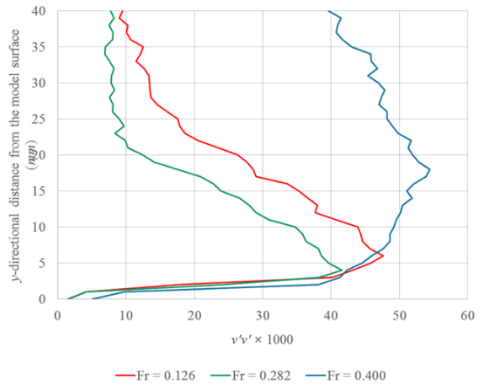
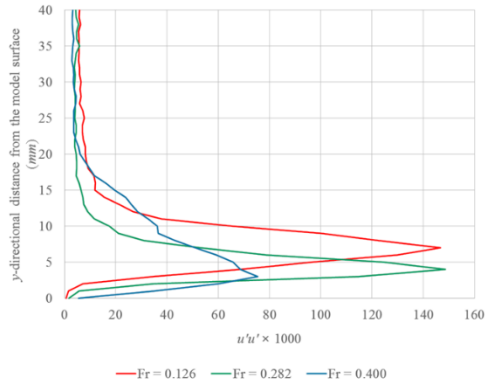


Figure 4-28. Comparisons of Reynolds normal stress distributions at $x/L = 0.450$.

Next, the Reynolds stresses at $x/L = 0.45$ with Fr variations were compared and are shown in Figure 4-28. For $Fr = 0.126$ and 0.282 , as shown in the figure, the turbulence in the boundary layer was highly anisotropic and only $\overline{u'u'}$ was dominant, but it became less anisotropic in high- Fr conditions with a bubbly free-surface and flow separation at the juncture. In general, the non-dimensionalized Reynold normal stress in the 2D boundary layer flow tended to decrease as Fr increased. In high- Fr conditions, however, the Reynolds normal stress increased near the free-surface due to flow separation under the bubbly free-surface.

To quantify the isotropic characteristics of turbulence, anisotropy was derived from the mean and standard deviation of the Reynolds normal stress at a certain location, as follows:

$$(\text{Anisotropy}) = \sqrt{\frac{(\overline{u'u'})^2 + (\overline{v'v'})^2 + (\overline{w'w'})^2}{\frac{\overline{u'u' + v'v' + w'w'}}{3}}} - 1. \quad (4-1)$$

If the anisotropy is zero, the turbulence is totally isotropic, as the magnitude of the Reynolds normal stresses are identical. Figure 4-29 shows the anisotropy distributions at $x/L = 0.450$ and at two different depths. In every case, the anisotropy increased near the model surface, because the no-slip wall condition caused a strong anisotropic turbulent boundary layer. The anisotropy from the boundary layer converged to 0.25 at $z/L = -0.1$.

The violent free-surface decreased the anisotropy. Near the free-surface, *i.e.*, $z/L = -0.01$, the anisotropy from the boundary layer converged at around 0.05 for $Fr = 0.400$. In other Fr conditions, the anisotropy also decreased at the juncture of the flow regions, but it converged in the same manner as the flow in deep locations.

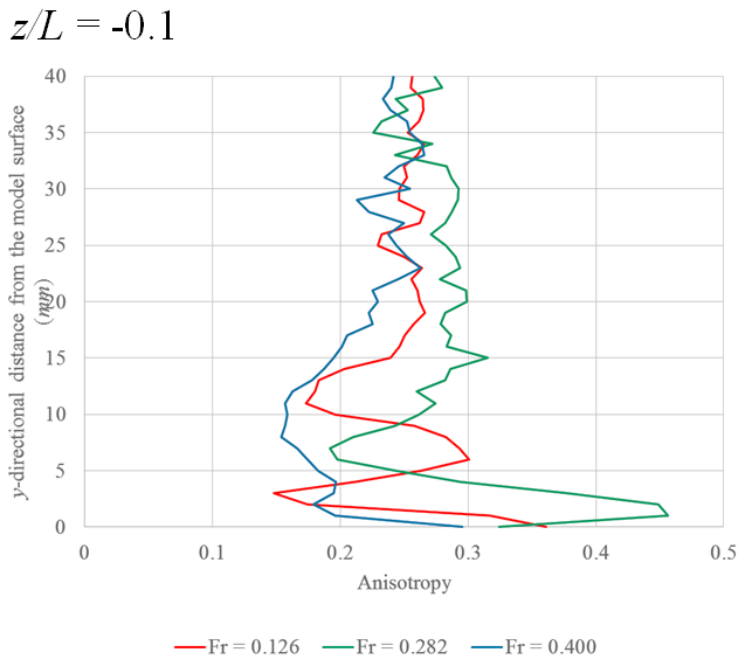
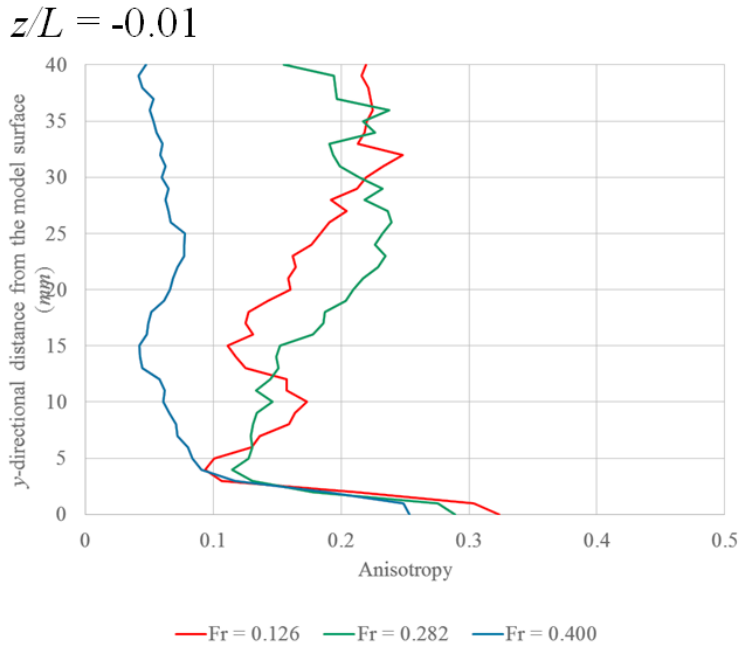


Figure 4-29. Anisotropy distribution at $x/L = 0.45$.

The turbulent eddy generation at the juncture reduced the anisotropy. As discussed above, the momentum loss and turbulence generation increased at the juncture region. As more turbulence eddies appeared in this region, the transfer of turbulence energy in random directions became more frequent. In high- Fr conditions, a bubbly free-surface can stimulate the vertical fluctuation of velocity. Thus, a Reynolds normal stress perpendicular to the free-surface is also produced and propagated, whereas it had been limited to a small region around the juncture in smooth free-surface conditions.

Figure 4-30 shows the turbulent kinetic energy distributions around the model for $Fr = 0.400$. k was concentrated at the boundary of the stationary flow region, but it dissipated as the flow progressed downstream, similar to the behavior of k in the boundary layer in low- Fr cases. While there was turbulence in the boundary layer, the magnitude of k in this region was smaller than that at the stationary flow region near the free-surface and model surface juncture.

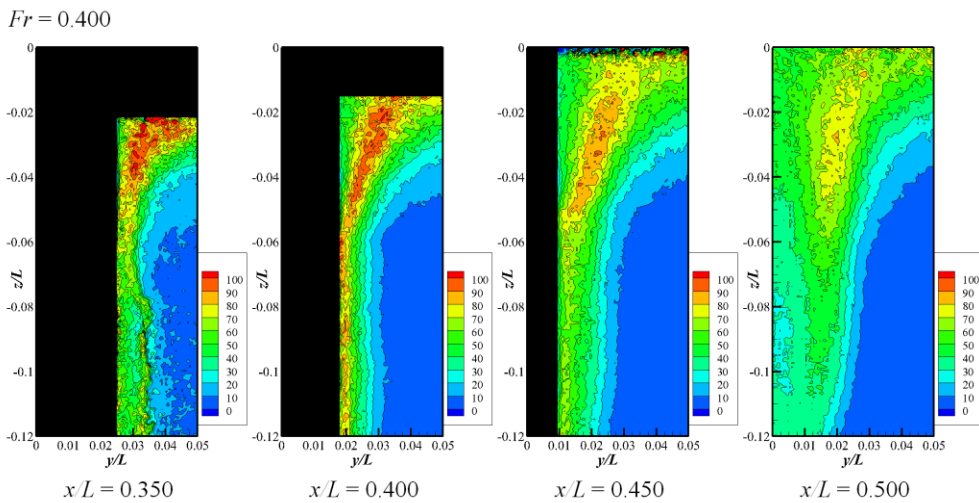


Figure 4-30. $k/U^2 \times 1000$ distribution of boundary layer region at $Fr = 0.400$.

Figure 4-31 shows the k distributions at $x/L = 0.45$. To compare the magnitude of k and its relative strength, dimensional and non-dimensional data were examined. As the free-surface was smooth and steady for $Fr = 0.126$ and 0.282 , the k distribution for these two Fr conditions should be compared to identify the Stokes wave effects on the turbulence.

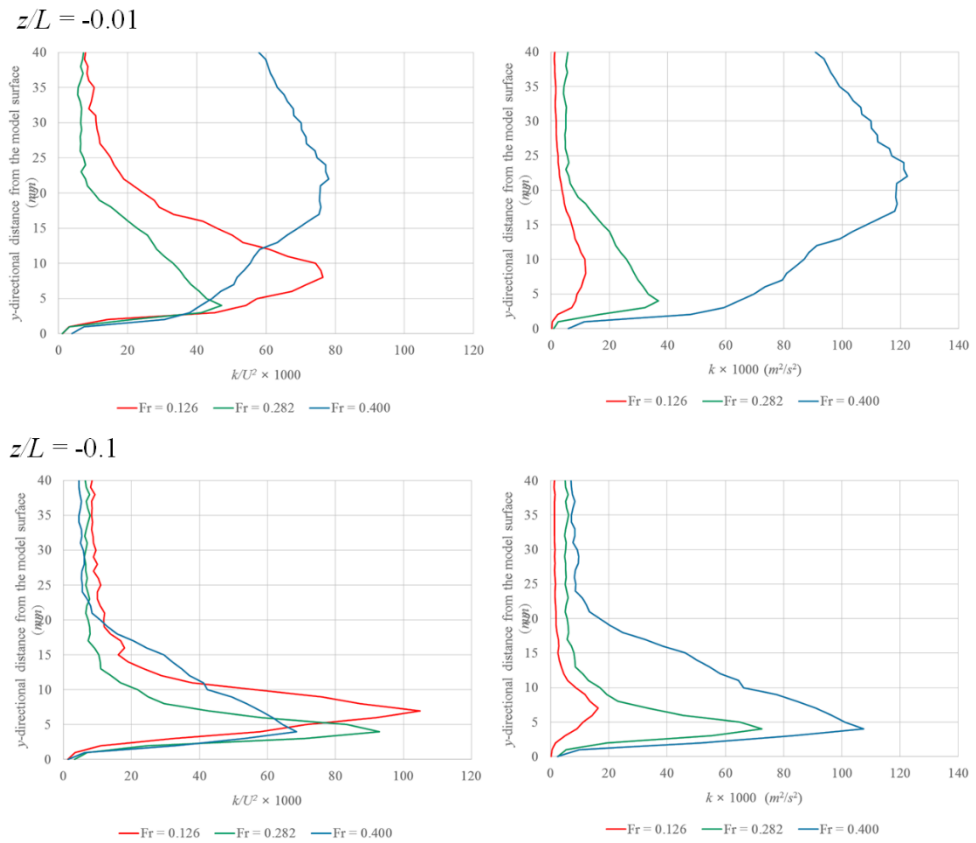


Figure 4-31. Turbulence kinetic energy distribution on the model surface at $x/L = 0.45$.

The magnitude of the local maxima of k/U^2 in deep locations was similar where free-surface waves had no effect. The local maxima of k/U^2 was

degraded near the free-surface, because the smooth free-surface boundary condition forced the transport of active y -directional turbulence by restraining the z -directional velocity fluctuation, such that the turbulence became more isotropic than that in the boundary layer.

The Stokes wave for $Fr = 0.282$ decreased the flow velocity near the free-surface by the orbital motion of the wave. Thus, the shear stress in the boundary layer and k/U^2 were also reduced. When the free-surface became unsteady in $Fr = 0.400$ conditions, enormous turbulence was produced near the free-surface, due to the bubbly free-surface and the flow separation.

Figure 4-32 shows a schematic of the flow field in the boundary layer region. By considering the wave elevation and flow field measurements, the characteristics of the free-surface and no-slip wall juncture flow could be identified.

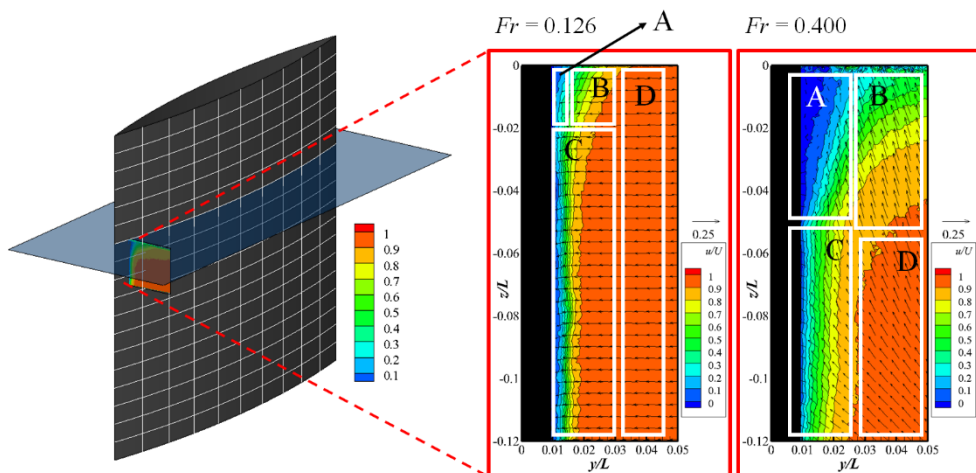


Figure 4-32. Schematic of flow characteristics in the boundary layer region: (A) free-surface and solid-wall juncture layer, (B) free-surface boundary layer, (C) solid-wall boundary layer, and (D) outer flow.

Near the juncture of the free-surface and the model wall (Region A in Figure 33), the flow is diminished even in low- Fr conditions due to free-surface fluctuation and small-scale turbulence production. If an adverse pressure gradient from a free-surface wave was added to the flow field as Fr increased, excessive flow velocity retardation resulted in a flow separation with reverse flow. The stationary flow region expanded in the z -direction, primarily as the Fr and Re values increased, because the momentum loss of the boundary layer contributed most to the flow separation.

The turbulence generated by the free-surface fluctuation propagated in the horizontal direction along the free-surface (Region B in Figure 4-33), as turbulence energy was transported in 3D by turbulent eddies. In low- Fr conditions, the free-surface was smooth and steady and the fluctuation was restricted to the microscale, whereas excessive bubbly free-surfaces induced more isotropic turbulence in high- Fr conditions, especially in the y - and z -directions in this study.

Region C in Figure 4-33 could be identified as where the boundary layer thickness along the z -direction was constant. In this region, however, the on-plane velocity vectors from the orbital motion of water particles in the waves and the flow along the converged model geometry were still visible. Outside Region C, the water particle motion in Stokes waves was dominant and no flow retardation due to the boundary layer was observed (Region D in Figure 4-33).

4.3. Wake field flows: large model case

4.3.1. $Fr = 0.126$ (smooth and steady free-surface with negligible waves)

Turbulence dissipation and wake recovery were mainly investigated by performing near-wake flow field measurements ($x/L = 0.50$ to 0.70). Figure 4-33 shows the mean flow velocity in the wake region. Wake recovery in the downstream was delayed near the free-surface.

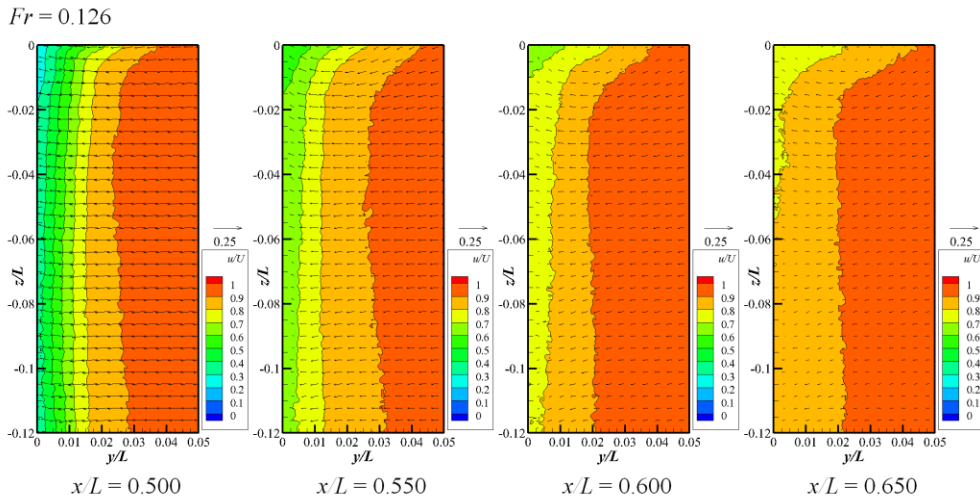


Figure 4-33. Mean velocity distribution in the near-wake fields for $Fr = 0.126$.

Figure 4-34 shows the u/U distributions in the near-wake region. The flow near the free-surface at the TE was slower than that in the 2D flow as the free-surface boundary layer interaction degraded the momentum in the juncture flow, but the wake near the free-surface recovered more rapidly than that in deep locations. A low u/U near the free-surface induced a strong shear stress in the wake field, which seemed to stimulate rapid wake recovery.

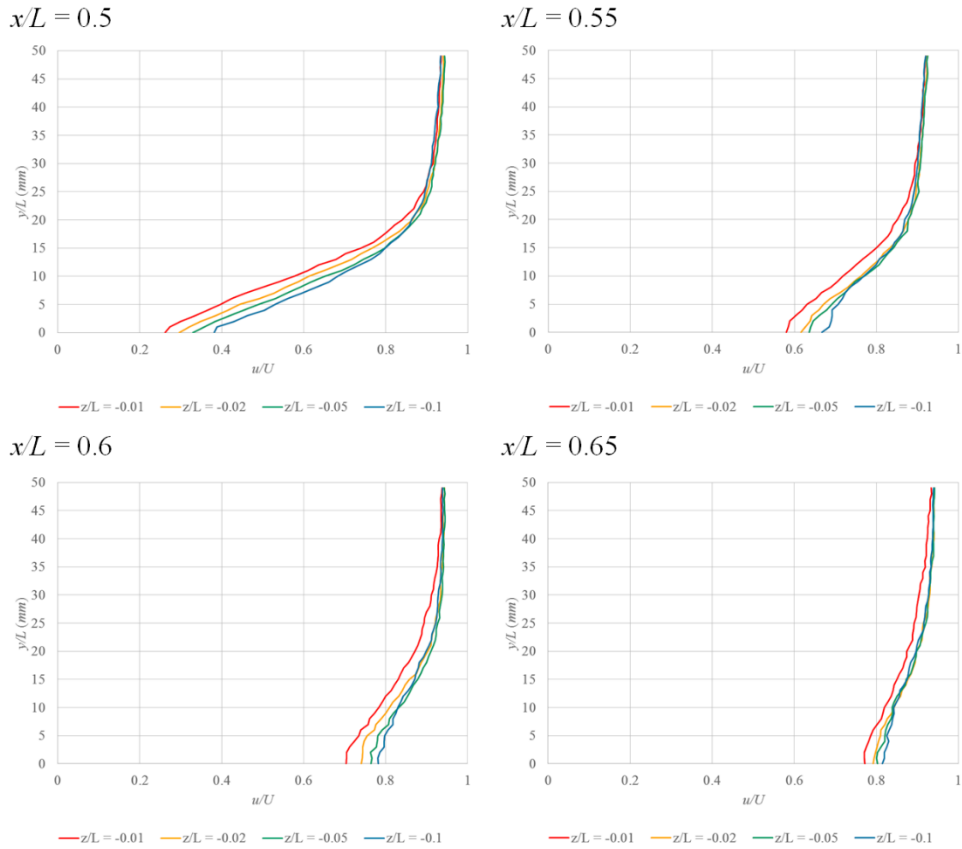


Figure 4-34. u/U distribution in near-wake region for $Fr = 0.126$.

In the same manner as the boundary layer thickness in the analysis of the boundary layer region, the displacement of flow due to the diminished flow in the wake could be quantified and defined as wake width. Figure 4-35 shows the results. The wake width changes at $z/L = -0.05$ and -0.1 were similar, but increased near the free-surface. At $0.5 \leq x/L \leq 0.6$, the wake width reduced linearly. Decreasing and converging wake width were similar with those of flat plate wake results (Chevray and Kovasznay, 1969), however, changes of wake width according to depth was remarkable.

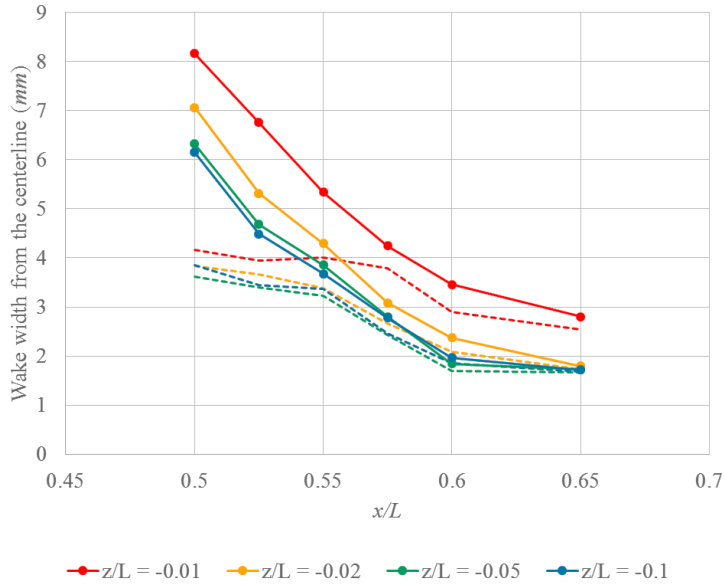
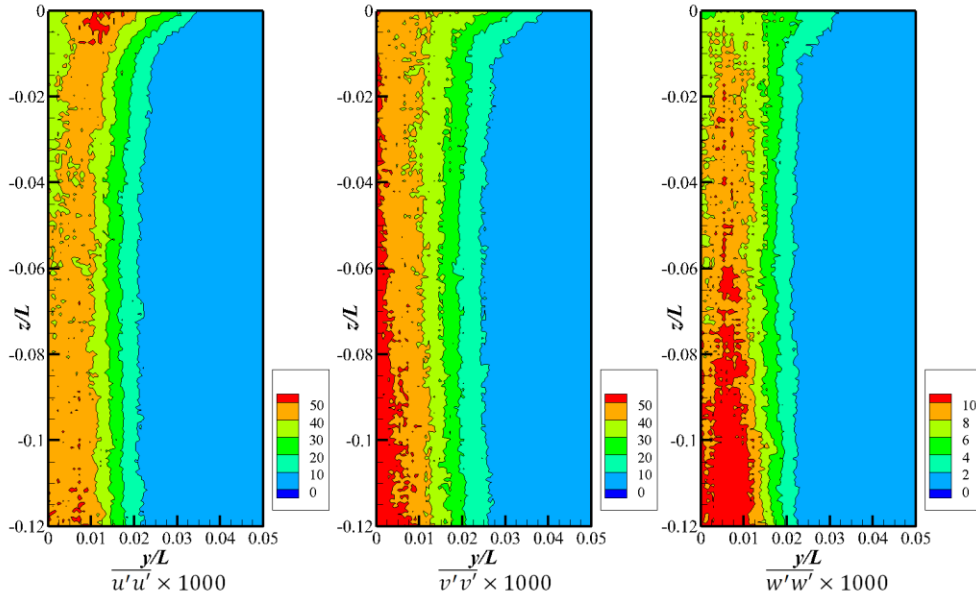


Figure 4-35. Wake width from the centerline in the near-wake region for $Fr = 0.126$: displacement width (solid line) and momentum width (broken line).

Figure 4-36 shows the Reynolds normal stress at $x/L = 0.5$ and 0.6 . The Reynolds stresses decreased downstream due to the turbulence dissipation. In contrast to the boundary layer flows, there were no no-slip wall effects and $\overline{u'u'}$ became similar to $\overline{v'v'}$, which increased the anisotropy. Still, the $\overline{w'w'}$ was smaller than in other Reynolds normal stresses and the flow showed 2D flow characteristics. Near the free-surface, the flow was not 2D.

Figure 4-37 shows the Reynolds normal stress distributions in the near-wake region for $Fr = 0.126$. $\overline{u'v'}$ was dominant in the Reynolds shear stress distributions, which means that the eddies were rotated in the z -direction of the boundary shear layer.

$x/L = 0.50$



$x/L = 0.60$

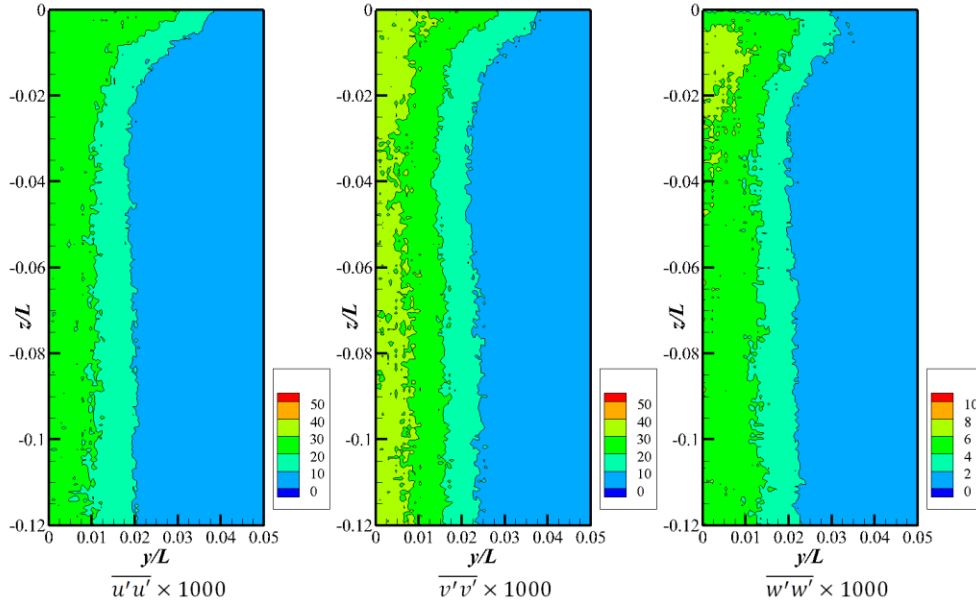
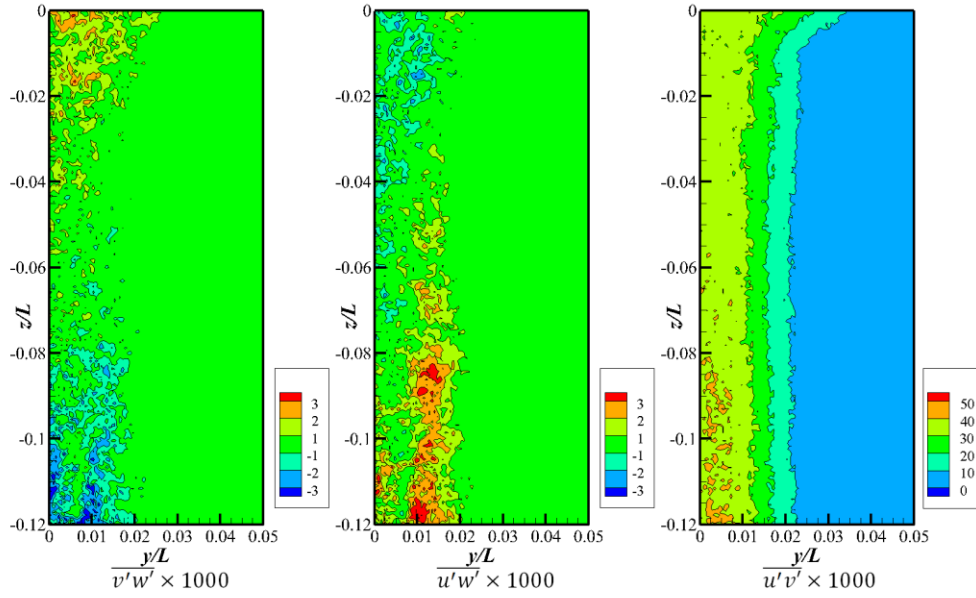


Figure 4-36. Reynolds normal stress distribution in the near-wake region for $Fr = 0.126$.

$x/L = 0.50$



$x/L = 0.60$

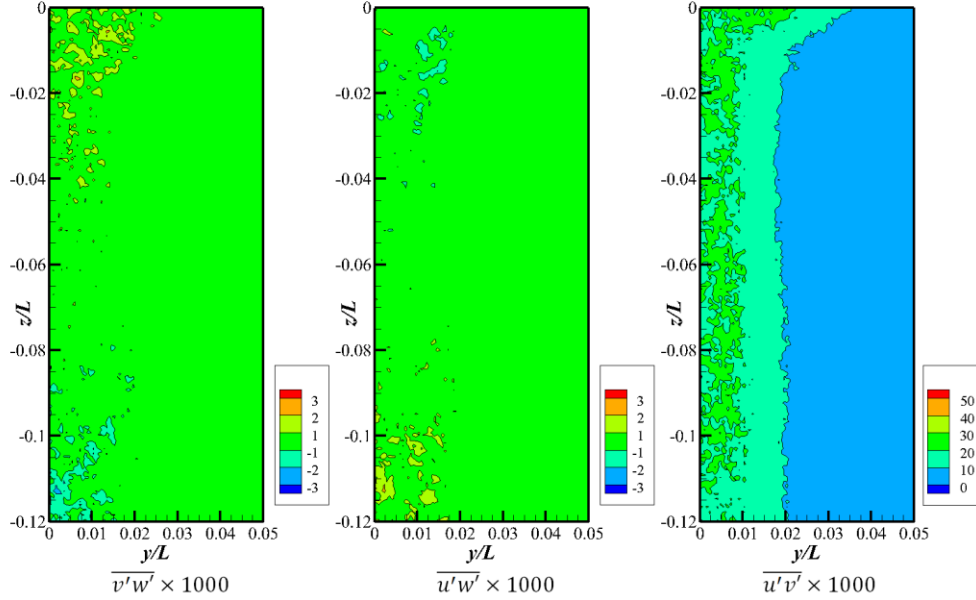


Figure 4-37. Reynolds shear stress distributions in the near-wake region for $Fr = 0.126$.

Figures 4-38 and 4-39 show the k distributions in the near-wake region for $Fr = 0.126$. Turbulent dissipation was clearly observed. The intense turbulence region expanded near the free-surface, as occurred in the boundary layer region.

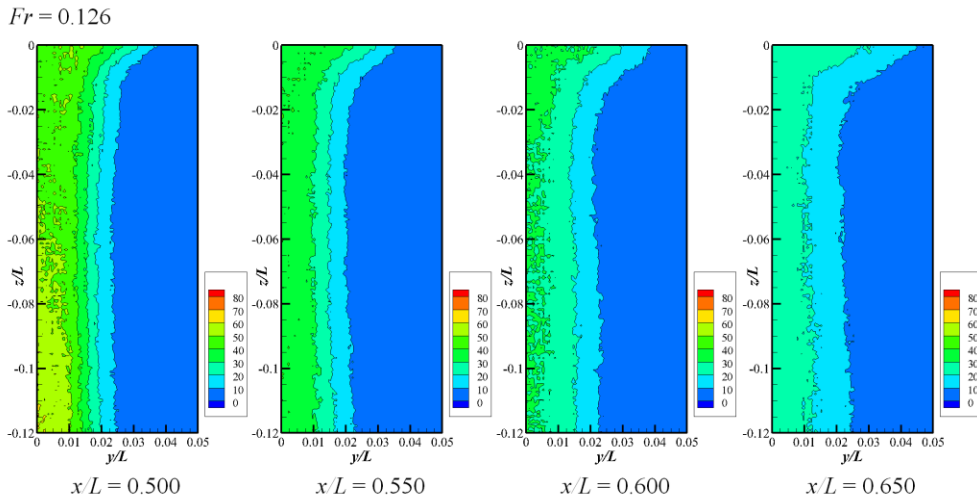


Figure 4-38. $k/U^2 \times 1000$ distribution in the near-wake region for $Fr = 0.126$.

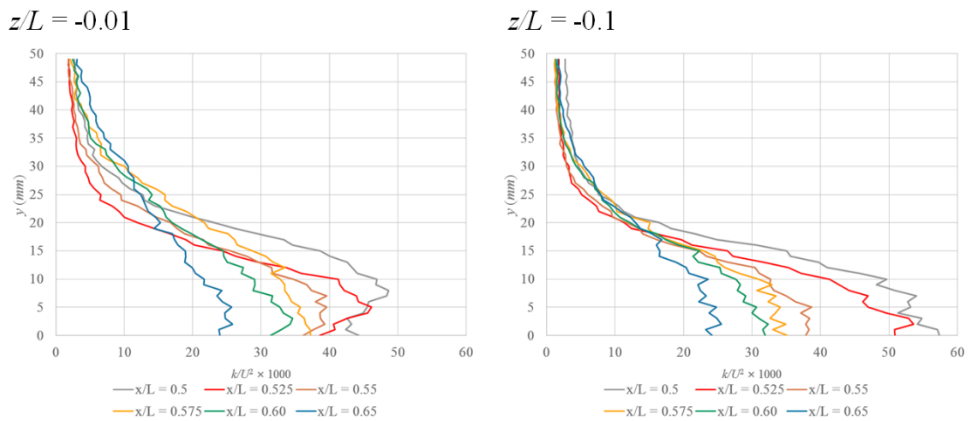


Figure 4-39. $k/U^2 \times 1000$ distribution in the near-wake region at $z/L = -0.01$ and -0.1 and $Fr = 0.126$.

To quantify the turbulence dissipation, the spatial mean of $k/U^2 \times 1000$ at constant depth was obtained, as shown in Figure 4-41. At the TE, the magnitude of k was almost constant along the z -direction, while the free-surface increased k in the boundary layer region. The free-surface degraded the turbulence dissipation and k decreased linearly at $z/L = -0.01$. In deep locations, turbulence dissipated rapidly at $0.5 \leq x/L \leq 0.55$.

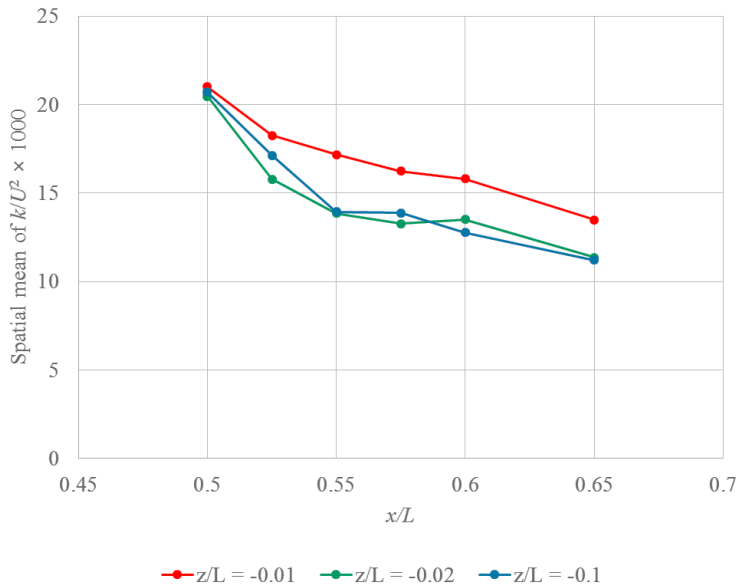


Figure 4-40. Spatial mean of $k/U^2 \times 1000$ in the near-wake region for $Fr = 0.126$.

4.3.2. $Fr = 0.282$ (smooth free-surface waves) and 0.400 (knobby wake)

Figure 4-41 shows the mean velocity fields in the near-wake field for $Fr = 0.282$. A stationary flow region was observed at the TE, but it disappeared in the downstream as the wake recovered.

$Fr = 0.282$

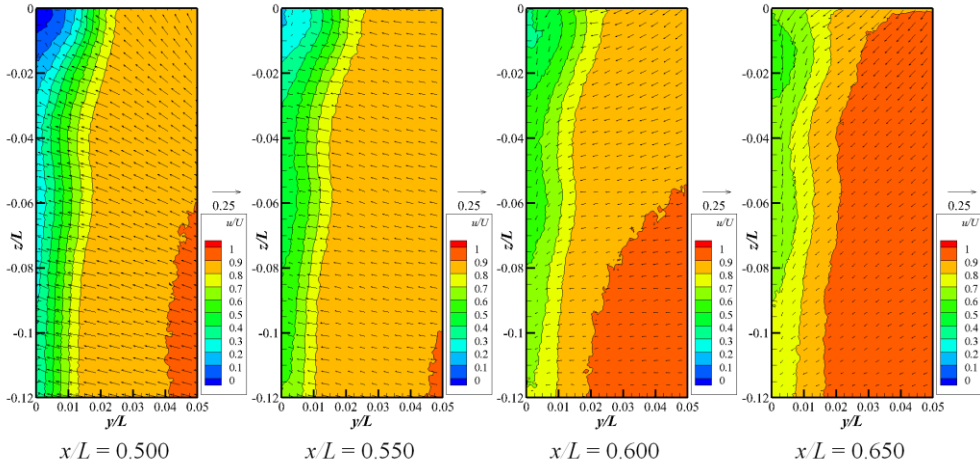


Figure 4-41. Mean velocity distribution in the near-wake fields for $Fr = 0.282$.

Figure 4-42 shows the mean velocity in the near-wake region for $Fr = 0.400$. A stationary flow region was also observed for this Fr condition, but it developed into a deep location.

$Fr = 0.400$

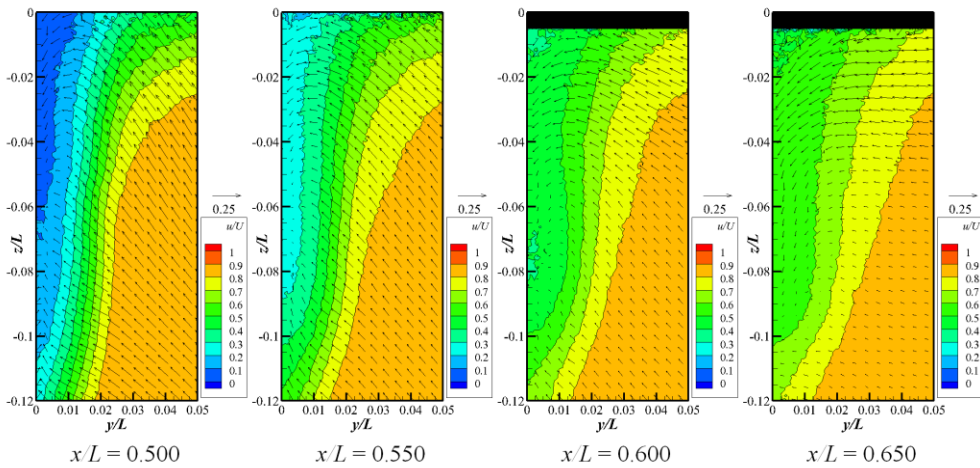


Figure 4-42. Mean velocity distribution in the near-wake fields for $Fr = 0.400$.

In the stationary flow region, flow headed downward. As the flow from the stationary flow region headed upward due to orbital motion in the Stokes wave, the flow at the border was affected by the strong shear and thus rotated.

The u/U value in different Fr conditions at $z/L = -0.01$ and -0.1 are shown in Figure 4-43. Reverse flow appeared by flow separation and the bubbly free-surface did not continue to the near-wake, although a knobby free-surface existed in the near-wake. This implies that the reverse flow in flow separation is correlated with air entrainment around the juncture only.

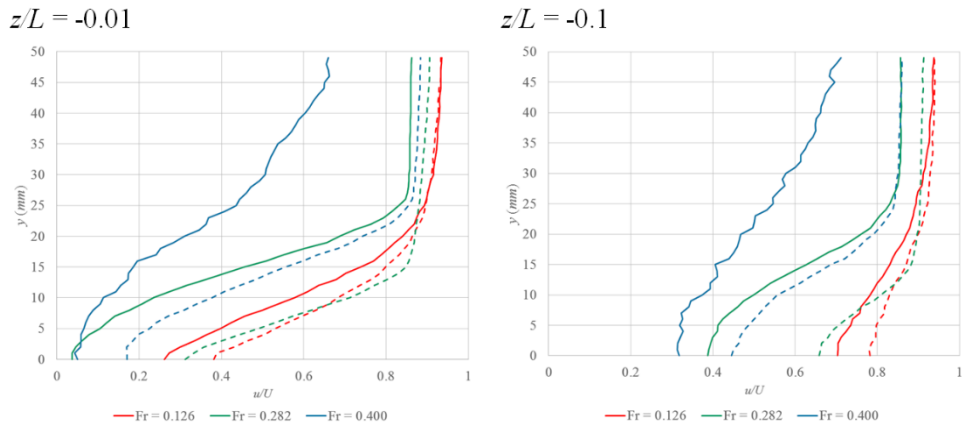


Figure 4-43. u/U distributions at $x/L = 0.5$ (solid line) and 0.6 (broken line).

Figure 4-44 shows the amount of wake recovery, as obtained from the difference in u/U values between $x/L = 0.5$ and 0.6 . As discussed above, the free-surface accelerated the wake recovery and this effect was more clear for $Fr = 0.400$. The wake recovery seems to be primarily affected by the initial retarded flow velocity. As the flow velocity slowed, the shear stress in the region increased and more turbulence was generated, which activated momentum transport by eddies, thus promoting wake recovery. Near the free-

surface, similar phenomena appeared. The low-velocity region expanded in the horizontal direction and the turbulence kinetic energy production increased near the free-surface, resulting in wake recovery.

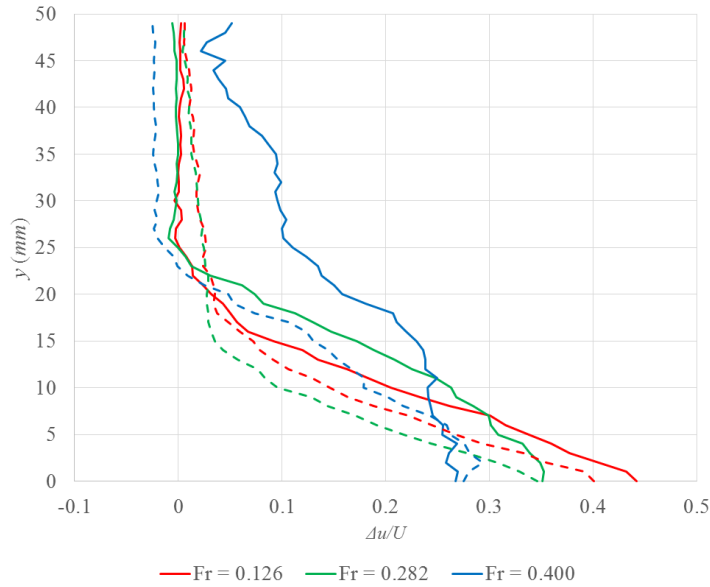
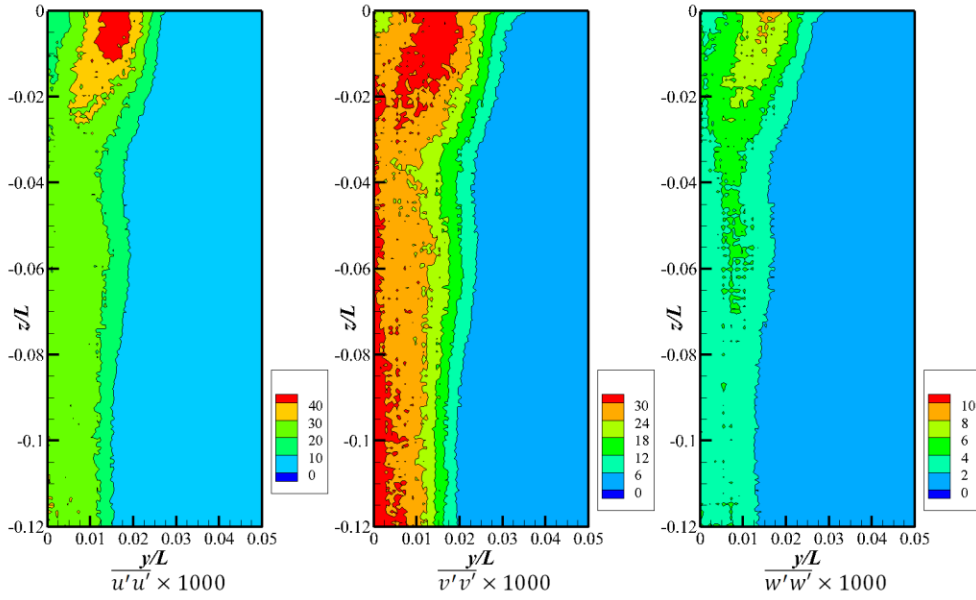


Figure 4-44. Difference of u/U between $x/L = 0.5$ (solid line) and 0.6 (broken line).

Figures 4-45 and 4-46 show the Reynolds normal and shear stress distributions for $Fr = 0.282$, respectively. Although there was orbital motion in the waves, the effects on the Reynolds stresses were not distinguishable and the tendency was similar to the Reynolds stress distribution in the near-wake for $Fr = 0.126$, in which $\overline{u'u'}$ and $\overline{v'v'}$ were dominant while $\overline{w'w'}$ was concentrated near the free-surface.

$x/L = 0.50$



$x/L = 0.60$

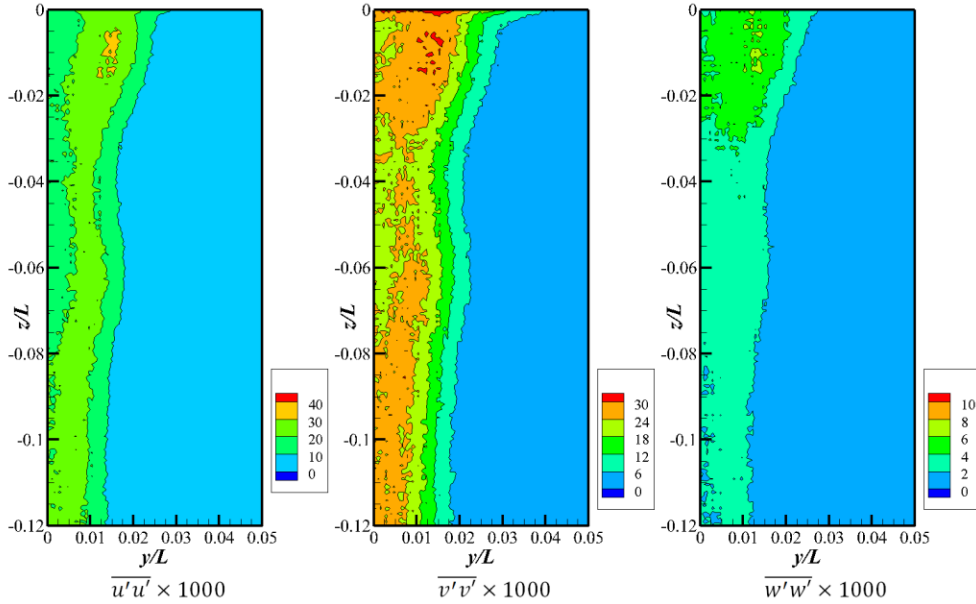
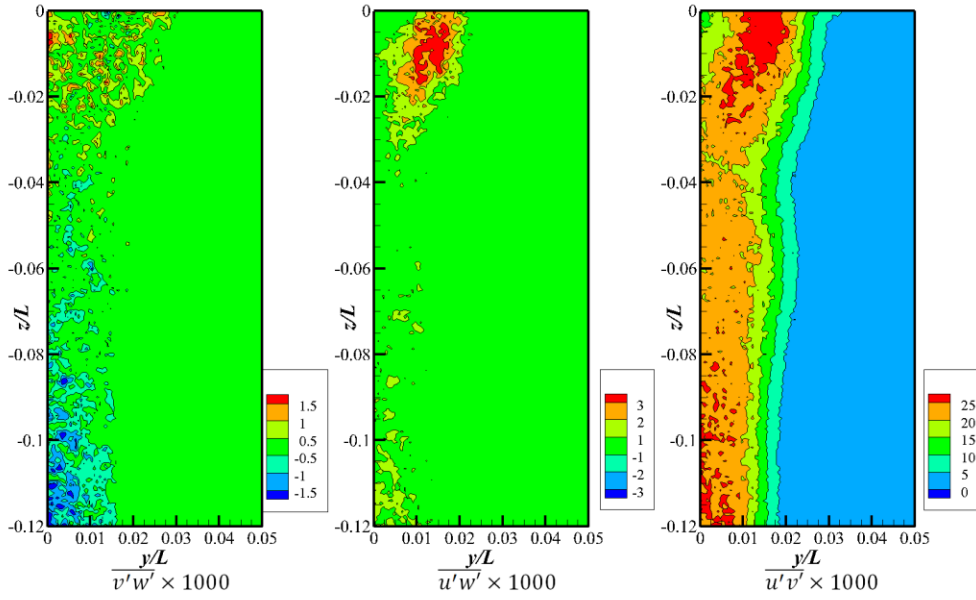


Figure 4-45. Reynolds normal stress distribution in the near-wake region for $Fr = 0.282$.

$x/L = 0.50$



$x/L = 0.60$

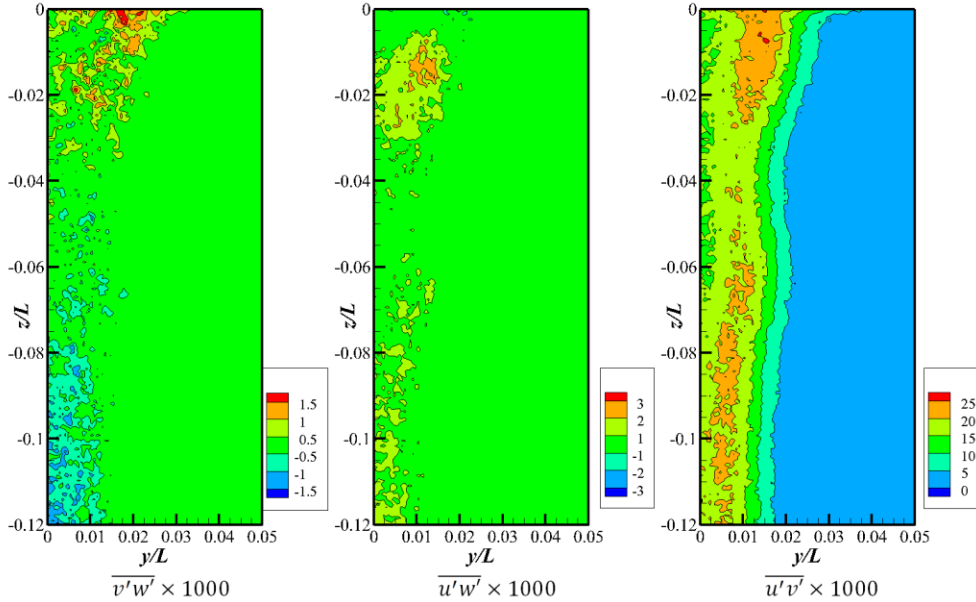
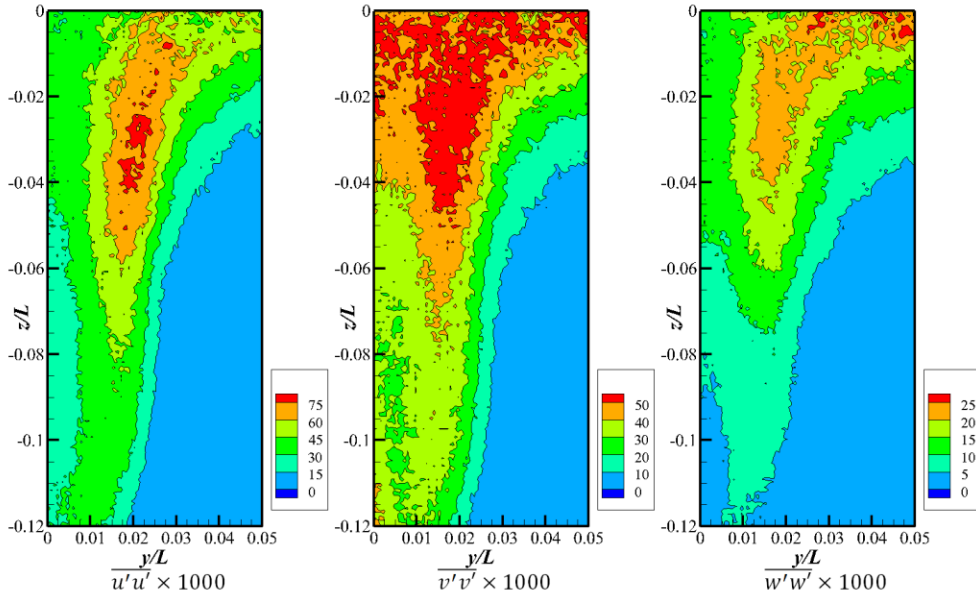


Figure 4-46. Reynolds normal stress distribution in the near-wake region for $Fr = 0.282$.

Due to the 2D flow characteristics, $\overline{u'v'}$ was also predominant in the Reynolds shear stresses. The local maxima of $\overline{u'u'}$ was found at the border of the stationary flow region near the free-surface. It dissipated in the downstream and the magnitudes of $\overline{u'u'}$ and $\overline{v'v'}$ were similar.

Figures 4-47 to 4-48 show the Reynolds stresses for $Fr = 0.400$, where flow separation and knobby free-surfaces were observed. At the stationary flow region, intense turbulence was produced and the violent free-surface behavior strengthened the vertical component of the Reynolds normal stress.

$x/L = 0.50$



$x/L = 0.60$

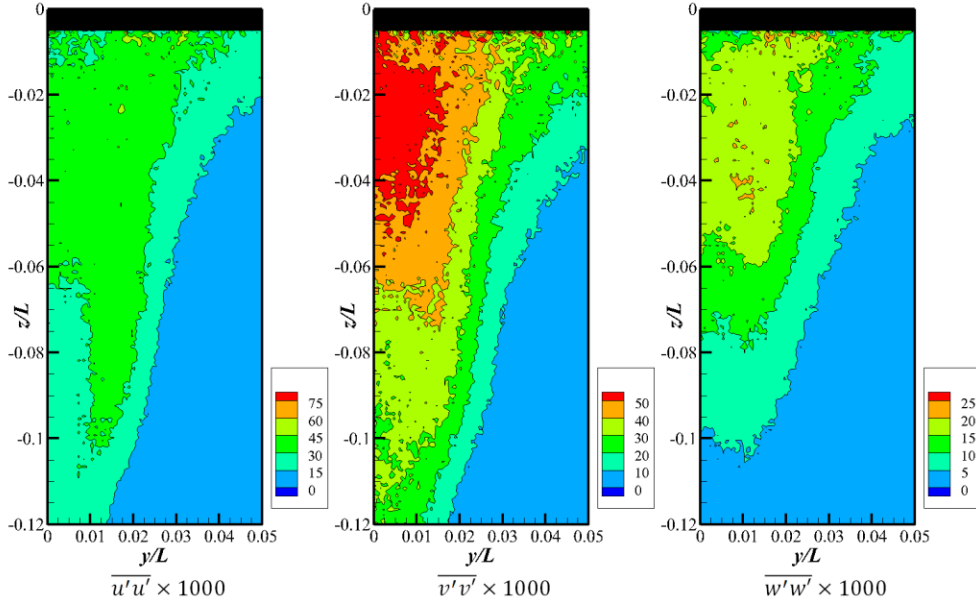
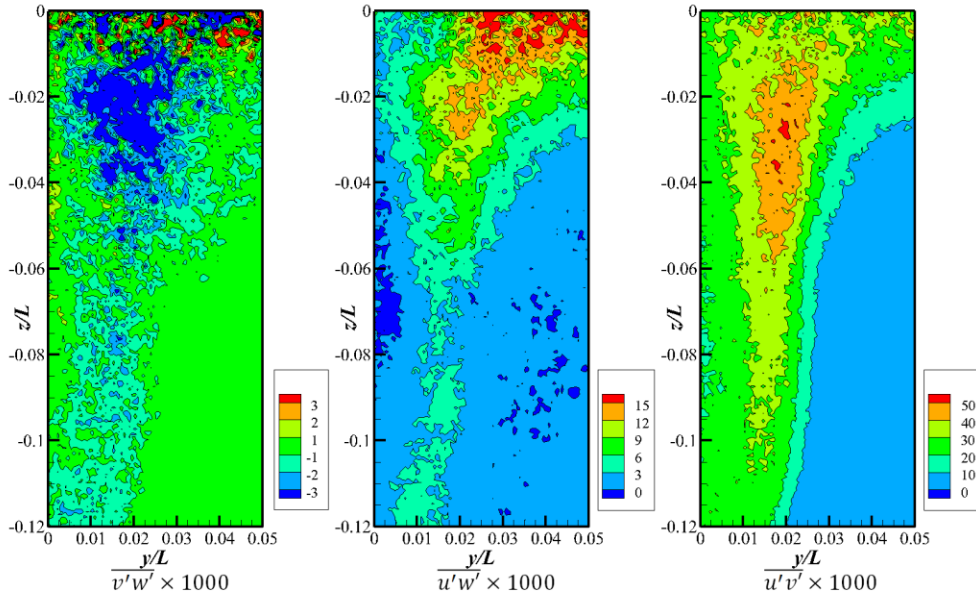


Figure 4-47. Reynolds normal stress distribution in the near-wake region for $Fr = 0.400$.

$x/L = 0.50$



$x/L = 0.60$

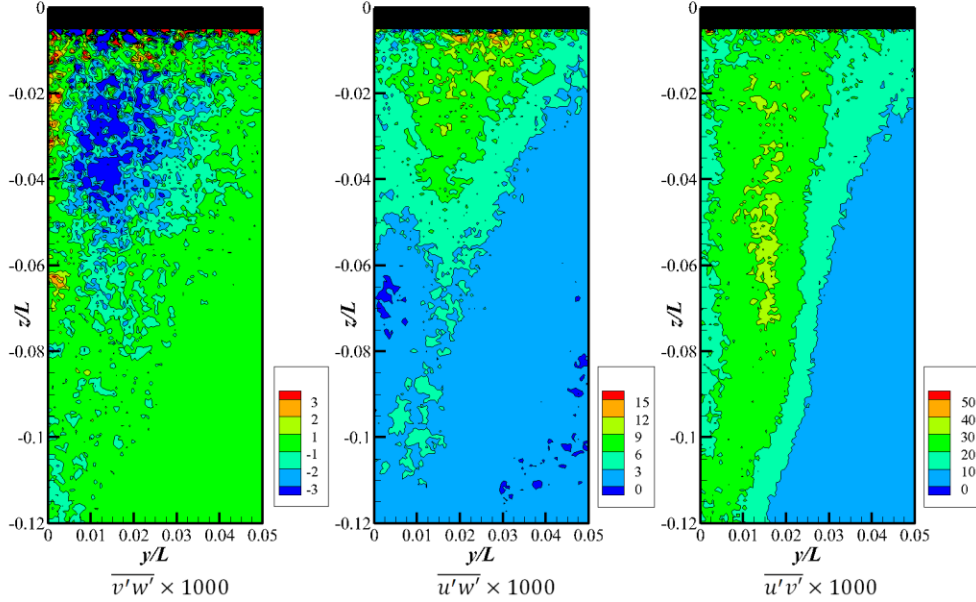
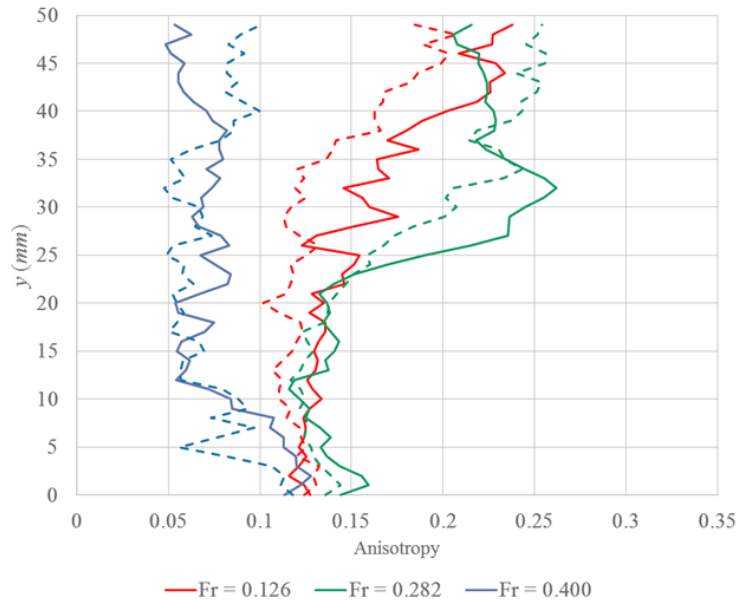


Figure 4-48. Reynolds normal stress distribution in the near-wake region for $Fr = 0.282$.

The turbulence, which increased near the free-surface for $Fr = 0.400$, consisted of random eddies and low anisotropy was expected, whereas the turbulence induced by the boundary layer was 2D and highly anisotropic in lower Fr conditions.

Figure 4-49 compares the anisotropy levels at $x/L = 0.5$ and 0.6 , according to the Fr conditions. In general, the free-surface degraded the anisotropy as the Fr value increased. It can be concluded that the vertical fluctuation of the free-surface by Stokes wave or air entrainment induced turbulence near the free-surface and contributed to the decrease in anisotropy. For high- Fr conditions, knobby and unsteady free-surface behavior in the near-wake dramatically reduced the anisotropy.

$z/L = -0.01$



$z/L = -0.1$

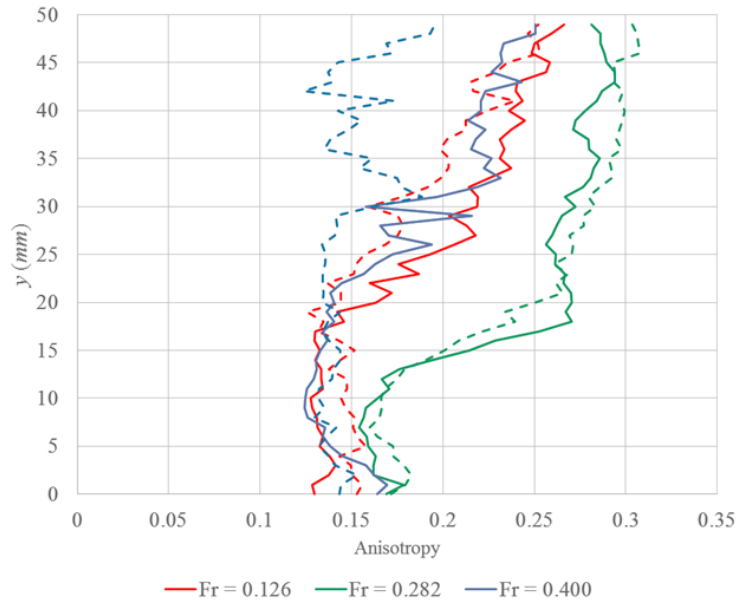


Figure 4-49. Anisotropy distribution at $x/L = 0.5$ (solid line) and 0.6 (broken line).

Figures 4-50 and 4-51 show the k distribution in the near-wake region for $Fr = 0.282$ and 0.400 , respectively. The investigations in this study mainly focused on the turbulence dissipation and diffusion in the near-wake. k was condensed at the boundary of the stationary region. In addition, the turbulent region broadened downstream.

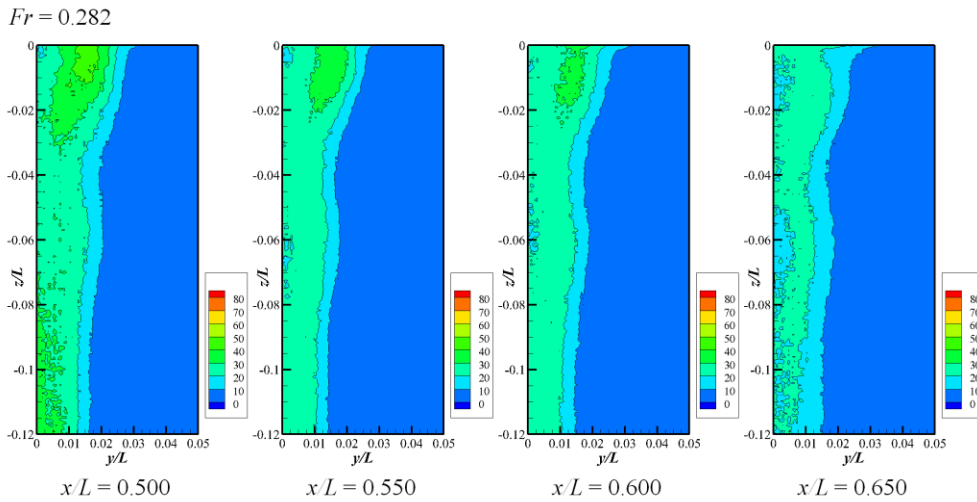


Figure 4-50. $k/U^2 \times 1000$ distribution in the near-wake region for $Fr = 0.282$.

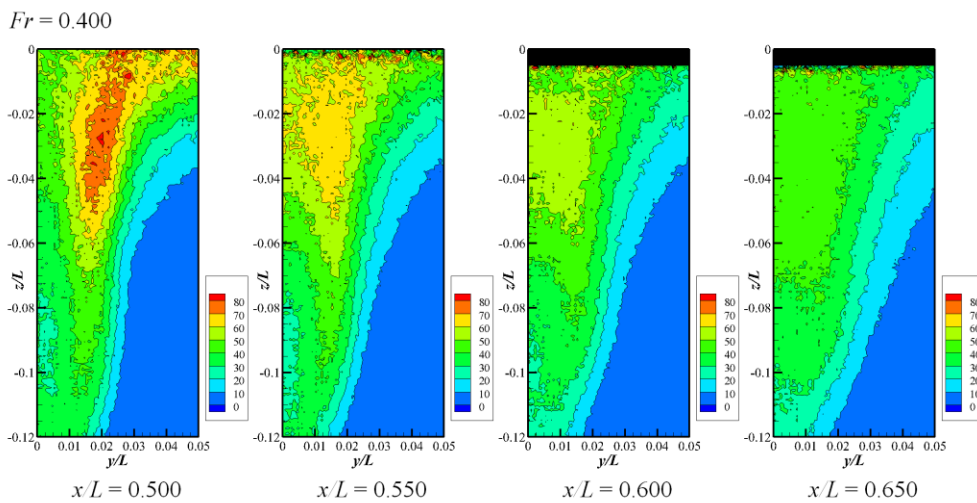


Figure 4-51. $k/U^2 \times 1000$ distribution in the near-wake region for $Fr = 0.282$.

To identify the free-surface effect on turbulence dissipation, the spatial means of $k/U^2 \times 1000$ were compared, as shown in Figure 4-52. For $Fr = 0.400$, the turbulence intensity near the free-surface was large, but it diminished more rapidly than that in other Fr and depth conditions. This implies that while the violent free-surface generated more turbulence, it also contributed to wake recovery by transporting the turbulence momentum.

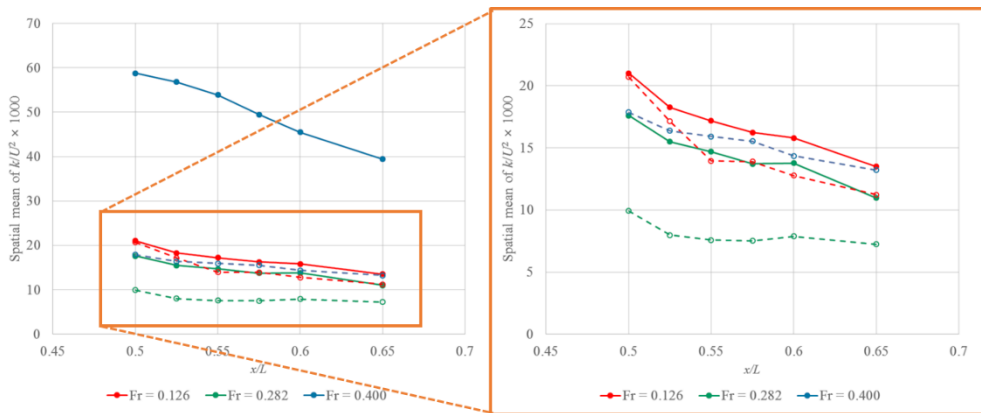


Figure 4-52. $k/U^2 \times 1000$ changes in near-wake region at $z/L = -0.01$ (solid line) and -0.1 (broken line).

Figure 4-53 shows the ratio of $k/U^2 \times 1000$ near the free-surface ($z/L = -0.01$) to that at $z/L = -0.1$. This ratio varied according to the Fr conditions and decreased in the downstream, except for $Fr = 0.126$, where the wake was fully developed.

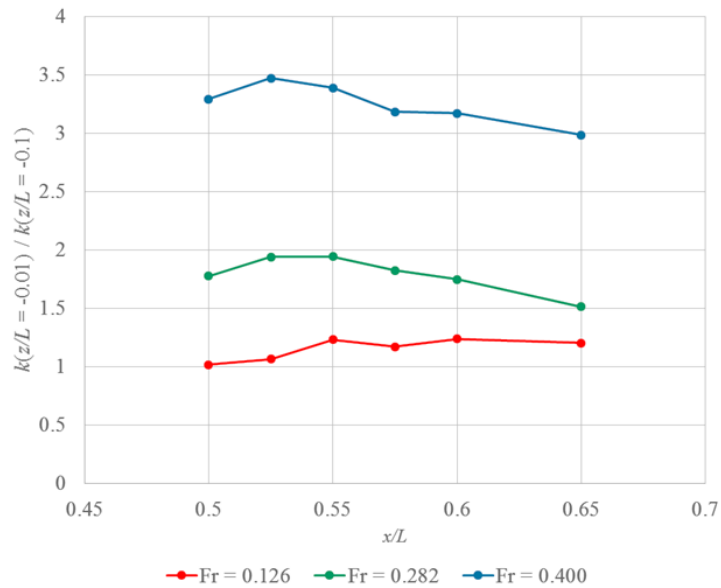


Figure 4-53. Comparison of $k/U^2 \times 1000$ in the near-wake region.

4.3. Coherent turbulence structure

In this section, POD analysis results of flow fields around the large model with Fr variations are presented. Development of coherent turbulence structures in the boundary layer and wake region and their frequency are reported and discussed.

Although Reynolds decompositions provide information of turbulence intensity and structures, POD results have higher dimension than Reynolds decomposition results and provide coherent turbulence structures in the order of their energy level. In this study, turbulence structures at the free-surface and model surface juncture, necklace vortex, and Karman vortex shedding from TE were mainly observed.

4.3.1. $Fr = 0.126$ (smooth and steady free-surface with negligible wave)

Figure 4-54 shows first to six modes of POD results at $x/L = 0.40$. For the Fr condition, free-surface wave was not developed clearly and the coherent turbulence structures were recognizable in the first and second modes only. Low modes showed intense turbulence near the free-surface and model surface juncture. As the mode number increased, the boundary layer turbulence in deep locations appeared whereas turbulence near the free-surface decreased rapidly. Overall, sum of turbulence energies in high modes at the boundary layer was comparable with those around the juncture, as shown in the k distributions in the previous section.

Besides, in the far field, velocity fluctuation in y -direction also appeared in the first mode. Its magnitude was around 30% of the x -directional

fluctuation at the boundary layer, but it only existed in the first mode and became insignificant in higher modes.

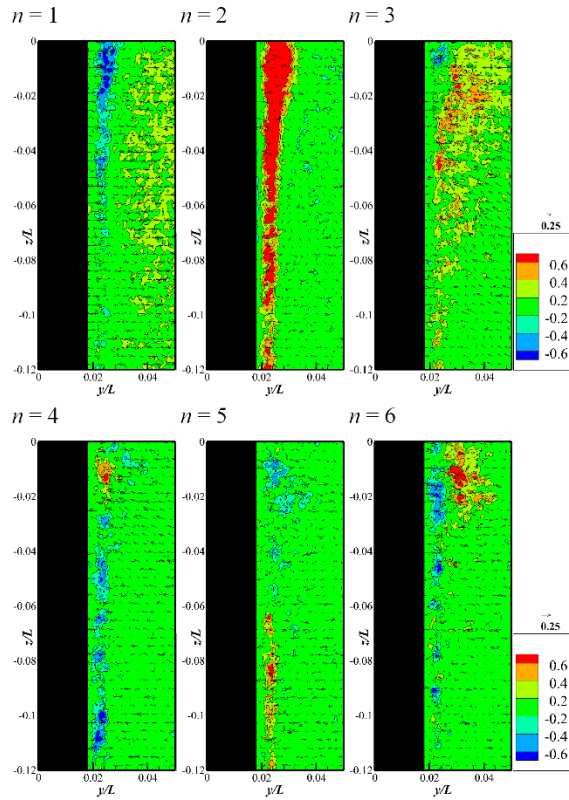


Figure 4-54. Coherent turbulence structures for low modes at $x/L = 0.4$ and $Fr = 0.126$.

Figure 4-55 shows FFT analysis results of $a_n(t)$ at $x/L = 0.40$. The frequency of turbulence fluctuation, f , was identified by FFT. Strouhal number based on the model length, St , was also presented in the results.

$$St = fL/U \quad (4-1)$$

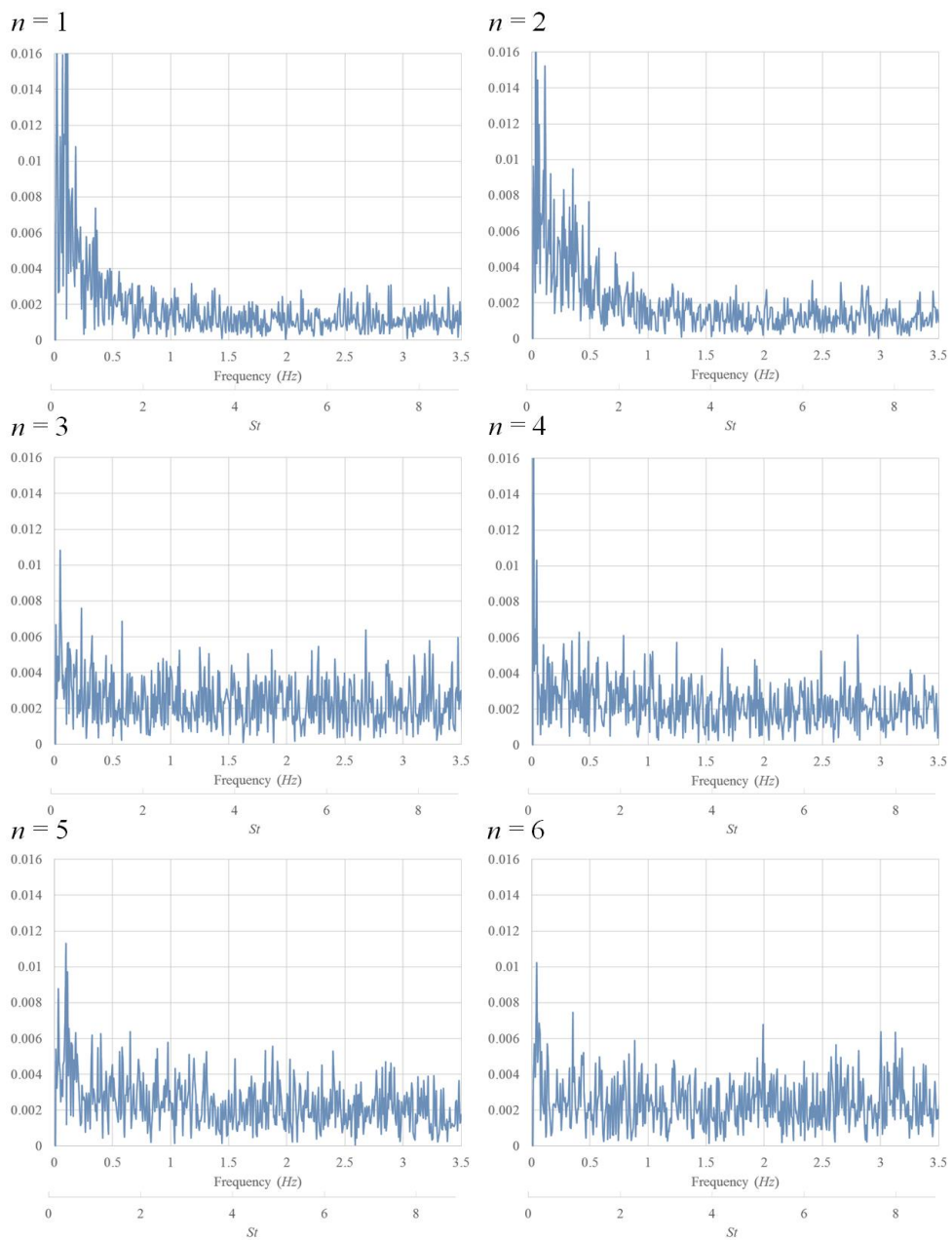


Figure 4-55. Frequency of turbulence fluctuation for low modes at $x/L = 0.4$ and $Fr = 0.126$.

For $n = 1$ and 2, fluctuation of a_n in low frequency was dominant. As the number of modes increased, turbulence structures in small scales appeared and the magnitude of turbulence fluctuation became regardless of frequency. In the high modes, fluctuations in high frequency was expected to be dominant, but spatial and temporal resolution of the SPIV system in this study was insufficient for detecting such small turbulence eddies.

Figures 4-56 and 4-57 show coherent turbulence structures and FFT analysis results of $a_n(t)$ of low modes at $x/L = 0.5$, respectively. At the first mode, u/U at the starboard and port side changed alternately, implying the vortex shedding at the TE. At the mode, horizontal fluctuation due to the vortex shedding was also observed.

The turbulence strength due to vortex shedding increased near the free-surface, but the increase did not continue in deep locations. Second mode showed symmetric longitudinal vortices near the free-surface. At the center of the longitudinal vortices, u/U fluctuated largely.

In high modes, turbulence structures in deep locations were observed, which represents small scale turbulence in 2D wake field. The dominant frequencies of vortex shedding and longitudinal vortices located around 0.5 Hz.

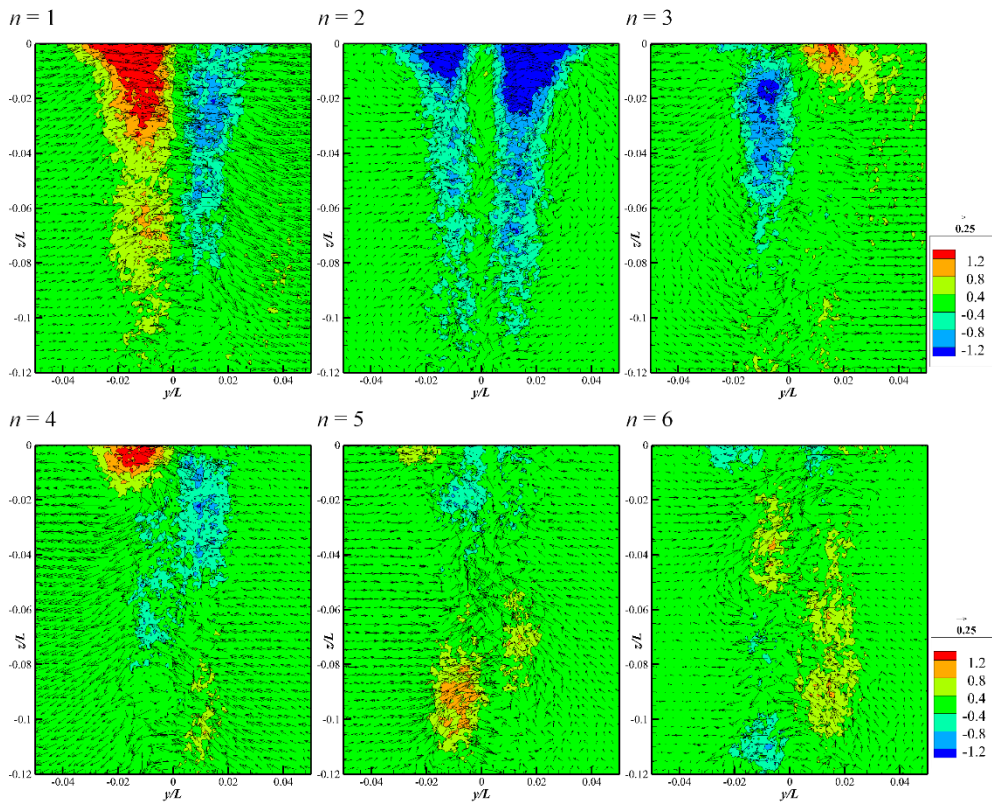


Figure 4-56. Coherent turbulence structures for low modes at $x/L = 0.5$ and $Fr = 0.126$.

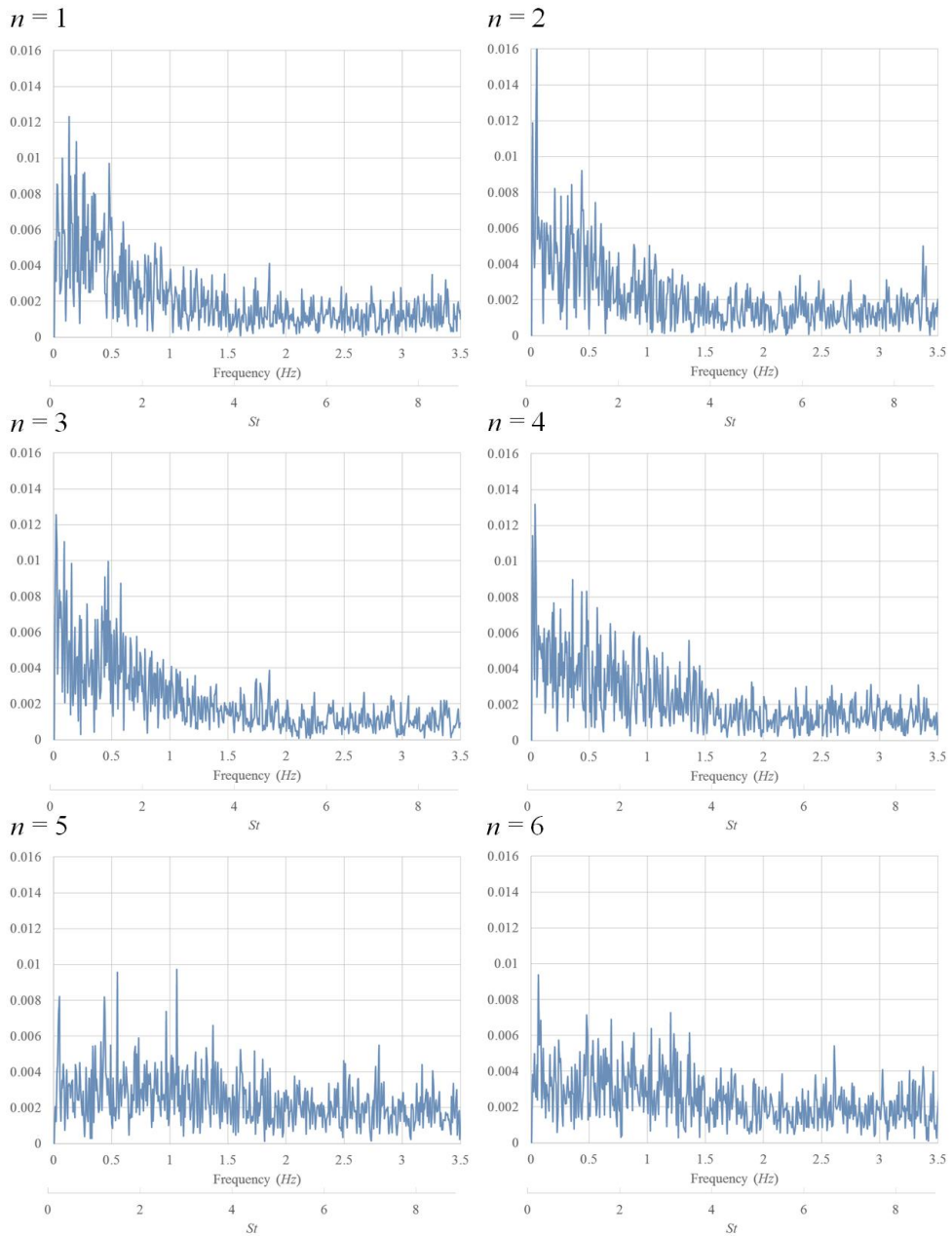


Figure 4-57. Frequency of turbulence fluctuation for low modes at $x/L = 0.5$ and $Fr = 0.126$.

Figure 4-58 shows modes at $x/L = 0.6$. In the near-wake region, strength of the coherent turbulence decreased and remained near the free-surface. First, third and fourth mode only showed turbulence structures affected by the free-surface. The first mode represented vortex shedding, but shed vortex dissipated easily in deep locations. It coincided with the k distribution results, which showed reduction of turbulence dissipation near the free-surface in the wake field. In the wake region, turbulence dissipation was more evident than previous locations and fluctuation in high frequency increased, as shown in Figure 4-59.

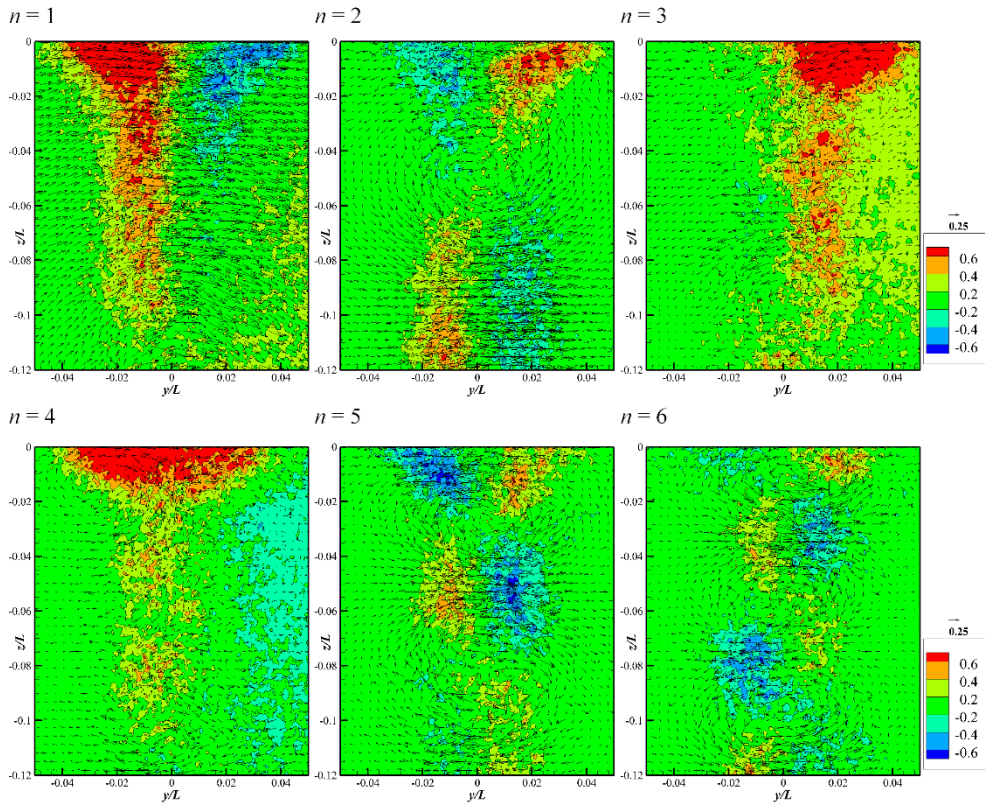


Figure 4-58. Coherent turbulence structures for low modes at $x/L = 0.6$ and $Fr = 0.126$.

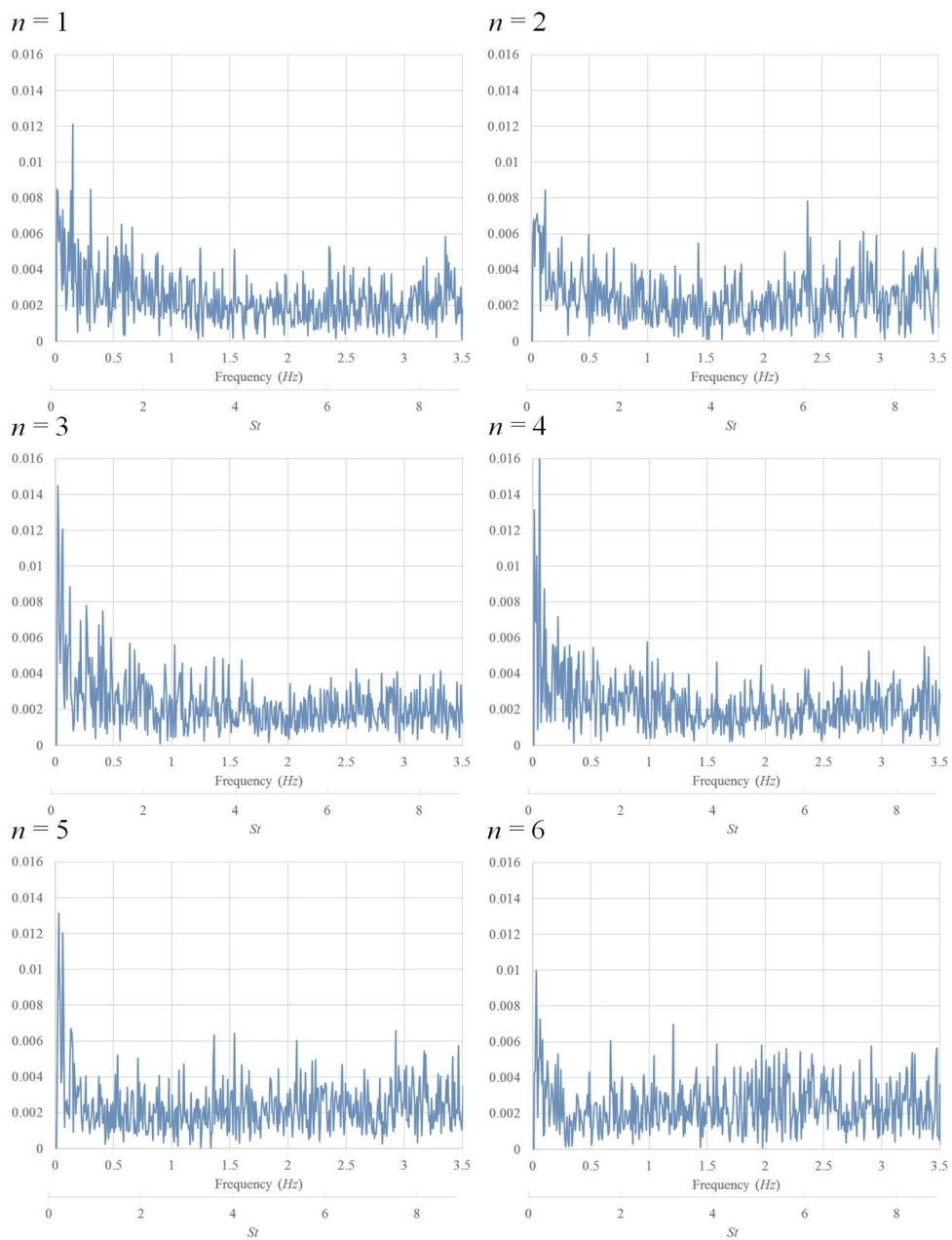


Figure 4-59. Frequency of turbulence fluctuation for low modes at $x/L = 0.6$ and $Fr = 0.126$.

4.3.2. $Fr = 0.282$ (smooth and steady free-surface waves)

For $Fr = 0.282$, the free-surface was smooth and the turbulence characteristics were similar to those for $Fr = 0.126$, but turbulence characteristics were totally different. As shown in Figure 4-60, the turbulence was only visible near the model surface, as the favorable pressure gradient induced by the wave trough suppressed the boundary layer and restrained turbulence generation.

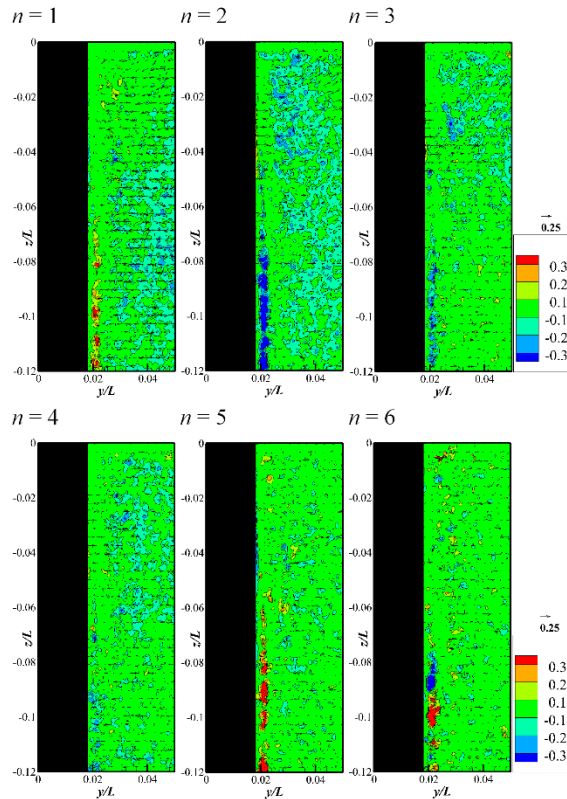


Figure 4-60. Coherent turbulence structures for low modes at $x/L = 0.4$ and $Fr = 0.282$.

Figure 4-61 shows coherent turbulence structures of low modes at $x/L = 0.5$. As the stationary flow region located near the TE, coherent turbulence was concentrated at the juncture. In the same manner as the results for $Fr = 0.126$, alternate u/U distributions and symmetric fluctuation near the juncture were observed in first and second mode respectively.

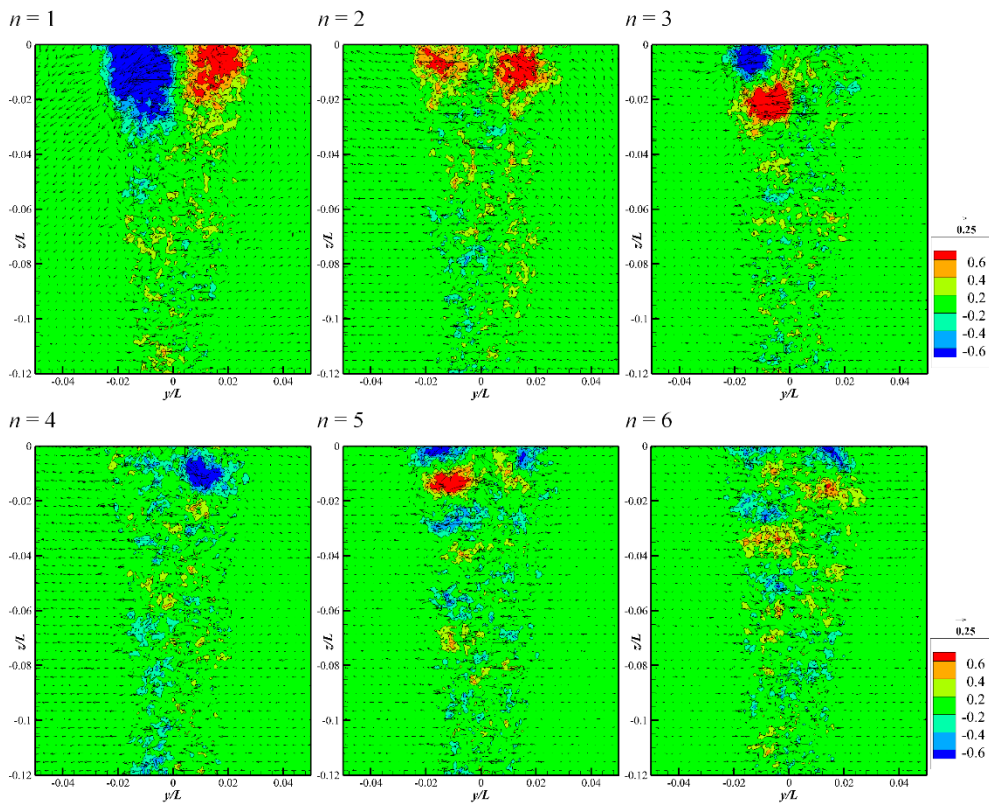


Figure 4-61. Coherent turbulence structures for low modes at $x/L = 0.5$ and $Fr = 0.282$.

Figure 4-62 shows results at $x/L = 0.6$. Turbulence structure in the first mode was alternate u/U distribution, but its strength degraded because of the momentum diffusion and dissipation. The symmetric structure which was

observed in the second mode at $x/L = 0.5$ disappeared and turbulence structure in small scales emerged.

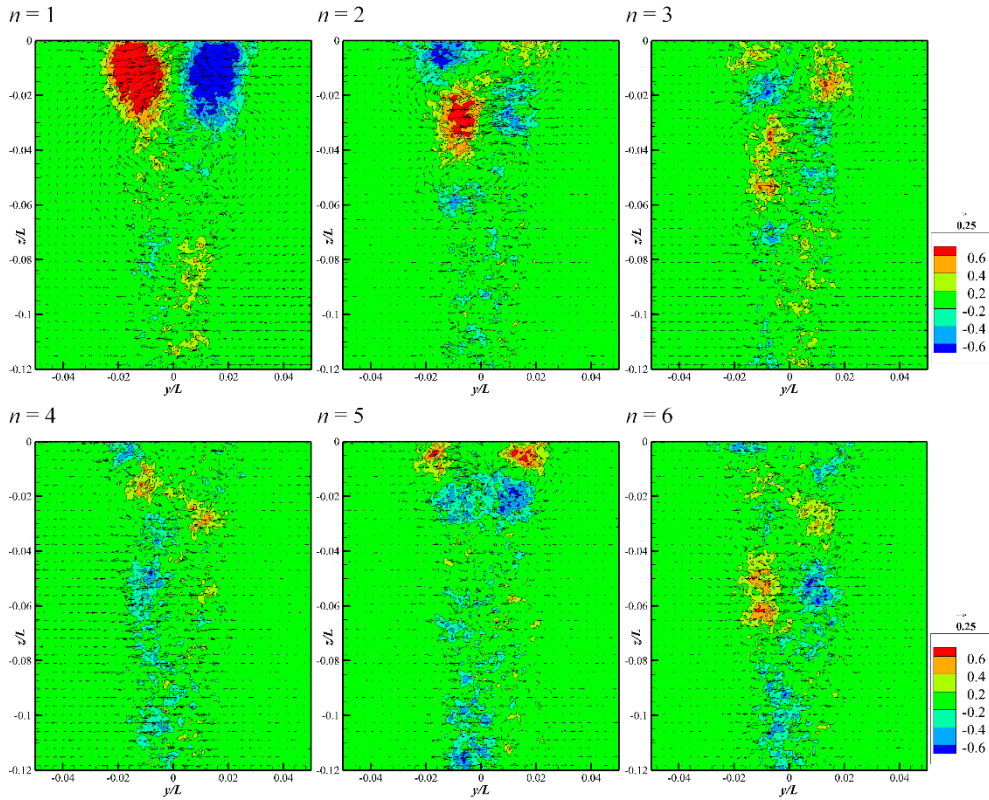


Figure 4-62. Coherent turbulence structures for low modes at $x/L = 0.6$ and $Fr = 0.282$.

FFT results of low modes in frequency domain at $x/L = 0.4, 0.5,$ and 0.6 are shown in Figures 4-63 to 4-65, respectively. As turbulence generation was restrained by free-surface wave at $x/L = 0.4$, turbulence in low frequency was rare. In the near-wake region, only vortex shedding around the stationary flow region had distinguishable turbulence generation in low frequency, but clear peak was not observed.

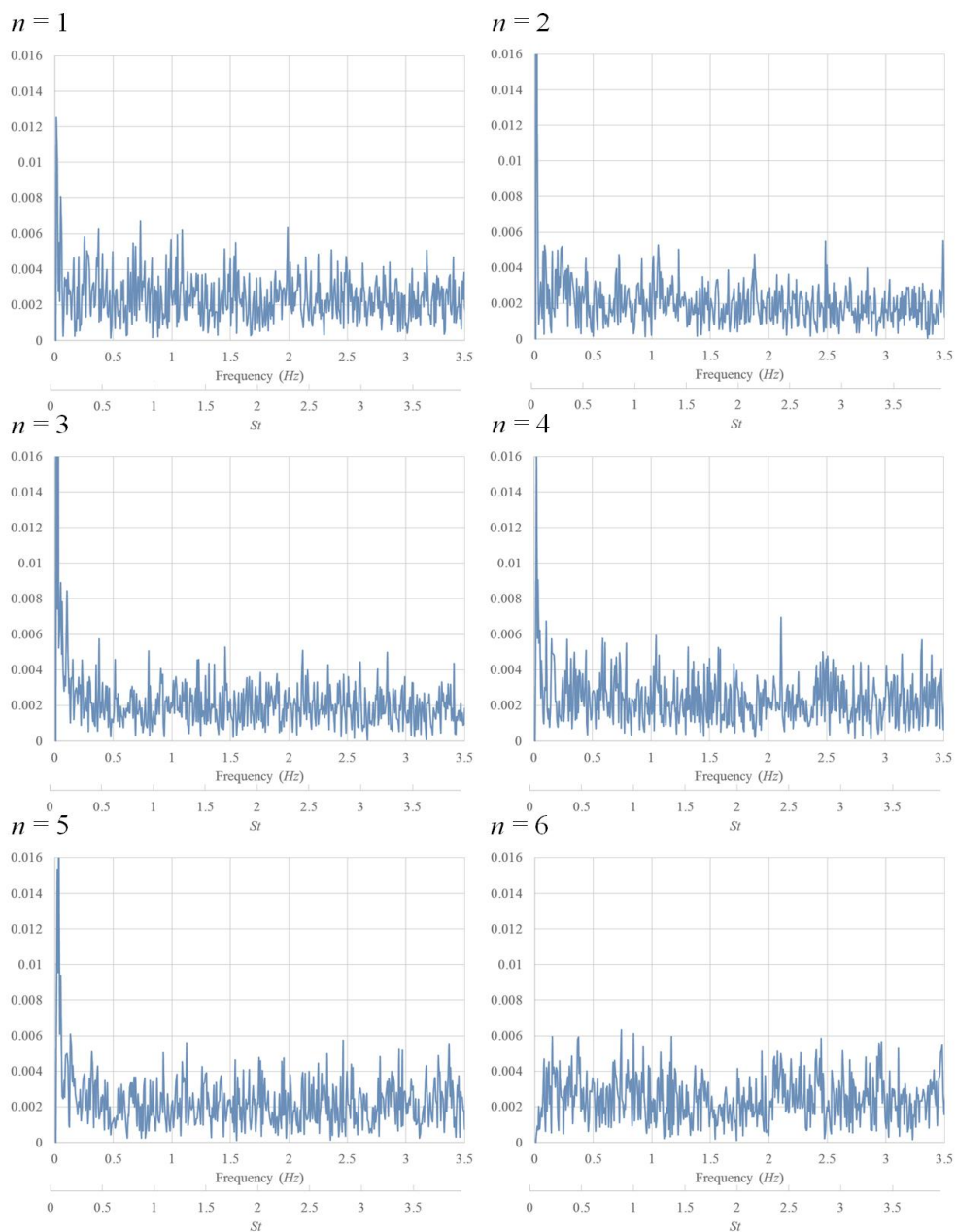


Figure 4-63. Frequency of turbulence fluctuation for low modes at $x/L = 0.4$ and $Fr = 0.282$.

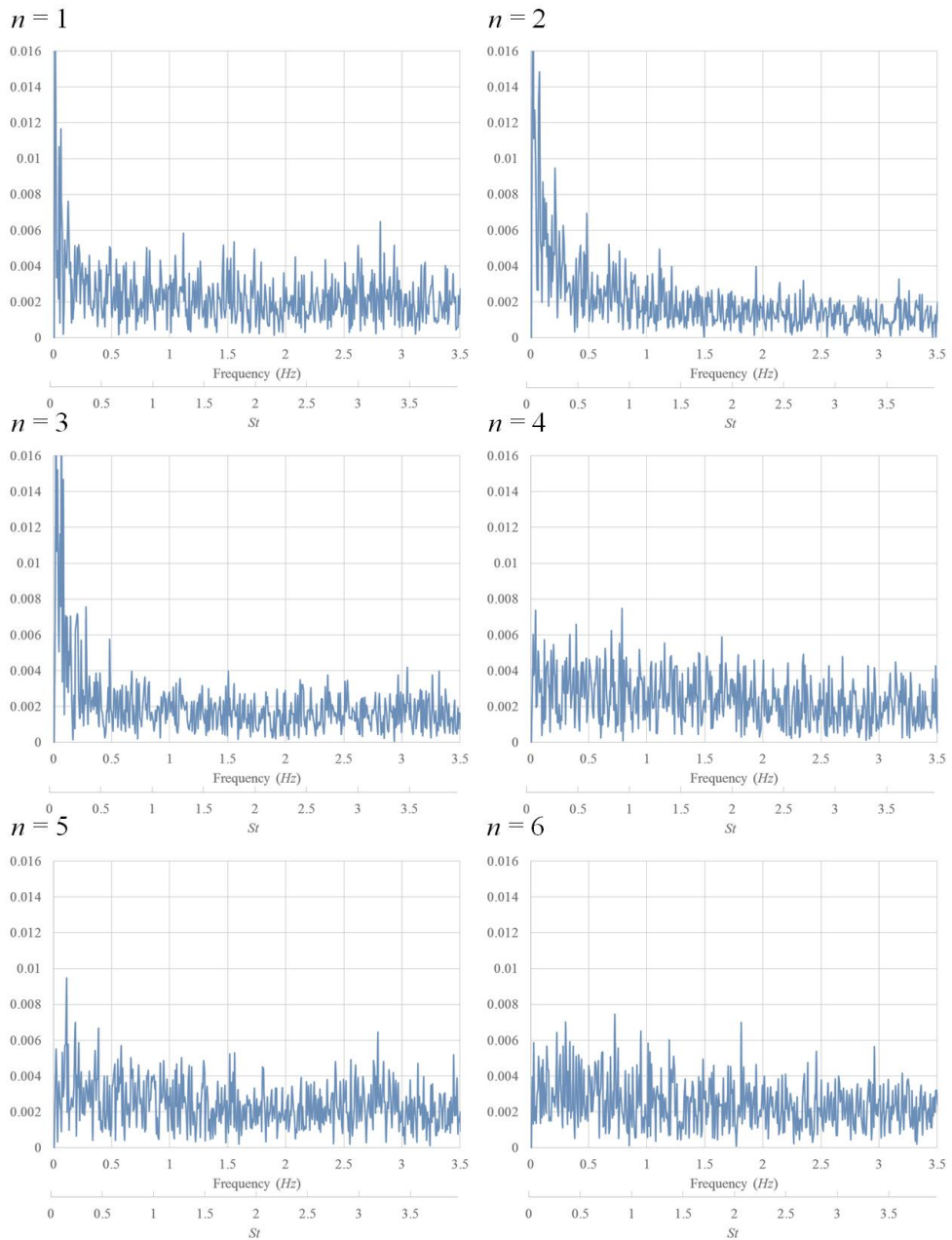


Figure 4-64. Frequency of turbulence fluctuation for low modes at $x/L = 0.5$ and $Fr = 0.282$.

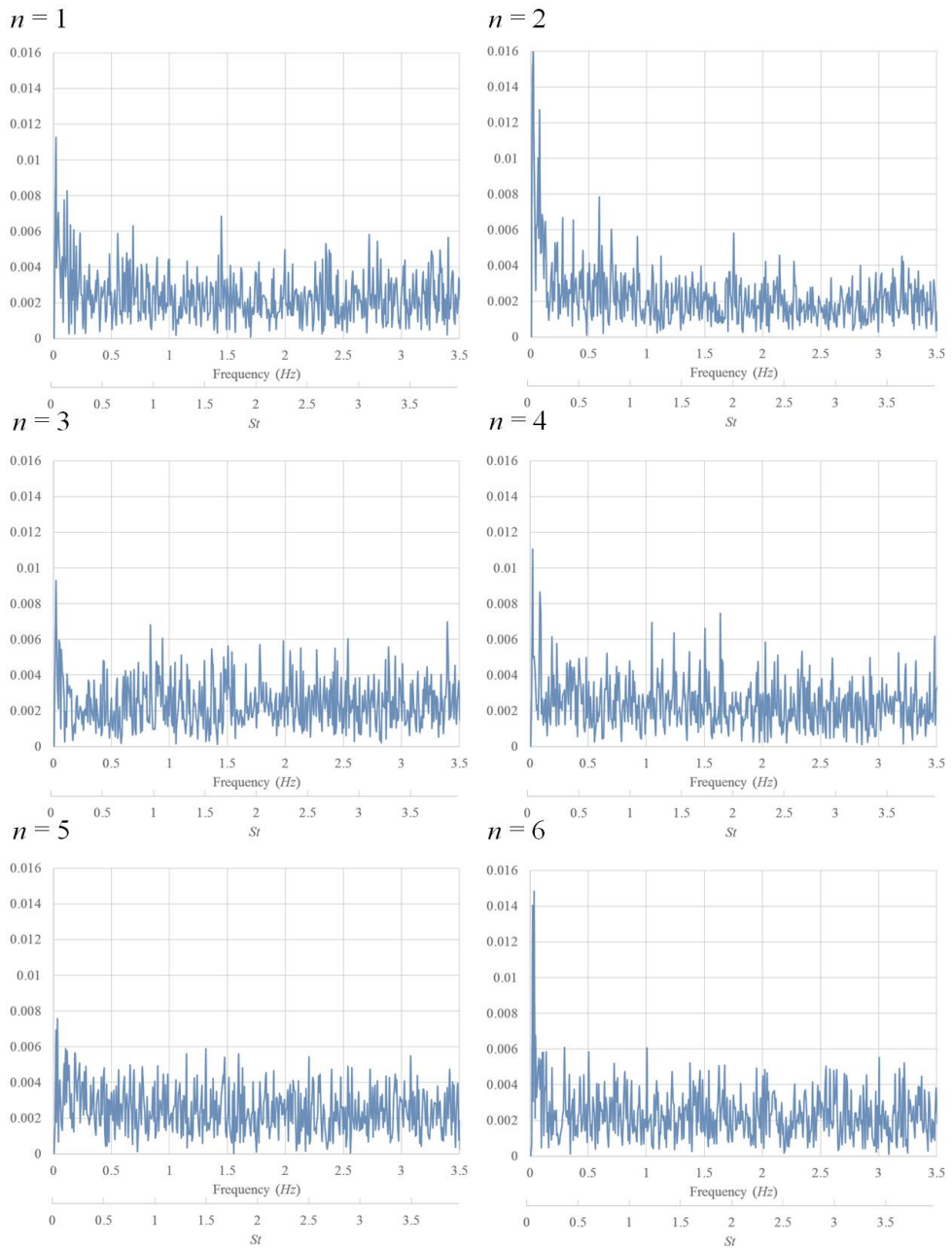


Figure 4-65. Frequency of turbulence fluctuation for low modes at $x/L = 0.6$ and $Fr = 0.282$.

4.3.3. $Fr = 0.400$ (bubbly and unsteady free-surface waves)

Figures 4-66 to 68 show coherent turbulence structures in low modes at $x/L = 0.4, 0.5,$ and $0.6,$ respectively. The air entrainment and bubbly free-surface were observed for the Fr condition, thus strong turbulences around the juncture and under the free-surface were observed. As the order of modes increased, small turbulence structures which are harmonic with the length scale of largest coherent turbulence structure in the first mode appeared.

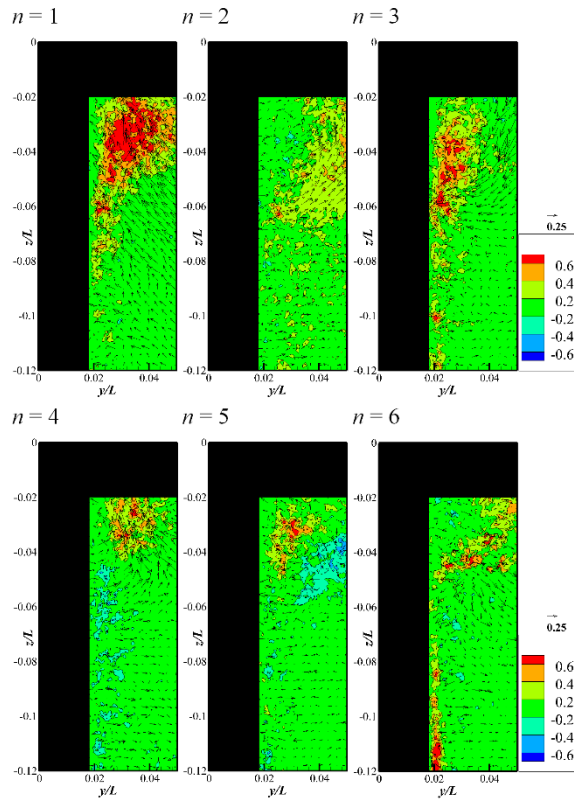


Figure 4-66. Coherent turbulence structures for low modes at $x/L = 0.4$ and $Fr = 0.400$.

Vortex shedding at TE was also observed for this Fr condition. In addition, longitudinal vortices existed at third and fifth mode. At $x/L = 0.6$, longitudinal component of turbulence decreased, but on-plane fluctuation increased.

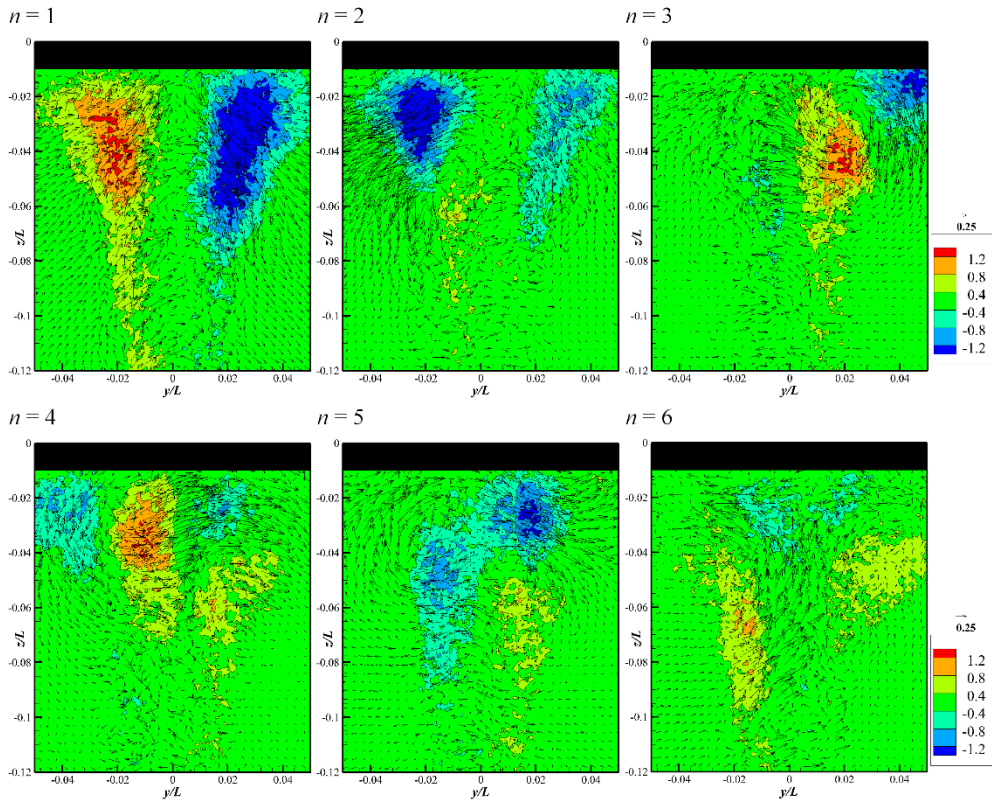


Figure 4-67. Coherent turbulence structures for low modes at $x/L = 0.5$ and $Fr = 0.400$.

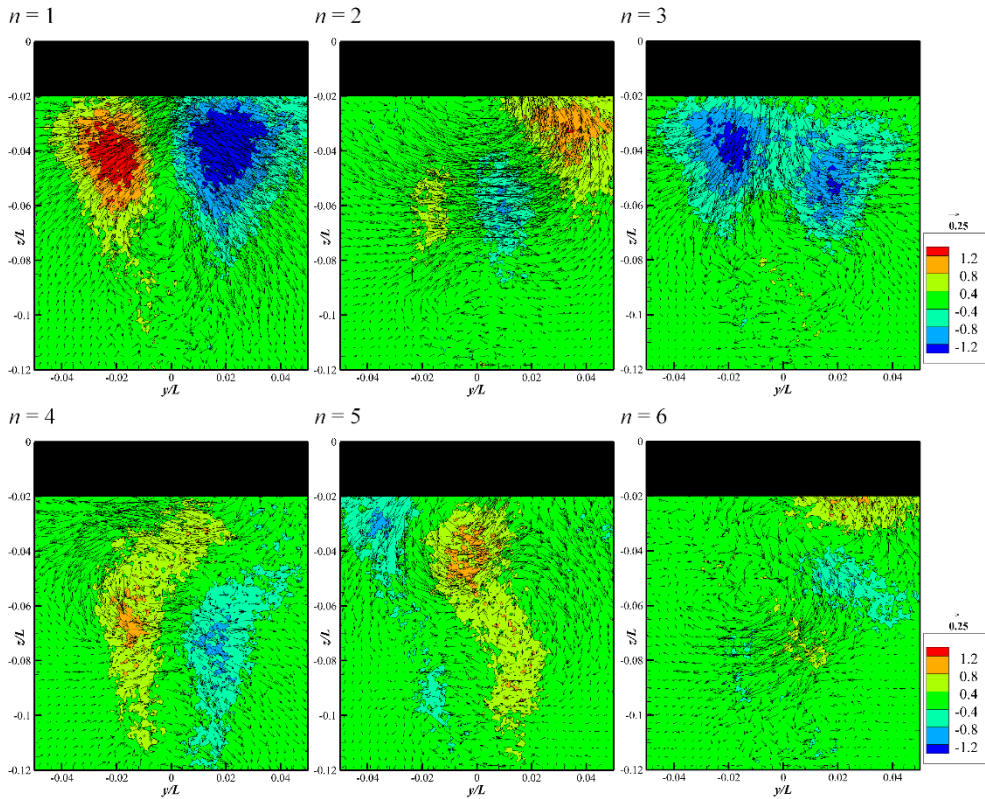


Figure 4-68. Coherent turbulence structures for low modes at $x/L = 0.6$ and $Fr = 0.400$.

Figure 4-69 to 71 show FFT analysis results. As the violent free-surface stirred flow and stimulated turbulence dissipation, time scale of coherent turbulence structures became regular from the second mode. One noteworthy is that there was local peak at 3.3 Hz in the first and second mode at $x/L = 0.4$. The peak was similar to results of wave elevation. Peak at the frequency was not observed at different longitudinal locations.

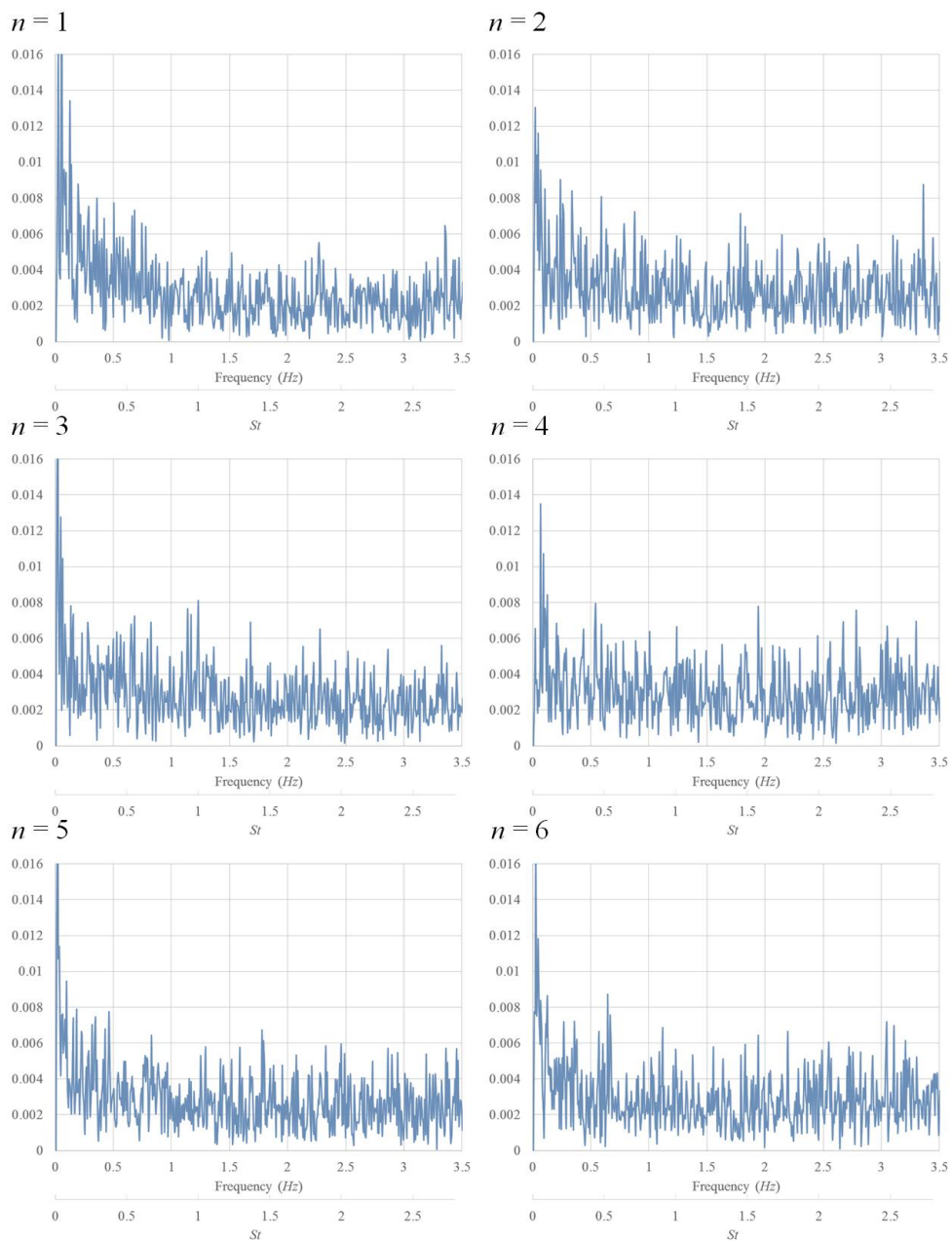


Figure 4-69. Frequency of turbulence fluctuation for low modes at $x/L = 0.4$ and $Fr = 0.400$.

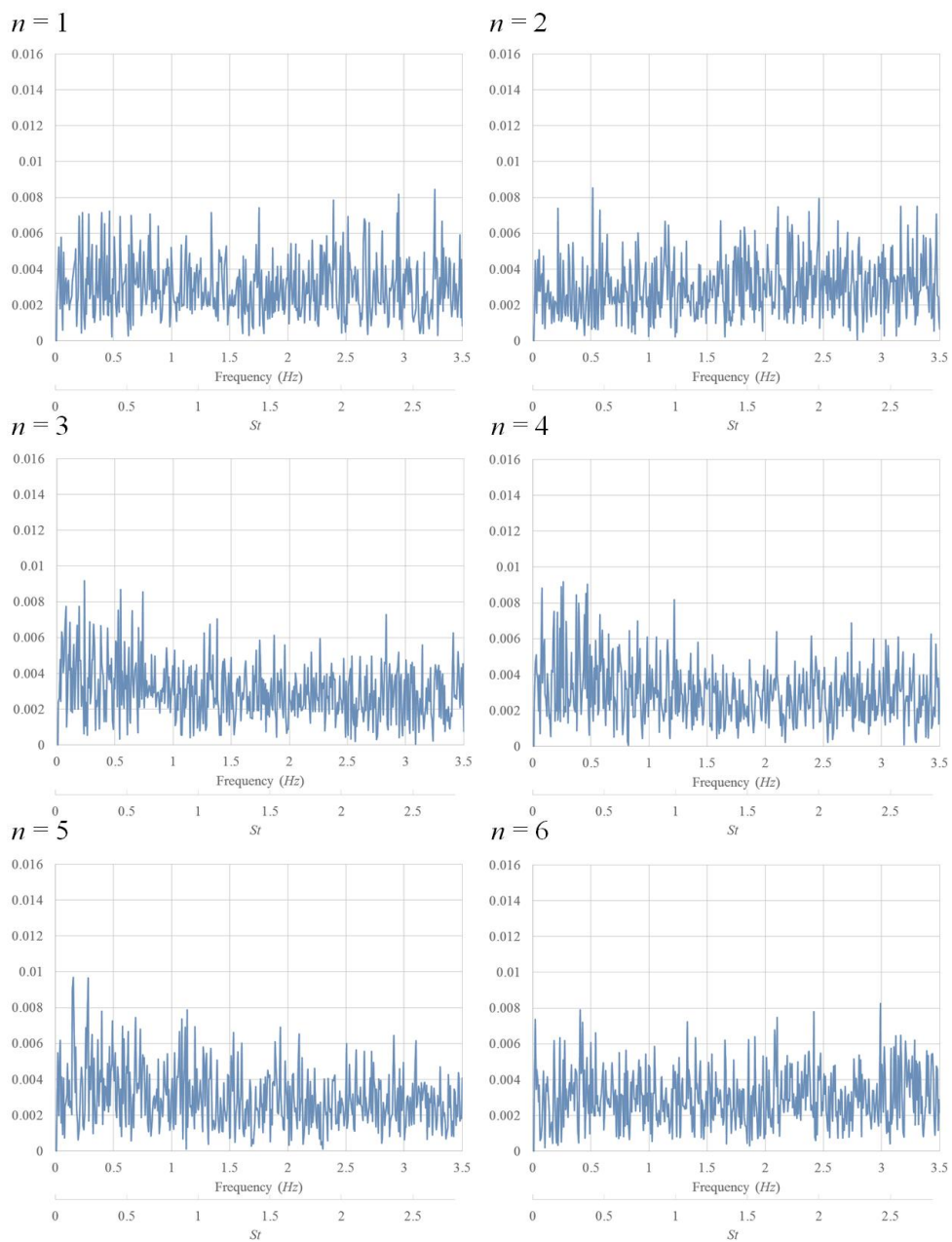


Figure 4-70. Frequency of turbulence fluctuation for low modes at $x/L = 0.5$ and $Fr = 0.400$.

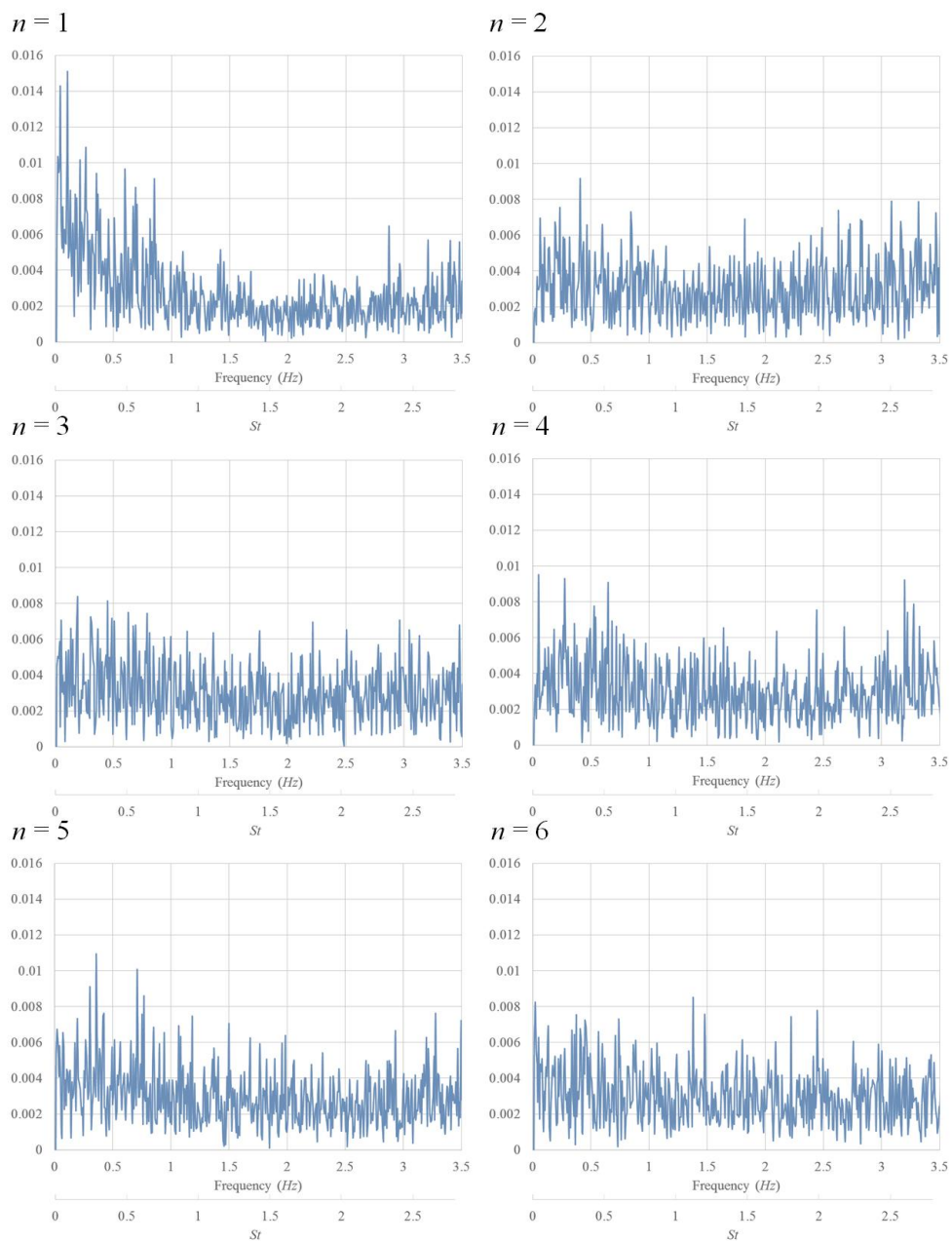


Figure 4-71. Frequency of turbulence fluctuation for low modes at $x/L = 0.6$ and $Fr = 0.400$.

Figure 4-72 shows energy distributions of coherent turbulence structures at $x/L = 0.6$, according to the order of modes. Most of energy modes were concentrated in low modes, regardless of Fr condition. It implies that the turbulence affected by the free-surface is dominant in energy distribution.

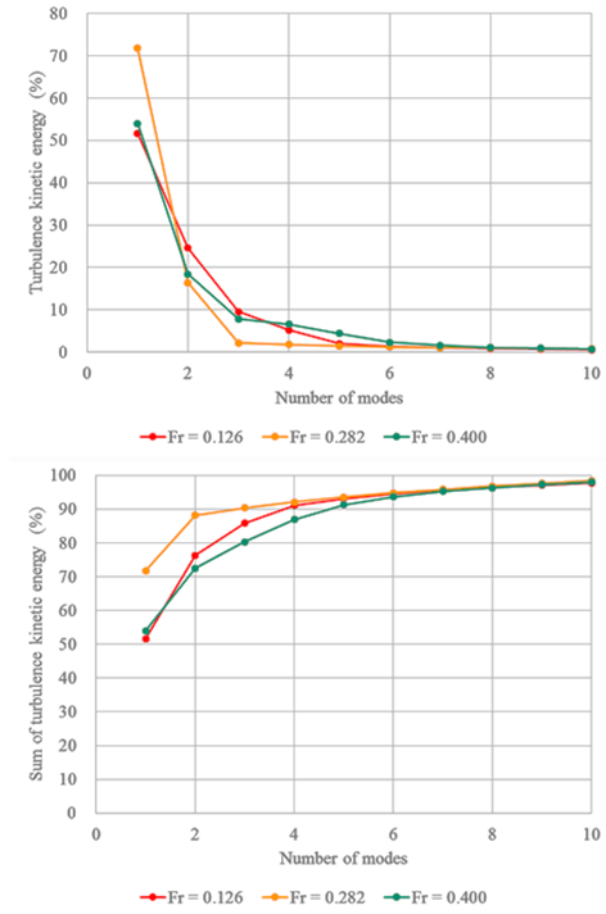


Figure 4-72. Energy distributions of POD results at $x/L = 0.5$.

4.4. Scale effects on the free-surface wave and flow fields

4.4.1. Free-surface elevation in different scales

Figure 4-73 shows changes of the free-surface waves for $Fr = 0.400$, according to Re conditions. In low Re condition, capillary waves were developed around the wave crest. Wave around the model in the intermediate Re condition showed characteristics of high and low Re conditions: capillary waves and bubbly free-surface. The recirculation line at the border of the knobby free-surface, however, was not observed for $Re = 342,000$.

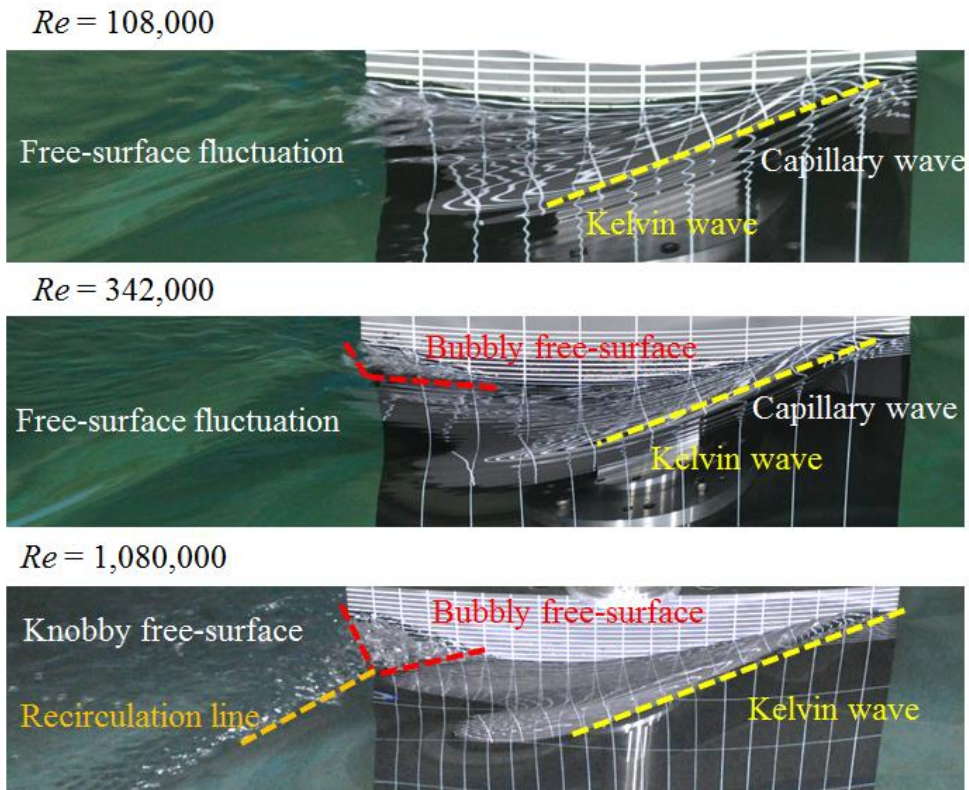
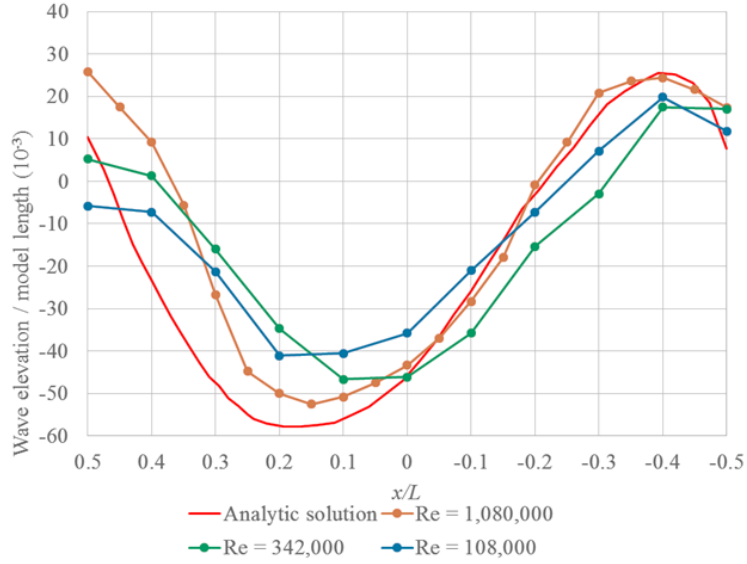


Figure 4-73. Free-surface wave changes for $Fr = 0.400$ according to Re variations.

$Fr = 0.400$



$Fr = 0.282$

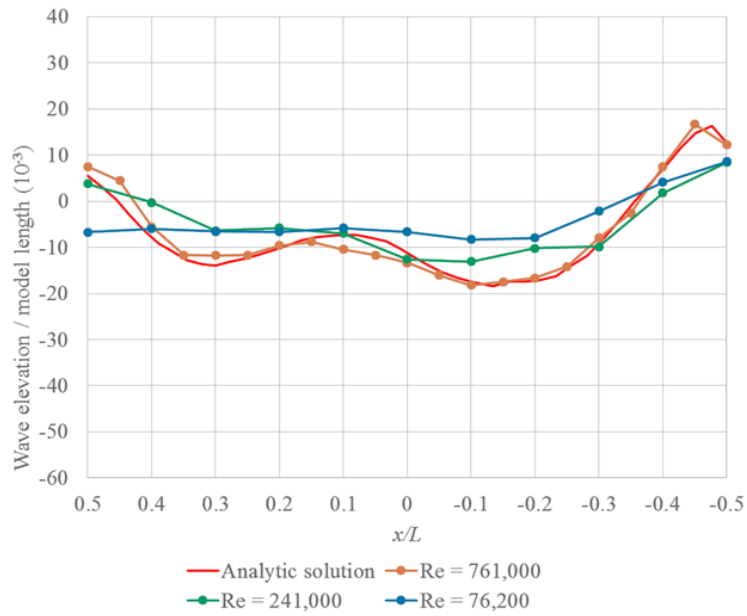


Figure 4-74. Wave elevation around the model for $Fr = 0.400$ and 0.282 with Re variations.

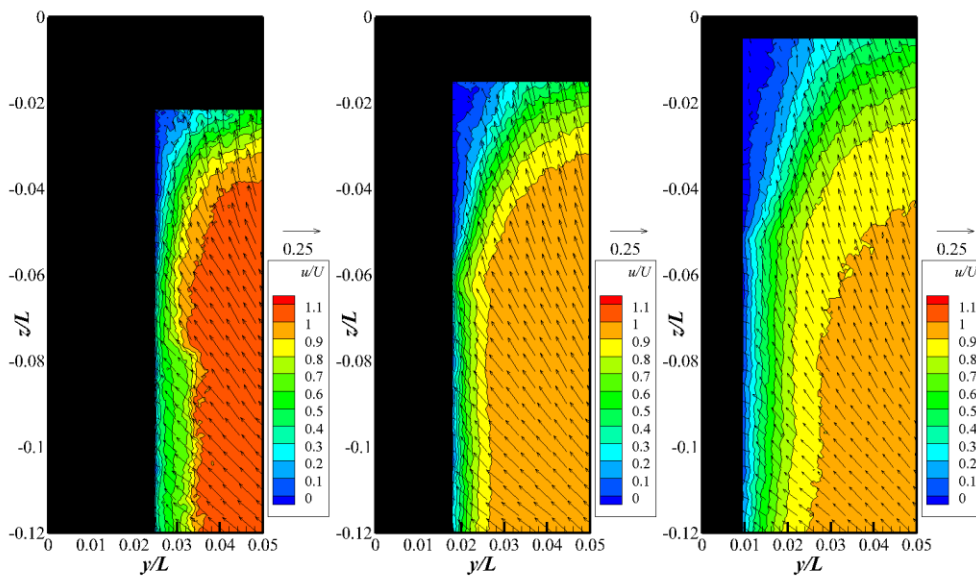
Wave elevations around the model for $Fr = 0.400$ and 0.282 are compared in Figure 4-74. In low Re conditions, viscous drag effects increased; thus, the flow around the model lost its kinetic energy more. It resulted in decrease of wave height changes downstream. The viscous nature in low Re conditions was expected to also restrain orbital motion in waves and turbulence generation.

4.4.2. Boundary layer in different scales

Boundary layer flow fields according to Re variation for $Fr = 0.400$ are shown in Figure 4-75. For two Re conditions, bubbly free-surface behavior was observed and wave-induced separation accompanied. In the previous sections, free-surface effects at the juncture were identified as flow retardation and turbulence generation. As Re decreased, the depth affected by the free-surface decreased. For low Re condition, low-velocity region spread along free-surface, whereas it expanded in vertical direction for high Re condition.

As stated above, wave elevation decreased because of viscosity in low Re conditions. It caused small adverse pressure gradient by free-surface wave, thus free-surface wave effects were limited and the stationary flow region reduced. In the lowest Re condition, free-surface wave decreased more and wave-induced separation and air entrainment were not observed.

$Re = 1,080,000$



$Re = 342,000$

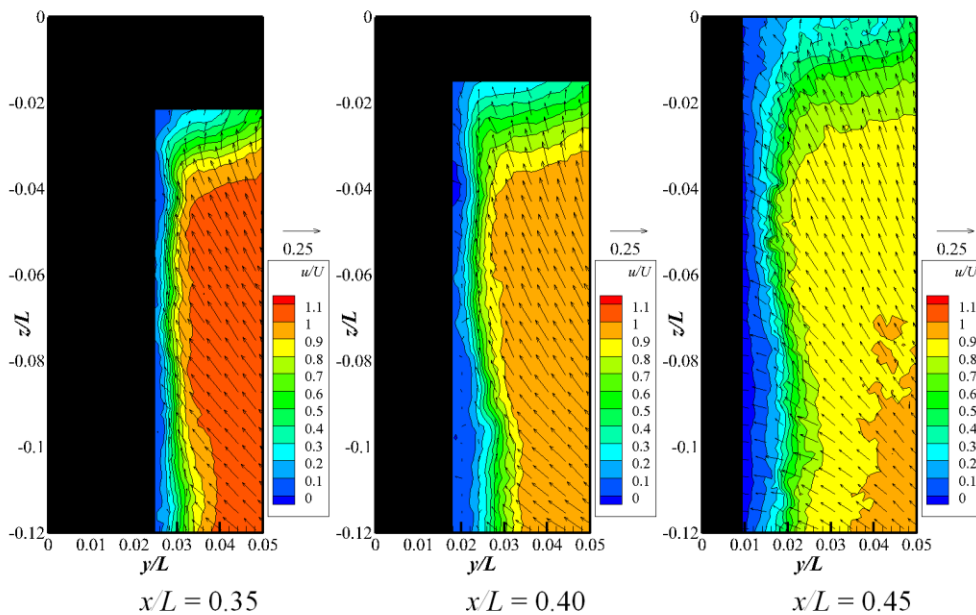


Figure 4-75. u/U contours and on-plane velocity vectors in the boundary layer region for $Fr = 0.400$.

4.4.3. Near-wake in different scales

Figure 4-76 shows mean velocity for $Fr = 0.126$ at $x/L = 0.5$. Free-surface wave was not observed, thus velocity reduction and turbulence generation at the juncture without adverse pressure gradient from free-surface wave could be compared in various Re conditions.

As Re decreased, non-dimensionalized boundary thickness and the depth affected by the free-surface increased. It implied that free-surface effects except wave-induced separation became dominant in low Re condition. Although the boundary layer thickened and flow retarded at TE, flow did not become reverse or separate.

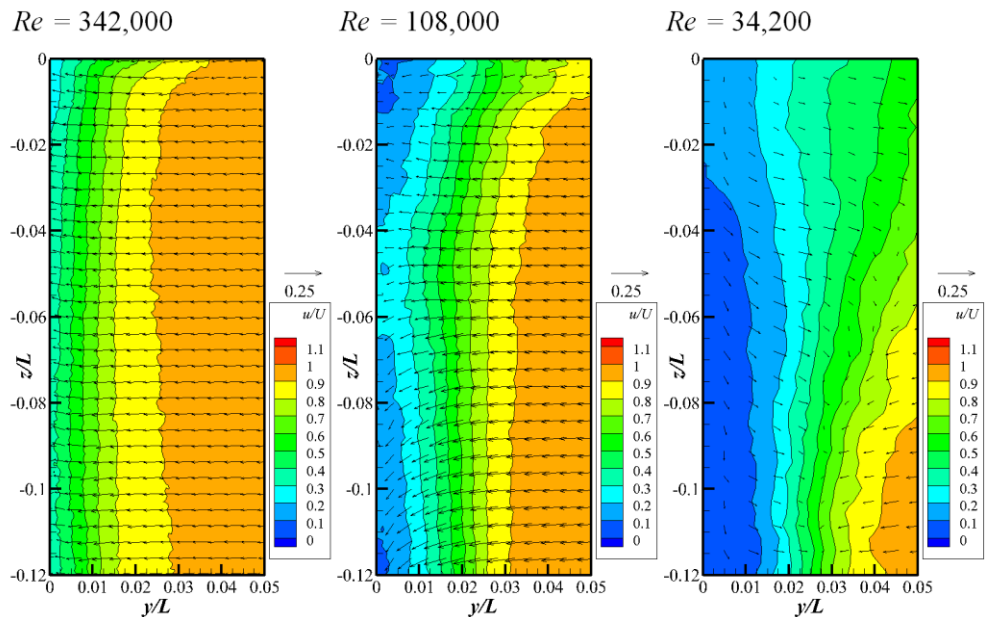


Figure 4-76. $\overline{u/U}$ contours and on-plane velocity vectors at TE with Re variations for $Fr = 0.126$.

Figure 4-77 shows k distribution at $x/L = 0.5$ and $Fr = 0.126$. Non-dimensionalized turbulence kinetic energy increased in low Re condition, as the boundary layer thickness and loss of momentum increased. Lost momentum changed into turbulence in this case.

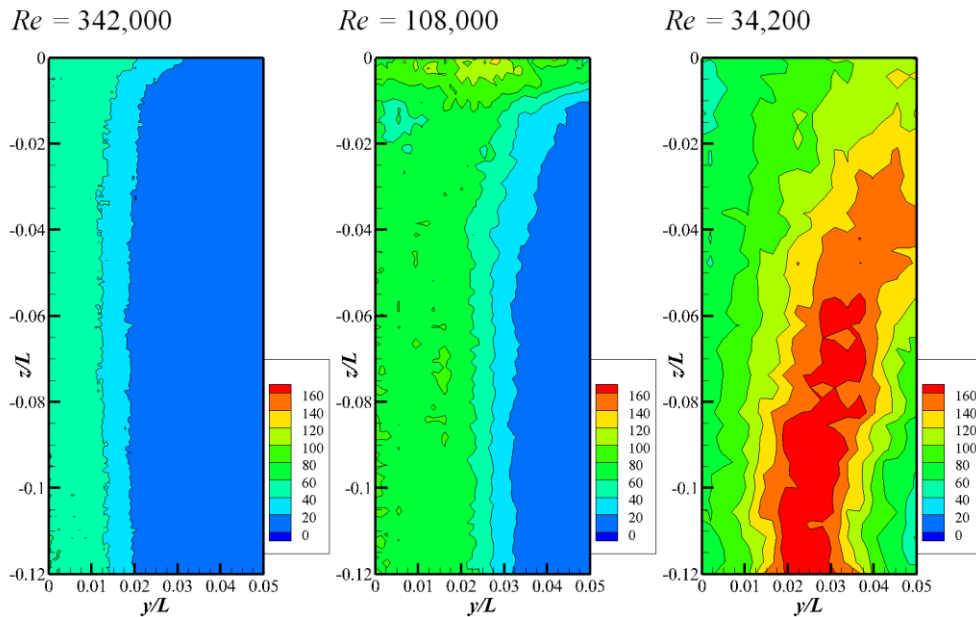


Figure 4-77. $k/U^2 \times 1000$ distribution at TE with Re variations for $Fr = 0.126$.

Figure 4-78 shows flow field at TE for $Fr = 0.400$ with Re variations. Although non-dimensionalized k increased in low Re condition for $Fr = 0.126$, results for $Fr = 0.400$ showed different tendency. The local maxima of k were located at the border of the low velocity region, but its magnitude was similar regardless of Re condition, whereas k due to the boundary layer increased in low Re conditions for $Fr = 0.126$.

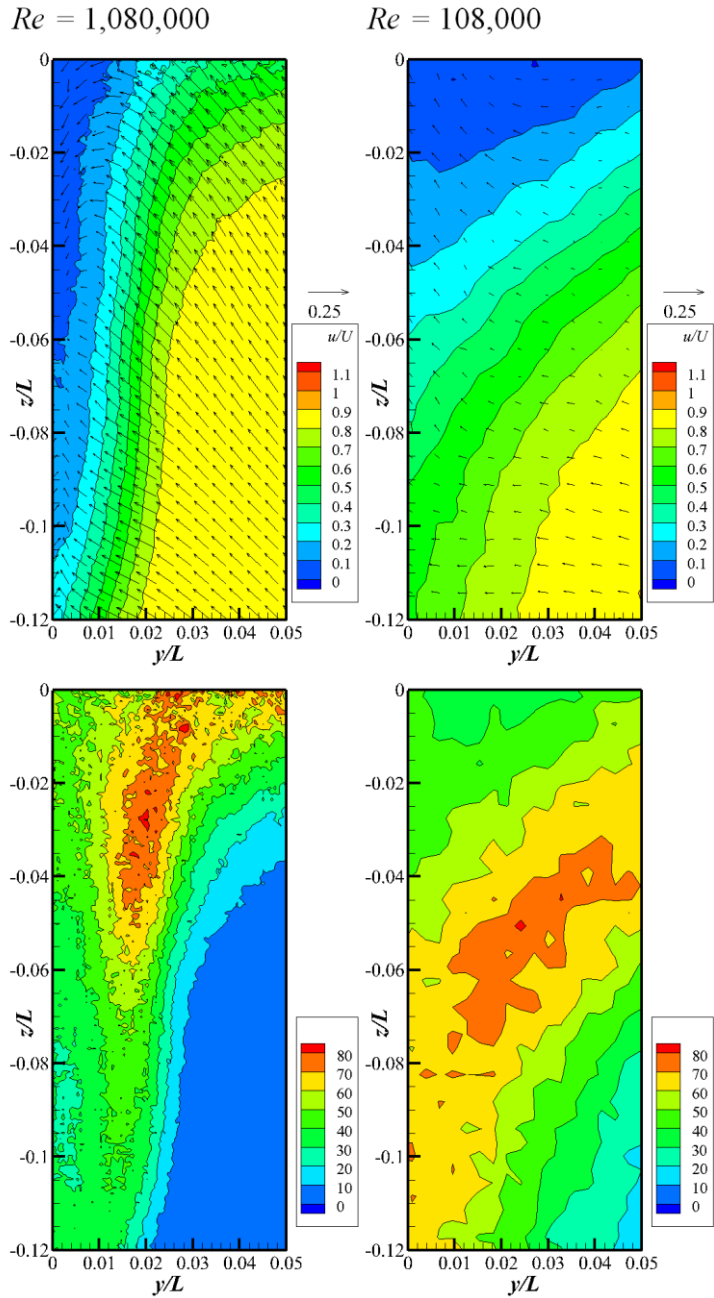
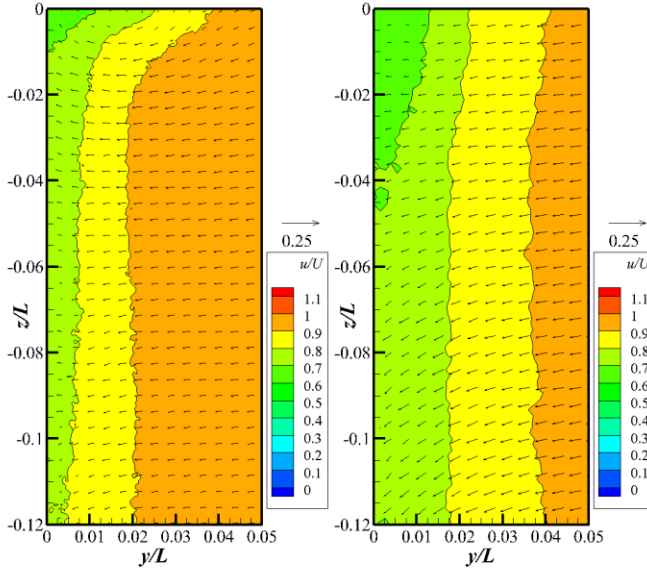
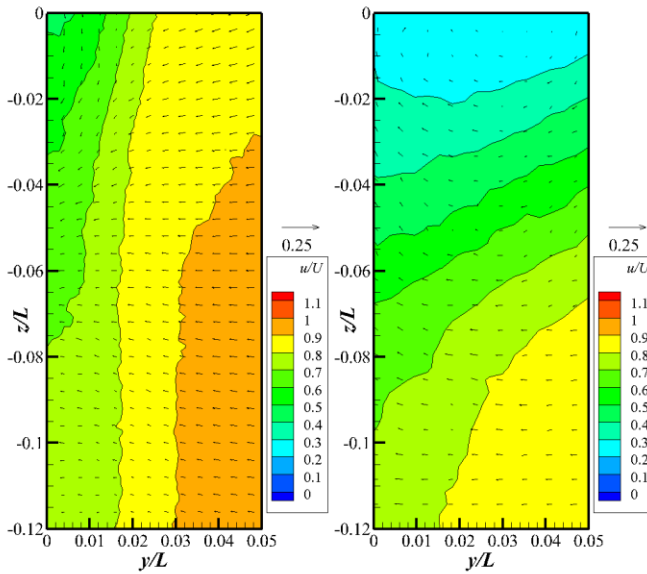


Figure 4-78. Mean velocity (top) and $k/U^2 \times 1000$ (bottom) distribution at TE with Re variations for $Fr = 0.400$.

$Fr = 0.126$



$Fr = 0.400$



$Re = 342,000$

$Re = 108,000$

Figure 4-79. Comparisons of mean velocity at $x/L = 0.6$ with Fr and Re variations.

Figure 4-79 shows mean velocity field at the near-wake region. Although the Fr condition was same, difference of Re caused significant changes. The near-wake fields for $Fr = 0.400$ were affected by the stationary flow region, thus flow velocity was decreased more than those for $Fr = 0.126$, even the Re was same.

Chapter 5. Summary and Conclusions

In this study, free-surface effects on boundary layer and wake field were investigated by flow field and wave elevation measurements around a slender free-surface piercing body. To provide three different wave conditions, *i.e.*, negligible free-surface wave, smooth and steady wave, and violent and unsteady wave with entrainment, three Fr conditions were applied for model tests: 0.126, 0.282, and 0.400. In addition, models of three different sizes were chosen to range Re from 34,200 to 1,080,000. By Fr and Re variations, scale effects on free-surface effects can be identified.

Flow field were measured by towed underwater SPIV and 1D LDV system. Towed SPIV measured 2D3C velocity fields, which were perpendicular to the longitudinal direction. 1D LDV system measured pointwise velocity, for validation of SPIV results. Wave elevation was measured by capacitance type wave height gauge and observation.

Test uncertainty of measurement systems were assessed first. Based on the uniform flow measurement in undisturbed water condition, the systematic error of SPIV and LDV systems were estimated. Owing to the measurement characteristics, SPIV underestimated the Reynolds normal stress.

By repeated tests on ship wake measurement, random error variation of mean velocity and Reynolds normal stress according to the data sample number was estimated. Total uncertainty of the SPIV measurement was 3.18% and 18.8% for mean velocity and Reynolds normal stress, respectively. Test results were compared with existing experimental database, to show good agreement.

Wave elevation around the large model was measured and compared with the analytic solution. The wave elevation decreased in tests because of viscous drag. Wave breaking and air entrainment were observed for $Fr = 0.400$, as reported in previous studies on the surface piercing body. At the entrainment region, fluctuation of the free-surface in certain frequency region appeared. Turbulence dissipation in the wake decreased the fluctuation and increased peak frequency, as the bubbles broke to generate small eddies.

By using the SPIV measurement, development of the boundary layer was investigated for $Fr = 0.126$ and free-surface effects on the boundary layer development were identified first. The boundary layer in deep locations was 2D and showed highly anisotropic turbulence, which mainly contained longitudinal and normal to the surface components. At the juncture of the free-surface and the model surface, flow fluctuation in vertical direction, which was normal to the free-surface, enabled and the turbulence strength increased; it reduced the flow velocity. In POD analysis results, dominant turbulence structure near the juncture appeared in low modes with large turbulence kinetic energy.

In the near-wake field, the free-surface affected the wake recovery and turbulence dissipation. Being compared with 2D flow in deep locations, it was confirmed that the recovery of the wake flow and turbulence dissipation near the free-surface was delayed. The turbulence in the near-wake region was still anisotropic and free-surface effects on the anisotropy did not appear.

The free-surface wave was developed in the intermediate Fr condition. It was steady and smooth, thus orbital motion of water particles in waves was well observed at outside of the boundary layer. The motion decreased exponentially along z -direction, following traditional wave theory. The

boundary layer restrained orbital motion due to no-slip wall. Besides, the turbulence kinetic energy more increased near the free-surface than that in the low Fr condition, but the anisotropy was not affected by the smooth free-surface wave and similar with that in the low Fr condition.

For the Fr condition, viscous boundary layer, free-surface wave and model geometry induced adverse pressure gradient. Near TE, the free-surface fluctuated and knobs were observed. At the free-surface and model surface juncture, reverse flow appeared and k increased at the boundary of the stationary flow region, due to strong shear.

By POD analysis, symmetric longitudinal vortices and vortex shedding at TE were detected. In low POD modes, coherent turbulence structures associated with free-surface were appeared. They fluctuated in low frequency region.

As Fr increased, the knobby free-surface region expended upstream and air entrainment affected the flow underneath it. The violent free-surface behavior stimulated intense turbulence generation, thus the turbulence characteristics at the region was different with that for previous two Fr conditions where smooth free-surface existed.

The bubble generation enabled to velocity fluctuation in vertical direction, which was suppressed in smooth free-surface conditions; thus the turbulence induced by the air entrainment was omnidirectional and decreased anisotropy near the free-surface. The bubbly free-surface also decreased flow velocity and increased turbulence strength. In the near-wake region, however, the knobby free-surface stimulated momentum transportation and turbulence dissipation.

The stationary flow region at $Fr = 0.400$ disturbed progress of the longitudinal vortices, thus POD analysis results showed that Karman vortex shedding near the free-surface was dominant. As the violent free-surface behavior dissipated turbulence in near-wake, turbulence fluctuation in low frequency decreased rapidly in downstream.

In addition, testing models of different sizes followed and the scale effect could be identified. By wave elevation measurement, it was confirmed that the wave elevation decreased in low Re conditions as viscous force became significant. Air entrainment reduced and capillary wave appeared as Re decreased. Viscous force effects were also visible in flow fields. The boundary layer thickness ratio increased, but flow separation along the TE in high Fr condition decreased and localized near the free-surface only.

By a series of model tests, free-surface effects on the boundary layer and wake fields were identified, as follows.

- At the free-surface and model surface juncture, kinetic energy of the flow changed into turbulence and the turbulence became isotropic. In addition, the low-velocity region expanded to the normal direction to the model surface, along the free-surface.
- In the near-wake region, vortex shedding from TE was dominant in turbulence structure. The shedding strengthened near the free-surface, as free-surface tended to enable turbulence generation.

Fr variation caused three different free-surface wave conditions. Comparing results for intermediate and high Fr conditions to that for low Fr condition, effects of smooth waves and air-entrained unsteady waves on the flow field could be examined.

- Smooth and steady wave effects were similar to those of negligible wave in low Fr condition. The orbital motion in waves, however, was appeared and diminished in the boundary layer.
- Violent free-surface resulted in flow separation and isotropic turbulence generation. The flow separation localized on the model surface and grew along z -direction, thus it was confirmed that entire flow under the bubbly free-surface was not reverse and separated.

Re variations changed portion of viscous effects on the flow field and free-surface behavior. Test conditions ranged from laminar to turbulent flow.

- For low Re condition, free-surface wave was restrained and wave elevation decreased. Free-surface wave for high Re conditions were similar to that of analytic solution, except disparity caused by air-entrainment in high Fr condition.
- Low free-surface wave caused small adverse pressure gradient, thus the flow separation at the juncture localized near the free-surface only. Besides, violent free-surface effects on turbulent flow field, *i.e.*, isotropic turbulence and rapid turbulence dissipation, did not exist for low Re condition.

This study concerned SPIV measurement with limited repetition rate, thus POD results showed quantitative results of turbulence frequency only and dominant frequency in free-surface elevation fluctuation did not coincide with the POD results. To analyze flow field results in frequency domain more precisely, PIV measurement with higher repetition rate is needed. In addition, if model surface pressure measurement is conducted, wave elevation, pressure, and flow field results can be compared to each other.

In addition, the flow phenomena revealed in this study were fundamentally

induced by the adverse pressure gradient. By applying drift angle to the model, pressure gradient on the model can be controlled; it can cause the promotion or delay of appearance of bubbly free-surface in high Fr condition, thus research area of the wave-induced separation study can be broaden.

References

Aloisio, G. and Felice, F., 2006, "PIV Analysis around the Bilge Keel of a Ship Model in a Free Roll Decay," *Proceedings of XIV National Meeting of the Italian Association of Laser Velocimetry and Non Invasive Diagnostics*, Rome, Italy, November 6-7.

American Society of Mechanical Engineers, 2005. Test Uncertainty. *The American Society of Mechanical Engineers Performance Test Code*, 19.1

Anschau, P. and Mach, K. P., 2007, "Application of a Stereo PIV System for Investigations of Flow Fields in Towing Tank and Cavitation Tunnel," *Archives of Civil and Mechanical Engineering*, Vol. 7, No. 3, pp. 5-17.

Anthony, D. G. and Willmarth, W. W., 1992, "Turbulence Measurements in a Round Jet beneath a Free-surface," *Journal of Fluid Mechanics*, Vol. 243, pp. 699-720.

Arienti, M. and Soteriou, M. C., 2009, "Time-Resolved Proper Orthogonal Decomposition of Liquid Jet Dynamics," *Physics of Fluids*, Vol. 21, No. 11, 112104.

Battjes, J. A. and Sakai, T., 1981, "Velocity Field in a Steady Breaker," *Journal of Fluid Mechanics*, Vol. 111, pp. 421-437.

Berkooz, G., Holmes, P., and Lumley, J. L., 1993, "The Proper Orthogonal Decomposition in the Analysis of Turbulent Flows," *Annual Review of Fluid Mechanics*, Vol. 25, No. 1, pp. 539-575.

Bertetta, D., Brizzolara, S., Canepa, E., Gaggero, S., and Viviani, M., 2012, "EFD and CFD Characterization of a CLT Propeller," *International Journal of Rotating Machinery*, 2012. DOI: <http://dx.doi.org/10.1155/2012/348939>

Bradshaw, P., 1987, "Turbulent Secondary Flows," *Annual Review of Fluid mechanics*, Vol. 19, pp. 53-74.

Castro, A. M., Carrica, P. M., and Stern, F., 2011, "Full Scale Self-Propulsion Computations Using Discretized Propeller for the KRISO Container Ship KCS," *Computers and Fluids*, Vol. 51, No. 1, pp. 35-47.

Chanson, H., 2007, "Bubbly Flow Structure in Hydraulic Jump," *European Journal of Mechanics-B/Fluids*, Vol. 26, No. 3, pp. 367-384.

Chen, J. H. and Chang, C. C., 2006, "A Moving PIV System for Ship Model Test in a Towing Tank," *Ocean Engineering*, Vol. 33, No. 14, pp. 2025-2046.

Chen, T. and Chwang, A. T., 2002, "Trailing Vortices in a Free-Surface Flow." *Physics of Fluids*, Vol. 14, No. 2, pp. 827-838.

Chevray, R. and Kovasznay, L. S. G., 1969, "Turbulence Measurements in the Wake of a Thin Flat Plate," *AIAA Journal*, Vol. 7, No. 8, pp. 1641-1643.

Chow, S. K., 1967, "Free-Surface Effects on Boundary Layer Separation on Vertical Struts," Ph.D. Thesis, The University of Iowa, Iowa City, IA.

Di Felice, F., Di Florio, D., Felli, M., and Romano, G. P., 2004, "Experimental Investigation of the Propeller Wake at Different Loading Conditions by Particle Image Velocimetry," *Journal of Ship Research*, Vol. 48, No. 2, pp. 168-190.

Diamessis, P. J., Gurka, R., and Liberzon, A., 2010, "Spatial Characterization of Vortical Structures and Internal Waves in a Stratified Turbulent Wake Using

Proper Orthogonal Decomposition,” *Physics of Fluids*, Vol. 22, No. 8, 086601.

El Lababidy, S., Bose, N., Liu, P., Walker, D., and Di Felice, F., 2005, “Experimental Analysis of the Near-wake from a Ducted Thruster at True and Near Bollard Pull Conditions Using Stereo Particle Image Velocimetry (SPIV),” *Journal of Offshore Mechanics and Arctic Engineering*, Vol. 127, No. 3, pp. 191-196.

Falchi, M., Felli, M., Grizzi, S., Aloisio, G., Broglia, R., and Stern, F., 2014, “SPIV Measurements around the DELFT 372 Catamaran in Steady Drift,” *Experiments in Fluids*, Vol. 55, No. 11, pp. 1-20.

Felli, M. and Di Felice, F., 2004, “Analysis of the Propeller-Hull Interaction by LDV Phase Sampling Techniques,” *Journal of Visualization*, Vol. 7, No. 1, pp. 77-84.

Felli, M. and Di Felice, F., 2005, “Propeller Wake Analysis in Nonuniform Inflow by LDV Phase Sampling Techniques,” *Journal of Marine Science and Technology*, Vol. 10, No. 4, pp. 159-172.

Felli, M., Roberto, C., and Guj, G., 2009, “Experimental Analysis of the Flow Field around a Propeller–Rudder Configuration,” *Experiments in Fluids*, Vol. 46, No. 1, pp. 147-164.

Felli, M. and Falchi, M., 2011, “Propeller Tip and Hub Vortex Dynamics in the Interaction with a Rudder,” *Experiments in Fluids*, Vol. 51, No. 5, pp. 1385-1402.

Graftieaux, L., Michard, M., and Grosjean, N., 2001, “Combining PIV, POD and Vortex Identification Algorithms for the Study of Unsteady Turbulent Swirling Flows,” *Measurement Science and Technology*, Vol. 12, No. 9, pp. 1422-1429.

Grizzi, S., Pereira, F., and Di Felice, F., 2010, "A Simplified, Flow-Based Calibration Method for Stereoscopic PIV," *Experiments in Fluids*, Vol. 48, No. 3, pp. 473-486.

Gui, L., Longo, J., and Stern, F., 2001, "Towing Tank PIV Measurement System, Data and Uncertainty Assessment for DTMB Model 5512," *Experiments in Fluids*, Vol. 31, No. 3, pp. 336-346.

Gurka, R., Liberzon, A., and Hetsroni, G., 2006, "POD of Vorticity Fields: A Method for Spatial Characterization of Coherent Structures," *International Journal of Heat and Fluid Flow*, Vol. 27, No. 3, pp. 416-423.

Irvine, M., Longo, J., and Stern, F., 2013, "Forward Speed Calm Water Roll Decay for Surface Combatant 5415: Global and Local Flow Measurements," *Journal of Ship Research*, Vol. 57, No. 4, pp. 202-219.

Jeong, J. and Hussain, F., 1995, "On the Identification of a Vortex," *Journal of Fluid Mechanics*, Vol. 285, pp. 69-94.

Johansson, P. B., George, W. K., and Woodward, S. H., 2002, "Proper Orthogonal Decomposition of an Axisymmetric Turbulent Wake behind a Disk," *Physics of Fluids*, Vol. 14, No. 7, pp. 2508-2514.

Johansson, P. B. and George, W. K., 2006, "The Far Downstream Evolution of the High-Reynolds-Number Axisymmetric Wake behind a Disk. Part 2. Slice Proper Orthogonal Decomposition," *Journal of Fluid Mechanics*, Vol. 555, pp. 387-408.

Jung, D., Gamard, S., and George, W. K., 2004, "Downstream Evolution of the Most Energetic Modes in a Turbulent Axisymmetric Jet at High Reynolds Number. Part 1. The Near-Field Region," *Journal of Fluid Mechanics*, Vol. 514, pp. 173-204.

Kandasamy, M., Xing, T., and Stern, F., 2009, "Unsteady Free-surface Wave-Induced Separation: Vortical Structures and Instabilities," *Journal of Fluids and Structures*, Vol. 25, No. 2, pp. 343-363.

Kim, H., 2014, "Phase-Averaged SPIV Wake Field Measurement for KVLCC2 Propeller Plane in Waves," Ph.D. thesis, Osaka University, Osaka, Japan.

Kim, S. E. and Rhee, S. H., 2006, "Large Eddy Simulation of Turbulent Free-surface Flow around Surface-Piercing Bodies," *Proceedings of the 26th Symposium on Naval Hydrodynamics*, Rome, Italy, September 17-22.

Kim, S. E. and Cokljat, D., 2007, "Evaluation of an URANS-LES Hybrid Approach for Turbulent Free-surface Flows around Surface-Piercing Bodies," *Proceedings of the 9th International Conference on Numerical Ship Hydrodynamics*, Ann Arbor, Michigan, August 5-8, 2007.

Kim, W.-J., Van, S. H., and Kim, D. H., 2001, "Measurement of Flows around Modern Commercial Ship Models," *Experiments in Fluids*, Vo. 31, No. 5, pp. 567-578.

Koo, B., Yang, J., Yeon, S. M., and Stern, F., 2014, "Reynolds and Froude Number Effect on the Flow Past an Interface-Piercing Circular Cylinder," *International Journal of Naval Architecture and Ocean Engineering*, Vol. 6, No. 3, pp. 529-561.

Kucukali, S. and Chanson, H., 2008, "Turbulence Measurements in the Bubbly Flow Region of Hydraulic Jumps," *Experimental Thermal and Fluid Science*, Vol. 33, No. 1, pp. 41-53.

LaVision GmbH., 2012, *Product-Manual for DAVIS 8.1*, LaVision GmbH, Gottingen, Germany.

Lee, J. Y., Paik, B. G., and Lee, S. J., 2009, "PIV Measurements of Hull Wake behind a Container Ship Model with Varying Loading Condition," *Ocean Engineering*, Vol. 36, No. 5, pp. 377-385.

Lee, S. J., Kim, H., Kim, W.-J., and Van, S.-H., 2003, "Wind Tunnel Tests on Flow Characteristics of the KRISO 3,600 TEU Containership and 300K VLCC Double-Deck Ship Models," *Journal of Ship Research*, Vol. 47, No. 1, pp. 24-28.

Lee, S. J., Paik, B. G., Yoon, J. H., and Lee, C. M., 2004, "Three-Component Velocity Field Measurements of Propeller Wake Using a Stereoscopic PIV Technique," *Experiments in Fluids*, Vol. 36, No. 4, pp. 575-585.

Lennon, J. M. and Hill, D. F., 2006, "Particle Image Velocity Measurements of Undular and Hydraulic Jumps," *Journal of Hydraulic Engineering*, Vol. 132, No. 12, pp. 1283-1294.

Liberge, E. and Hamdouni, A., 2010, "Reduced Order Modelling Method via Proper Orthogonal Decomposition (POD) for Flow around an Oscillating Cylinder," *Journal of Fluids and Structures*, Vol. 26, No. 2, pp. 292-311.

Lin, C., Hsieh, S.-C., Lin, I.-J., Chang, K.-A., and Raikar, R. V., 2012, "Flow Property and Self-Similarity in Steady Hydraulic Jumps," *Experiments in Fluids*, Vol. 53, No. 5, pp. 1591-1616.

Logory, L. M., Hirska, A., and Anthony, D. G., 1996, "Interaction of Wake Turbulence with a Free-surface," *Physics of Fluids*, Vol. 8, No. 3, pp. 805-815.

Longo, J., Huang, H. P., and Stern, F., 1998, "Solid-Fluid Juncture Boundary Layer and Wake," *Experiments in Fluids*, Vol. 25, No. 4, pp. 283-297.

Longo, J., Shao, J., Irvine, M., and Stern, F., 2007, "Phase-Averaged PIV for

the Nominal Wake of a Surface Ship in Regular Head Waves,” *Journal of Fluids Engineering*, Vol. 129, No. 5, pp. 524-540.

Lumley, J. L., 1967, “The Structure of Inhomogeneous Turbulent Flows,” *Atmospheric Turbulence and Radio Wave Propagation*, pp. 166-178.

Marquardt, M. W., 2009, "Effects of Waves and the Free-surface on a Surface-Piercing Flat-Plate Turbulent Boundary Layer and Wake," Ph.D. thesis, The University of Iowa, Iowa City, Iowa.

Metcalf, B., Longo, J., Ghosh, S., and Stern, F., 2006, “Unsteady Free-Surface Wave-Induced Boundary-Layer Separation for a Surface-Piercing NACA 0024 Foil: Towing Tank Experiments,” *Journal of Fluids and Structures*, Vol. 22, No. 1, pp. 77-98.

Meyer, K. E., Pedersen, J. M., and Özcan, O., 2007, “A Turbulent Jet in Crossflow Analysed with Proper Orthogonal Decomposition,” *Journal of Fluid Mechanics*, Vol. 583, pp. 199-227.

Misra, S. K., Kirby, J. T., Brocchini, M., Veron, F., Thomas, M., and Kambhamettu, C., 2008, “The Mean and Turbulent Flow Structure of a Weak Hydraulic Jump,” *Physics of Fluids*, Vol. 20, No. 3, 035106.

Murzyn, F., Mouaze, D., and Chaplin, J. R., 2007, “Air-Water Interface Dynamic and Free-surface Features in Hydraulic Jumps,” *Journal of Hydraulic Research*, Vol. 45, No. 5, pp. 679-685.

Muzaferija, S., Peric, M., Sames, P., and Schellin, T., 1998, “A Two-Fluid Navier-Stokes Solver to Simulate Water Entry,” *Proceedings of the 22nd Symposium on Naval Hydrodynamics*, Washington, D.C., August 9-14.

Nobach, H. and Bodenschatz, E., 2009, “Limitations of Accuracy in PIV due

to Individual Variations of Particle Image Intensities,” *Experiments in Fluids*, Vol. 47, No. 1, pp. 27-38.

Paik, B. G., Kim, K. Y., Lee, J. Y., and Lee, S. J., 2010, “Analysis of Unstable Vortical Structure in a Propeller Wake Affected by a Simulated Hull Wake,” *Experiments in Fluids*, Vol. 48, No. 6, pp. 1121-1133.

Paik, J., Escauriaza, C., and Sotiropoulos, F., 2007, “On the Bimodal Dynamics of the Turbulent Horseshoe Vortex System in a Wing-Body junction,” *Physics of fluids*, Vol. 19, 045107, DOI: 10.1063/1.2716813.

Paik, K. J., Hwang, S., Jung, J., Lee, T., Lee, Y. Y., Ahn, H., and Van, S. H., 2015, “Investigation on the Wake Evolution of Contra-Rotating Propeller Using RANS Computation and SPIV Measurement,” *International Journal of Naval Architecture and Ocean Engineering*, Vol. 7, No. 3, pp. 595-609.

Park, S., Oh, G., Rhee, S. H., Koo, B. Y., and Lee, H., 2015, “Full Scale Wake Prediction of an Energy Saving Device by Using Computational Fluid Dynamics,” *Ocean Engineering*, Vol. 101, pp. 254-263.

Patte-Rouland, B., Lalizel, G., Moreau, J., and Rouland, E., 2001, “Flow Analysis of an Annular jet by Particle Image Velocimetry and Proper Orthogonal Decomposition,” *Measurement Science and Technology*, Vol. 12, No. 9, pp. 1404-1412.

Pogozelski, E. M., Katz, J., and Huang, T. T., 1997, “The Flow Structure around a Surface Piercing Strut,” *Physics of Fluids*, Vol. 9, No. 5, pp. 1387-1399.

Rhee, S. H., Makarov, B. P., Krishinan, H., and Ivanov, V., 2005, “Assessment of the Volume of Fluid Method for Free-Surface Wave Flow,” *Journal of Marine Science and Technology*, Vol. 10, No. 4, pp. 173-180.

Rhee, S. H., 2009, "Unsteady Reynolds Averaged Navier–Stokes Method for Free-Surface Wave Flows around Surface-Piercing Cylindrical Structures," *Journal of Waterway, Port, Coastal, and Ocean Engineering*, Vol. 135, No. 4, pp. 135-143.

Richardson, W. J., Greene, C. R., Malme, C. I., and Thomson, D. H., 1995, *Marine Mammals and Noise*, Academic Press, San Diego, CA.

Rowley, C. W., 2005, "Model Reduction for Fluids, Using Balanced Proper Orthogonal Decomposition," *International Journal of Bifurcation and Chaos*, Vol. 15, No. 3, pp. 997-1013.

Salvesen, N., 1969, "On Higher-Order Wave Theory for Submerged Two-Dimensional Bodies," *Journal of Fluid Mechanics*, Vol. 38, No. 2, pp. 415-432.

Savitsky, D., DeLorme, M. F., and Datla, R., 2007, "Inclusion of Whicker Spray Drag in Performance Prediction Method for High-Speed Planing Hulls," *Marine Technology*, Vol. 44, No. 1, pp. 35-56.

Scarano, F., van Wijk, C., and Veldhuis, L., 2002, "Traversing Field of View and AR-PIV for Mid-Field Wake Vortex Investigation in a Towing Tank," *Experiments in Fluids*, Vol. 33, No. 6, pp. 950-961.

Sciacchitano, A., Wieneke, B., and Scarano, F., 2013, "PIV Uncertainty Quantification by Image Matching," *Measurement Science and Technology*, Vol. 24, No. 4, 045302.

Soto, N. A. and Schmid, P. J., 2010, "Dynamic Mode Decomposition of Numerical and Experimental Data," *Journal of fluid mechanics*, Vol. 656, pp. 5-28.

Sen, M., Bhaganagar, K., and Juttijudata, V., 2007, "Application of Proper Orthogonal Decomposition (POD) to Investigate a Turbulent Boundary Layer in a Channel with Rough Walls," *Journal of Turbulence*, Vol. 8, N41.

Seo, J., Seol, D. M., Lim, T. G., Park, S. T., Han, B. W., and Rhee, S. H., 2013, "A Stereo PIV Measurement of a Model Ship Wake in a Towing Tank with Uncertainty Assessment," *Proceedings of 10th International Symposium on Particle Image Velocimetry*, Delft, The Netherlands, July 1-3.

Seo, J., Seol, D. M., Han, B., and Rhee, S. H., 2016, "Turbulence Wake Field Reconstruction of VLCC Models Using two-Dimensional Towed Underwater PIV Measurements," *Ocean Engineering*, Vol. 118, pp. 28-40.

Seol, D. M., Seo, J., and Rhee, S. H., 2013, "Towed Underwater PIV Measurement for Free-Surface Effects on Turbulent Wake of a Surface-Piercing Body," *International Journal of Naval Architecture and Ocean Engineering*, Vol. 5, No. 3, pp. 404-413.

Sherry, M., Nemes, A., Jacono, D. L., Blackburn, H. M., and Sheridan, J., 2013, "The Interaction of Helical Tip and Root Vortices in a Wind Turbine Wake," *Physics of Fluids*, Vol. 25, No. 11, 117102.

Simpson, R. L., 2001, "Junction Flows," *Annual Review of Fluid Mechanics*, Vol. 33, pp. 415-443.

Sirovich, L., 1987, "Turbulence and the Dynamics of Coherent Structures. Part I: Coherent Structures," *Quarterly of Applied Mathematics*, Vol. 45, No. 3, pp. 561-571.

Smith, T. R., Moehlis, J., and Holmes, P., 2005, "Low-Dimensional Modelling of Turbulence Using the Proper Orthogonal Decomposition: a Tutorial," *Nonlinear Dynamics*, Vol. 41, No. 1, pp. 275-307.

Soto, A. A., Johnson, M., Madsen, P. T., Tyack, P. L., Bocconcelli, A., and Borsani, J., 2006, "Does Intense Ship Noise Disrupt Foraging in Deep-Diving Cuvier's Beaked Whales (*Ziphius Cavirostris*)?," *Marine Mammal Science*, Vol. 22, No. 3, pp. 690-699.

Sreedhar, M. and Stern, F., 1998, "Large Eddy Simulation of Temporally Developing Juncture Flows," *International Journal for Numerical Methods in Fluids*, Vol. 28, pp.47-72.

Stella, A., Guj, G., and Di Felice, F., 2000, "Propeller Wake Flow Field Analysis by Means of LDV Phase Sampling Techniques," *Experiments in Fluids*, Vol. 28, No. 1, pp. 1-10.

Stern, F., Hwang, W. S., and Jaw, S. Y., 1987, "Effects of Waves on the Wake of a Surface-Piercing Flat Plate: Experiment and Theory," *IHR Report No. 318*, Iowa Institute of Hydraulic Research, The University of Iowa, Iowa City, Iowa.

Stern, F., Hwang, W. S., and Jaw, S. Y., 1989, "Effects of Waves on the Boundary Layer of a Surface-Piercing Flat Plate: Experiment and Theory," *Journal of Ship Research*, Vol. 33, No. 1, pp. 63-80.

Stern, F., Choi, J. E., and Hwang, W. S., 1993, "Effects of Waves on the Wake of a Surface-Piercing Flat Plate: Experiment and Theory," *Journal of Ship Research*, Vol. 37, No. 2, pp. 102-118.

Svendsen, IB A., Veeramony, J., Bakunin, J., and Kirbvy, J. T., 2000, "The Flow in Weak Turbulent Hydraulic Jumps," *Journal of Fluid Mechanics*, Vol. 418, pp. 25-57.

Taunton, D. J., Hudson, D. A., and Shenoi, R. A., 2010, "Characteristics of a Series of High Speed Hard Chine Planing Hulls – Part 1: Performance in Calm

Water,” *International Journal of Small Craft Technology*, Vol. 152, pp.55-75.

Timmins, B. H., Wilson, B. W., Smith, B. L., and Vlachos, P. P. 2012, “A Method for Automatic Estimation of Instantaneous Local Uncertainty in Particle Image Velocimetry Measurements,” *Experiments in Fluids*, Vol. 53, No. 4, pp. 1133-1147.

Wieneke, B., 2005, “Stereo-PIV Using Self-Calibration on Particle Images,” *Experiments in Fluids*, Vol. 39, No. 2, pp. 267-280.

Wigley, W. C. S., 1934, "A Comparison of Experiment and Calculated Wave-Profiles and Wave-Resistances for a Form Having Parabolic Waterlines," *Proceedings of the Royal Society of London. Series A, Containing Papers of a Mathematical and Physical Character*, Vol. 144, No. 851, pp. 144-159.

Xing, T., Kandasamy, M., and Stern, F., 2007, “Unsteady Free-Surface Wave-Induced Separation: Analysis of Turbulent Structures Using Detached Eddy Simulation and Single-Phase Level Set,” *Journal of Turbulence*, Vol. 8, No. 44.

Yoon, H., Gui, L., Bhushan, S., and Stern, F., 2014, “Tomographic PIV Measurements for a Surface Combatant at Straight Ahead and Static Drift Conditions,” *Proceedings of 30th Symposium on Naval Hydrodynamics*, Hobart, Tasmania, Australia. November 2-7.

Yoon, H., Longo, J., Toda, Y., and Stern, F., 2015, “Benchmark CFD Validation Data for Surface Combatant 5415 in PMM Maneuvers–Part II: Phase-Averaged Stereoscopic PIV Flow Field Measurements,” *Ocean Engineering*, Vol. 109, pp. 735-750.

Zhang, Z. J., and F. Stern, 1996, "Free-Surface Wave-Induced Separation," *Journal of Fluids Engineering*, Vol. 118, No. 3, pp. 546-554.

초 록

본 연구에서는 수면 관통 물체 주위의 경계층과 후류 유동에 자유수면이 미치는 영향을 유동장과 수면 계측을 통해 확인하였다. 세 가지의 다른 파 조건을 적용하기 위해 0.126, 0.282, 0.400 의 Froude 수 조건에 대해 실험을 수행하였다. 그리고 세 가지 크기의 모형을 이용하여 Reynolds 수는 34,200 에서 1,080,000 의 범위에 놓여 있도록 하였다.

모형 주위 수면 변화를 용량식 파고계를 통해 기록하였다. 이전 연구와 같이, 쇄파와 거품이 이는 수면 현상이 Froude 수 0.400 조건에서 모형 뒷날 근처에서 발달하는 것을 확인하였다. 이러한 수면에서는 수면 파고가 특정한 주파수로 요동하였다.

실험 모형 주위의 유동장은 뒷날 전후의 경계층과 후류 영역에 대해 계측되었다. 스테레오스코픽 입자영상유속계(Stereoscopic Particle Image Velocimetry, SPIV)를 이용하였으며, 모형의 길이 방향에 대해 수직인 평면에서의 3 차원 속도 성분을 얻을 수 있었다.

SPIV 를 이용하여 우선 수면파가 거의 발생하지 않은 0.126 의 Froude 수 조건에서의 유동장을 계측하였다. 자유수면과 모형 표면의 접점에서 유동이 수면에 대해 수직 방향으로 요동하였으며, 유속을 감소시켰다. 이 영역에서 난류강도가 증가하였고, 유동이 등방성을 띠었다. 후류 영역에서는 자유수면은 유속 회복과 난류 소산을 지연시켰다.

중간 Froude 수 조건에서는 자유수면파가 발생하였는데, 전체적으로 매끄러운 수면이 나타났다. SPIV 계측을 통해 난류 경계층 바깥에서의 오비탈 운동이 잘 확인되었다. 경계층은 오티발 운동을 제한하는 역할을 하였다. 모형의 뒷날을 지나서는 자유수면이 요동하였으며, 모형과 이러한 자유수면의 교점에서는 역방향의 유동이 나타났다. 이 영역 경계에서는 강한 전단 응력으로 인해 난류운동에너지가 증가하였다.

Froude 수가 증가함에 따라 수면의 요동이 앞으로 발달하였고 그 아래의 유동에 영향을 미치는 것을 확인하였다. 자유수면 요동으로 인해 발생한 난류는 등방성의 성질을 가졌다. 후류 영역에서는 수면 요동이 운동량의 전달과 난류 소산에 영향을 미쳤으며 적합직교분해를 통해 지배적인 난류 구조가 상대적으로 긴 주기로 나타남을 알게 되었다.

이에 더하여 서로 다른 크기의 모형을 이용한 실험을 통해 Reynolds 수의 영향을 확인하였다. 낮은 Reynolds 수 조건에서는 점성의 영향이 증가하여 파고 변화가 줄어들었다. 그리고 경계층 두께가 증가하였으며 파인성 박리 현상은 수면 근처에만 한정하여 발생하였다.

주요어: 자유수면, 난류경계층, 파인성 박리, 모형시험, 스테레오스코픽 입자영상유속계

학번: 2010-21102